Topological phases with ultracold atoms and photons

Alexandru Petrescu

Yale

Topological phases with ultracold atoms and photons

A Dissertation
Presented to the Faculty of the Graduate Schools
of the École Polytechnique
and of Yale University
in Candidacy for the Degree of
Doctor of Philosophy

by
Alexandru Petrescu

Defended on August 27^{th}, 2015, at Yale University, in front of a committee composed of École Polytechnique and Yale University faculty members.

Prof. Karyn Le Hur	École Polytechnique	Dissertation Director
Prof. S. M. Girvin	Yale University	President of the Committee
Prof. R. Shankar	Yale University	Committee Member
Prof. David DeMille	Yale University	Committee Member
Prof. Liang Jiang	Yale University	Committee Member
Prof. Eugene Demler	Harvard University	External Reader

Abstract

Topological phases with ultracold atoms and photons

Alexandru Petrescu

2015

We propose theoretical models that support topological phases and which are relevant to current experiments on lattices hosting photonic modes or ultracold atoms. In the first part of this thesis, we introduce a topological phase on a Kagomé lattice whose degrees of freedom are photons. In that context, we discuss two protocols to access the local Berry curvature and the Chern number of Bloch bands from semiclassical dynamics of wavepackets. Secondly, we obtain the phase diagram for bosons at unit filling with repulsive on–site interactions whose kinetic term corresponds to a Chern insulator defined on the honeycomb lattice. In the second part, we turn to recently realized quasi one–dimensional lattices, and uncover their phase diagrams, comprising low–dimensional Meissner phases, chiral Mott insulating phases as well as abelian fractional quantum Hall states.

Résumé

Phases topologiques avec des atomes froids et des photons

Alexandru Petrescu

2015

Dans cette thèse, nous proposons des modèles qui présentent des phases topologiques. Ces modèles sont réalisables expérimentalement dans des systèmes d'atomes froids et dans des systèmes de circuit d'éléctrodynamique quantique. Dans la première partie de cette thèse, nous introduisons une phase topologique sur un réseau Kagomé, dont les degrés de liberté sont des photons. Nous discutons deux méthodes pour mesurer la courbure de Berry et le nombre de Chern pour les bandes de Bloch. Ces deux protocoles se basent sur la dynamique semi–classique des paquets d'onde. Nous obtenons aussi le diagramme de phases pour des bosons avec une interaction répulsive de type Bose-Hubbard sur chaque site d'un réseau hexagonal proposé par F.D.M. Haldane. Nous découvrons un état isolant de Mott avec des courants locaux quand la densité moyenne est d'un boson par site. Les excitations de cet isolant de Mott ont des caractéristiques topologiques. Dans la deuxième partie de cette thèse, nous nous concentrons sur des réseaux quasi-uni-dimensionnels récemment réalisés dans des systèmes d'atomes froids. Nous étudions leurs diagrammes de phases, étant composés de phases Meissner, d'isolants de Mott chiraux, et d'états d'effet Hall quantique fractionnaire abélien.

Contents

Acknowledgement **vii**

Introduction **ix**

I Topological bandstructures **1**

1 Review of concepts **2**

1.1 Geometric phase 3

1.2 Geometry of Bloch bands 11

1.2.1 Bloch's theorem 11

1.2.2 Geometry of Wannier states 13

1.2.3 Polarization 18

1.2.4 The first Chern number 21

1.2.5 Quantum Anomalous Hall Effect 22

1.3 Other formulations of the Chern number 27

1.4 Experiments 28

2 Photon QAHE on the Kagomé lattice **30**

2.1 Tight-binding model 33

2.2 Chiral edge states 36

2.2.1 Analytic solution 37

2.2.2 Local observables 39

2.3 Anomalous Hall Effect 41

2.4 Berry curvature from dynamics . . . 44
2.5 Chern numbers from interferometry . . . 49
2.6 Bound on the strength of the magnetic field . . . 51
2.7 Topological Bogoliubov Quasiparticles . . . 53
2.8 Conclusions . . . 55

3 Bose-Hubbard Haldane model 57

3.1 Model . . . 59
3.2 Study of the ground state . . . 60
3.2.1 Weakly interacting bosons . . . 60
3.2.2 Mott Insulator with Plaquette Currents . . . 65
3.2.3 Exact diagonalization . . . 71
3.3 Excitations of the Mott phase . . . 74
3.3.1 Strong coupling expansion . . . 74
3.3.2 Topological particle or hole excitations . . . 77
3.4 Conclusions . . . 79

II Quasi–one dimensional topological states 81

4 Chiral Phases of Ladders 82

4.1 The Josephson ladder . . . 86
4.1.1 Continuum limit and gauge invariance . . . 88
4.1.2 *Meissner* phase . . . 92
4.1.3 *Rung Mott* . . . 94
4.1.4 *Rung Mott – Meissner* stability . . . 96
4.1.5 *Laughlin* state at $\nu = \frac{1}{2}$ . . . 97
4.2 Observables . . . 99
4.2.1 Current operator and lattice flux quantization . . . 99
4.2.2 Current operators in the *Rung Mott – Meissner* phase . . . 100
4.2.3 Flux quantization in the *Rung Mott – Meissner* phase . . . 101

4.2.4 σ_{xy} from the Laughlin argument in the *Rung Mott – Meissner* phase . . . 102
4.2.5 Local probes of the *Laughlin* phase . . . 103
4.2.6 Chiral edge modes in the *Laughlin* phase . . . 104
4.3 Strong coupling expansion in the *Rung Mott* phase . . . 107
4.4 Hybrid fermion–Cooper pair analogues . . . 110
4.4.1 Cooper pair *Rung Mott – Meissner* phase . . . 116
4.4.2 Cooper pair *Laughlin* phase . . . 117
4.4.3 Dual phase: fermionic Mott insulator with spinon currents . 119
4.5 Experimental realizations . . . 121
4.5.1 Ultracold atom implementation . . . 121
4.5.2 Quantum circuit implementation . . . 123
4.6 Two-dimensional generalizations . . . 126
4.6.1 N-chain construction for the Meissner phase . . . 127
4.6.2 3-leg construction for the boson Mott insulator with Meissner current . . . 129
4.6.3 2D construction for fermionic Mott insulator with spinon currents . . . 131
4.6.4 Coupled planes . . . 132
4.7 Conclusions . . . 135

5 Conclusions and Outlook **137**

A Realization of a synthetic gauge field **140**
A.1 Magnetic field from lattice modulation . . . 140
A.2 Spectrum in a magnetic field . . . 142

B Bogoliubov transformation **145**

C RG equations for sine–Gordon models **149**

D Hamiltonian for spinful fermion ladders **153**

E Effective Hamiltonian at second order in perturbation theory 156

F Effective edge Hamiltonian 159

G *Rung Mott* – *Rung superfluid* phase boundary 164

G.1 Atomic limit 164

G.2 Phase diagram from mean-field theory 165

G.3 DMRG phase diagram 166

H Strong coupling expansion for the *Rung Mott* phase 168

Acknowledgement

It has been a great privilege to be Karyn's student. She is a thoughtful advisor and we, past and present members of her group, can only be inspired by her dedication, creativity and diverse scientific reach. She has supported my endeavors, and has taught me much of the physics that I know now.

Steve Girvin had a good piece of advice whenever I was encountering a roadblock. I remember carefully preparing for our meetings, which were memorable and enlightening.

I have learned a lot from my professors: Leonid Glazman, Walter Goldberger, Nick Read, Tom Appelquist, Witek Skiba, Walter Goldberger, Francesco Iachello or Yoram Alhassid. Critical questions from Liang Jiang, David DeMille and R. Shankar have helped shape this thesis. Moreover, I have spent significant amounts of time discussing with Stephan Rachel, Zoran Ristivojevic, Akiyuki Tokuno, Guillaume Roux, Ivana Vasić and Walter Hofstetter. I would like to acknowledge Patrick Mora, my tutor at École Polytechnique, as well as Antoine Georges and Silke Biermann for their advice through my three years spent in France.

I should remember that I came to Yale as an aspiring student in high energy experimental physics, and that Tobias Golling and Paul Tipton gave me the chance to work at CERN for one summer. That was such a charming time and I know that I would have been as happy had my PhD been in elementary particle physics.

There were quite a few that have conspired in veering me towards condensed matter: Peter Orth, Prasenjit Dutt, Francis Song, Stephan Rachel, Thomas Schmidt,

Jean-François Rupprecht.

I am thanking the bats and tea club members, Claudia de Grandi, Matti Silveri, Richard Brierley, Hendrik Meier, Ivana Petkovic, Barry Bradlyn, Victor Albert, Jukka Vayrynen, Michal Macek, Kostya Nesterov, Ion Garate, for witty conversation over lunch or elsewhere, and always welcoming me back. In Paris, I have enjoyed the company of my colleagues Tianhan Liu, Loïc Henriet, Loïc Herviou, Kirill Plekhanov.

I am grateful to Cathy Barabas, Daphne Klemme, Sandy Tranquilli, John Fox, Malika Lang, and Florence Auger for all the help in making my back and forth travel easy.

My PhD time was a happy time due to friends such as Camille Avestruz, Daniel Guest, Tomomi Sunayama, Nicole Larsen, Eustace Edwards, Marco Bonett-Matiz, Kent Riley, Filip Kos, Keerthi Shetty, Mehmet Dogan, Arvin Kakekhani, Alex Georgescu, Daniel Semenciuc, Otilia Pupezeanu, Bianca Gioadă, Parimal Deodhar and Duncan Reid, Cristina Pop and Ioan Pop.

Finally, I would like to thank my close ones for their unconditional encouragement to go on with this adventure.

Introduction

Quantum phases such as the crystalline solid, magnets, or superconductors can be described by the spontaneous breaking of a symmetry (translational, rotational, gauge symmetry, respectively). There are phases whose description must go beyond the Ginzburg–Landau theory of spontaneous symmetry breaking [1], such as topologically ordered states [2, 3], except when field theory successfully captures the physics [4, 5, 6, 7], as in the case of Laughlin's paradigmatic state [8] describing the $\nu = 1/m$ fractional quantum Hall effect [9]. The classification of topological phases relies on topological invariants, which remain unchanged by smooth deformations. This kind of classification does not make use of local geometric properties, and hence a local order parameter cannot distinguish between states that are topologically distinct.

A large class of topological phases is akin to the integer quantum Hall effect [10], in that their single particle spectrum has a large band gap. The ground state is characterized by a topological invariant corresponding to the filled single–particle bands [11]. Phases that fall into this class are Haldane's proposal for an integer quantum Hall effect without Landau levels, also called "quantum anomalous Hall effect"(QAHE) or Chern insulator [12], the topological insulators supporting the quantum spin Hall effect (QSHE) [13], or topological superconductors [14]. While such states have an energy gap in the bulk of the sample, boundaries between the topological and non–topological states are metallic, which is protected by a bulk symmetry. These examples fall under the category of "symmetry protected topological phases" [15, 16], which are short–range entangled quantum

states that do not exhibit topological order. Quantum spin Hall devices promise the realization of ballistic one–dimensional channels with potential applications in spintronics [17, 18]. Symmetry protected topological phases might shed light on more fundamental phenomena: They may provide an avenue for the realization of the Majorana fermion, pairs of which may encode qubits with unusually long coherence time [19]. Finally, the underlying theory of topological insulators is a topological field theory [20], whose unusual responses might be revealed in current experiments [21].

On the other hand, topological order [2, 3], the prime example of which was R. B. Laughlin's many–body wavefunction for the fractional quantum Hall effect [8], relies on inherently quantum many–body effects. Topologically ordered phases have a degenerate ground state in the thermodynamic limit, whose degeneracy cannot be split by local perturbations. Above this degenerate ground state there exist excitations with fractional charge and fractional statistics, called anyons [22, 23]. Those may be thought of as a means towards fault–tolerant quantum computation [24, 25, 26]. Since the discovery of the fractional quantum Hall effect, other models which do not need a nonzero net magnetic field have been put forth, such as the fractional Chern insulator [27, 28, 29, 30, 31] and the fractional topological insulator [32]. The main ingredient of such models is that their single particle bandstructure contains a topologically nontrivial Bloch band whose bandwidth is much smaller than the bandgap that separates it from the rest of the spectrum. This opens the possibility for high temperature fractional quantum Hall phases with zero net field, rendering some of the applications of topologically ordered systems more feasible.

While the identification of material candidates providing the right energetics for such fractional phases is an intriguing question, one may look into quantum simulation [33] for their realization. One key ingredient for the simplest of topological phases is to break time–reversal symmetry, which in nature is supplied by a magnetic field. Artificial magnetic fields have been realized in ultracold atoms

[34, 35] and photonic systems [36]. The quest for lattice equivalents of integer quantum Hall phases (with [37] or without [12] Landau levels) has led to implementations of artificial gauge fields with ultracold atoms [38, 39, 40, 41, 42, 43], gyromagnetic photonic crystals at microwave frequency [44, 45, 46], coupled resonator optical waveguides [47, 48, 49], metamaterials based on pillar-shaped photonic waveguides [50, 51, 52], optomechanical systems [53], radio frequency devices [54, 55], or coupled mechanical oscillators [56]. Similar topological phases have been theoretically predicted to appear in Circuit Quantum Electrodynamics [57, 58]. In tunable systems such as these band topology and edge transport can be probed. The interplay of a strong magnetic field and filling leads to the fractional quantum Hall effect, or the closely related spin liquids [59]. Originally discovered in two-dimensional electron gases [9], the fractional quantum Hall effect has eluded implementation in quantum emulators, despite multiple theoretical proposals suitable for ultracold atoms [60, 61, 62, 63, 64, 65, 66] or photons [67, 68].

In this thesis, we present work on quantum phase transitions and topological phases in experimentally feasible low dimensional systems. The model Hamiltonians introduced here are realizable with ultracold atoms in optical lattices or in superconducting quantum circuits. Our results span two themes: *free particle topological bandstructures*; *interacting boson chiral phases and topological order*. For the first theme, we will discuss probes of the topology of bandstructures and transport in arrays of microwave cavities and ultracold atoms [58] which support equivalents of the integer quantum Hall effect. For the second topic, we will introduce Mott insulators which exhibit some degree of quantum entanglement brought about by persistent currents in either quasi-one dimensional [69] or two-dimensional [70] lattices. These featureful, chiral Mott insulators can transition into abelian bosonic fractional quantum Hall states [71].

In Chapter 1, we review a selection of concepts about topological phases. This pedagogical chapter aims to start from textbook quantum mechanics and introduce topics necessary in further chapters. For noninteracting systems, we introduce the

geometric phase appearing in the quantum adiabatic theorem. We move on to periodic lattices and show how geometric phases necessarily appear in the construction of localized Wannier orbitals. After this we arrive at Chern numbers for Bloch bands, and present in detail the Haldane model for the quantum anomalous Hall effect.

In Chapter 2, we consider an array of microwave cavities situated on a Kagomé lattice, which could support artificial gauge fields [57]. A preliminary version of this array, exhibiting many of the interesting properties of graphene [72], has been experimentally realized by Underwood *et al.* [73] in Andrew A. Houck's lab at Princeton. Our study begins with the observation that the proposal of [57] realizes the quantum anomalous Hall effect on the Kagomé lattice, in a manner analogous to Haldane's model [12]. However, this system features a topologically trivial band inside of a topological band gap (between two bands with nonzero Chern numbers), which allows us to study its interplay with edge eigenstates. For this topological bandstructure of photonic excitations, we devise probes of the quantum anomalous Hall phase with focus on edge eigenstates and the possibility to tune the system into an anomalous Hall phase where the Chern number is not defined, and edge states degenerate with bulk states are no longer protected against backscattering. We show how the local Berry curvature can be measured from the semiclassical dynamics of wavepackets, and design an interferometry experiment to deduce band Chern numbers by counting cyclotron orbits. Finally, we show that the weakly interacting system contains topological Bogoliubov quasiparticles. The material presented in Chapter 2 overlaps significantly with that of Ref. [58] (also publication 1 in the list at the end of this introduction).

In Chapter 3, we consider a strongly–correlated Hamiltonian, based on Haldane's model [12] for a Chern insulator. Correlations come from strong on site Bose–Hubbard interactions [74] in a dense system with one boson per site. The Haldane model has been recently realized for fermionic atoms [41], which paves the way for the study of interacting topological phases. We uncover a rich phase

diagram containing a plaquette Mott insulator supporting local chiral currents, and two types of superfluid connected to each other by a first order transition at weak interactions, or by a pair of second order transitions at strong interactions. We arrive at this phase diagram using variational methods, an analysis of bands within strong–coupling perturbation theory, and validate our results using exact diagonalization. These three techniques are the author's contributions to Ref. [70] (publication number 4 in the list at the end of this introduction). In that reference, these methods are complemented by real space dynamical mean–field theory and the analysis of quantum fluctuations in the superfluid phase, carried out by our collaborators Ivana Vasić and Walter Hofstetter.

In Chapter 4, we shift from two–dimensional systems to (quasi) one–dimensional systems with artificial gauge fields which are closely related to quantum wires with spin–orbit coupling. From the theoretical standpoint, one dimensional systems are favorable since we can reliably characterize the low–energy behavior with the technique of bosonization [75], and confront analytical results against exact ones from density matrix renormalization group [76, 77]. More importantly, one–dimensional systems that break time–reversal symmetry are highly relevant experimentally, with rich activity that led to the realization of a low–dimensional Meissner effect [78], quantum Hall effect in synthetic dimensions [79], or realizations of the Harper–Hofstadter model [38, 40]. We study lattice Bose–Hubbard models whose ground states can be a Meissner phase, a vortex phase, Mott insulators with chiral currents, or a charge density wave that is a precursor of the Laughlin trial state. There exist two publications whose content overlaps with Chapter 4, namely Refs. [69] and [71] (publications 2 and 5 in the list at the end of the introduction, respectively).

Below is a list of articles that were published during the preparation of this thesis.

- 5. A.P. and Karyn Le Hur, *Chiral Mott Insulators, Meissner Effect, and Laughlin States in Quantum Ladders*, Phys. Rev. B **91**, 054520 (2015),

arXiv:1410.6105

- 4. Ivana Vasić, A.P., Karyn Le Hur, and Walter Hofstetter, *Chiral Bosonic Phases on the Haldane Honeycomb Lattice*, Phys. Rev. B 91, 094502 (2015), arXiv:1408.1411

- 3. A.P., H. Francis Song, Stephan Rachel, Zoran Ristivojevic, Christian Flindt, Nicolas Laflorencie, Israel Klich, Nicolas Regnault and Karyn Le Hur, *Fluctuations and Entanglement spectrum in quantum Hall states*, for JSTAT special issue on "Entanglement spectra and entanglement entropies", Eds. S. Rachel, M. Haque, A. Bernevig, A. Läuchli, and E. Fradkin. J. Stat. Mech. P10005 (2014), arXiv:1405.7816

- 2. A.P. and Karyn Le Hur, *Bosonic Mott Insulator with Meissner Currents*, Phys. Rev. Lett. **111**, 150601 (2013), arXiv:1306.5986

- 1. A.P., Andrew A. Houck and Karyn Le Hur, *Anomalous Hall Effects of Light and Chiral Edge Modes on the Kagomé lattice*, Phys. Rev. A **86**, 053804 (2012), arXiv:1206.1539

In addition, some topics on artificial gauge fields and topological phases with photons also make the object of a recent review:

- 1. Karyn Le Hur, Loïc Henriet, A.P., Kirill Plekhanov, Guillaume Roux, Marco Schiró, *Many-Body Quantum Electrodynamics Networks: Non-Equilibrium Condensed Matter Physics with Light*, to be submitted to Comptes Rendus de l'Académie des Sciences, arXiv:1505.00167

Part I

Topological bandstructures

Chapter 1

Review of concepts

In this chapter, we introduce concepts leading up to the topological description of the quantum anomalous Hall effect (or the Chern insulator phase [12]). While our presentation is pedagogical and relies on elementary concepts of quantum mechanics, literature on the role of topology in condensed matter physics is vast, and the reader may find the following references useful: Thouless [80] discusses the topology of the integer and fractional quantum Hall effects. Volovik [81] includes a thorough discussion of momentum space topology in two–dimensional quantum systems. Nakahara [82] discusses the Berry connection on a fiber bundle and derives Berry's phase. Mermin's review [83] focuses on the homotopy theory of defects in ordered media. Girvin's lecture notes on integer and fractional quantum Hall effects [84] features a discussion of topological defects in quantum Hall ferromagnetism. For the understanding of topological bandstructures, the reader may refer to a number of review papers on the subject of topological insulators and superconductors [14, 13, 85].

Our review of concepts will proceed in the following order. Sec. 1.1 contains the derivation of Berry's phases from the quantum adiabatic theorem. Sec. 1.2 starts from the Bloch band theory and builds up to band Chern numbers, approaching the problem via the construction of localized Wannier orbitals. This section continues with a couple of interpretations of the topological character of

the Chern number, and with a discussion of the quantum anomalous Hall effect introduced by Haldane [12]. In Sec. 1.3 we discuss alternate formulations of the Chern number, which will be used throughout this dissertation. Finally, in 1.4 we enumerate the many recent experiments on topological phases.

1.1 Geometric phase

This section discusses the concept of geometric phase, central to many results in this thesis. We reproduce here Berry's argument [86] based on the proof of the quantum adiabatic theorem [87]. Previously, Pancharatnam discussed the geometric phase in the superposition of coherent beams prepared in distinct states of elliptic polarization [88]. In his proof of the quantum adiabatic theorem, Berry established that a wavefunction of a Hamiltonian $H(\mathbf{R})$ acquires a $U(1)$ phase when the multi–dimensional parameter $\mathbf{R}$ continuously traverses a closed curve in parameter space. This phase depends on the geometry of the curve and is distinct from the dynamical phase [86]. Simon [89] identified Berry's geometric phase as the holonomy of a Hermitian line bundle, and drew the connection with the Thouless *et al.* proof of the quantization of Hall conductance [11]. Zak [90] discussed the dynamics of Bloch electrons in solids in terms of Berry's phase.

Consider a Hamiltonian $H(\mathbf{R})$ which is parametrized by a set of real numbers denoted $\mathbf{R} = (R_1, R_2, ...)$. More concretely, $\mathbf{R}$ can be a real space position, a magnetic field, or the momentum of a Bloch wave. Assume, without loss of generality, that the spectrum of $H(\mathbf{R})$ is discrete at any point $\mathbf{R}$

$$H(\mathbf{R})\,|n\mathbf{R}\rangle = E_n(\mathbf{R})|n\mathbf{R}\rangle,\ n = 0, 1, 2, ...\ \textit{for all}\ \mathbf{R}. \tag{1.1}$$

Suppose that the spectrum has no degeneracy, *i.e.* that $E_n(\mathbf{R}) \neq E_m(\mathbf{R})$ for whatever m and n, and at each $\mathbf{R}$. Moreover, the eigenstates are normalized according to the condition $\langle n\mathbf{R}|n\mathbf{R}\rangle = 1$, whatever the choice of $\mathbf{R}$.

Now assume that $\mathbf{R}$ is varied along a closed path denoted C. Taking $\mathbf{R} = \mathbf{R}(t)$,

with $t \in [0, T]$, the requirement $\mathbf{R}(T) = \mathbf{R}(0)$ is equivalent to enforcing that after time T the Hamiltonian operator returns to its initial value. If at $t = 0$ the state of the system is an eigenstate of $H[\mathbf{R}(t = 0)]$, say $|n\mathbf{R}(0)\rangle$, what is the eigenstate $|\psi(t)\rangle$ at a later time? Most generally, this state must obey the time-dependent Schrödinger equation

$$i\hbar\partial_t|\psi(t)\rangle = H[\mathbf{R}(t)]|\psi(t)\rangle, \tag{1.2}$$

together with the initial condition $|\psi(0)\rangle = |n\mathbf{R}(0)\rangle$. M. V. Berry studied the solution to (1.2) in the limit where the quantum adiabatic theorem is applicable: Given that the projectors $|n\mathbf{R}(t)\rangle\langle n\mathbf{R}(t)|$ are sufficiently smooth functions of time [87], the quantum adiabatic theorem states that, for any t, the state $|\psi(t)\rangle$ is asymptotically equal up to a phase factor to $|n\mathbf{R}(t)\rangle$, in the limit where the total sweep time is infinite: $T \to \infty$. Berry found that, in addition to the dynamical phase factor, a second phase factor arises, which derives from the geometry of the eigenvectors $|n\mathbf{R}\rangle$ as $\mathbf{R}$ is varied in time.

Thus, in the limit $T \to \infty$, the adiabatic theorem gives[1]

$$|\psi(t)\rangle = e^{-\frac{i}{\hbar}\int_0^t dt' E_n[\mathbf{R}(t')]} e^{-i\Gamma_n(t)}|n\mathbf{R}(t)\rangle, \tag{1.3}$$

where the phase $\Gamma_n(t)$ is determined by the fact that the wavefunction $|\psi(t)\rangle$ must satisfy the time–dependent Schrödinger equation (1.2). Upon plugging (1.3)

1. At finite sweep duration T, Eq. (1.3) is the adiabatic approximation to the exact solution of Eq. (1.2). A condition for the approximation to be valid is that the probability $p_{n\to m}$ to find the system in any distinct state $|m\mathbf{R}(T)\rangle$, having evolved with (1.2) from the initial state $|n\mathbf{R}(0)\rangle$, is negligible. A weak bound [87] for this probability is $p_{m\to n} \leq \max_{t\in[0,T)}|\alpha_{mn}(t)/\omega_{mn}(t)|^2$, where

$$\alpha_{mn} = \langle m\mathbf{R}(t)|d/dt|n\mathbf{R}(t)\rangle$$

measures the rate with which the eigenvectors of $H[\mathbf{R}(t)]$ rotate. This needs to be compared with the transition frequency for the two levels of $H[\mathbf{R}(t)]$

$$\omega_{mn}(t) = \left(E_m[\mathbf{R}(t)] - E_n[\mathbf{R}(t)]\right)/\hbar.$$

This yields a strong condition for adiabaticity, $\max_{t\in[0,T)}|\alpha_{mn}(t)/\omega_{mn}(t)|^2 \ll 1$, which can be evaluated for a given parametrization $\mathbf{R}(t)$.

into (1.2) and using (1.1), one obtains

$$\frac{d\Gamma_n(t)}{dt} = -i\left[\langle n\mathbf{R}|\partial_{\mathbf{R}}|n\mathbf{R}\rangle\right]_{\mathbf{R}=\mathbf{R}(t)} \cdot \frac{d\mathbf{R}(t)}{dt}, \tag{1.4}$$

where $\partial_{\mathbf{R}}$ denotes the gradient with respect to the coordinates of $\mathbf{R}$. Then the wavefunction after one full period T differs from the original one by two phase factors, one coming from a property of eigenvectors $|n\mathbf{R}\rangle$ for $\mathbf{R}$ belonging to C, and one from dynamics, respectively

$$|\psi(T)\rangle = e^{-i\Gamma_n(C)} e^{-\frac{i}{\hbar}\int_0^T dt E_n[\mathbf{R}(t)]} |n\mathbf{R}(0)\rangle, \tag{1.5}$$

with the following expression for *Berry's phase*:

$$\Gamma_n(C) = -i \oint_C \langle n\mathbf{R}|\partial_{\mathbf{R}}|n\mathbf{R}\rangle \cdot d\mathbf{R}. \tag{1.6}$$

Normalization implies that $\langle n\mathbf{R}|\partial_{\mathbf{R}}|n\mathbf{R}\rangle$ is imaginary. The first consequence of this is that $\Gamma_n(C)$ is real. Secondly, remark that if all components of $|n\mathbf{R}\rangle$ are real, then $\Gamma_n(C)$ must vanish. Consequently, if time–reversal symmetry is obeyed then $\Gamma_n(C)$ vanishes.

We may express (1.6) in a more compact form by introducing the *Berry gauge field* associated with level n:

$$\mathcal{A}_n(\mathbf{R}) \equiv -i\langle n\mathbf{R}|\partial_{\mathbf{R}}|n\mathbf{R}\rangle. \tag{1.7}$$

Then Eq. (1.6) becomes the line integral of $\mathcal{A}_n(\mathbf{R})$ on C:

$$\Gamma_n(C) = \oint_C \mathcal{A}_n(\mathbf{R}) \cdot d\mathbf{R}. \tag{1.8}$$

Inspection of (1.6) shows that $\Gamma_n(C)$ could, in principle, change if we modify the eigenvector $|n\mathbf{R}\rangle$ by multiplying it by some arbitrary $\mathbf{R}$–dependent phase factor. It is easy to see that adding an arbitrary prefactor to the eigenstates amounts to

a gauge transformation on the Berry gauge field

$$\begin{aligned} |n\mathbf{R}\rangle &\rightarrow e^{i\phi_n(\mathbf{R})}|n\mathbf{R}\rangle, \\ \mathcal{A}_n(\mathbf{R}) &\rightarrow \mathcal{A}_n(\mathbf{R}) + \partial_{\mathbf{R}}\phi_n(\mathbf{R}). \end{aligned} \tag{1.9}$$

Under this transformation, Berry's phase can only change by an integer multiple of 2π:

$$\Gamma_n(C) \rightarrow \Gamma_n(C) + \oint_C \partial_{\mathbf{R}}\phi_n(\mathbf{R}) \cdot d\mathbf{R} = \Gamma_n(C) + 2\pi m, \tag{1.10}$$

for some integer number m, which is not a measurable difference.

To compute Berry's phase using Eq. (1.8) poses the difficulty that the phase factor of the ket $|n\mathbf{R}\rangle$ must be chosen consistently at every point $\mathbf{R}$. We will explicitly show how this can be done at the end of this subsection. For the moment, let us point out that this gauge fixing procedure would be avoided if we could express the Berry phase in a gauge invariant way. The *Berry curvature*

$$\mathcal{F}_n(\mathbf{R}) \equiv \partial_{\mathbf{R}} \times \mathcal{A}_n(\mathbf{R}) \tag{1.11}$$

is invariant under (1.9) for smooth $\phi_n(\mathbf{R})$. The Berry curvature is the analogue of the magnetic field $\mathbf{B} = \partial_{\mathbf{r}} \times A(\mathbf{r})$ in coordinate space. The Berry phase in parameter space then corresponds to the Aharonov–Bohm phase [91] in real space. Assuming that all the components of $\mathcal{A}_n(\mathbf{R})$ vary smoothly with $\mathbf{R}$ on some surface S whose boundary is C, Stokes' theorem implies that:

$$\Gamma_n(C) = \oint_C \mathcal{A}_n(\mathbf{R}) \cdot d\mathbf{R} = \iint_S \mathcal{F}_n(\mathbf{R}) \cdot d\mathbf{S}. \tag{1.12}$$

To bring this to a form that can be calculated, let us insert identity $1 = \sum_m |m\mathbf{R}\rangle\langle m\mathbf{R}|$ in (1.12) to obtain

$$\Gamma_n(C) = i \iint_S \sum_{m \neq n} \left(\partial_{\mathbf{R}}\langle n\mathbf{R}|\right)|m\mathbf{R}\rangle \times \langle m\mathbf{R}|\left(\partial_{\mathbf{R}}|n\mathbf{R}\rangle\right) \cdot d\mathbf{S}. \tag{1.13}$$

Whenever $m \neq n$, Eq. (1.1) allows us to obtain an expression with energy denominators

$$\frac{\langle m\mathbf{R}|H(\mathbf{R})|n\mathbf{R}\rangle}{E_n(\mathbf{R}) - E_m(\mathbf{R})} = \langle m\mathbf{R}|\partial_{\mathbf{R}}|n\mathbf{R}\rangle. \tag{1.14}$$

Inserting this into (1.13), we find

$$\mathcal{F}_n(\mathbf{R}) = i \sum_{m \neq n} \frac{\langle n\mathbf{R}|\partial_{\mathbf{R}} H(\mathbf{R})|m\mathbf{R}\rangle \times \langle m\mathbf{R}|\partial_{\mathbf{R}} H(\mathbf{R})|n\mathbf{R}\rangle}{\left[E_n(\mathbf{R}) - E_m(\mathbf{R})\right]^2}, \tag{1.15}$$

which may be used along with (1.12) to calculate Berry's phases. Note that the curvature peaks at points $\mathbf{R}$ where $|E_n(\mathbf{R}) - E_m(\mathbf{R})|$ is minimized. In other words, energy levels which are closest to n contribute most to $\Gamma_n(C)$. It also follows from the above that Berry curvature (1.15) is singular at degeneracy points.

Let us now consider an instructive example which makes all the concepts outlined this far explicit. Assume that the spectrum consists of two levels $E_{\pm}(\mathbf{R}) = \pm R$, with $|\mathbf{R}| = R$, which become degenerate at $\mathbf{R} = 0$. Further suppose that these levels correspond to a (dimensionless) Hamiltonian

$$H(\mathbf{R}) = \mathbf{R} \cdot \sigma = \begin{pmatrix} R_3 & R_1 - iR_2 \\ R_1 + iR_2 & -R_3 \end{pmatrix}, \tag{1.16}$$

where $\sigma = (\sigma_1, \sigma_2, \sigma_3)$ is a three component vector containing the Pauli matrices

$$\sigma_1 = \begin{pmatrix} 0 & 1 \\ 1 & 0 \end{pmatrix}, \ \sigma_2 = \begin{pmatrix} 0 & -i \\ i & 0 \end{pmatrix}, \ \sigma_3 = \begin{pmatrix} 1 & 0 \\ 0 & -1 \end{pmatrix}. \tag{1.17}$$

The three Pauli matrices obey the algebra $[\sigma_j, \sigma_k] = 2i\epsilon_{jkl}\sigma_l$, as well as $\{\sigma_i, \sigma_j\} = 2\delta_{ij}\sigma_0$, where σ_0 is the 2×2 identity matrix. The four matrices $\sigma_0, \sigma_1, ..., \sigma_3$ form a basis for 2×2 Hermite matrices.

Equation (1.15) for the Berry curvature gives

$$\mathcal{F}_{\pm}(\mathbf{R}) = \pm \frac{\mathbf{R}}{2R^3}. \tag{1.18}$$

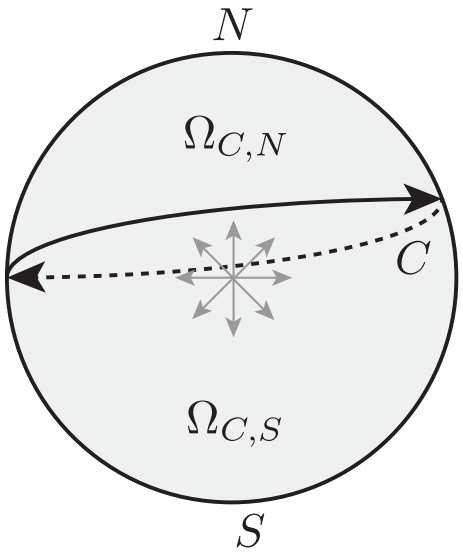

Figure 1.1: The Berry curvature of Eq. (1.18) corresponds to a monopole of strength $\pm 1/2$ at the origin $\mathbf{R} = 0$. Berry's phase around a closed curve C on the unit sphere amounts to half of the solid angle circumscribed by C. Different choices of this solid angle, such as the complementary regions $\Omega_{C,N}$ and $\Omega_{C,S}$, will yield Berry's phases which are equal up to 2π, as discussed in the text.

This is the field of a magnetic monopole located at the degeneracy point $\mathbf{R} = 0$. The strength of the monopole is given by $\frac{1}{4\pi} \iint_{S^2} d\mathbf{S} \cdot \mathcal{F}_{\pm}(\mathbf{R}) = \pm\frac{1}{2}$ through the unit sphere S^2 defined by $|\mathbf{R}| = 1$, as depicted in Fig. 1.1.

Now assume without loss of generality that the parameter $\mathbf{R}$ is varied along a curve C which lies entirely on the unit sphere S^2 as shown in Figure 1.1. In a region of the sphere where the Berry gauge field $\mathcal{A}_{\pm}(\mathbf{R})$ can be smoothly defined, in a way that we will make explicit shortly, Stokes' theorem applies as in Eq. (1.12). Then the Berry phase $\Gamma_{\pm}(C)$ measures the flux of the monopole through the solid angle circumscribed by C on the sphere, denoted generically Ω_C,

$$\Gamma_{\pm}(C) = \mp\frac{1}{2}\Omega_C \bmod 2\pi. \tag{1.19}$$

There is an ambiguity in how to pick the solid angle Ω_C in Eq. (1.19). In Fig. 1.1, we see that there are two such choices, $\Omega_{C,N}$ or $\Omega_{C,S}$, depending on whether Ω_C contains the North pole or the South pole, respectively. In order for Stokes' theorem to apply, one needs that $\mathcal{A}_{-}(\mathbf{R})$ be smooth on Ω_C, which will decide between the two choices. To illustrate this, we rederive (1.18) from (1.11) by

explicitly fixing a gauge for $\mathcal{A}_{\pm}(\mathbf{R})$. Using Euler angles to parametrize $\mathbf{R} = (\sin\theta\cos\phi, \sin\theta\sin\phi, \cos\theta)$, the normalized eigenvector $|-,\mathbf{R}\rangle$ of (1.16) corresponding to energy $E_{-}(\mathbf{R})$ may be chosen to have the following components

$$\begin{pmatrix} -\sin\frac{\theta}{2}e^{-i\phi} \\ \cos\frac{\theta}{2} \end{pmatrix}. \tag{1.20}$$

Next, let us calculate $\mathcal{A}_{-}(\mathbf{R})$ of Eq. (1.7). After applying the gradient in spherical coordinates to (1.20), we arrive at

$$\mathcal{A}_{-}(\mathbf{R}) = -\frac{1-\cos\theta}{2R\sin\theta}\hat{e}_{\phi} = -\frac{1}{R}\tan\frac{\theta}{2}\,\hat{e}_{\phi}, \tag{1.21}$$

where $\hat{e}_{\phi}$ is the azimuthal unit vector in spherical coordinates. Taking the curl of (1.21) yields $\mathcal{F}_{-}(\mathbf{R})$ in (1.18). To calculate the Berry phase using Eq. (1.12), note that the Berry gauge field (1.21) is singular at the South pole of the unit sphere. (As $\theta \to \pi$ the azimuthal component of $\mathcal{A}_{-}$ becomes $-\infty$). Let then $\Omega_{C,N}$ for Stokes' theorem be the solid angle bounded by C on the unit sphere which does not include the South pole (Fig. 1.1). This will give

$$\Gamma_{-}^{N}(C) = -\frac{1}{2}\Omega_{C,N}. \tag{1.22}$$

We have seen in (1.10) that a change of gauge should leave $\Gamma_{-}(C)$ unchanged. To see this here, note that the singularity of $\mathcal{A}_{-}(\mathbf{R})$ at the South pole arises from the choice of gauge in Eq. (1.20), where the lower component $|-,\mathbf{R}\rangle$ is real and positive at every $\mathbf{R}$. Exactly at the South pole the lower component of $|-,\mathbf{R}\rangle$ in (1.20) vanishes, making it impossible to fix the gauge. Application of a gauge transformation as in (1.9) would result in moving the singularity of $\mathcal{A}_{-}(\mathbf{R})$ somewhere else on the unit sphere. For example, picking the components of $|-,\mathbf{R}\rangle$ to be

$$\begin{pmatrix} \sin\frac{\theta}{2} \\ -\cos\frac{\theta}{2}e^{i\phi} \end{pmatrix}, \tag{1.23}$$

we would obtain $\mathcal{A}_-(\mathbf{R}) = \frac{1}{R}\cot\frac{\theta}{2}\,\hat{e}_\phi$, whose curl is again $\mathcal{F}_-(\mathbf{R})$. Then $\mathcal{A}_-(\mathbf{R})$ would be singular at the North pole $\theta = 0$. Evaluation of the Berry phase using Stokes' theorem with the solid angle $\Omega_{C,S}$ not containing the North pole would yield

$$\Gamma_-^S(C) = \frac{1}{2}\Omega_{C,S}. \tag{1.24}$$

However, since $\Omega_{C,S}+\Omega_{C,N} = 4\pi$ is the solid angle of the unit sphere, the difference between the two calculations is $\Gamma_-^S(C) - \Gamma_-^N(C) = 2\pi$, which is not a measurable quantity.

The last two paragraphs illustrate a more general fact about fixing the gauge for $\mathcal{A}_n(\mathbf{R})$. For $\Gamma_n(C)$ to be well-defined, a smooth choice of the phase prefactor of $|n\mathbf{R}\rangle$ is required. A consistent choice of the phase prefactor can be made by fixing an ordered basis $\{|\alpha_1\rangle, |\alpha_2\rangle, ...\}$ and requiring that the first component of the wavefunction expressed in this basis, namely $\langle\alpha_1|n\mathbf{R}\rangle$, be a real number for all $\mathbf{R}$ in C. If $\Gamma_n(C)$ is nonvanishing, then $\langle\alpha_1|n\mathbf{R}\rangle$ has to vanish for some $\mathbf{R}$. We will return to this point in Sec. 1.2.4 in the context of topological bandstructures.

Finally, let us highlight the relation between the formalism for geometric phases presented here and familiar problems in condensed matter or quantum mechanics. Let us take the Hamiltonian in (1.16) to be real and symmetric, *i.e.* $R_2 = 0$, and let C be contained in the (R_1, R_3) plane. If C encircles the origin once, the Berry phase is $\pm\pi$ depending on whether C is oriented clockwise or counterclockwise, whereas if the interior of C does not contain the degeneracy point the Berry phase is 0. This example is relevant for the bandstructure of graphene. With (R_1, R_3) denoting the two components of Bloch electron momentum, this is the result for the Berry phase around a Dirac point [72]. Secondly, note that Eq. (1.16) is the Hamiltonian of a spin $S = 1/2$ particle that is Zeeman–coupled to a magnetic field $\mathbf{R}$. The π Berry phase is the phase shift acquired by a spinor when the magnetic field is rotated once around a great circle of the unit sphere [92].

1.2 Geometry of Bloch bands

We now show that the Hall conductance of a band insulator is a geometric property of the Bloch wavefunctions. Simon [89] has identified the connection between Berry's geometric phase and the Thouless *et al.* integers [11].

1.2.1 Bloch's theorem

Statement. Consider the first quantized Hamiltonian of a particle in a one-dimensional potential

$$H = \frac{\hbar^2 \hat{k}^2}{2m} + U(\hat{x}). \tag{1.25}$$

Note that we will only drop the hat symbol for objects which are unambiguously operators. Assume that the lattice potential has periodicity $U(x) = U(x+a)$, where a is the lattice spacing. Assume that the wavefunctions obey periodic boundary conditions $\psi(x) = \psi(x+L)$, where the site number is $L/a \equiv N$. Then any eigenfunction of (1.25) satisfies

$$\begin{aligned} \psi_k(x) &= \frac{1}{\sqrt{N}} e^{ikx} u(x), \text{ for } k \in \frac{2\pi\mathbb{Z}}{L} \\ u(x) &= u(x+a). \end{aligned} \tag{1.26}$$

To build intuition, note that in the absence of a lattice potential $u(x) = 1$, and the solutions are merely plane waves. When $U(x) \neq 0$, the wavefunctions consist of plane waves with periodicity L, modulated by a function periodic over the unit cell $0 \leq x < a$. Eigenstates are labeled by the wavenumber k, corresponding to crystal momentum $\hbar k$.

Proof. The operator that translates a state by one unit cell can be expressed in the following form

$$T = e^{-i\hat{k}a} = \sum_k e^{-ika} |k\rangle\langle k|, \tag{1.27}$$

where $|k\rangle$ is the eigenstate of the momentum operator $\hat{k}$ with eigenvalue k. The lattice translation operator and the momentum operator commute with H. Conse-

quently, T and H can be simultaneously diagonalized, and we may consider some eigenstate of the Hamiltonian,

$$H|\psi\rangle = E|\psi\rangle, \tag{1.28}$$

which is at the same time an eigenstate of the translation operator

$$T^\dagger|\psi\rangle = t_a|\psi\rangle. \tag{1.29}$$

The eigenstates of momentum are also eigenstates of T,

$$T|k\rangle = e^{-ika}|k\rangle. \tag{1.30}$$

System periodicity implies that translation by one full system length is identity, *i.e.* $T^N = 1$. This constrains the values of the wavenumber $k \in \frac{2\pi\mathbb{Z}}{L}$. By definition $\langle x|T|\psi\rangle = \langle x + a|\psi\rangle$, where $|x\rangle$ are eigenstates of the position operator. Let us return to the characterization of the eigenstates $|\psi\rangle$ common to H and T. Multiplying (1.29) by $\langle k|$ leads to

$$\langle k|T^\dagger|\psi\rangle = e^{ika}\langle k|\psi\rangle = t_a\langle k|\psi\rangle. \tag{1.31}$$

Therefore,

$$\text{if } \langle k|\psi\rangle \neq 0, \text{ then } t_a = e^{ika}. \tag{1.32}$$

If there exists a k such that $\langle k|\psi\rangle \neq 0$, then it is unique. If there existed a distinct eigenstate $|l\rangle$ with $l \neq k$ such that $\langle l|\psi\rangle \neq 0$ then we would obtain a contradiction $t_a = e^{ika} = e^{ila}$. Hence, the state $|\psi\rangle$ may have nonzero overlap with only one eigenstate of the lattice translation operator $|k\rangle$. Then eigenstates $|\psi\rangle$ may be labeled by the momentum quantum number $|\psi_k\rangle$.

Moreover, for fixed k, there may exist multiple $|\psi_k\rangle$ which have nonvanishing overlap with $|k\rangle$. We use the index n to iterate through all such states with the

property $\langle k|\psi_{nk}\rangle \neq 0$.

Then the set of common eigenstates of H and T is labeled by two quantum numbers n (which may be called "band") and momentum k:

$$\begin{aligned} H|\psi_{nk}\rangle &= E_{nk}|\psi_{nk}\rangle, \\ T^{\dagger}|\psi_{nk}\rangle &= e^{ika}|\psi_{nk}\rangle. \end{aligned} \tag{1.33}$$

Note that the eigenfunction $\psi_{nk}(x) = \langle x|\psi_{nk}\rangle$ falls short of being periodic in the unit cell:

$$\psi_{nk}(x+a) = e^{ika}\psi_{nk}(x). \tag{1.34}$$

However $u_{nk}(x) \equiv \sqrt{N}e^{-ikx}\psi_{nk}(x)$ is invariant under changes of x to $x+a$, and inverting this proves the theorem. An alternate proof based on an explicit solution of Schrödinger's equation can be found in [93].

One consequence of Bloch's theorem is that $\psi_{nk}(x) = \psi_{n,k+\frac{2\pi}{a}}(x)$, such that it is sufficient to consider only wavefunctions with crystal momentum defined in the first Brillouin zone $-\frac{\pi}{a} \leq k = \frac{2\pi j}{L} < \frac{\pi}{a}$. Note that the Bloch wavefunctions should be normalized to unity in the following way

$$\delta_{kl}\delta_{nm} = \int_0^L dr\psi^*_{nk}(r)\psi_{ml}(r) = \int_0^a dr u_{nk}(r)u_{ml}(r). \tag{1.35}$$

1.2.2 Geometry of Wannier states

In this section, we will show that the center coordinate of a localized Wannier orbital is related to the Berry phase. Wannier orbitals in one dimension are optimally localized if the phase ambiguity of Bloch wavefunctions is resolved using the Berry connection.

Let us define a set of Wannier states [94], consisting of Fourier transforms of the Bloch wavefunctions:

$$w_n(R,r) = \frac{1}{\sqrt{N}}\sum_k e^{-ikR}e^{i\phi_n(k)}\psi_{nk}(r). \tag{1.36}$$

Here R are coordinates on the Bravais lattice, $R = ja$, and the sum is over $k = 2\pi j/L$ which belong to the first Brillouin zone. The coordinate R in this section should not be confused with the parameter $\mathbf{R}$ in our treatment of Berry's phases. There is a phase ambiguity in the definition of Bloch waves ψ_{nk}, which we made explicit by the arbitrary function $\phi_n(k)$. The Wannier states have the property that $w_n(R, r) = w_n(R+R', r+R')$, so that $w_n(R, r)$ depends on r and R only through $r-R$. Moreover, using (1.35) and (1.36), together with the resolution of the δ-function

$$N\delta_{RR'} = \sum_k e^{ik(R-R')}, \tag{1.37}$$

we find that Wannier functions are normalized over the entire lattice

$$\int_0^L dr w_n^*(R, r) w_{n'}(R', r) = \delta_{RR'}\delta_{n,n'}. \tag{1.38}$$

Consider first expectation values of the form

$$\langle O(r)\rangle_n = \int_0^L dr w_n^*(r) O(r) w_n(r) \tag{1.39}$$

with $w_n(r) \equiv w_n(0, r)$.

We will prove the following properties explicitly [93, 95, 96]:

$$\langle r\rangle_n = -\sum_k \mathcal{A}_n(k) \tag{1.40}$$

$$\mathcal{A}_n(k) = -i\langle nk|\partial_k|nk\rangle = -i\int_0^a dr u_{nk}^*(r)\partial_k u_{nk}(r)$$

$$\langle r^2\rangle_n = -\sum_k \langle nk|\partial_k^2|nk\rangle. \tag{1.41}$$

Equation (1.41) holds if ϕ_n vanishes, and (1.40) holds even if $\phi_n \neq 0$.

Proof of (1.40). Using $u_{nk}(r) = \sqrt{N}e^{-ikr}\psi_{nk}(r)$ in (1.40), let us first calculate

$$\sum_k \mathcal{A}_n(k) = -\sum_k i\int_0^a dr u_{nk}^*(r)\partial_k u_{nk}(r)$$

$$
\begin{aligned}
&= -Ni \sum_k \int_0^a dr \psi^*_{nk}(r)[-ir\psi_{nk}(r) + \partial_k \psi_{nk}(r)] \qquad (1.42)\\
&= -N \sum_k \int_0^a dr \psi^*_{nk}(r) r \psi_{nk}(r) - N \sum_k \int_0^a dr \psi^*_{nk}(r) i \partial_k \psi_{nk}(r).
\end{aligned}
$$

Next, invert the definition of Wannier states to obtain

$$
\psi_{nk}(r) = \frac{e^{-i\phi_n(k)}}{\sqrt{N}} \sum_R w_n(R, r) e^{ikR}. \qquad (1.43)
$$

Plug this form for $u_{nk}(r)$ into the first term of (1.42), to obtain

$$
-\frac{1}{N} \sum_k \int_0^a dr \sum_{RR'} w^*_n(R, r) r w_n(R', r) e^{ik(R'-R)} = -\sum_R \int_0^a dr w^*_n(R, r) r w_n(R, r). \qquad (1.44)
$$

In the last step we have used the resolution of the δ–function. The second term of (1.42) becomes

$$
\begin{aligned}
& -\frac{1}{N} \sum_k \int_0^a dr \sum_{RR'} e^{i\phi_n(k)} w^*_n(R, r) e^{-ikR} i\partial_k [e^{-i\phi_n(k)} w_n(R', r) e^{ikR'}]\\
= \quad & -\frac{1}{N} \sum_k \int_0^a dr \sum_{RR'} e^{i\phi_n(k)} w^*_n(R, r) e^{-ikR} w_n(R', r) [\partial_k \phi_n(k) - R' e^{-i\phi_n(k)}] e^{ikR'}\\
= \quad & -\frac{1}{N} \sum_k \int_0^a dr \sum_{RR'} w^*_n(R, r) w_n(R', r) \partial_k \phi_n(k) e^{ik(R'-R)}\\
+ \quad & \int_0^a dr \sum_R w^*_n(R, r) R\, w_n(R, r). \qquad (1.45)
\end{aligned}
$$

We now show that the $\phi_n(k)$ dependent term vanishes. First noting that $\sum_k \partial_k \phi_n(k) e^{ik(R'-R)} = -i(R'-R)\sqrt{N}\phi_n(R'-R)$, we have

$$
\begin{aligned}
& -\frac{1}{N} \sum_k \int_0^a dr \sum_{RR'} w^*_n(R, r) w_n(R', r) \partial_k \phi_n(k) e^{ik(R'-R)}\\
= \quad & -\frac{1}{N} \int_0^a dr \sum_{RR'} w^*_n(R, r) w_n(R', r) \sqrt{N} i (R - R') \phi(R' - R). \qquad (1.46)
\end{aligned}
$$

To test the independence of $\langle r \rangle_n$ on $\phi_n(k)$, take a functional derivative $\delta/\delta\phi_n(R'')$

of (1.46), which gives

$$\begin{aligned} & -\frac{1}{N}\int_0^a dr \sum_R w_n^*(R,r) w_n(R+R'',r) R'' \\ = \quad & -\frac{1}{N}\int_0^L dr w_n^*(0,r) w_n(R'',r) = \delta_{R'',0} R'' = 0. \end{aligned} \tag{1.47}$$

Therefore $\langle r \rangle_n$ does not depend on $\phi_n(k)$, which we further set to 0. Collecting terms in (1.44) and (1.45),

$$-\sum_k \mathcal{A}_n(k) = \frac{1}{N}\int_0^a dr \sum_R w_n^*(R,r)(r-R) w_n(R,r) = \int_0^L dr w_n^*(r) r w_n(r) = \langle r \rangle_n. \tag{1.48}$$

We have used that $w_n(R,r) = w_n(r-R)$. This completes the proof of (1.40).

Proof of (1.41). Set $\phi_n = 0$. The effect of $\phi_n \neq 0$ on the spread of Wannier orbitals will be analyzed separately. Start with the following sum

$$-\sum_k \int_0^a dr u_{nk}^*(r) \partial_k^2 u_{nk}(r). \tag{1.49}$$

Using the same formulae as before,

$$u_{nk}^*(r)\partial_k^2 u_{nk}(r) = N\psi_{nk}^*(r)\left[-r^2 - 2ir\partial_k + \partial_k^2\right]\psi_{nk}(r). \tag{1.50}$$

Reexpressing Bloch states in terms of Wanniers according to Eq. (1.43), we arrive at

$$\int_0^a dr \sum_R w_n^*(R,r)(r-R)^2 w_n(R,r) = \int_0^L dr w_n^*(r) r w_n(r) = \langle r^2 \rangle_n, \tag{1.51}$$

which completes the proof.

Next, we optimize the spread of a Wannier state. Consider $\langle r^2 \rangle_n - \langle r \rangle_n^2$ as a functional over phase functions $\phi_n(k)$. Then the spread is minimized whenever

$$\partial_k^2 \phi_n(k) = -\partial_k \mathcal{A}(k). \tag{1.52}$$

Proof of (1.52). Make the replacement $u_{nk}(r) \to v_{nk}(r) = u_{nk}(r)e^{i\phi_n(k)}$ in Eq. (1.41). We evaluate the second derivative of v_{nk}

$$\begin{aligned}\partial_k^2 v_{nk}(r) &= \partial_k^2 u_{nk}(r)e^{i\phi_n(k)} + i\partial_k u_{nk}(r)\partial_k\phi_n(k)e^{i\phi_n(k)} \\ &\quad + iu_{nk}(r)\partial_k^2\phi_n(k)e^{i\phi_n(k)} - u_{nk}(r)[\partial_k\phi_n(k)]^2 e^{i\phi_n(k)}. \end{aligned} \tag{1.53}$$

Then we find the following relation between $\langle r^2\rangle_n(\phi_n)$ and $\langle r^2\rangle_n(\phi_n = 0)$:

$$\begin{aligned}\langle r^2\rangle_n(\phi_n) &= \langle r^2\rangle_n(\phi_n = 0) - \sum_k \mathcal{A}_n(k)\partial_k\phi_n(k) \\ &\quad + i\sum_k \partial_k^2\phi_n(k) - \sum_k [\partial_k\phi_n(k)]^2 . \end{aligned} \tag{1.54}$$

The third term vanishes if we assume that $\partial_k\phi_n(k)$ is single valued on $k \in [-\pi, \pi)$. To minimize the spread, extremize $\langle r^2\rangle_n - \langle r\rangle_n^2$ with respect to ϕ_n. Since $\langle r\rangle$ does not depend on ϕ_n, it is therefore sufficient to minimize (1.54). The functional derivative with respect to $\phi_n(k)$ vanishes if and only if

$$\partial_k^2\phi_n(k) = -\partial_k\mathcal{A}_n(k), \tag{1.55}$$

which completes the proof.

Equation (1.55) can be solved numerically [95]. In one dimension (1.55) can be integrated analytically. One solution is

$$\phi_n(k) - \phi_n(0) = -\int_0^k \mathcal{A}_n(\tilde{k})d\tilde{k}. \tag{1.56}$$

Remark that the solution of (1.55) is ambiguous up to a linear function of k, which amounts to shifting the centers of the resulting Wannier functions, but not their spread. Returning to the definition of Wannier states, a maximally localized Wannier state takes the form

$$W_n(R, r) = \frac{1}{\sqrt{N}}\sum_k e^{ikR}e^{-i\int_0^k \mathcal{A}_n(\tilde{k})d\tilde{k}}\psi_{nk}(r). \tag{1.57}$$

This expression shows that Wannier states are optimally localized if their phase ambiguity is resolved by adding a factor containing the Berry phase. This form will prove essential to the concept of polarization discussed in the next section.

1.2.3 Polarization

In this section, we prove that the polarization of a two-dimensional band insulator is related to the Chern number. We consider a Bloch Hamiltonian on a generic two-dimensional lattice

$$H = \sum_{\mathbf{k}} \sum_{\alpha\beta} h_{\alpha\beta}(\mathbf{k}) a^{\dagger}_{\alpha\mathbf{k}} a_{\beta\mathbf{k}}. \tag{1.58}$$

The Greek indices run over sites in the unit cell, equivalently the number of distinct bands. Assume that there are exactly two Bloch bands (at least two are necessary), corresponding to two sites per unit cell. The wavenumbers are denoted using the vector notation $\mathbf{k} = (k_1, k_2)$ in the first Brillouin zone. Equation (1.58) is the Hamiltonian of a periodic one-dimensional system along direction k_1, parameterized by k_2. To see this, denote

$$\begin{aligned} H &= \sum_{k_2} H_{k_2} \\ H_{k_2} &= \sum_{\alpha\beta} \sum_{k_1} h_{\alpha\beta}[(k_1, k_2)] a^{\dagger}_{\alpha,(k_1,k_2)} a_{\beta,(k_1,k_2)}. \end{aligned} \tag{1.59}$$

Hamiltonian H_{k_2} may be diagonalized in terms of Bloch waves in the argument k_1, which we denote as $|n, (k_1, k_2)\rangle$. The function $\psi_{n,(k_1,k_2)}(\mathbf{r}) = \langle \mathbf{r}|n, (k_1, k_2)\rangle$ is the Bloch wave defined previously in Sec. 1.2.1. It is a doublet (or spinor) with one entry for each site in the unit cell. We associate to this the Berry gauge field

$$\mathcal{A}^j_n(k_1, k_2) = -i\langle u_n(k_1, k_2)|\partial_{k_j}|u_n(k_1, k_2)\rangle, \tag{1.60}$$

where $j = 1, 2$. Let us make a choice of gauge such that $\mathcal{A}^2_n(k_1, k_2) = 0$.

We now introduce Wannier orbitals

$$w_n(R_1, \mathbf{r}, k_2) = \frac{1}{\sqrt{N_1}} \sum_{k_1} e^{-ik_1 R_1} e^{i\phi_n(k_1,k_2)} \psi_{n(k_1,k_2)}(\mathbf{r}). \tag{1.61}$$

Kohn has proved [97] that a complete set of exponentially localized Wannier states exists for any one–dimensional Hamiltonian. The phase factor $\phi_n(k_1, k_2)$ comes from the $U(1)$ gauge freedom of Bloch wavefunctions, and it can be fixed to $-\int_0^{k_1} dp_1 \mathcal{A}_n^1(p_1, k_2)$ in order to maximally localize the wavefunction along direction 1 as shown in Sec. 1.2.2. The center coordinate of the Wannier state along direction 1 is

$$\langle r_1 \rangle_{n,k_2} = -\sum_{k_1} \mathcal{A}_n^1(k_1, k_2). \tag{1.62}$$

Suppose that one flux quantum is adiabatically threaded so as to boost k_2 from 0 to $2\pi/a$ along a closed loop in the Brillouin zone. To realize this, note that a time–dependent magnetic flux $A_2(t)$ produces an electric field

$$E_2(t) = -\frac{\partial A_2}{\partial t} \tag{1.63}$$

which provides the necessary acceleration $\dot{k}_2$. Then the deviation of the center of the wavepacket in direction 1 is

$$\begin{aligned} \langle r_1 \rangle_{n,2\pi/a} - \langle r_1 \rangle_{n,0} &= -\sum_{k_1} \left[\mathcal{A}_n^1(k_1, k_2) \right]_{k_2=0}^{k_2=2\pi/a} \\ &= -\sum_{k_1} \sum_{k_2} \Delta_2 \mathcal{A}_n^1(k_1, k_2) \to a\nu_n, \end{aligned} \tag{1.64}$$

where Δ_2 is a "lattice" derivative between two consecutive values of k_2 in the discretized Brillouin zone, which tends to the partial derivative with respect to k_2 when the number of sites is taken to infinity. We have introduced

$$\nu_n = \frac{1}{2\pi} \iint_{BZ} dk_1 dk_2 \left[\partial_{\mathbf{k}} \times \mathcal{A}_n(\mathbf{k}) \right]. \tag{1.65}$$

ν_n represents the number of unit cells that the Wannier state shifts in direction 1, should a flux quantum be threaded such that k_1 is taken once around the Brillouin zone. This is related to the change in polarization which occurs upon adiabatically changing the Hamiltonian [98, 95, 93]. In the next section we will show that ν_n is an integer called the Chern number. In anticipation of this, we digress to enumerate cases when ν_n vanishes.

Firstly, the right hand side of (1.64) would vanish if $\mathcal{A}_n^1(k_1, k_2)$ were periodic under $k_1 \to k_1 + 2\pi/a$. Moreover, assume that both components of $\mathcal{A}_n(\mathbf{k})$ depend smoothly on $\mathbf{k}$. Then one can apply Stokes' theorem in (1.65), which states that

$$\iint_{BZ} dk_1 dk_2 \, [\partial_{\mathbf{k}} \times \mathcal{A}_n(\mathbf{k})] = \oint_{\partial BZ} \mathcal{A}_n(\mathbf{k}) \cdot d\mathbf{k} = 0. \tag{1.66}$$

The last equality follows from the fact that the boundary of the Brillouin zone, denoted ∂BZ, vanishes. Therefore, for ν_n to be nonzero, $\mathcal{A}_n(\mathbf{k})$ cannot be smooth on the torus. In fact, whenever a complete set of Wannier functions, which form a representation of the translation group in two dimensions, can be formed, then the Bloch wavefunctions are smooth and single-valued functions of $\mathbf{k}$. This implies a smooth Berry connection $\mathcal{A}_n(\mathbf{k})$, which implies $\nu_n = 0$. The fact that $\nu_n \neq 0$ is equivalent with the impossibility to form a basis of exponentially localized Wannier orbitals in band n [99, 100, 101].

Secondly, $\nu = 0$ if H had a single band (corresponding to a single site per unit cell, like the square lattice). For then we could define $\langle \mathbf{r}|\mathbf{k}\rangle \equiv u_{\mathbf{k}}(\mathbf{r})$, the Bloch wavefunction periodic in the unit cell. Since $u_{\mathbf{k}}(\mathbf{r})$ is the wavefunction, it is nonvanishing everywhere. We may therefore fix the arbitrary phase of the Bloch wavefunction such that $u_{\mathbf{k}}(\mathbf{r})$ is real everywhere in the Brillouin zone. Then the Berry gauge field associated to the band is

$$\begin{aligned} \mathcal{A}(\mathbf{k}) &= -i \int_{unit\ cell} d^2\mathbf{r} u_{\mathbf{k}}(\mathbf{r}) \partial_{\mathbf{k}} u_{\mathbf{k}}(\mathbf{r}) \\ &= -i\frac{1}{2}\partial_{\mathbf{k}} \int_{unit\ cell} d^2\mathbf{r} u_{\mathbf{k}}^2(\mathbf{r}) = 0. \end{aligned} \tag{1.67}$$

This argument implies that a lattice with at least two sites in the unit cell is necessary to have $\nu_n \neq 0$ for some n.

1.2.4 The first Chern number

In this section we show that ν_n, introduced in Eq. (1.65), is an integer. The argument presented here is due to Kohmoto [102]. We will first show that a Bloch wavefunction whose entries are nonzero everywhere in the Brillouin zone implies that $\nu_n = 0$. The existence of zeros of the Bloch wavefunction makes it impossible to select a smooth gauge for the Berry gauge field across the entire Brillouin zone. This procedure is, however, possible piecewise, by splitting the Brillouin zone into regions where some component of the wavefunction is nonzero. Then the number ν_n will turn out to be the total winding number of certain transition functions between these regions.

Proof that ν_n is an integer. Assume a two–band model, corresponding to a lattice with two sites in the unit cell, denoted A and B. Assume that the Hamiltonian is such that a finite energy gap separates the two bands. Let the spinor $u^T_{n\mathbf{k}} = (a_{n\mathbf{k}}, b_{n\mathbf{k}})$ denote the Bloch wavefunction for band n. The two components correspond to the two sublattices. Assume that $\nu_n \neq 0$. Then there exists $\mathbf{k}_a$ at which $a_{n\mathbf{k}_a} = 0$ and $\mathbf{k}_b$ such that $b_{n\mathbf{k}_b} = 0$. Without loss of generality, assume that each spinor component has only one zero.

Having identified the positions of the zeros, split the Brillouin zone into disjoint regions A_a and A_b, such that $\mathbf{k}_{a,b}$ belongs to the interior of $A_{a,b}$, respectively. In each region, fix the gauge by using the component of the wavefunction which is nonvanishing. We introduce Berry gauge field $\mathcal{A}^{a,b}_n(\mathbf{k})$ written in a gauge fixed by the condition that b, a, respectively, is real. Explicitly, Bloch vectors obtained in A^a must be multiplied by

$$e^{-i\theta^b_n(\mathbf{k})} = \frac{b^*_n(\mathbf{k})}{|b_n(\mathbf{k})|}, \tag{1.68}$$

to make the b component real. The scalars $\theta^{a,b}_n(\mathbf{k})$ are smooth functions over the regions $A^{b,a}$, respectively.

Armed with piecewise smooth $U(1)$ phase choices for the Bloch waves, split the Berry curvature integral over the torus into

$$\nu_n = \frac{1}{2\pi}\iint_{BZ} d^2\mathbf{k}\,[\partial_{\mathbf{k}} \times \mathcal{A}_n(\mathbf{k})] = \frac{1}{2\pi}\iint_{A_a} d^2\mathbf{k}\,[\partial_{\mathbf{k}} \times \mathcal{A}_n^a(\mathbf{k})] + \frac{1}{2\pi}\iint_{A_b} d^2\mathbf{k}\,\left[\partial_{\mathbf{k}} \times \mathcal{A}_n^b(\mathbf{k})\right]. \tag{1.69}$$

In each region Stokes' theorem applies since the integrand is smooth

$$\frac{1}{2\pi}\iint_{A^{a/b}} d^2\mathbf{k}\,\left[\partial_{\mathbf{k}} \times \mathcal{A}_n^{a/b}(\mathbf{k})\right] = \frac{1}{2\pi}\oint_{\partial A^{a/b}} d\mathbf{l}\cdot\mathcal{A}_n^{a/b}(\mathbf{l}). \tag{1.70}$$

Since the union of the surfaces A^a and A^b equals the torus, whose boundary vanishes, their boundaries are oppositely oriented: $\partial A^a = -\partial A^b$. Equation (1.69) reduces to computing the amount by which the two gauge choices disagree at the boundary:

$$\nu_n \;=\; \frac{1}{2\pi}\oint_{\partial A^a} d\mathbf{l}\cdot\left[\mathcal{A}^a(\mathbf{k}) - \mathcal{A}^b(\mathbf{k})\right] = \frac{1}{2\pi}\oint_{\partial A^a} d\mathbf{l}\cdot\left[\partial_{\mathbf{k}}\theta_n^a(\mathbf{k}) - \partial_{\mathbf{k}}\theta^b(\mathbf{k})\right]_{\mathbf{k}=\mathbf{l}}. \tag{1.71}$$

This form presents ν_n as the winding number of smooth phase field $\theta_n^a(\mathbf{k}) - \theta_n^b(\mathbf{k})$ around the closed loop ∂A^a. Then ν_n is an integer which completes the proof. The generalization of this, possibly including multiple zeros, follows from the theory of fiber bundles [102]. In that theory, ν_n is the first Chern class of the principal $U(1)$ fiber bundle [103, 89, 102]. The base manifold is the torus (the first Brillouin zone), and the associated fiber vector space is the space of Bloch wavefunctions.

The arguments in this section and in Section 1.2.3 are analogues of Laughlin's proof [104, 105, 106] of the quantization of the Hall conductance, in the language of Wannier orbitals.

1.2.5 Quantum Anomalous Hall Effect

Consider the model in (1.58) with just two bands, which we denote by $n = +, -$. Then $h_{\alpha\beta}(\mathbf{k})$ denotes a 2×2 Hermite matrix which can be expressed in the basis

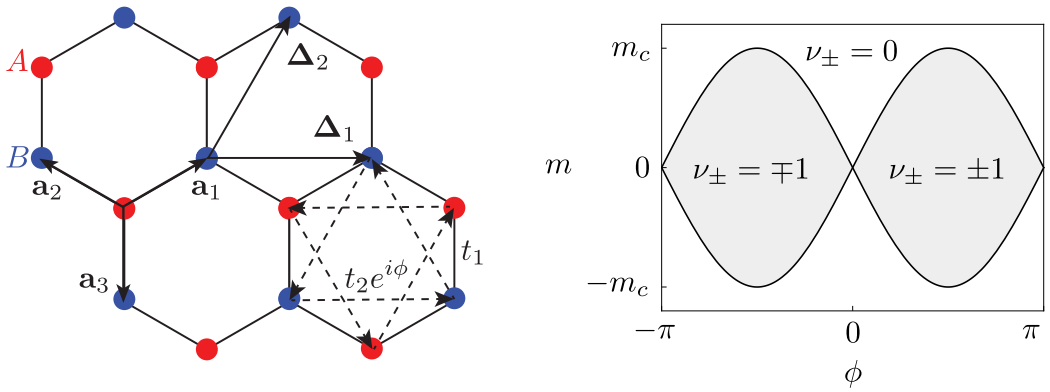

a) *b)*

Figure 1.2: a) Staggered fluxes on the honeycomb lattice amount to zero flux per unit cell. b) Phase diagram of the model (1.75): quantum anomalous Hall phase for $m < 3\sqrt{3}t_2 \sin(\phi)$, band insulator for $m > 3\sqrt{3}t_2 \sin(\phi)$, and semimetal at $m = 0, \phi = 0$.

of Pauli matrices:

$$h(\mathbf{k}) = h_0(\mathbf{k})\sigma_0 + \mathbf{h}(\mathbf{k}) \cdot \sigma = \begin{pmatrix} h_0 + h_3 & h_1 - ih_2 \\ h_1 + ih_2 & h_0 - h_3 \end{pmatrix}. \tag{1.72}$$

We have associated to the Hamiltonian the vector $\mathbf{h}(\mathbf{k}) = (h_1(\mathbf{k}), h_2(\mathbf{k}), h_3(\mathbf{k}))$. The two band dispersion relations are given by

$$\epsilon_\pm = h_0(\mathbf{k}) \pm |\mathbf{h}(\mathbf{k})|, \tag{1.73}$$

indicating that for a band degeneracy to occur one needs $\mathbf{h}(\mathbf{k}) = 0$. For later use, the projector onto the band denoted by $\pm$ is

$$P_\pm(\mathbf{k}) = |\pm, \mathbf{k}\rangle\langle\pm, \mathbf{k}| = \frac{1 \pm \hat{\mathbf{h}} \cdot \sigma}{2}, \tag{1.74}$$

where we have introduced the unit vector $\hat{\mathbf{h}}(\mathbf{k}) \equiv \mathbf{h}(\mathbf{k})/|\mathbf{h}(\mathbf{k})|$.

F. D. M. Haldane introduced a model on the honeycomb lattice which breaks time reversal symmetry with zero net flux through the lattice unit cell. Fig-

ure 1.2a) depicts the terms of the tight binding model. The honeycomb lattice is generated by translating the two-site unit cell by the lattice translation vectors $\mathbf{\Delta}_1 = a\sqrt{3}(1,0)$ and $\mathbf{\Delta}_2 = a\sqrt{3}(1/2, \sqrt{3}/2)$. The reciprocal lattice is defined by the condition $\mathbf{\Delta}_i \cdot \mathbf{g}_j = 2\pi\delta_{ij}$. Then $\mathbf{g}_1 = \big(2\pi/(\sqrt{3}a), -2\pi/(3a)\big)$ and $\mathbf{g}_2 = (0, 4\pi/(3a))$, which span the Brillouin zone. We define two special points in the Brillouin zone $\mathbf{K}_A = \mathbf{g}_1/3 + 2\mathbf{g}_2/3$, and $\mathbf{K}_B = -\mathbf{K}_A = 2\mathbf{g}_1/3 + \mathbf{g}_2/3$.

The length of a nearest neighbor bond is a. A site on sublattice A has three nearest neighbors on sublattice B denoted by vectors: $\mathbf{a}_1 = a(\sqrt{3}/2, 1/2)$, $\mathbf{a}_2 = a(-\sqrt{3}/2, 1/2)$ and $\mathbf{a}_3 = a(0, -1)$. The next–nearest neighbor vectors are defined by the equation $\mathbf{b}_1 = \mathbf{a}_2 - \mathbf{a}_3$ together with its cyclic permutations. Then we may express the Bloch Hamiltonian in the form (1.72) with

$$\begin{aligned} h_0(\mathbf{k}) &= -2t_2\cos(\phi)\sum_{i=1}^{3}\cos(\mathbf{k}\cdot\mathbf{b}_i), \\ h_1(\mathbf{k}) &= -t_1\sum_{i=1}^{3}\cos(\mathbf{k}\cdot\mathbf{a}_i),\ h_2(\mathbf{k}) = -t_1\sum_{i=1}^{3}\sin(\mathbf{k}\cdot\mathbf{a}_i), \\ h_3(\mathbf{k}) &= m + 2t_2\sin(\phi)\sum_{i=1}^{3}\sin(\mathbf{k}\cdot\mathbf{b}_i). \end{aligned} \tag{1.75}$$

The mass term m breaks inversion symmetry [107], defined as $Ih_{\mathbf{k}}I = \sigma_1 h_{-\mathbf{k}}\sigma_1$, which consists in reversing the momentum and interchanging the two sublattices. The terms $t_2 e^{i\phi}$ break time–reversal symmetry, defined $Th_{\mathbf{k}}T = h^*(-\mathbf{k})$, where * denotes complex conjugation. When the inversion symmetry breaking term dominates, the system is a band insulator. The band insulator is adiabatically connected to an atomic insulator, in a sense that we make precise below. If time–reversal symmetry breaking terms dominate, the system is in the quantum anomalous Hall (or Chern insulator) phase, associated with $\nu_\pm = \pm 1$. The phase diagram can be described by three regimes:

- **Gapped bands, band insulator.** For $m > 3\sqrt{3}t_2\sin(\phi)$, the model describes a band insulator with $\nu_\pm = 0$. The case with $\phi = 0$ and $m \neq 0$ corresponds to graphene with a staggered sublattice potential [72]. The

Berry curvature at $\mathbf{K}_{A,B}$ has opposite signs (Figure 1.3). As the gap decreases toward the graphene limit $m \to 0$, the Berry curvature peaks due to the divergent energy denominator in Eq. (1.15), turning into δ–functions amounting to $\pm\pi$ Berry's phase around the Dirac cones $\mathbf{K}_{A,B}$.

- **Gapless bands.** At $|m| = 3\sqrt{3}t_2|\sin(\phi)|$, the bands touch at $\mathbf{K}_A$ or $\mathbf{K}_B$. At the degeneracy the band dispersions are linear. If $m = 0$, $\phi = 0$, then the bands touch at Dirac cones at $\mathbf{K}_A$ and $\mathbf{K}_B$. This Hamiltonian describes graphene [72].

- **Gapped bands, quantum anomalous Hall phase**. If m and ϕ are such that $h_3(\mathbf{k})$ has opposite signs at $\mathbf{K}_A$ and $\mathbf{K}_B$, then the Berry curvatures add up (see Figure 1.3) and the Chern number of the lower band is $\nu_- = \pm 1$, where the sign depends on ϕ. This occurs for $m < 3\sqrt{3}t_2 \sin(\phi)$.

We now provide another interpretation of the topological invariant. Note that $\hat{\mathbf{h}}(\mathbf{k})$ denotes a map from the torus T^2 the unit sphere S^2. Then the integral of the Berry curvature can be reexpressed as the winding number of $\hat{\mathbf{h}}(\mathbf{k})$

$$\nu_\pm = \pm\frac{1}{4\pi}\iint_{BZ} d\mathbf{k}\ \hat{\mathbf{h}} \cdot \left[\partial_{k_1}\hat{\mathbf{h}}(\mathbf{k}) \times \partial_{k_2}\hat{\mathbf{h}}(\mathbf{k})\right]. \tag{1.76}$$

If $\nu_\pm = 0$ then the map $\hat{\mathbf{h}}(\mathbf{k})$ can be deformed smoothly into the uniform vector field: $\hat{\mathbf{h}}(\mathbf{k}) = \hat{\mathbf{z}}$ (see Figure 1.3). This, in turn, corresponds to a Hamiltonian whose bands are dispersionless $h(\mathbf{k}) = m\sigma_3$, i.e. an "atomic insulator" formed by disconnected unit cells. In the $\nu_\pm \neq 0$ phase, the map $\hat{\mathbf{h}}(\mathbf{k})$ cannot smoothly deform to the constant map, unless parameters are changed such that a degeneracy occurs in the Brillouin zone amounting to $\mathbf{h}(\mathbf{k}) = 0$. We have showed that the transition between the band insulator phase and the quantum anomalous Hall phase can only occur if the band gap collapses. We will call this "gap closing and reopening transition".

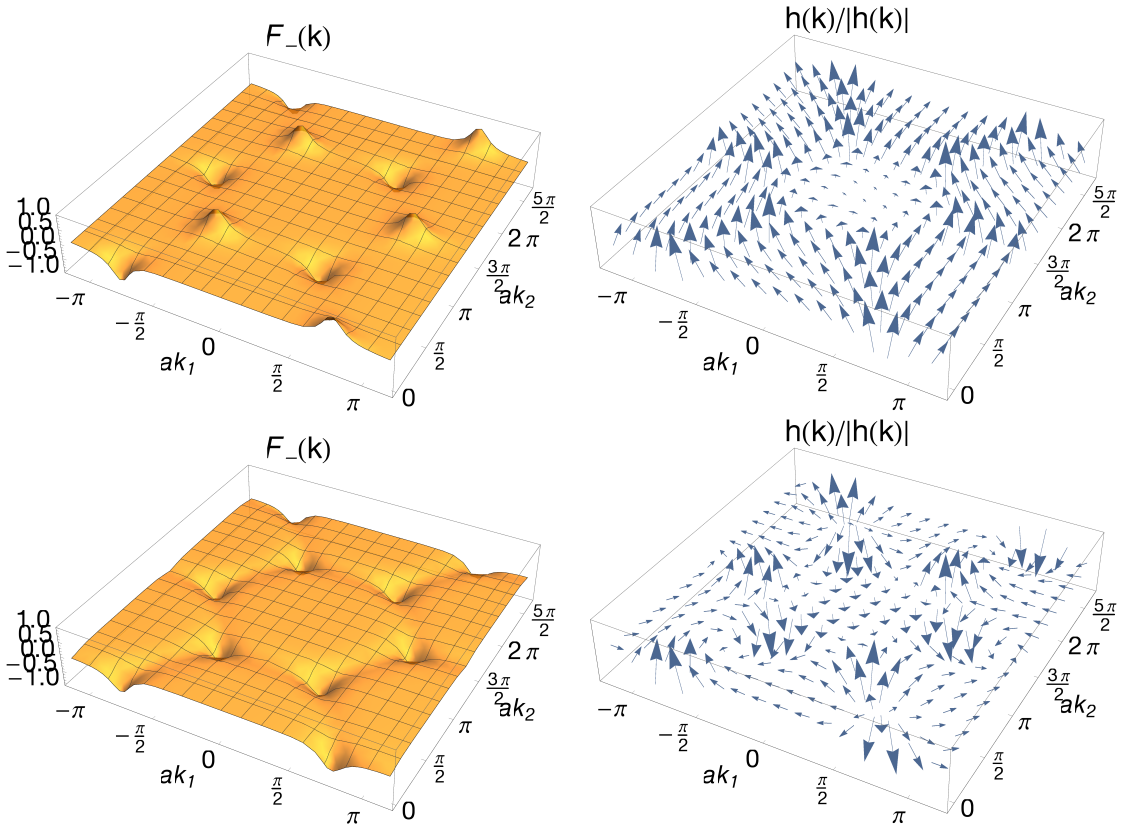

Figure 1.3: Plots of Berry curvature $\mathcal{F}_{-}(\mathbf{k})$ (**left**) and Hamiltonian $\hat{\mathbf{h}}(\mathbf{k})$ (**right**) over four times the surface of the 1^{st} Brillouin zone. **First row:** For a band insulator (here $t_2 = 0$, $m = t_1/2$), the Berry curvature takes opposite signs at $\mathbf{K}_{A,B}$. The vector field $\hat{\mathbf{h}}(\mathbf{k})$ is smoothly connected to the uniform field $\hat{\mathbf{h}}(\mathbf{k}) = \hat{\mathbf{z}}$. **Second row:** In the quantum anomalous Hall phase (here $t_2 = t_1/10$, $\phi = \pi/2$) the topological charges of merons [81, 84] at $\mathbf{K}_{A,B}$ add up to give $\nu_{\pm} = \pm 1$. The field $\hat{\mathbf{h}}(\mathbf{k})$ is not smoothly connected to a constant vector field.

1.3 Other formulations of the Chern number

Starting from Eqs. (1.76) and (1.74) we may now derive a formula for the Chern number which was introduced by Avron *et al.* [103], whose benefit is that it is written in terms of gauge–invariant quantities:

$$\nu_{\pm} = -\frac{i}{2\pi} \iint_{BZ} d\mathbf{k} \mathrm{Tr} \left\{ P_{\pm}(\mathbf{k}) \left[\partial_{k_1} P_{\pm}(\mathbf{k}), \partial_{k_2} P_{\pm}(\mathbf{k}) \right] \right\} . \tag{1.77}$$

The trace is taken over the Bloch band basis. To prove (1.77), simply replace $P_{\pm}(\mathbf{k})$ from (1.74), and make use of the identities $\mathrm{Tr}\,(\sigma_i \sigma_j) = 2\delta_{ij}$ and $[\sigma_i, \sigma_j] = 2i\epsilon_{ijk}\sigma_k$, where ϵ_{ijk} is the Levi–Civita tensor. The projector $P_{\pm}(\mathbf{k})$ is gauge invariant [cf. Eq. (1.9)]. Therefore, unlike (1.76), there is no need to fix a gauge consistently across the Brillouin zone, which makes (1.77) suitable for numerical evaluation. The applicability of this expression extends beyond translationally invariant systems. For example, in Ch. 2, we will use this formula to calculate Chern numbers for disordered systems, where momentum is no longer a good quantum number, but projectors onto eigenstates are still meaningful. In that same chapter, Eq. (1.77) will be used to calculate the topological invariant for topological Bogoliubov quasiparticles, where (1.74) must be replaced by the correct projector onto the bands of a Bogoliubov–de Gennes Hamiltonian.

In addition to Eqs. (1.77), (1.76) and (1.65), which were all written for a non-interating problem whose single–particle eigenstates were known, the first Chern number can be defined for an interacting problem via the Ishikawa–Matsuyama formula [108],

$$\nu = \frac{1}{24\pi^2} \iiint d\mathbf{k} d\omega \epsilon^{\mu\nu\rho} \mathrm{Tr} \left[G\partial_{\mu} G^{-1} G\partial_{\nu} G^{-1} G\partial_{\rho} G^{-1} \right] . \tag{1.78}$$

In (3.46), $G(\mathbf{k}, \omega)$ represents the single particle Green's function calculated in the interacting problem. This expression is equivalent to a more general form for the topological invariant which measures the Berry phase acquired by the ground state

wavefunction with respect to twisted boundary conditions on a torus [106]. Expression (3.46) is a topological invariant: infinitesimal deformations to the Green's function $G(\mathbf{k}, \omega)$ lead to zero variation of ν [20]. Studying an interacting problem in Ch. 3, we use this formula to calculate the topological invariant of quasiparticle and quasihole excitations of a Mott insulator.

1.4 Experiments

We conclude this chapter with an overview of current experiments on topological phases. The time–reversal symmetric counterpart of the QAHE, the quantum spin Hall effect (QSHE), can be realized in the presence of spin–orbit coupling [17, 109, 110, 111]. This state was first observed in HgTe/HgCdTe quantum wells with low density, high mobility carriers [112]. Upon tuning the well thickness in a heterostructure of HgTe and HgCdTe obtained by molecular beam epitaxy, two bands in the low–energy manifold are inverted, which marks a topological quantum phase transition. In the trivial regime, the longitudinal four–terminal conductance vanishes, while in the topological phase it is twice the quantum unit of conductance, $2e^2/h$, where e is the electron charge, and h is Planck's constant. Independence of this result on sample width is indicative of dissipationless transport at the edge, by one pair of counter propagating helical edge channels [113], whose existence can be probed in a three terminal setup [17, 18] to selectively measure nonzero spin–polarized current. Later, the QAHE was observed in thin films of a QSH insulator $(\mathrm{Bi}, \mathrm{Sb})_2\mathrm{Te}_3$, which was chromium doped to break time–reversal symmetry [114]. When the Fermi level is in the magnetically induced gap, the Hall conductance has a plateau at e^2/h, whereas the longitudinal conductance vanishes. The experimentally proved dissipationless helical transport in the edge channels may fuel the quest for low–power spintronic devices.

At the same time, there has been a vast array of experiments on topological phases in photonic systems and in ultracold atoms. Photonic systems with time re-

versal symmetry breaking are now possible [36]. The quest for lattice equivalents of integer quantum Hall phases has led to implementations of artificial gauge fields in gyromagnetic photonic crystals at microwave frequency [44, 45, 115, 46], coupled resonator optical waveguides [47, 48, 49], metamaterials based on pillar-shaped photonic waveguides [50, 51, 52], optomechanical systems [53], or radio frequency devices [54, 55], and a variety of theoretical proposals [116, 117]. Photonic experiments have typically probed the edge eigenstates, but there exist theoretical proposals to directly measure topological invariants [118, 119] in these systems. Topological transitions have been directly probed in quantum circuits of interacting superconducting qubits [120], where the qubit dynamics is mapped to that of the Haldane model [12]. Photonic systems typically work in the dissipative–driven regime [48, 116].

The study of phases which break time–reversal symmetry is well motivated by recent experimental progress with Floquet–type systems in optical lattices [121, 122, 123]. The definition of topological invariants in periodically driven systems has been the subject of several studies [124, 125, 126]. The Haldane model has been recently realized with fermionic potassium atoms [41]. In that experiment, shaking the retroreflecting mirrors of the optical lattice breaks time–reversal symmetry. A band–mapping technique [127] was adapted to probe quantum anomalous transport and observe the local Berry curvature and prove the topological character of the bands. Berry curvature in a graphene–like optical lattice loaded with ^{87}Rb atoms has been measured using Aharonov–Bohm interferometry [128, 129], revealing the $\pm\pi$ Berry's phase around the Dirac points. The square lattice Hofstadter model [37] has been realized with rubidium atoms [38] allowing to resolve cyclotron orbits, and in such systems Chern numbers can be determined to 1% accuracy [39]. A pending experimental goal is to explore strongly interacting phases, given a variety of theoretical proposals for fractional quantum Hall effect equivalents in two–dimensional lattice systems [27, 29, 31, 130, 131, 132, 133, 134, 135, 136].

Chapter 2

Photon QAHE on the Kagomé lattice

This chapter is dedicated to a model on the Kagomé lattice which supports the quantum anomalous Hall phase (for an introduction, see Chapter 1). The photonic Kagomé lattice without time–reversal symmetry breaking has been implemented by Underwood *et al.* [73] with an array of microwave cavities [137]. The cavities, which are superconducting transmission line resonators [138], are disposed in a planar honeycomb array, such that three resonators meet at each junction. Additionally, the three–way junction may be replaced by superconducting ring coupling circuits, whose virtual excitations mediate photon transfer between resonators. When the coupling ring is threaded with magnetic flux, the effective photon hopping Hamiltonian [57], which may be obtained upon adiabatic elimination of the superconductor degrees of freedom, breaks time–reversal symmetry. The resulting Peierls phases mimic a magnetic field with zero net flux through each unit cell, in close analogy with Hamiltonians responsible for the quantum anomalous Hall effect [12].

A photon cavity array with such properties may facilitate a variety of many–body states [139, 140], arising from the interplay of the delocalization across the lattice and nonlinearities at each cavity. For example, should qubits be placed

in each resonator [141, 137], the ensuing Jaynes–Cummings model [142] modeling the light–qubit coupling sustains polariton Mott insulator or superfluid phases [143, 144, 145, 146, 147, 148, 149, 150]. (Polaritons are dressed particles formed by a coherent superposition of the photonic mode of the cavity and the states of the two–level system, and kinetic terms correspond to overlaps of these extended light–matter states.) The more general Rabi–Hubbard model has novel quantum criticality, such as a $\mathbb{Z}_2$ symmetry–breaking quantum phase transition [151]. Other novel situations, such as Bose–Hubbard models with attractive interactions [152], may arise in arrays of resonators coupled to two–level systems. All systems enumerated in this paragraph are permanently laser driven and subject to photon decay and qubit relaxation, such that phase transitions occur between steady states [137], in contrast to equilibrium quantum phase transitions at zero temperature [153, 154].

Moreover, the Kagomé bandstrucure supports a flat band, which introduces a small energy scale that enhances the effect of perturbations such as disorder, interactions or dissipation. The ground state is determined fully by the interactions acting in the macroscopically degenerate ground state manifold. In particular, Bogoliubov perturbation theory [155] for the weakly interacting Bose gas fails for a condensate in a flat band. Ground states of flat band lattices such as the Kagomé, or the zig–zag lattice may include supersolids or fractionally filled solids [156]. The Bose condensed state in the flat band of the quasi one–dimensional Lieb lattice fragments into localized modes sustained by lattice frustration [157]. If in addition to a flat band time–reversal symmetry is broken, one has the principal ingredients to realize fractional quantum Hall phases in strongly–coupled arrays of electromagnetic cavities [158, 159, 160].

The results presented in this chapter were previously reported in Ref. [58]. The starting point of this work was the observation that the time–reversal symmetry breaking Hamiltonian in Ref. [57] supports a quantum anomalous Hall phase analogous to that proposed originally by Haldane [12]. Nevertheless, the result-

ing tight–binding model is distinct from the QAHE honeycomb lattice model of Ref. [12]: it has three bands, one of which can be tuned to be perfectly flat. The time–reversal symmetry breaking terms open bandgaps, and the outer Bloch bands acquire nonzero Chern numbers whereas the middle band always has Chern number zero. Therefore there exists a region in the energy gap where topologically protected edge eigenstates are degenerate with the trivial band. If the latter acquires dispersion, the otherwise protected edge states can scatter into the bulk, which causes the anomalous Hall effect, characterized by a Berry phase around the first Brillouin zone which is not an integer multiple of 2π.

The aim of this chapter is to focus on the single–particle physics of the Kagomé lattice and to study the robustness of the quantum anomalous Hall phase to disorders and nonlinearities, as well as discuss probes of band topology. The remainder of this chapter is organized as follows. We introduce the tight-binding model in Sec. 2.1. We find the edge eigenstates in open-boundary lattices in Sec. 2.2, and study edge currents and the local density of states. In Sec. 2.3, we numerically test the robustness of the quantum anomalous Hall phase to scalar and flux disorders by computing Chern numbers in finite disordered lattices. In Sec. 2.4 we use equations of motion for wavepackets prepared in a specific Bloch band in order to extract its local Berry curvature. We focus on the interesting case of placing the quantum anomalous Hall phase in a uniform magnetic field, for which we devise a protocol in App. A. In Sec. 2.5 we extend the results of Sec. 2.4 to show how one can determine band Chern numbers from interferometry experiments. In Sec. 2.6 we derive conditions on the strength of the external field in order for the semiclassical approach of the previous sections to be valid. Finally, in Sec. 2.7 we address the stability of the topological phase to weak nonlinearities of the photon cavities, which we model with the repulsive Bose–Hubbard model, and compute topological invariants that indicate the existence of gapless Bogoliubov edge excitations. Most of the results presented in this chapter can be found in published form in [58].

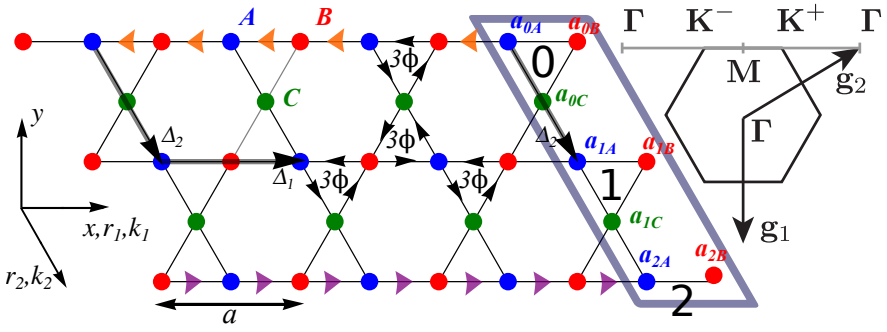

Figure 2.1: The Kagomé lattice with nonuniform flux [57]. **Left:** lattice periodic in the x direction, with line boundaries (no C sites). The blue contour marks a superunit cell generating the cylinder. **Right:** Projection of the first Brillouin zone on the k_1 direction.

2.1 Tight-binding model

In the typical circuit QED system, a coplanar resonator with length of a few millimeters typically supports a single photonic mode. Furthermore, this photonic mode may carry no polarization label, and can be thought of as the single type of excitation of the microwave resonator [161]. These excitations may be transfered from one waveguide to another via inductive or capacitive couplings.

In Ref. [57], a honeycomb array of waveguides with nano–Josephson circulators was considered. Time–reversal symmetry was broken by threading magnetic flux through nano–Josephson circulators at which three waveguides are capacitively coupled in a 120 degree pattern. A tight–binding model for the microwave cavity photons was obtained upon tracing out coupler circuit degrees of freedom. The tight–binding model contains nearest–neighbor hopping terms on the Kagomé lattice (Figure 2.1), which is the line graph of the honeycomb lattice. The magnetic flux is nonuniform but amounts to 0 over the whole unit cell as in the quantum anomalous Hall system of Ref. [12]. Here, triangular plaquettes are threaded by flux 3ϕ, whereas flux through hexagonal plaquettes is -6ϕ.

Denote the three sites of the unit cell by A, B, C. Let a be twice the length of

a bond, and pick lattice vectors

$$\boldsymbol{\Delta}_1 = a(1,0), \quad \boldsymbol{\Delta}_2 = a\left(\frac{1}{2}, -\frac{\sqrt{3}}{2}\right). \tag{2.1}$$

Two integers $\mathbf{m} = (m_1, m_2)$ determine the position of any unit cell, $\mathbf{r_m} \equiv m_1\boldsymbol{\Delta}_1 + m_2\boldsymbol{\Delta}_2$. The first Brillouin zone (Figure 2.1) is spanned by:

$$\mathbf{g}_1 = \frac{2\pi}{a}\left(1, \frac{1}{\sqrt{3}}\right), \quad \mathbf{g}_2 = \frac{2\pi}{a}\left(0, -\frac{2}{\sqrt{3}}\right). \tag{2.2}$$

We denote high symmetry points in the first Brillouin zone by $\boldsymbol{\Gamma} = (0,0)$ and $\mathbf{K}^{\pm} = \pm\left(\frac{4\pi}{3a}, 0\right)$ (see Figure 2.1).

Letting $\psi^{\dagger}_{\mathbf{k}} = \left(a^{\dagger}_{A\mathbf{k}}, a^{\dagger}_{B\mathbf{k}}, a^{\dagger}_{C\mathbf{k}}\right)$, the tight–binding model can be written in the basis of Bloch waves,

$$H = \sum_{\mathbf{k}\in BZ} \psi^{\dagger}_{\mathbf{k}} h(\mathbf{k}) \psi_{\mathbf{k}}, \tag{2.3}$$

where the Bloch Hamiltonian is expressed in matrix form

$$h(\mathbf{k}) = \begin{pmatrix} \hbar\omega & 2|t|e^{i\phi}\cos\alpha_1 & 2|t|e^{-i\phi}\cos\alpha_2 \\ 2|t|e^{-i\phi}\cos\alpha_1 & \hbar\omega & 2|t|e^{i\phi}\cos\alpha_3 \\ 2|t|e^{i\phi}\cos\alpha_2 & 2|t|e^{-i\phi}\cos\alpha_3 & \hbar\omega \end{pmatrix}, \tag{2.4}$$

in terms of the following three dimensionless functions of momentum

$$\alpha_1(\mathbf{k}) \equiv \mathbf{k}.\frac{\boldsymbol{\Delta}_1}{2}, \ \alpha_2(\mathbf{k}) \equiv \mathbf{k}.\frac{\boldsymbol{\Delta}_2}{2}, \text{ and } \alpha_3(\mathbf{k}) \equiv \mathbf{k}.\frac{\boldsymbol{\Delta}_1 - \boldsymbol{\Delta}_2}{2}. \tag{2.5}$$

Since H is unchanged by $\phi \to \phi + \frac{2\pi}{3}$, we restrict to $\phi \in \left[0, \frac{2\pi}{3}\right]$. The diagonal elements of (2.4) are the waveguide frequencies ω, which are typically one order of magnitude larger than the band gap: $|t|/\hbar$ is expected to lie below 100 MHz, whereas ω is in the microwave (GHz) range in typical cQED implementations.

For $\phi = \frac{m\pi}{3}$ with m even, the energies of the three bands are $E_0 - \hbar\omega = -2|t|$ and $E_{\pm} - \hbar\omega = |t|(1 \pm \sqrt{3 + 2\sum\cos(\alpha_j)})$, where the sum is over $j = 1, 2, 3$. The middle band and the flat band are degenerate at $\mathbf{k} = 0$ with energy $-2|t|$. The

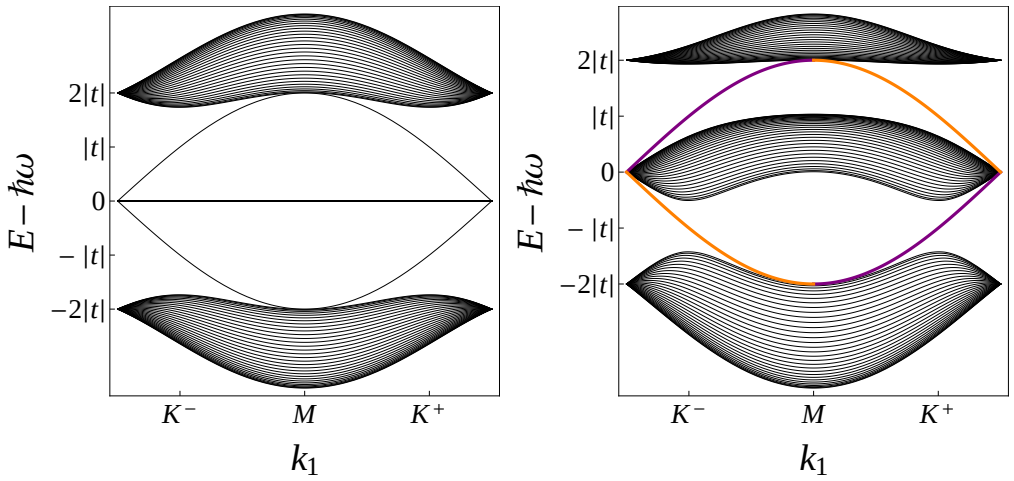

Figure 2.2: **Left:** Bandstructure along a line in the Brillouin zone which is parallel to k_1 (see Fig. 2.1). At $\phi = \pi/6$ the middle band is flat. **Right:** At $\phi = \pi/4$ the middle band is dispersive. In both cases, the lower and upper bands are topological. Chiral modes are localized at each edge of a cylinder (purple right mover on lower edge, orange left mover on upper edge, with corresponding currents sketched in Fig. 2.1.

top band and the middle band are degenerate at $\mathbf{K}^{\pm}$ with energy $|t|$. The case of odd m is analogous, with the exception that the bands flip sign. The flat band consists of a set of orbitals localized on the hexagonal plaquettes. If the lattice is periodic, state counting reveals that the $\mathbf{\Gamma}$ point degeneracy is topologically protected [162]. The degeneracy at $\mathbf{K}^{\pm}$ is protected by inversion symmetry I

$$Ih(\mathbf{k})I = h(-\mathbf{k}), \tag{2.6}$$

and time reversal time–reversal symmetry T

$$Th(\mathbf{k})T = h^*(-\mathbf{k}). \tag{2.7}$$

More precisely, for $\phi = \frac{m\pi}{3}$, $h(\mathbf{k})$ and its I and T transforms are similar up to a gauge transformation. An important consequence of inversion and time–reversal symmetry is that the Berry curvature of the dispersive bands is 0 everywhere in the Brillouin zone except at $\mathbf{K}^{\pm}$, where the Berry phases are $\pm\pi$. The only way to open the gap while I and T hold is via anisotropies [58]. Hopping term anisotropies can be tuned to bring the $\pm\pi$ Dirac cones together at an I and T

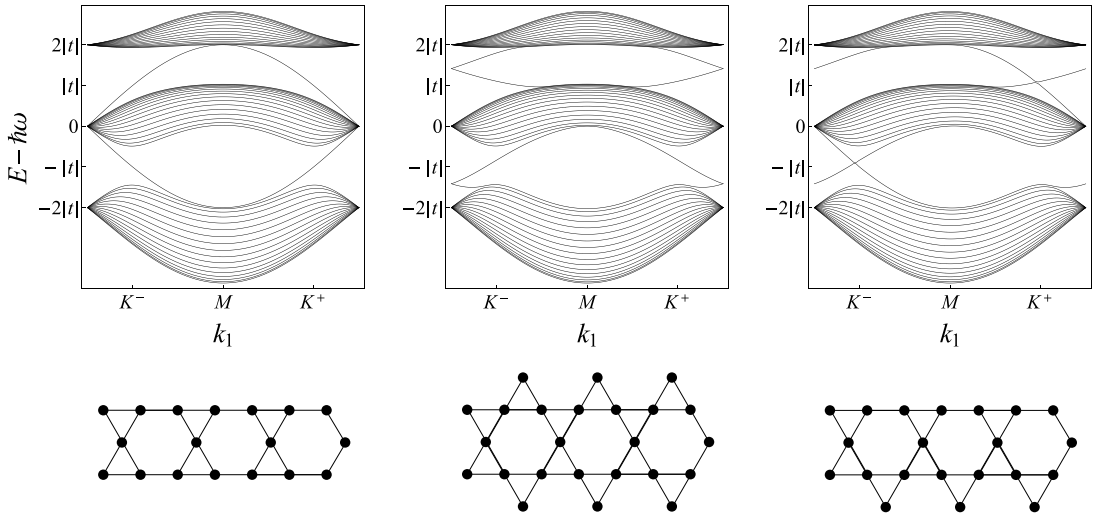

Figure 2.3: Edge and bulk eigenstate energy dispersion for three different choices of boundary conditions (line–line, armchair–armchair, line–armchair), at $\phi = \frac{\pi}{4}$. The panels on the second row exhibit the smallest number of unit cells in the direction with open boundaries, for which edge modes are supported.

symmetric point ($\mathbf{\Gamma}$ or $\mathbf{M}$) and annihilate them.

Values $\phi \neq \frac{m\pi}{3}$ break T (but not I), opening both gaps. For $\phi = \frac{\pi}{6} + \frac{m\pi}{3}$ the middle band is flat (Figure 2.2). Employing (1.65), we find that the band Chern numbers of the lower, middle, and upper bands, respectively, are $-\mathrm{sgn}\left(\sin 3\phi\right), 0$ and $+\mathrm{sgn}\left(\sin 3\phi\right)$, where $\phi \in \left[0, \frac{2\pi}{3}\right)$. The $\sin(3\phi)$ function was chosen to obey the $2\pi/3$ periodicity of the bandstructure with respect to the phase ϕ. The perfectly flat band, if isolated from the other bands by energy gaps (at $\phi = \frac{\pi}{6}$), is necessarily non–topological [163].

2.2 Chiral edge states

The result of bulk–edge correspondence implies that eigenstates must exist in certain gaps. The condition is that the total Chern numbers of the bands below the gap be nonzero. In this section, we find the edge mode dispersion relation and eigenfunction for different choices of boundaries (Sec. 2.2.1). We numerically study local observables accessible with current experiments in Sec. 2.2.2.

2.2.1 Analytic solution

To obtain the edge eigenstates, consider a cylinder periodic in the $\mathbf{\Delta}_1$ direction. Assume for example that its boundary sites are of A, B type only (see Figure 2.1). The cylinder is generated by translating the superunit cell (blue parallelogram in Fig. 2.1) by integer multiples of $\mathbf{\Delta}_1$. The superunit cell is obtained by translating the triangular plaquette along $\mathbf{\Delta}_2$. We number plaquettes in the superunit cell by $m_2 = 0, 1, ..., m_{2\max}$, as in Fig. 2.1. We will employ a partial Fourier transform along $\mathbf{\Delta}_1$,

$$a_{\alpha m_2}(k_1) = \frac{1}{\sqrt{N_1}} \sum_{m_1} e^{-ik_1(m_1 a)} a_{m_1,m_2}, \tag{2.8}$$

where $\alpha = A, B, C$ and N_1 counts unit cells along $\mathbf{\Delta}_1$. The problem is to diagonalize the one–dimensional Hamiltonian parametrized by k_1:

$$\begin{aligned} h(k_1) &= |t| \sum_{m_2} \Big[2e^{i\phi} a^\dagger_{Bm_2} a_{Am_2} \cos\left(k_1 \frac{a}{2}\right) \\ &\quad + e^{i\phi + ik_1 \frac{a}{4}} a^\dagger_{Cm_2} a_{Bm_2} + e^{i\phi - ik_1 \frac{a}{4}} a^\dagger_{Cm_2} a_{B,m_2+1} \\ &\quad + e^{i\phi + ik_1 \frac{a}{4}} a^\dagger_{Am_2} a_{Cm_2} + e^{i\phi - ik_1 \frac{a}{4}} a^\dagger_{Am_2} a_{C,m_2-1} + \text{H.c.} \Big]. \end{aligned} \tag{2.9}$$

Eigenstates of (2.9) are best written in the basis $\{|\alpha m_2\rangle\}$, whose elements are kets corresponding to wavefunctions that are exponentially localized on sublattice α of the m_2^{th} triangular plaquette along the super unit cell (this is analogous to the basis of Sec. 1.2.3):

$$|\Psi(k_1)\rangle \equiv \sum_{\alpha=A,B,C} \sum_{m_2} \psi_{\alpha m_2}(k_1) \, |\alpha m_2\rangle \, . \tag{2.10}$$

The eigenvalue equation $h(k_1)|\Psi(k_1)\rangle = E_\Psi(k_1)|\Psi(k_1)\rangle$ becomes, upon writing the energy dispersion as $U(k_1) \equiv -\left[E(k_1) - \hbar\omega\right]/|t|$,

$$\begin{aligned} -U\psi_{Am_2} &= e^{-ik_1\frac{a}{4} - i\phi} \psi_{C,m_2-1} + 2\cos\left(k_1 \frac{a}{2}\right) e^{i\phi} \psi_{Bm_2} + e^{ik_1\frac{a}{4} - i\phi} \psi_{Cm_2}, \\ -U\psi_{Bm_2} &= e^{ik_1\frac{a}{4} + i\phi} \psi_{C,m_2-1} + 2\cos\left(k_1 \frac{a}{2}\right) e^{-i\phi} \psi_{Am_2} + e^{-ik_1\frac{a}{4} + i\phi} \psi_{Cm_2}, \end{aligned} \tag{2.11}$$

$$-U\psi_{C,m_2} = e^{ik_1\frac{a}{4}-i\phi}\psi_{Bm_2} + e^{-ik_1\frac{a}{4}+i\phi}\psi_{Am_2} + e^{-ik_x\frac{a}{4}-i\phi}\psi_{B,m_2+1} + e^{ik_1\frac{a}{4}+i\phi}\psi_{A,m_2+1}.$$

These equations hold for the bulk $m_2 = 0, ..., m_{2,\max}$. The next three equations correspond to unit cells at the boundary:

$$\begin{aligned} -U\psi_{C,-1} &= e^{-ik_1\frac{a}{4}-i\phi}\psi_{B0} + e^{ik_1\frac{a}{4}+i\phi}\psi_{A0}, \\ -U\psi_{Am_{2\max}} &= e^{-ik_1\frac{a}{4}-i\phi}\psi_{Cm_{2\max}} + 2\cos\left(k_1\frac{a}{2}\right)e^{i\phi}\psi_{Bm_{2\max}}, \\ -U\psi_{Bm_{2\max}} &= e^{ik_1\frac{a}{4}+i\phi}\psi_{C,m_{2\max}} + 2\cos\left(k_1\frac{a}{2}\right)e^{-i\phi}\psi_{Am_{2\max}}. \end{aligned} \tag{2.12}$$

For the line boundary the wavefunction vanishes on the missing C sites:

$$\psi_{C,-1} = \psi_{C,m_{2\max}} = 0. \tag{2.13}$$

Finally, edge eigenstates follow from (2.11,2.12,2.13) using the *Ansatz*

$$\psi_{\alpha m_2} = \lambda^{m_2}\psi_{\alpha 0}. \tag{2.14}$$

The wavefunction $\psi_{\alpha m_2}$, $\alpha = A, B, C$, decays exponentially along $\mathbf{\Delta}_2$, away from the boundary sites.

The energy solutions are identical to those of a one-dimensional tight-binding chain of lattice constant $\frac{a}{2}$:

$$\begin{aligned} E_+ &= 2|t|\cos\left(\frac{k_1 a}{2}\right) \quad \text{and} \quad \lambda_+ = -\frac{\cos\left(\frac{k_1}{4}-\frac{3\phi}{2}\right)}{\cos\left(\frac{k_1}{4}+\frac{3\phi}{2}\right)}, \\ E_- &= -2|t|\cos\left(\frac{k_1 a}{2}\right) \quad \text{and} \quad \lambda_- = \frac{\sin\left(\frac{k_1}{4}-\frac{3\phi}{2}\right)}{\sin\left(\frac{k_1}{4}+\frac{3\phi}{2}\right)}. \end{aligned} \tag{2.15}$$

Note that the edge state dispersion relation is independent of ϕ (see Figure 2.2). If $|\lambda_\pm| < (>)1$, then the wavefunction is localized at the top (bottom) boundary, and the group velocity dE/dk_1 is positive (negative). $\lambda_\pm$ may become singular or 0, in which case the normalized wavefunction has 0 weight in the bulk and is nonvanishing on sites corresponding to a unit cell situated at one of the two edges.

For other boundary shapes (Figure 2.3), the edge mode and the middle bulk band may overlap in energy or in momentum. The smallest lattice supporting a pair of edge modes must contain at least one row of hexagonal plaquettes, regardless of boundary condition, as shown in the bottom panels of Figure 2.3.

2.2.2 Local observables

The local density of states spatially resolves eigenstates within a narrow energy window. Consider the full set of eigenstates $\{|\Psi\rangle\}$ and eigenenergies $\{E_\Psi\}$ of (2.3). We define the local density of states as

$$\rho(E, \mathbf{r}) \equiv \sum_\Psi \delta(E - E_\Psi) |\langle \mathbf{r}|\Psi\rangle|^2. \tag{2.16}$$

The local density of states is normalized to the total number of energy levels

$$\int dE \sum_{\mathbf{m}} \rho(E, \mathbf{r_m}) = 3N, \tag{2.17}$$

where N is the total number of unit cells. We have numerically evaluated $\rho(E, \mathbf{r})$ for the cylinder lattice with line edges considered in 2.2.1. Figure 2.4 contains plots of local density of states in several cases. In the flat band at $\phi = \frac{\pi}{6}$ the wavefunctions are localized in the hexagonal plaquettes due to destructive interference. When the flux ϕ is detuned from $\frac{\pi}{6}$, the states in the dispersive middle band are extended. If disorder is introduced into the flat band system at $\phi = \frac{\pi}{6}$, the states inside the middle band are no longer perfectly localized on the hexagon plaquettes. Edge eigenstates have non-zero spectral weight only close to the edges of the sample.

The introduction of a small impurity at the boundary can mix all momenta and the edge state can scatter into the bulk. One consequence of this is that edge currents leak into the bulk. We may study this by introducing a δ–function impurity at one of the sites on the boundary of the system. The lattice current operator measures the number of particles that flow from site $\mathbf{m}$ to site $\mathbf{n}$ per unit

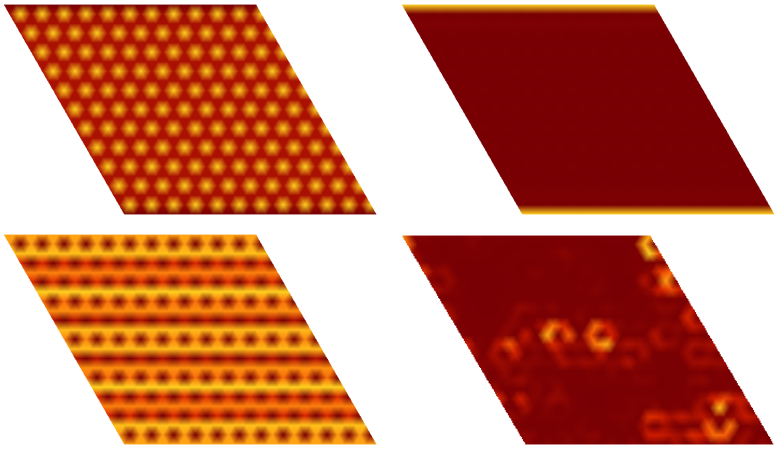

Figure 2.4: The local density of states for a 23×23 site lattice is represented here on color plots where lighter colors correspond to higher values (in arbitrary units). The panels, in order, show: the flat band at $\phi = \frac{\pi}{6}$ with spectral weight confined to the hexagonal plaquettes; spectral weight at midgap energies indicating wavefunctions confined to the edges of the sample; the dispersive middle band for $\phi = \frac{\pi}{4}$ containing extended states; local density of states of the disordered $\phi = \frac{\pi}{6}$ system for an energy E close to the middle band.

time [164]

$$j_{\mathbf{mn}} = -ia^{\dagger}_{\mathbf{m}}(t_{\mathbf{mn}} + t^{*}_{\mathbf{nm}})a_{\mathbf{n}} + ia^{\dagger}_{\mathbf{n}}(t^{*}_{\mathbf{mn}} + t_{\mathbf{nm}})a_{\mathbf{m}}. \tag{2.18}$$

Results for the current expectation values $\langle\Psi|j_{\mathbf{mn}}|\Psi\rangle$ for $\phi = \frac{\pi}{4}$ are shown in Figure 2.5. For an edge eigenstate with energy in the gap just above and not overlapping with the middle band, the current will surround the δ–function obstruction without leaking into the bulk. If the edge eigenstate and the bulk band are degenerate, particle current is transferred from the edge into the bulk with finite probability. If we replaced the impurity by strong phase disorder (uniformly distributed with amplitude $W_{\Phi} = \frac{\pi}{3}$), bulk states would spread into the gap. There is again a finite probability for the edge mode to scatter into the bulk. The nonvanishing backscattering probability for edge eigenstates that are degenerate with the bulk is associated with a nonquantized value for the Chern number integral, which is indicative of a phase distinct from the quantum anomalous Hall phase, named the anomalous Hall phase [165].

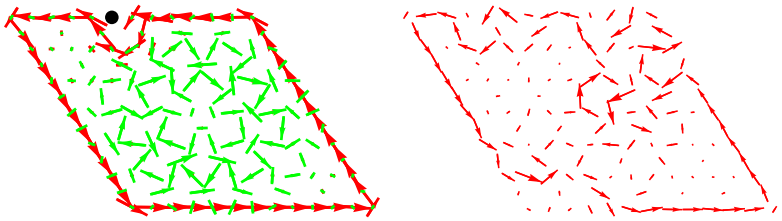

Figure 2.5: Expectation value of the lattice current operator for $\phi = \frac{\pi}{4}$ (band-structure in Figure 2.2). **Left panel:** For intragap eigenstates, a δ–function impurity will deviate edge current (red), which maintains chirality. The current in a state with energy within the overlap region with the middle band is shown in green. This corresponds to the anomalous quantum Hall phase. **Right panel:** with disorder, the edge state can leak into the bulk with a finite probability.

2.3 Anomalous Hall Effect

While in the previous section we have discussed local observables, we now turn to geometric phases for clean and disordered systems. This approach addresses the robustness of edge states from the topological properties of the Bloch eigenstates, discussed at length in Section 1.2.

Why edge states are not robust when degenerate with bulk bands can be understood from geometric arguments. If the system is probed at an energy E which intersects a bulk band, then the Berry phase in units of 2π takes the form

$$\nu_n(E) = \frac{1}{2\pi} \oint_{C(E)} d\mathbf{k} \cdot \mathcal{A}_n(\mathbf{k}). \tag{2.19}$$

The curve $C(E)$ is the intersection of the two-dimensional surface of the band $E_n(\mathbf{k})$ with the (k_x, k_y) plane at fixed energy E. We may form the following quantity from Eq. (2.19):

$$\nu(E) = \sum_n \nu_n(E) = \frac{1}{2\pi} \sum_n \int_{\mathrm{BZ}} d^2\mathbf{k}\, \theta\left[E - E_n(\mathbf{k})\right] \mathcal{F}_n(\mathbf{k}), \tag{2.20}$$

which is a summation over the states whose energy falls below E (note that θ is the Heaviside function [166]). For numerical evaluation it is convenient to recast this in terms of the gauge invariant projector $P_{\mathbf{k}} = P_{\mathbf{k}}(E)$ onto the Bloch states whose

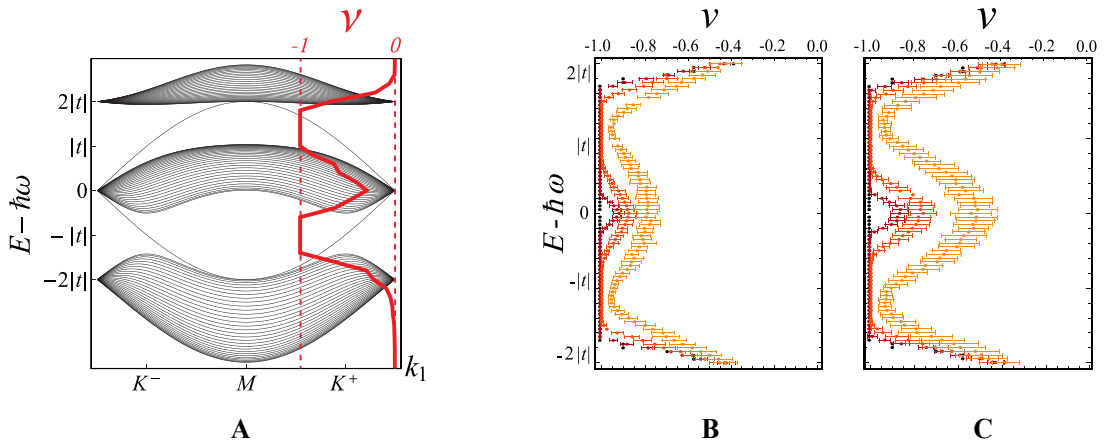

Figure 2.6: **A:** $\nu(E)$ of (2.21) for $\phi = \pi/4$. **B:** $\nu(E)$ for $\phi = \frac{\pi}{6}$ with increasing amplitude of phase disorder: $6W_\Phi/\pi = 0, 2/5, 1, 9/5$. For high enough disorder $\nu(E)$ is nowhere quantized. Points represent ensemble averages over 40 randomly picked disorder configurations, and error bars the standard deviation within the ensemble. **C:** Analogous study with increasing amplitude of on-site disorder $W/|t| = 0, 1/2, 1, 3/2$.

energy is less than E, the Avron–Seiler–Simon formula introduced in Eq. (1.77):

$$\nu(E) = \frac{1}{2\pi i} \int d^2\mathbf{k} \, \mathrm{Tr} \left(P_\mathbf{k} \left[\partial_{k_x} P_\mathbf{k}, \partial_{k_y} P_\mathbf{k} \right] \right), \tag{2.21}$$

with the trace taken over the band basis. We plot (2.21) as a function of energy over the entire bandwidth in Figure 2.6**A**. The number $\nu(E)$ non–integer whenever the energy E overlaps with a bulk band, which corresponds to edge modes that can decay into the bulk of the sample.

In fermion systems, the non-quantized part is the intrinsic contribution to the anomalous Hall effect [167, 168] of a partially filled band (non-quantized Hall conductivity σ_{xy}), and can be interpreted as a Berry phase of quasiparticles at the Fermi surface [165]. For bosons nonzero $\nu_n(E)$ signals anomalous transport of a wavepacket at energy E in band n. Despite its form (2.20) as an integral over a "Fermi sea" of occupied states, $\nu_n(E)$ is a property of single-particle eigenstates (independent of particle statistics).

It turns out that the fate of the edge eigenstates is similar in a disordered system. If translation symmetry is broken, as is the case with nonuniform disorder potentials, the trace (2.21) can be taken with respect to the basis of states localized

at each site, $|\mathbf{r_m}\rangle$:

$$\nu(E) = -\lim_{N_{sites}\to\infty} \frac{2\pi i}{N_{sites}} \sum_{\mathbf{m}} \langle \mathbf{r_m}|P(E)\left[-i[x,P(E)],-i[y,P(E)]\right]|\mathbf{r_m}\rangle. \qquad (2.22)$$

The total number of sites in the system is N_{sites}. In the thermodynamic limit of a clean system, this formula is equivalent to (2.21).

In the presence of disorder, $\nu(E)$ is an integer as long as the energy E belongs to an energy gap [169]. Transitions between distinct integer values occur if the energy E crosses a region of extended bulk states. If the lattice is finite, it is necessary to average over an ensemble of disorder configurations [170, 171, 169]. (No disorder average is necessary in an infinite system, if the disorder is self-averaging). To set up the numerical calculation, assume that disorder configurations are distributed with measure $d\mu(\delta)$. In a finite system, and for a fixed disorder function δ, (2.22) becomes

$$\nu_\delta(E) = -\frac{2\pi i}{N_{sites}} \sum_{\mathbf{m}} \langle \mathbf{r_m}|P_\delta(E)\left[-i[x,P_\delta(E)],-i[y,P_\delta(E)]\right]|\mathbf{r_m}\rangle, \qquad (2.23)$$

where all operators with subscripts δ are evaluated for a fixed disordered Hamiltonian H_δ. In (2.23), x, y are the position operators in Cartesian coordinates. We retrieve the infinite system result by computing the ensemble average

$$\nu(E) = \int d\mu(\delta)\nu_\delta(E). \qquad (2.24)$$

We have computed the Chern number at $\phi = \frac{\pi}{6}$, for two sorts of disorder: uniform diagonal disorder $\hbar\omega \to \hbar(\omega + \delta\omega_{\mathbf{m}})$, with $\hbar\delta\omega_{\mathbf{m}}$ uniformly distributed with maximum amplitude $W/2$; and uniform hopping phase disorder $\phi_{\mathbf{mn}} \to \phi_{\mathbf{mn}} + \delta\phi_{\mathbf{mn}}$ where $\delta\phi_{\mathbf{mn}}$ has maximum amplitude $W_\Phi/2$. We implemented the computation on a lattice of 24×24 sites (192 unit cells). Each $\nu(E)$ was averaged over 40 disorder configurations yielding the means and error bars in Figs. 2.6**B**,**C**. The originally flat middle band spreads with disorder; the broadening of the middle

band is associated with states leaking out of the hexagonal plaquettes due to the detuning of the flux. Comparatively, the role of scalar or vector disorder potentials is the same.

2.4 Berry curvature from dynamics

So far, we have shown how the Berry phase helps to discern between a quantum anomalous Hall phase, with edge eigenstates protected against disorder, and the anomalous Hall phase. Now we would like to turn our attention to a local probe of the geometric phase, which derives from the study of dynamics of wavepackets.

The essential idea is that the Berry curvature of band n, $\mathcal{F}_n(\mathbf{k})$, acts as a $\mathbf{k}$–space analogue of the magnetic field. Its effect is measurable in the semiclassical dynamics of accelerated wavepackets prepared in band n. Interferometry of wavepackets allows us to access Berry's phase around closed loops in $\mathbf{k}$–space. We recall that wavepackets accelerated in the $\hat{\mathbf{\Delta}}_1$ direction drift in the $\hat{\mathbf{\Delta}}_2$ direction, which is associated with the phenomenon of polarization that was discussed in Sec. 1.2.3. The motion of wavepackets subject to a uniform force is complicated due to Bloch oscillations, but proposals do exist to access Berry's phases in a cold atom system relying on a measurement of the group velocity of a wavepacket in an external gradient of the scalar potential [172]. Here we present an alternative method to map Berry's phases of wavepackets, based solely on interference, and without the need to measure the group velocity of wavepackets.

Assume that it is possible to realize synthetic classical electric and magnetic fields, $\mathbf{E}$ and $\mathbf{B}$. To maintain the analogy with charged particles, assume that this synthetic electromagnetic field couples to an effective charge for the particles, denoted q. We may express the electric field in terms of the scalar potential $\mathbf{E}(\mathbf{r}) = -\frac{\partial \Phi(\mathbf{r})}{\partial \mathbf{r}}$. In the following, we will consider a single Bloch band $E_n(\mathbf{k})$. In addition, we will assume that this band does not become degenerate with the other bands. We are interested in the semiclassical dynamics of a wavepacket

of mean momentum and coordinate $\mathbf{k}_c, \mathbf{r}_c$ prepared in band n. The wavepacket contains Bloch waves according to a distribution of wavenumbers around $\mathbf{k}_c$. For good $\mathbf{k}$–space resolution, this distribution must occupy a small fraction of the first Brillouin zone. The spread of the wavepacket in $\mathbf{r}$–space will be over many lattice sites, but must be sufficiently localized when compared to the confining potential. The dynamics of a wavepacket are described by the coupled equations of motion [93, 173, 174, 175, 176, 168] corresponding to its wavenumber and position

$$\begin{aligned} \dot{\mathbf{r}}_c &= \frac{1}{\hbar}\frac{\partial E_n(\mathbf{k}_c)}{\partial \mathbf{k}_c} - \dot{\mathbf{k}}_c \times \mathcal{F}_n(\mathbf{k}_c), \\ \hbar\dot{\mathbf{k}}_c &= -q\frac{\partial \Phi(\mathbf{r}_c)}{\partial \mathbf{r}_c} + q\dot{\mathbf{r}}_c \times \mathbf{B}(\mathbf{r}_c). \end{aligned} \tag{2.25}$$

An implicit assumption for (2.25) is that the external fields are weak enough so as to not cause Landau–Zener transitions to other bands. We will return to this point in Sec. 2.6. Let us remark that in Eqs. (2.25) we are neglecting contributions to the band energy from the rotation of the wavepacket about its central coordinate $\mathbf{r}_c$ due to the external magnetic field [174]. These contributions take the form $-\frac{q}{2m}\mathbf{B}\cdot\mathbf{L}_n$, where $\mathbf{L}_n$ is the magnetic moment of a wavepacket prepared in band n and m is the effective mass of the wavepacket. We prove that these contributions are indeed negligible in Sec. 2.6.

Note that $\mathcal{F}_n(\mathbf{k}_c)$ participates in a $\mathbf{k}$–space analogue of the Lorentz force in (2.25). This Berry–curvature induced contribution to the velocity of the wavepacket is nonzero only for an accelerated wavepacket. This is the anomalous velocity introduced by Karplus and Luttinger [177]. A direct consequence of Eqs. (2.25) is that wavepackets which are accelerated by a tilt $q\mathbf{E} \neq 0$ while keeping $\mathbf{B} = 0$ deviate according to the sign of the Berry curvature. This fact was successfully used in a recent experiment on Haldane's honeycomb Chern insulator with fermionic potassium atoms [41].

In [58], we have considered the effect of a uniform perpendicular magnetic field, $\mathbf{B} = |\mathbf{B}|\hat{\mathbf{z}}$, without any electric field $\mathbf{E} = 0$. If the magnitude of the external

magnetic field $B = |\mathbf{B}|$ is small in a sense that we will make precise in Sec. 2.6, then the semiclassical equations above hold true and can be used to measure Berry's phases around closed contours in $\mathbf{k}$–space. We refer the reader to App. A, where we introduce a time–periodic lattice potential which in the rotating wave approximation has the same effect as the Peierls phases corresponding to a uniform magnetic field.

To derive the equations of motion in a uniform magnetic field, we use the identity

$$\mathbf{a} \times (\mathbf{b} \times \mathbf{c}) = \mathbf{b}(\mathbf{a} \cdot \mathbf{c}) - \mathbf{c}(\mathbf{a} \cdot \mathbf{b}) \tag{2.26}$$

to eliminate either the momentum or the position variable between the two equations in (2.25). We obtain

$$\dot{\mathbf{r}}_c = \frac{Z_B(\mathbf{k}_c)}{\hbar} \frac{\partial E_n(\mathbf{k}_c)}{\partial \mathbf{k}_c}, \tag{2.27}$$

$$\hbar \dot{\mathbf{k}}_c = \frac{q}{\hbar} Z_B(\mathbf{k}_c) \frac{\partial E_n(\mathbf{k}_c)}{\partial \mathbf{k}_c} \times \mathbf{B}. \tag{2.28}$$

We have introduced in (2.28) the Berry curvature dependent scale factor

$$Z_{\mathbf{B}}(\mathbf{k}_c) = \frac{1}{1 - \frac{q}{\hbar} \mathcal{F}_n(\mathbf{k}_c) B}, \tag{2.29}$$

which is 1 if either the magnetic field or the band Berry curvature is vanishing.

Equation (2.28) implies that the force $\dot{\mathbf{k}}_c$ is perpendicular to the group velocity $\frac{\partial E_n(\mathbf{k}_c)}{\partial \mathbf{k}_c}$. Consequently, the motion conserves energy, as can also be seen by varying the energy and using the second equation in (2.28)

$$\delta E_n(\mathbf{k}_c) = \frac{\partial E_n}{\partial \mathbf{k}_c} \cdot \frac{d\mathbf{k}_c}{dt} \, \delta t = 0. \tag{2.30}$$

Thus, any closed trajectory $\mathbf{k}_c(t)$ from (2.28) is a constant energy trajectory as shown in Fig. 2.7 . To obtain the trajectory in real space, use the expression for

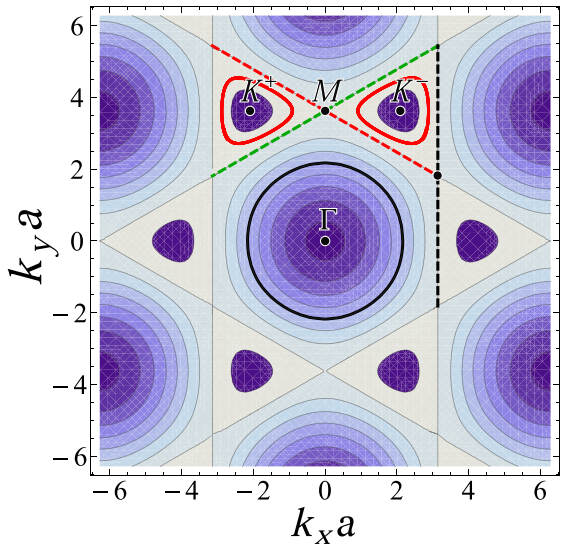

Figure 2.7: Constant energy trajectories of a wavepacket prepared in the lowest band for $\phi = \frac{\pi}{6}$. Whenever the initial $\mathbf{k}_c$ lies on a separatrix (dashed lines), the trajectory can only close in the extended Brillouin zone; in $\mathbf{r}$–space the particle executes Bloch oscillations. Note that we have reverted to the cartesian components of momentum (k_x, k_y).

the Lorentz force, $\hbar\dot{\mathbf{k}}_c = q\dot{\mathbf{r}}_c \times \mathbf{B}$, which implies

$$\dot{\mathbf{r}}_c = -\frac{\hbar}{qB}\dot{\mathbf{k}}_c \times \hat{z}. \tag{2.31}$$

The trajectory in real space is rotated by 90 degrees and rescaled by a magnetic field–dependent prefactor, as compared to that in momentum space. If the $\mathbf{k}_c(t)$ is closed in the 1^{st} Brillouin zone (continuous lines in Fig. 2.7), then $\mathbf{r}_c(t)$ is also closed. On any high-symmetry line (separatrix), $\mathbf{k}_c$ is periodic in the extended Brillouin zone (dashed lines in Fig. 2.7), whereas $\mathbf{r}_c(t)$ undergoes Bloch oscillations. The magnitude of the acceleration $\hbar\dot{\mathbf{k}}_c$ will be affected by the Berry curvature dependent prefactor $Z_B(\mathbf{k}_c)$, which deviates significantly from 1 wherever the band gap is small, as follows from Eqs. (1.15) and (2.29). This occurs in the vicinity of the Brillouin zone corners $\mathbf{K}^{\pm}$.

Upon traversing its periodic trajectory [denoted $C(E)$ for energy E] once, a wavepacket acquires a phase factor. If this phase factor amounts to 1, then the wavepacket interferes constructively with itself and can form a standing wave. To determine the condition for the formation of a standing wave, we may requantize

the semiclassical dynamics. For this purpose, note that the following Langrangian [174] yields the second equation in (2.28)

$$L(\mathbf{k}_c, \dot{\mathbf{k}}_c) = -\frac{\hbar^2}{2qB}(k_{c,1}\dot{k_{c,2}} - k_{c,2}\dot{k}_{c,1}) + \hbar\mathcal{A}_n \cdot \dot{\mathbf{k}}_c - E_n(\mathbf{k}_c). \tag{2.32}$$

It is easy to show that the Euler–Lagrange [178] equations $\frac{d}{dt}\frac{\partial L}{\partial \dot{\mathbf{k}}_c} - \frac{\partial L}{\partial \mathbf{k}_c} = 0$ applied for (2.32) are equivalent to (2.28).

The standing wave condition for wavepackets then takes the form of a Bohr–Sommerfeld condition that the action associated with the phase space variables $\mathbf{k}_c, \dot{\mathbf{k}}_c$ be quantized in units of Planck's constant [174, 93]

$$\oint_C \pi_c \cdot d\mathbf{k}_c = 2\pi\left(n + \frac{1}{2}\right)\hbar, \tag{2.33}$$

where the momentum conjugate to the phase space variable $\mathbf{k}_c$ is

$$\pi_c = \frac{\partial L}{\partial \dot{\mathbf{k}}_c} = \frac{\hbar^2}{2qB}\mathbf{k}_c \times \hat{\mathbf{z}} + \hbar\mathcal{A}_n(\mathbf{k}_c). \tag{2.34}$$

Using this form for π_c, the associated action is

$$\oint_C \pi_c \cdot d\mathbf{k}_c = -\frac{\hbar^2}{qB}\frac{1}{2}\oint_C (\mathbf{k}_c \times d\mathbf{k}_c) \cdot \hat{\mathbf{z}} + \hbar\Gamma_C, \tag{2.35}$$

where we have denoted the Berry phase accumulated around C by

$$\Gamma_C \equiv 2\pi\nu_n(E) = \oint_C d\mathbf{k} \cdot \mathcal{A}_n(\mathbf{k}). \tag{2.36}$$

Note that $\nu_n(E)$ corresponds to the n^{th} *band* only as defined in Eq. (2.19). Furthermore, identifying $\frac{1}{2}(\mathbf{k}_c \times d\mathbf{k}_c) \cdot \hat{\mathbf{z}} = d\mathscr{S}_C$ as the (signed) differential area swept in $\mathbf{k}_c$ space by the wavepacket on trajectory C during a time interval dt, Eq. (2.33) becomes

$$\frac{\hbar\mathscr{S}_C}{qB} + 2\pi\left(n + \frac{1}{2}\right) - \Gamma_C = 0. \tag{2.37}$$

The first term may be interpreted as the inverse of the magnetic flux through the area bounded by the real–space trajectory $\mathbf{r}_c(t)$. This can be seen by recasting $\oint_C(\mathbf{k}_c \times d\mathbf{k}_c) \cdot \hat{\mathbf{z}}$ in terms of $\mathbf{r}_c$ and $\dot{\mathbf{r}}_c$ by using the expression of the Lorentz force. Equation (2.37) is a Bohr–Sommerfeld quantization condition for closed trajectories in phase space. An analogous situation occurs in electronic systems for the de Haas–van Alphen effect [93], where peaks in magnetization as a function of the external magnetic field are a result of such resonant behavior. Tuning the magnitude B through two consecutive resonances yields the momentum space area $\mathscr{S}_C$ of the momentum space trajectory $C(E)$, which fixes the Berry phase along $C(E)$ up to multiples of 2π in (2.37). Thus, standing waves may be used to detect the Berry curvature enclosed in contours of constant energy.

2.5 Chern numbers from interferometry

In the previous section, we determined a way to obtain the local Berry curvature from semiclassical dynamics. In this section we directly determine the Chern numbers of Bloch bands from the spectrum in a synthetic magnetic field. In a magnetic field, the three original Bloch bands will split into magnetic subbands. The resonant semiclassical trajectories of Sec. 2.4 correspond to magnetic subbands which form when an infinitesimal synthetic magnetic field $\mathbf{B}$ is turned on. The Chern number of the original Bloch band determines how this band splits into magnetic subbands [173, 174, 175].

The maximum number of closed resonant trajectories within the Brillouin zone is obtained by observing that the maximal area of a single resonant closed trajectory C, $\mathscr{S}_C$, has to be equal to the area of the first Brillouin zone. This implies that the number of subbands obtained from the n^{th} Bloch band is given by:

$$D_n = \left[\nu_n + \frac{1}{f}\right], \tag{2.38}$$

where ν_n is the Chern number associated with the n^{th} band, and $f = \frac{Ba^2\sqrt{3}}{2}$ is the

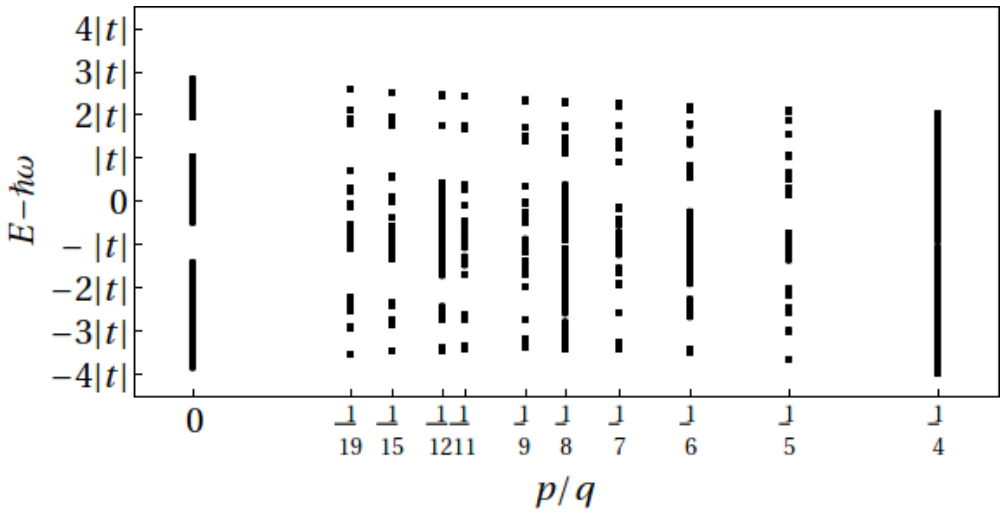

Figure 2.8: Low magnetic field **B** spectrum of the Kagomé lattice with $\phi = \frac{\pi}{4}$: at 0 external field, we recover the original bandstructure of Fig. 2.2. At flux p/q there are $3q$ subbands with possible degeneracies. For example, at $p/q = 1/5$, there are 6 separated subbands in the upper band, 5 degenerate subbands in the middle band, and 4 separated subbands in the lower band in agreement with Eq. (2.38) and consistent Chern numbers -1 and 1 for the lower and upper Bloch bands in the $B = 0$ bandstructure. The bands become degenerate at $p/q = 1/4$.

flux through the unit cell of a uniform synthetic magnetic field **B**, in units of $\frac{h}{e^2}$. In (2.38), $[x]$ is the floor function, i.e. the largest positive integer smaller than x. For small enough field **B** the resulting subbands are non–degenerate.

The required ingredient is the spectrum of (2.3) when placed in a uniform magnetic field. This is the Hofstadter problem [37, 179]. Let us pick the Landau gauge, $\mathbf{A} = (-By, 0)$, where the two components are Cartesian. Due to the presence of a magnetic field, the Hamiltonian couples different points in the Brillouin zone. If f is a rational number p/q with p and q relatively prime non-negative integers, then the resulting Hamiltonian couples k_2 to $k_2 \pm \frac{4\pi f}{a\sqrt{3}}$ and to $k_2 \pm \frac{8\pi f}{a\sqrt{3}}$. This momentum space coupling can be removed by remarking that translational invariance is recovered if one reverts to a q times larger unit cell in real space, and a q times smaller Brillouin zone, defined for our lattice as $\left[0, \frac{2\pi}{qa}\right] \times \left[0, \frac{4\pi}{a\sqrt{3}}\right]$. The original 3-band Hamiltonian becomes a $3q$-band problem defined on the reduced Brillouin zone. Details of this calculation are given in App. A.2. For now we focus on counting the magnetic subbands obtained from a given Bloch band, which provides a direct way of determining the Chern number of the original (zero field)

bands.

Assume for simplicity that the dimensionless flux per unit cell is $f = \frac{1}{Q}$ for some positive integer Q (see Fig. 2.8). For large enough Q, the field is weak, and (2.38) becomes $D_n = [\nu_n + Q]$. First note that $D_1 + D_2 + D_3 = 3Q$, since $\nu_1 + \nu_2 + \nu_3 = 0$, which is consistent with the fact that the spectrum has $3Q$ levels. Taking the band-structure at $\phi = \frac{\pi}{4}$ as representative for our time-reversal symmetry broken phase with gapless edge modes, we predict that the lower, middle and upper bands will split into $Q - 1$, Q and $Q + 1$ subbands, respectively. Thus Chern numbers can be measured by fixing the external magnetic field to a small rational value and counting resonant trajectories. The caveat is that for special fractions f the magnetic subbands may be degenerate [173, 174, 175, 11]. For example, at $f = 1/5$, the lower, middle, and upper Bloch bands split into $[\nu_n + 5] = 4, 5, 6$ subbands, consistent with their Chern numbers $\nu = -1, 0, 1$. There are a total of 15 subbands, but the 5 subbands corresponding to the middle band are degenerate. The method described here would allow one to experimentally measure Chern numbers by observing the bandstructure of Fig. 2.8, for example by accessing the density of states from transmission spectra [73].

2.6 Bound on the strength of the magnetic field

When the gap between the magnetic subbands is large, it is not sensible to express the wavepacket velocity in terms of the dispersion relation in zero magnetic field, $\partial E_n / \partial \mathbf{k}_c$. We may, however, assume that the band Hamiltonian (2.4) is perturbed by a small $\mathbf{B}$. In this case the group velocity corresponding to the unperturbed band $E_n(\mathbf{k})$ is the leading contribution in $\dot{\mathbf{r}}_c$.

To be safe from Landau–Zener tunneling of accelerated particles into a different band [180, 181], the magnetic field has to be small. This translates to a condition [93] on the period of a closed trajectory:

$$\frac{\hbar}{T} \ll E_g \sqrt{\frac{E_g}{E}}, \tag{2.39}$$

where E_g is the size of the gap, which in our problem is of order $|t|$, and E is the constant energy along the loop $C(E)$. The period of motion can be further reexpressed by making an estimate from Eq. (2.28),

$$T \sim \frac{\hbar l_C(E)}{\frac{q}{\hbar}\overline{Z_{\mathbf{B}}|\partial E_n/\partial \mathbf{k}_c|}B}, \tag{2.40}$$

where the averages are taken over the path C, whose length in momentum space is denoted $l_C(E)$. Collecting equations yields the following condition

$$\frac{\hbar l_C(E)}{q\overline{Z_{\mathbf{B}}(\mathbf{k}_c)|\partial E_n/\partial \mathbf{k}_c|}B} \gg \frac{1}{|t|}\sqrt{\frac{E}{|t|}}. \tag{2.41}$$

For typical values, this bound is satisfied by taking the flux per unit cell in units of the flux quantum to be very small $f \ll 1$.

Finally, let us recall that we have dropped in Eqs. (2.25) a contribution due to the rotation of the wavepacket in a magnetic field (see, for example, work by Chang and Niu [174]). This contribution would be incorporated by replacing the Bloch band energy $E_n(\mathbf{k})$ by $\tilde{E}_n(\mathbf{k}) \equiv E_n(\mathbf{k}) - \frac{q}{2m}\mathbf{B}\cdot\mathbf{L}_n(\mathbf{k})$ in Eqs. (2.25) and in the resulting treatment. The angular momentum of the wavepacket is $\mathbf{L}_n(\mathbf{k}) = L_n(\mathbf{k})\hat{\mathbf{z}}$, where

$$L_n(\mathbf{k}) = i\frac{m}{\hbar}\sum_{n'\neq n}\left[\frac{\langle n\mathbf{k}|\partial h(\mathbf{k})/\partial k_1|n'\mathbf{k}\rangle\langle n'\mathbf{k}|\partial h(\mathbf{k})/\partial k_2|n\mathbf{k}\rangle}{E_{n'}(\mathbf{k}) - E_n(\mathbf{k})} - \text{c.c.}\right], \tag{2.42}$$

consisting of a summation over bands distinct from n, and with $h(\mathbf{k})$ as given in (2.4). Note that the effective mass m drops out of $\tilde{E}_n(\mathbf{k})$. Direct evaluation of (2.42) shows that it is a contribution of order 1, and therefore the deviation from the Bloch band energy $\tilde{E}_n(\mathbf{k}) - E_n(\mathbf{k}) = O(B)$ may be neglected in the limit of infinitesimal field (or large band gap). We have checked numerically that the inclusion of contributions from Eq. (2.42) into the semiclassical equations of motion produces an insignificant change in the trajectories of Fig. 2.7.

2.7 Topological Bogoliubov Quasiparticles

In this section we address the stability of the topological phase in the presence of interactions. A quantum spin Hall phase of fermions is stable to interactions which are weak compared to the band gap [182, 183]. Strong enough repulsive interactions stabilize a "topological Mott insulator" that has quantum Hall responses [184]. In boson systems, when the interactions are strong, the quasiparticle or quasihole bands of a Mott insulating phase at commensurate filling retain the topological properties of the single particle problem [185, 186, 70] (see also Chapter 3). Moreover, Bogoliubov quasiparticle bands inherit topological properties from the single particle bandstructure [187, 188, 189, 190]. Here, using the Bogoliubov approximation, we show that weak repulsive interactions will not change the effective free particle bands in such a way as to close the band gap and reopen it.

The Bose–Hubbard Hamiltonian [74] exhibits a quantum phase transition from a superfluid to a bosonic Mott insulator. Another model with effectively Hubbard–type interactions and a similar quantum phase transition [144, 143, 150, 191] is the Jaynes–Cummings Hamiltonian [142, 141], in which the photons are coupled to a two level system situated at each site. Such interactions are realizable in cQED experiments [140, 137]. Here we would like to restrict to the Bose–Hubbard repulsive interactions and study the robustness of the topological phase if weak interactions are turned on, while remaining in the superfluid phase. To work out the effect of weak Bose–Hubbard terms, we start with the unperturbed Hamiltonian (2.4). The interaction Hamiltonian for the Bose-Hubbard model is quartic in the creation and annihilation operators

$$H_{BH} = \frac{U}{2}\sum_{\mathbf{m}} a^\dagger_{\mathbf{m}} a_{\mathbf{m}} (a^\dagger_{\mathbf{m}} a_{\mathbf{m}} - 1) = \frac{U}{2N}\sum_{\mathbf{k}_1,\mathbf{k}_2,\mathbf{k},\alpha} a^\dagger_{\alpha,\mathbf{k}_1-\mathbf{k}} a^\dagger_{\alpha,\mathbf{k_2}+\mathbf{k}} a_{\alpha,\mathbf{k}_2} a_{\alpha,\mathbf{k}_1}, \quad (2.43)$$

where N counts unit cells and we have used the Fourier transform on each sublattice $\alpha = A, B, C$ as $a_{\alpha,\mathbf{k}} = \frac{1}{\sqrt{N}} \sum_{\mathbf{m}\,\in\,\alpha} e^{-i\mathbf{k}\mathbf{R}_\mathbf{m}} a_{\mathbf{m}}$. We would like to describe

the spectrum of elementary excitations above the ground state. The minimum of the single–particle spectrum is at the $\mathbf{\Gamma}$ point: the ground state of the bosonic system is a product state corresponding to all bosons condensing at $\mathbf{k} = 0$ in the lowest band (see Fig. 2.2). Let the minimum single particle energy at the $\mathbf{\Gamma}$ point be E_0. We restrict to a subspace of constant particle number n, where $n \equiv Nn_0$, where n_0 is the number of condensate particles per unit cell. In the Bogoliubov approximation [192] let,

$$a_{\alpha,\mathbf{k}} \equiv \sqrt{Nn_0}\delta_{\mathbf{k}} + b_{\alpha,\mathbf{k}}. \tag{2.44}$$

Equation (2.44) defines the excited state operators $b_{\alpha,\mathbf{k}\neq 0}$. Neglecting cubic and quartic terms in $b_{\alpha,\mathbf{k}}$ we find:

$$\begin{aligned} H_t = H + H_{BH} = \quad & E_{\mathrm{G}} + \sum_{\mathbf{k}\alpha\beta} b^\dagger_{\alpha,\mathbf{k}} \left[h^{\alpha\beta}(\mathbf{k}) - E_0\delta^{\alpha\beta}\right] b_{\beta,\mathbf{k}} \\ & + \frac{Un_0}{2} \sum_{\mathbf{k}\neq 0,\alpha} \left(2b^\dagger_{\alpha,\mathbf{k}} b_{\alpha,\mathbf{k}} + b_{\alpha,\mathbf{k}} b_{\alpha,-\mathbf{k}} + b^\dagger_{\alpha,\mathbf{k}} b^\dagger_{\alpha,-\mathbf{k}}\right). \end{aligned} \tag{2.45}$$

We let $E_{\mathrm{G}} \equiv nE_0$ be the total ground state energy, and the remainder describes the excitation spectrum. Focusing on the excitation spectrum, we drop the ground state energy from the calculation. The Hamiltonian is diagonalized by a Bogoliubov transformation [192], amounting to a rotation to a new set of operators $\tilde{b}_{n,\mathbf{k}}$, which annihilates a quasiparticle in the n^{th} band at momentum $\mathbf{k}$ (see App. B for the diagonalization). Then (2.45) becomes, letting quasiparticle dispersions be $\xi_n(\mathbf{k})$,

$$H_t = \sum_{\mathbf{k},n} \xi_n(\mathbf{k}) \tilde{b}^\dagger_{n\mathbf{k}} \tilde{b}_{n\mathbf{k}}. \tag{2.46}$$

We assume that the topological phase is stable as long as the bands are not significantly changed by the Bose-Hubbard interaction so as to close a band gap in the single particle spectrum. The Hubbard interaction induced dispersion $\xi_n(\mathbf{k})$ only changes significantly from $E_n(\mathbf{k})$ of the original model in the vicinity of the Γ point (see Figure 2.9). There, the quasiparticles and quasiholes have a

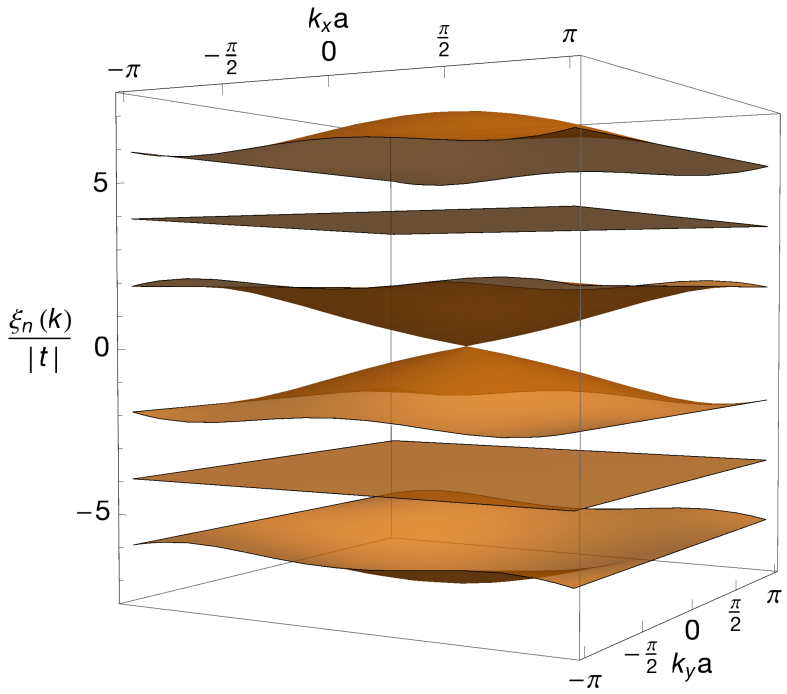

Figure 2.9: Bogoliubov quasiparticle and quasihole dispersion $\xi_n(\mathbf{k})$ for $U/|t| = 0.5$ at $\phi = \frac{\pi}{6}$. The low energy quasiparticle spectrum has a sound mode in the vicinity of the $\mathbf{\Gamma}$ point.

linear dispersion corresponding to the sound mode [192]. Chern numbers can be computed for Bogoliubov bands [189] extending the Avron *et al.* formula [103]. We carry out the procedure in App. B and summarize the result of the computation here: the top and bottom bands in Fig. 2.9 have Chern number -1. The flat bands each have Chern number 0. The two middle bands have a total Chern number of 2. We conclude that Bogoliubov quasiparticles in the superfluid region at $U \ll |t|$ have nonzero Chern numbers. At weak interactions we expect quasiparticles with a long lifetime, and the corresponding gapless edge excitations can be detected experimentally.

2.8 Conclusions

Motivated by the recent experimental progress in the context of arrays of electromagnetic superconducting resonators [73], we have investigated the Hall effects of light on the Kagomé lattice with artificial gauge fields introduced by Koch *et al.* [57]. We have found that this model exhibits equivalents of the quantum Hall

effect without Landau levels, and the anomalous Hall effect with a non-quantized Chern number. In particular, we have shown that a topologically trivial band can affect the quantization of Chern numbers as well as the robustness of the chiral edge modes. We have discussed observables which are accessible experimentally. We have introduced a method to measure Berry's phases around loops of constant energy in the Brillouin zone. The method is based solely on wavepacket interference and can be used to determine band Chern numbers or the photonic equivalent of the anomalous Hall response. It provides an alternative to a recent method proposed to measure line integrals of the Berry gauge field in cold-atomic systems, which relies on the measurement of group velocities of wavepackets and a force-reversal protocol [172]. Interference experiments can also be envisioned to probe the Landau levels, emerging when placing the Kagomé lattice in a uniform magnetic field. Finally, we have shown that Bogoliubov quasiparticles arising in the presence of weak nonlinearities in each cavity have nonzero topological invariants. An open and stimulating question for the future is concerned with the influence of artificial gauge fields on the superfluid–Mott transition of light in cQED photon-based lattices and the possibility of topologically ordered states.

Chapter 3

Bose-Hubbard Haldane model

At the end of the previous chapter, we studied the properties of photons with weak cavity nonlinearities on the Kagomé lattice and showed that the resulting Bogoliubov quasiparticles have a well–defined topological bandstructure. In this chapter we will consider the physics occuring in the vicinity of the Mott transition at unit boson filling on the honeycomb lattice. In this case as well we will start with a Chern insulator single–particle bandstructure, which will yield topologically nontrivial quasiparticle excitations of the Mott insulator. These can be revealed in a systematic expansion in t/U around the Mott insulator groundstate. In addition, the presence of frustration in the kinetic terms leads to chiral ground states, among which the Mott insulator with triangular plaquette currents is noteworthy.

In the presence of kinetic frustration, the superfluid state can spontaneously break a symmetry since the condensate forms over a linear combination of degenerate minima in the single particle spectrum. More importantly, for strong interactions, the broken symmetry may not be restored. This leads to Mott insulators with a spontaneously broken discrete symmetry, such as time-reversal. Such chiral Mott insulators have been predicted in quasi-one dimensional systems [193, 194, 195, 196], and in two dimensions [197, 198, 199, 200, 201, 202]

In this chapter we consider the Haldane model defined in Eq. (1.75), for bosons with Hubbard repulsive interactions and at fixed filling of one particle per site

$n = 1$. Our goal is to understand the influence of band topology in the superfluid and Mott insulating phases. For weak interactions, the Bose condensed ground state may be topologically trivial [203, 204, 205, 206], and determined solely by the position of band minima. Band topology nevertheless affects transport properties of bosons in the ground and excited states [203, 204, 205, 206, 185, 186]. We uncover a zero temperature phase diagram with three distinct phases: a uniform superfluid (*SF*), a chiral superfluid (*CSF*) and a plaquette Mott insulator with local current loops (*PMI*). Nearest-neighbor and next-nearest neighbor currents distinguish *CSF* from *SF*, and the phase transition between them is first order. We combine here mean–field theory based on a strong–coupling expansion, variational methods, and numerical exact diagonalization to reveal the ground state phase diagram. The results presented here make up the author's contribution to Ref. [70], where they are complemented by real space bosonic dynamical mean field theory [207, 208, 209, 210, 211] as well as a detailed Gross–Pitaevskii study performed by our collaborators I. Vasić and W. Hofstetter. The characteristic density fluctuations, current correlation functions, and excitation spectra are measurable in ultracold atom experiments.

This chapter is organized as follows. In Sec. 3.1 we introduce the model. Section 3.2 is dedicated to the study of the ground state. Subsection 3.2.1 is concerned with the weakly interacting model and the two types of superfluid that it supports. In Sec. 3.2.2 we discuss the plaquette Mott insulator, whereas in Sec. 3.2.3 we present our exact diagonalization studies of the ground states of finite sized systems. Section 3.3 deals with the excitations inside of the Mott insulating phase, and with the analysis of the topology of the quasiparticle bands resulting from a strong–coupling expansion at strong interactions.

3.1 Model

Our starting point is the Haldane model Hamiltonian introduced in Eq. (1.75), which we rewrite in the form

$$H_H = -t_1 \sum_{\langle i,j \rangle} b_i^\dagger b_j - t_2 \sum_{\langle\langle i,j \rangle\rangle} e^{i\phi_{ij}} b_i^\dagger b_j, \tag{3.1}$$

where we set the next–nearest neighbor phases to $\phi_{ij} = \pm\frac{\pi}{2}$. The Fourier transformed Bloch Hamiltonian reads

$$H_H = \sum_{\mathbf{k}} \psi^\dagger(\mathbf{k}) \left[h_0(\mathbf{k})\sigma_0 + \mathbf{h}(\mathbf{k}) \cdot \sigma \right] \psi(\mathbf{k}), \tag{3.2}$$

where $\psi^\dagger(\mathbf{k}) = (b_{A\mathbf{k}}^\dagger b_{B\mathbf{k}}^\dagger)$ is a spinor containing boson creation operators, and

$$\mathbf{h}(\mathbf{k}) = \left(-t_1 \sum_i \cos(\mathbf{k}\cdot\mathbf{a}_i), -t_1 \sum_i \sin(\mathbf{k}\cdot\mathbf{a}_i), 2t_2 \sum_i \sin(\mathbf{k}\cdot\mathbf{b}_i) \right). \tag{3.3}$$

Note that by virtue of the fact that $h_0(\mathbf{k}) = 0$, the spectrum $E_\pm(\mathbf{k}) = \pm|\mathbf{h}(\mathbf{k})|$ is particle–hole symmetric. In Fig. 3.1 we plot the dispersion relation of the lower band for three choices of the hopping integrals t_1, t_2. There is a unique band minimum at $\mathbf{\Gamma}$ for $t_1 < t_2\sqrt{3}$. In the opposite case, at $t_1 < t_2\sqrt{3}$, there are two inequivalent band minima at $\mathbf{K}_{A,B}$, whereas at the critical hopping $t_1 = t_2\sqrt{3}$ the three minima are degenerate. We can anticipate that this energy landscape will give rise to two distinct types of superfluidity.

To the noninteracting Hamiltonian representing the Haldane model we add repulsive on–site Hubbard interactions between the bosons [74, 154]

$$H = H_H + \frac{U}{2} \sum_i n_i \left(n_i - 1 \right) - \mu \sum_i n_i. \tag{3.4}$$

We have written (3.4) with a finite chemical potential μ, and we will mention explicitly whenever we switch to the canonical ensemble. In the following sections,

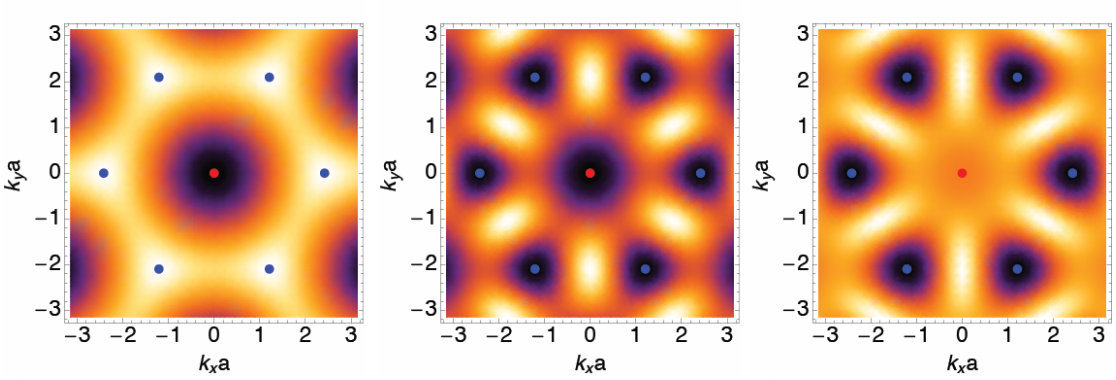

a) b) c)

Figure 3.1: Dispersion of the lowest band $E_{-}(\mathbf{k})$: a) At $t_1 < t_2\sqrt{3}$ there is a unique band minimum at the center of the Brillouin zone $\mathbf{\Gamma}$. b) For $t_1 = t_2\sqrt{3}$, this band minimum becomes degenerate with two inequivalent others at $\mathbf{K}_{A,B}$. c) When $t_1 > t_2\sqrt{3}$, the band minima are shifted to $\mathbf{K}_{A,B}$.

we characterize different phases by the value of the condensate order parameter

$$\psi_i = \langle b_i \rangle, \tag{3.5}$$

local density fluctuations

$$\Delta n_i = \langle n_i^2 \rangle - \langle n_i \rangle^2, \tag{3.6}$$

and patterns of lattice currents. The expectation value of the current operator for the bond $j \to i$ on the lattice is given by

$$J_{ij} = -i(t_{ji}\langle b_j^\dagger b_i \rangle - t_{ij}\langle b_i^\dagger b_j \rangle) = -2\mathrm{Im}\left(t_{ij}\langle b_i^\dagger b_j \rangle\right), \tag{3.7}$$

as can be derived from the lattice continuity equation, where t_{ij} is the hopping integral between sites i and j.

3.2 Study of the ground state

3.2.1 Weakly interacting bosons

In this section we study the possible Bose condensed phases. Figure 3.1 indicates two limits that give rise to distinct superfluids: At $t_2 = 0$ our model corresponds

to the graphene lattice and condensation occurs at the center of the Brillouin zone $\mathbf{\Gamma}$. For $t_1 = 0$, the triangular sublattices A and B are decoupled, forcing the condensate to separate into two components, one for each sublattice. To study the condensate at finite t_1 and t_2, let us focus on the non–interacting case and set $U = 0$. The momenta at the corners of the Brillouin zone satisfy

$$e^{i\mathbf{K}_A\cdot\mathbf{b}_i} = e^{i\frac{2\pi}{3}}, \quad e^{i\mathbf{K}_B\cdot\mathbf{b}_i} = e^{-i\frac{2\pi}{3}}, \tag{3.8}$$

for $i = 1, 2, 3$. At the high symmetry points, the Hamiltonian takes the following forms:

$$h(\mathbf{\Gamma}) = 3t_1\sigma_1 \tag{3.9}$$

and

$$h(\mathbf{K}_{A,B}) = \mp 3\sqrt{3}t_2\sigma_3, \tag{3.10}$$

which shows that the minimum of the lowest band shifts from the $\mathbf{\Gamma}$ point at the center of the Brillouin zone to its two inequivalent corners at $\mathbf{K}_{A,B}$, whenever $t_1 < \sqrt{3}t_2$.

The *SF* phase forms when $t_1 > \sqrt{3}t_2$. The condensate order parameter is $\langle b_i\rangle = \sqrt{n}$, where $n = N/N_{\text{sites}}$ is the filling. To evaluate the ground state energy of the *SF* state, consider the variational Ansatz

$$|\Phi_{SF}\rangle = \frac{1}{\sqrt{N_{sites}!}}\left[b_-^\dagger(\mathbf{\Gamma})\right]^{N_{sites}}|0\rangle, \tag{3.11}$$

where the operator $b_-^\dagger(\mathbf{k} = \mathbf{\Gamma}) = \frac{1}{\sqrt{2}}[b_A^\dagger(\mathbf{\Gamma}) + b_B^\dagger(\mathbf{\Gamma})]$ creates a boson of zero momentum, corresponding to the minimum of the lower band. The wavefunction of Eq. (3.11) corresponds to N_{sites} bosons condensing at this minimum. The energy of (3.11) evaluated with the full interacting model (3.4) is

$$\frac{E_0}{N_{sites}} = -3t_1 n + \frac{1}{2}Un^2, \tag{3.12}$$

which is independent of the next–nearest neighbor hopping strength t_2. This energy is independent of a common phase rotation of $b_-^\dagger(\mathbf{\Gamma})$, which corresponds to the existence of one Goldstone boson. Note that this ground state energy can be obtained equivalently from the Gross–Pitaevskii energy functional [212, 70]. In (3.11), the next–nearest neighbor current expectation value (3.7) is

$$J_{AA}^{SF} = -2\, n\, t_2\, \mathrm{Im} \exp(-i\pi/2) = 2nt_2. \tag{3.13}$$

Next, we are concerned with the *CSF*, which is the ground state for $t_1 < \sqrt{3}t_2$. Condensation can occur in an arbitrary linear combination of single particle ground states at $\mathbf{K}_A$ and $\mathbf{K}_B$, leading to a large degeneracy. We show below that repulsive interactions in a finite size system favor condensation of equal numbers of bosons on the two sublattices. Solving for the boson creation operator in the lower band, we find that

$$b_-^\dagger(\mathbf{K}_A) = b_A^\dagger(\mathbf{K}_A),\ b_-^\dagger(\mathbf{K}_B) = b_B^\dagger(\mathbf{K}_B). \tag{3.14}$$

The twofold degeneracy of the band minimum is analogous to that found in the problem of a Bose-Einstein condensate in a double–well potential [213, 214]. In the following, we prove that the presence of defects, or open boundary conditions, produces a condensate in which A and B sublattices are phase coherent. Secondly, we show that if discrete lattice symmetries are preserved, the ground state for weak $U > 0$ consists of decoupled condensates on sublattices A and B.

We form first a condensate wavefunction from *coherent superpositions* of the degenerate minima

$$|\Phi'_{CSF}(\varphi)\rangle = \frac{1}{\sqrt{N!}} \left[\frac{1}{\sqrt{2}} b_A^\dagger(\mathbf{K}_A) + \frac{e^{i\varphi}}{\sqrt{2}} b_B^\dagger(\mathbf{K}_B) \right]^N |0\rangle. \tag{3.15}$$

The variational energy of this state is

$$\frac{E'_0}{N_{sites}} = -3\sqrt{3}t_2 n + \frac{Un}{2}\left(n + 1 - \frac{1}{N_{sites}} \right). \tag{3.16}$$

Note that in (3.15) the sublattices A, B are phase coherent; consequently the nearest–neighbor current J_{AB} on the unit cell at coordinate $\mathbf{r}_i$ has a well defined value $\propto \sin\left[\varphi - (\mathbf{K}_A - \mathbf{K}_B)\cdot \mathbf{r}_i\right]$. The fact that $J_{AB} \neq 0$ is consistent with the fact that $|\Phi'_{CSF}\rangle$ breaks lattice translation and inversion symmetries.

We form a second wavefunction for the chiral superfluid from a uniform superposition of all $|\Phi'_{CSF}(\varphi)\rangle$ for φ between 0 and 2π. This new wavefunction corresponds to *decoupled condensates*, and is both lattice translation and inversion symmetric:

$$|\Phi''_{CSF}\rangle = \frac{1}{(N/2)!}\left[b_A^\dagger(\mathbf{K}_A)\right]^{N/2}\left[b_B^\dagger(\mathbf{K}_B)\right]^{N/2}|0\rangle. \tag{3.17}$$

Note that now the nearest neighbor current J_{AB}^{CSF} vanishes, in the absence of phase coherence between the sublattices. The phases of the two sublattices can be rotated independently without changing the energy, which corresponds to the existence of two Goldstone modes. We find that the energy per site of $|\Phi''_{CSF}\rangle$ is

$$\frac{E''_0}{N_{\rm sites}} = -3\sqrt{3}t_2 n + \frac{Un}{2}\left(n + 1 - \frac{2}{N_{\rm sites}}\right). \tag{3.18}$$

This is lower by $nU/(2N_{\rm sites})$ than (3.16). Thus, if the system is finite, if the interactions are weakly repulsive and if all discrete lattice symmetries are preserved, then the variational ground state is $|\Phi''_{CSF}\rangle$. Moreover, the corresponding momentum distributions are $\rho_A(\mathbf{k}) \approx \frac{N_{sites}}{2}\,\delta_{\mathbf{k},\mathbf{K}_A}$, $\rho_B(\mathbf{k}) \approx \frac{N_{sites}}{2}\,\delta_{\mathbf{k},\mathbf{K}_B}$.

For the operators $b_{A,i}$ on the same sublattice we find from Eq. (3.8) that

$$\begin{aligned}\langle b_{A,i}^\dagger b_{A,j}\rangle &= \frac{2}{N_{\rm sites}}\sum_{\mathbf{k}} e^{i\mathbf{k}(\mathbf{r}_i - \mathbf{r}_j)}\langle b_A^\dagger(\mathbf{k}) b_A(\mathbf{k})\rangle \\ &= n\exp\left(i\frac{2\pi}{3}m\right),\end{aligned} \tag{3.19}$$

where m is some integer. The condensate at nonzero momentum exhibits nonuniform phase differences between next–nearest neighbors. Phase ordering directly

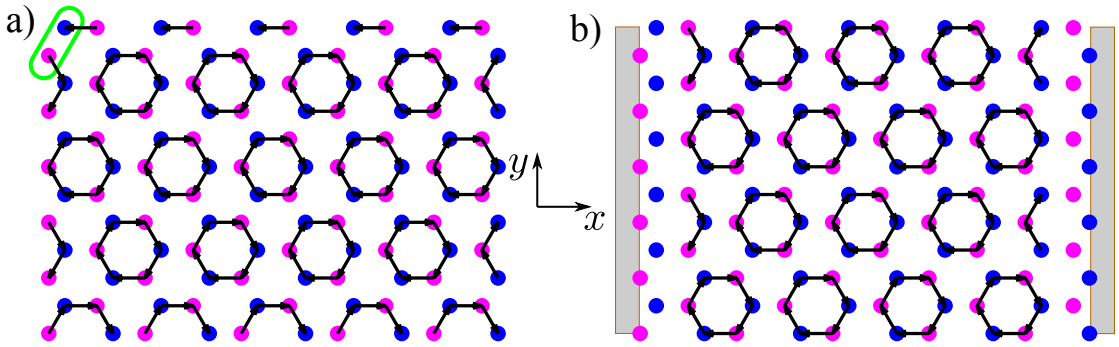

Figure 3.2: Reproduced from Ref. [70]. Sublattices become phase coherent in the presence of defects, or in open boundary geometries. J_{AB} currents develop in the *CSF* if: in a) the top left link hosts a defect $t_1 = 4t_2$; in b) we impose open boundary conditions in the horizontal direction. Arrows represent local currents $|J_{\rm AB}| \approx |2t_1 n \sin\frac{2\pi}{3}| = \sqrt{3}nt_1$. Bond currents which vanish away from the defect, as well as J_{AA} and J_{BB}, are not represented. Results are obtained by minimizing a Gross–Pitaevskii energy functional for a 120 site lattice for $U = 1, t_1 = 10, t_2 = 10$, and average filling $n = 1$, corresponding to the *CSF* phase.

affects the next–nearest neighbor current expectation value

$$\begin{aligned} J_{AA}^{CSF} &= -2\ \mathrm{Im}\left(t_2 e^{-i\pi/2}\left\langle b_{Ai}^{\dagger} b_{Aj}\right\rangle\right) \\ &= -2t_2 n \sin\left[-\pi/2 + \mathbf{K}_A \cdot (\mathbf{r}_i - \mathbf{r}_j)\right] = -nt_2. \end{aligned} \tag{3.20}$$

We use the change of sign of the current operator expectation value between *CSF* and *SF*, Eqs. (3.20) and (3.13) respectively, to identify a first order phase transition between the two superfluids.

These results are confirmed numerically using Lanczos methods for small translation and inversion symmetric clusters in Subsec. 3.2.3. Nonetheless, the fact that the states (3.15) and (3.17) become degenerate in the thermodynamic limit opens up a possibility of a ground state that breaks lattice symmetries [215]. We investigate this issue further in Sec. 3.2.3.

The ground state is significantly different in the presence of a defect or open boundaries, when coherence between the sublattices may be established. For example, at the boundary of the lattice, A and B sublattice phases can be pinned since the number of B neighbors for any A site is 2 instead of 3. Once the phases are pinned at the boundary, the A–B sublattice phase coherence proliferates into

the bulk. Another possibility to establish phase coherence between A and B sublattices is to create a strong nearest neighbor bond at a given unit cell (possibly imprinting a phase difference). As a consequence of long–range correlations between sites on the same sublattice, J_{AB} at any other bond acquires a definite value.

We conclude that

$$J_{AB}^{CSF} = 0 \tag{3.21}$$

in a finite system obeying lattice translation and inversion symmetries (*i.e.* a lattice on a torus with finitely many sites), whereas

$$J_{AB}^{CSF} \neq 0 \tag{3.22}$$

in the presence of defects or if the system has open boundaries, which is the case in experiment. These qualitative points were substantiated numerically through a minimization of the Gross–Pitaevskii energy functional for finite geometries by our collaborator Ivana Vasić in [70] (as exemplified in Fig. 3.2).

At the critical hopping strength $t_1 = \sqrt{3}t_2$, there are three degenerate minima of the lowest band, but the mean-field analysis indicates that condensation either at $\mathbf{\Gamma}$ or at both $\mathbf{K}_A$ and $\mathbf{K}_B$ is preferred. Finally, remark that although at mean–field level in the *CSF* phase the two sublattices are decoupled, quantum fluctuations obtained from Bogoliubov quasiparticles restore sublattice phase coherence in periodic clean systems and select a sixfold degenerate ground state whose J_{AB} current patterns organize on hexagonal plaquettes analogous to the ones in Figure 3.2 [70].

3.2.2 Mott Insulator with Plaquette Currents

In this section we do two things: we derive the boundaries of the unit filling Mott insulating phase using the random phase approximation; by variational arguments we prove that the Mott insulator supports local plaquette current patterns, but

without long–range order.

The phase boundary between *PMI* and any one of the two superfluids can be determined to good accuracy perturbatively in t_{ij}, the hopping integral matrix in (3.4). There are a number of approaches to do this, but the key point is that one starts with the "atomic insulator" limit where $t_{ij} = 0$. The ground state in this limit is a product state over the atomic limit eigenstates of each site. Then one organizes a perturbative expansion in t. In a standard mean–field approach [154], the atomic limit Hamiltonian is obtained from (3.4) by decoupling the kinetic terms $b_i^\dagger b_j \approx \langle b_i^\dagger \rangle b_j + b_i^\dagger \langle b_j \rangle - \langle b_i^\dagger \rangle \langle b_j \rangle$ to obtain the mean–field Hamiltonian

$$H_{mf} = \sum_i H_{mf}^i + \text{const.}, \tag{3.23}$$

given by a sum of local terms

$$H_{mf}^i = -\Psi_i^{\text{mf}} b_i^\dagger - \left(\Psi_i^{\text{mf}}\right)^* b_i + \frac{U}{2} n_i \left(n_i - 1\right) - \mu \, n_i. \tag{3.24}$$

Each lattice site is coupled to the neighboring sites through a sum of condensate order parameters $\Psi_i^{\text{mf}} = \sum_j t_{ij} \psi_j$, where the relation between ψ_j and the boson annihilation operator is given in Eq. (3.5). To proceed, solve for the ground state of (3.23), perturbatively in Ψ_i^{mf}. Then use this ground state as a variational state for the original interacting Hamiltonian: the variational energy is a functional of the fields Ψ_i^{mf}. Proving that quartic terms are bounded below, and carrying out the expansion to second order allows one to detect whenever the Ψ_i^{mf} that minimize the variational energy develop a nonzero expectation value, which corresponds to a superfluid ground state. On the opposite side, $\Psi_i^{\text{mf}} = 0$ signifies that the ground state was unchanged by the perturbation coming from kinetic terms. The drawback of this method is that any resulting Mott state is featureless, a mere product state with, say, one particle at each site $\prod_i |1\rangle_i$.

We can incorporate kinetic terms at all orders in perturbation theory using the Random Phase Approximation (RPA) [216, 217, 218, 219], which will allow us to

achieve a Mott phase which exhibits entanglement between next–nearest neighbors on the lattice. Specifically, we will determine the quantum phase transition by inspecting the spectral function associated with the single particle Green's function:

$$G_{ij}(\tau_1 - \tau_2) = -\langle \mathcal{T} b_i(\tau_1) b_j^\dagger(\tau_2) \rangle, \tag{3.25}$$

where $\mathcal{T}$ is the time–ordering operator. The single particle Green's function can be reexpressed in terms of bosonic Matsubara frequencies $\omega_n = 2\pi n/\beta$, where β is the inverse temperature ($\beta \to \infty$)

$$G_{ij}(i\omega_n) = \int d\tau \exp(i\omega_n \tau) G_{ij}(\tau). \tag{3.26}$$

An analysis of the poles of $G_{ij}(i\omega_n)$ will allow us to determine when the gap associated with the Mott insulator closes.

The RPA relies on the approximation that the self–energy is local, which we will make precise in the following treatment. First we note that this approximation becomes exact in the limit of infinite lattice coordination number. The local self–energies are determined from the site Hamiltonian [216, 217, 218, 219]

$$H_j = \frac{U}{2} n_j(n_j - 1) - \mu n_j, \tag{3.27}$$

together with the associated local Green's function

$$G_{jj}^0(i\omega_n) = -\langle \Phi_{0j} | b_j^\dagger \frac{1}{i\omega_n - E_0 + H_j} b_j | \Phi_{0j} \rangle + \langle \Phi_{0j} | b_j \frac{1}{i\omega_n + E_0 - H_j} b_j^\dagger | \Phi_{0j} \rangle, \tag{3.28}$$

where we have denoted by $|\Phi_{0j}\rangle$ the ground state of H_j:

$$H_j |\Phi_{0,j}\rangle = E_0 |\Phi_{0,j}\rangle, \tag{3.29}$$

assuming a translationally invariant system (uniform U and μ).

At zero temperature, when the ground state is $\prod_i |n\rangle_i$, equation (3.28) becomes

$$G^0_{jj}(i\omega_n) = G^0(i\omega_n) = -\frac{n}{-(n-1)U + \mu + i\omega_n} + \frac{n+1}{-nU + \mu + i\omega_n}. \tag{3.30}$$

The local self–energy is defined from the local Dyson equation

$$\Sigma^0_j(i\omega_n) = i\omega_n + \mu - \left[G^0_{jj}(i\omega_n)\right]^{-1}. \tag{3.31}$$

The RPA consists of approximating the self–energy of the full lattice problem, $\Sigma_{ij}(i\omega_n)$, by the one site self–energy given in (3.31). This leads to an approximation for the single particle Green's function G_{ij} of (3.26) from the lattice Dyson equation. Denoting the approximate form $G^{\rm RPA}$, the lattice Dyson equation reads

$$\left[G^{\rm RPA}\right]^{-1}_{ij}(i\omega_n) = (i\omega_n + \mu)\,\delta_{ij} + t_{ij} - \delta_{ij}\Sigma^0_i(i\omega_n). \tag{3.32}$$

For the calculation of the phase boundary it is convenient to introduce its Fourier transform

$$\left[G^{\rm RPA}\right]^{-1}(i\omega_n, \mathbf{k}) = \left[i\omega_n + \mu - \Sigma^0_{ii}(i\omega_n)\right]\sigma_0 - \mathbf{h}(\mathbf{k})\cdot\sigma. \tag{3.33}$$

Equation (3.33) allows us to derive the single particle excitation spectrum of the Mott state. The first step is to perform the analytic continuation to real frequencies $i\omega_n \to \omega + i\delta$, where δ is a positive number, which is related to the particle or hole excitation lifetime. The energy dispersion relations of particle or hole excitations appear as poles of $G^{\rm RPA}(\omega, \mathbf{k})$. By performing a unitary transformation to diagonalize $\mathbf{h}(\mathbf{k})\cdot\sigma$ in (3.33) we can read off the particle or hole excitation dispersion relations (denoted by $\omega_{+,\alpha}$ or $\omega_{-,\alpha}$, respectively) [216, 217, 220]

$$\omega_{\pm,\alpha}(\mathbf{k}) = \frac{U}{2}\left[(2n-1) - 2\frac{\mu}{U} + \frac{E_\alpha(\mathbf{k})}{U} \pm \sqrt{1 + 2(2n+1)\frac{E_\alpha(\mathbf{k})}{U} + \frac{E_\alpha(\mathbf{k})^2}{U^2}}\right], \tag{3.34}$$

where α takes values $\pm$ corresponding to one of the two non–interacting bands $E_{\pm}(\mathbf{k})$.

We may now use Eqs. (3.9) and (3.10) for the minima of $E_{\pm}(\mathbf{k})$ to determine the phase boundaries. At filling $n = 1$, the gap in the spectrum closes at $t_1^{\mathrm{RPA},c} = U\frac{3-2\sqrt{2}}{3}$ for $t_1 > \sqrt{3}t_2$ where the transition from Mott insulator into *SF* occurs, while for $t_1 < \sqrt{3}t_2$ the transition into the *CSF* is found for $t_2^{\mathrm{RPA},c} = U\frac{3-2\sqrt{2}}{3\sqrt{3}}$. These two boundaries meet at a tricritical point with the line $t_1 = \sqrt{3}t_2$ corresponding to a direct transition between the two superfluids [see the dashed lines on Fig. 3.4c)].

The important feature of the Mott insulating phase is that it supports non–vanishing density fluctuations at finite values of the hopping parameters t_1, t_2. These density fluctuations are produced by the complex hopping term it_2. Generally, we may express bond operator expectation values in terms of the single particle Green's function

$$\langle b_i^{\dagger} b_j \rangle = -\frac{1}{\beta} \sum_n \exp(i\omega_n 0^+) G_{ji}(i\omega_n). \tag{3.35}$$

In RPA, we replace G_{ji} by G_{ji}^{RPA}, invert the matrix in (3.32), and expand in the kinetic terms t_{ij} up to cubic contributions, which amount to closed loops on the lattice which are threaded by some nonzero flux. From the result for $\langle b_i^{\dagger} b_j \rangle$ given in Refs. [218, 219], we may read off the following expression for the current:

$$\frac{J_{ij}^{(2)}}{U} = -2\mathrm{Im}\, t_{ij} \left(\sum_k t_{jk} t_{ki} \right) \frac{3n(n+1)(2n+1)}{U^3} + \ldots,$$

leading us to

$$\frac{J_{AA}^{(2)}}{U} = \frac{36}{U^3} t_2 \left(t_1^2 - 2t_2^2 \right). \tag{3.36}$$

Note that the triangular plaquette currents (3.36) would be vanishing in the absence of flux. Moreover, at this order in perturbation theory the current between nearest neighbors vanishes. Contributions to J_{AB} and J_{AA} which are quadratic in

t's vanish because Peierls phases cancel when a particle hops from one site to its neighbor and back. Third order contributions to J_{AB} cancel when summed over the 4 lattice paths composed of two bonds that begin at a site and end at a nearest neighboring site.

It is informative to construct a variational state for the *PMI* which exhibits the type of inter–site coherence described here. It amounts to exciting particle–hole pairs on top of the uniform Mott insulator background:

$$\begin{aligned} |\Phi_{PMI}\rangle &= \mathcal{N} e^{\frac{\alpha}{U}\sum_{ij} t_{ij} b_i^\dagger b_j} |\Phi_{MI}\rangle, \\ |\Phi_{MI}\rangle &= \prod_i |1\rangle_i \end{aligned} \tag{3.37}$$

where $\mathcal{N}$ is a normalization constant, and α is a real variational parameter. This is a well founded guess: the only term in the Hamiltonian that can produce particle–hole excitations is some kinetic term t_{ij}, and the cost of a particle–hole pair in the uniform Mott state is U. The problem is to minimize the variational energy $E_0^{PMI} = \langle \Phi_{PMI}|H|\Phi_{PMI}\rangle$ with respect to α.

If we let $A \equiv \frac{\alpha}{U}\sum_{ij} t_{ij}$, the variational energy can be expressed as

$$\begin{aligned} E_0^{PMI} &= \langle \Phi_{MI}|(1 + A + A^2/2 + \ldots)H(1 + A + A^2/2 + \ldots)|\Phi_{MI}\rangle \\ &= E_0^{MI} + \langle \Phi_{MI}|AH + HA|\Phi_{MI}\rangle + \frac{1}{2}\langle \Phi_{MI}|A^2H + HA^2|\Phi_{MI}\rangle \\ &\quad + \langle \Phi_{MI}|AHA|\Phi_{MI}\rangle + \ldots \end{aligned} \tag{3.38}$$

After some algebra this gives

$$\frac{E_0^{PMI} - E_0^{MI}}{U} = (2\alpha + \alpha^2) n(n+1) \sum_{\mathbf{k}} |\mathbf{h}(\mathbf{k})|^2, \tag{3.39}$$

where the summation is over the first Brillouin zone. Note that the variational energy is minimized for $\alpha = -1$, and moreover that at this value the energy of $|\Phi_{PMI}\rangle$ is lower than that of $|\Phi_{MI}\rangle$ by $n(n+1)\sum_{\mathbf{k}} |\mathbf{h}(\mathbf{k})|^2$. The current expectation values up to cubic order in t_{ij} agree with the ones obtained from strong coupling

perturbation theory (3.36).

Finally, the *PMI* has no long range current–current correlations. For $\langle J_{AA} J_{AA} \rangle$ between currents belonging to plaquettes which are not connected by a kinetic term factorize and are proportional to the square of (3.36). Therefore, the connected correlation functions of plaquette currents vanish identically for separated plaquettes. This characterizes the plaquette Mott insulator as a state with local plaquette currents *without long range current-current correlations*.

3.2.3 Exact diagonalization

In this section we use the ALPS implementation [221] of the Lanczos algorithm [222] in order to study the ground state of the interacting model in Eq. (3.4) at unit filling $n = 1$. We consider a lattice of 3×3 unit cells, implying $N_{sites} = 18$ and $N = 18$ particles. The truncated boson Hilbert space contains states for which the number expectation value at any site is bounded above $\langle n_i \rangle \leq 2$. The Hilbert subspace with this constraint has dimension 44152809. With periodic boundary conditions, total momentum $\mathbf{Q} = \sum_{i=1}^{N} \mathbf{k}_i$ is a good quantum number and the dimension of the Hilbert space for each momentum sector is reduced by a factor of 9. The Brillouin zone contains 3×3 points and includes the inequivalent points $\mathbf{\Gamma}$ and $\mathbf{K}_A, \mathbf{K}_B$, as shown in Figure 3.3.

Since total particle number is conserved, the spontaneous breaking of the $U(1)$ symmetry is not observable in the ground state. We rather identify the Mott insulator phase as the region of the $(t_1/U, t_2/U)$ plane where number fluctuations at a site $\langle n_i^2 \rangle - \langle n_i \rangle^2$ are small [see Figure 3.4d)].

As shown in Sec. 3.2.1, bond current expectation values distinguish the chiral superfluid from the uniform superfluid phase. The nearest neighbor current J_{AB} vanishes identically at $n = 1$. The next-nearest neighbor bond current J_{AA} as a function of t_1 and t_2 is consistent with the result from strong-coupling perturbation theory [Eq. (3.36)]. The next-nearest neighbor current J_{AA} changes sign at $t_1 = t_2\sqrt{3}$, and J_{BB} has analogous behavior [their common absolute value is plotted in

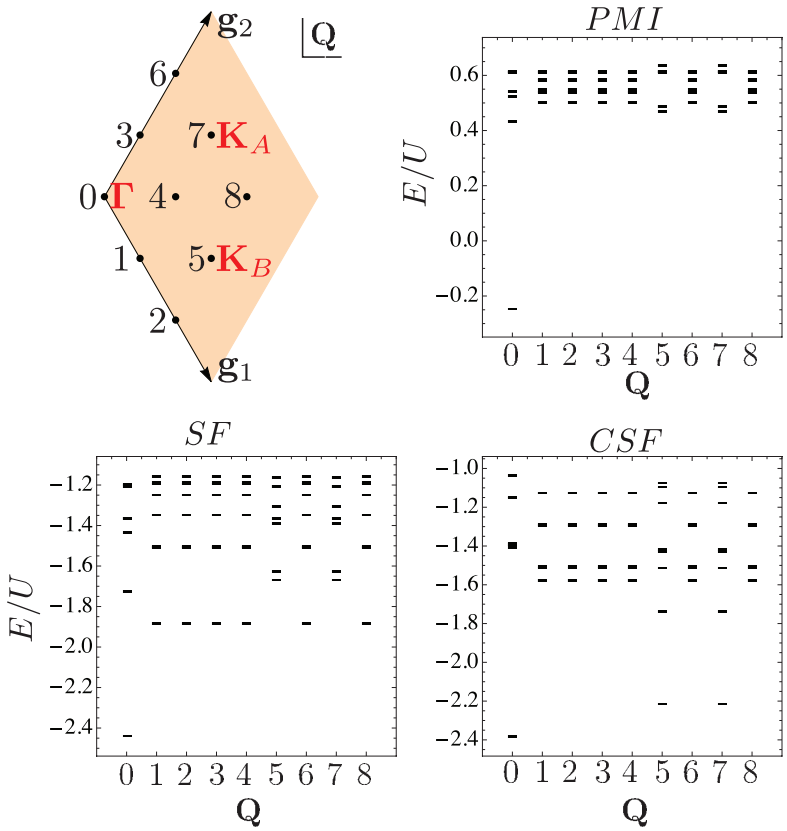

Figure 3.3: Reproduced from Ref. [70]. Low lying energy levels in the spectra of the 3×3 unit cell lattice at unit filling, for: *PMI* ($t_1/U = 0.04$, $t_2/U = 0.02$), *SF* ($t_1/U = 0.14$, $t_2/U = 0.02$), and *CSF* ($t_1/U = 0.04$, $t_2/U = 0.08$). The first 8 energy levels in each sector of total momentum $\mathbf{Q}$ are plotted. The 9 momentum sectors in the Brillouin zone spanned by the vectors $\mathbf{g}_1$ and $\mathbf{g}_2$ are represented in the top left panel. For example, sectors labeled 0, 7, 5 correspond to $\mathbf{\Gamma}$, $\mathbf{K}_A$ and $\mathbf{K}_B$, respectively.

Figure 3.4b)]. This is the exact phase boundary found previously in the weakly interacting regime and with DMFT for arbitrarily strong interactions. We thus confirm the existence of the *PMI* state with nonzero triangular plaquette currents at order $t_1^2 t_2/U^3$ but vanishing nearest-neighbor currents.

To understand the momentum structure of the ground state, we consider the momentum distributions,

$$n_a(\mathbf{k}) \equiv \langle b_a^\dagger(\mathbf{k}) b_a(\mathbf{k}) \rangle = \sum_j e^{i\mathbf{k}\cdot\mathbf{r}_j} \langle b_{a0}^\dagger b_{aj} \rangle, \tag{3.40}$$

where $a = A$ or B denotes the sublattice. In agreement with analytical results in the weakly interacting limit [Sec. 3.2.1], we find that in the *SF* the momentum dis-

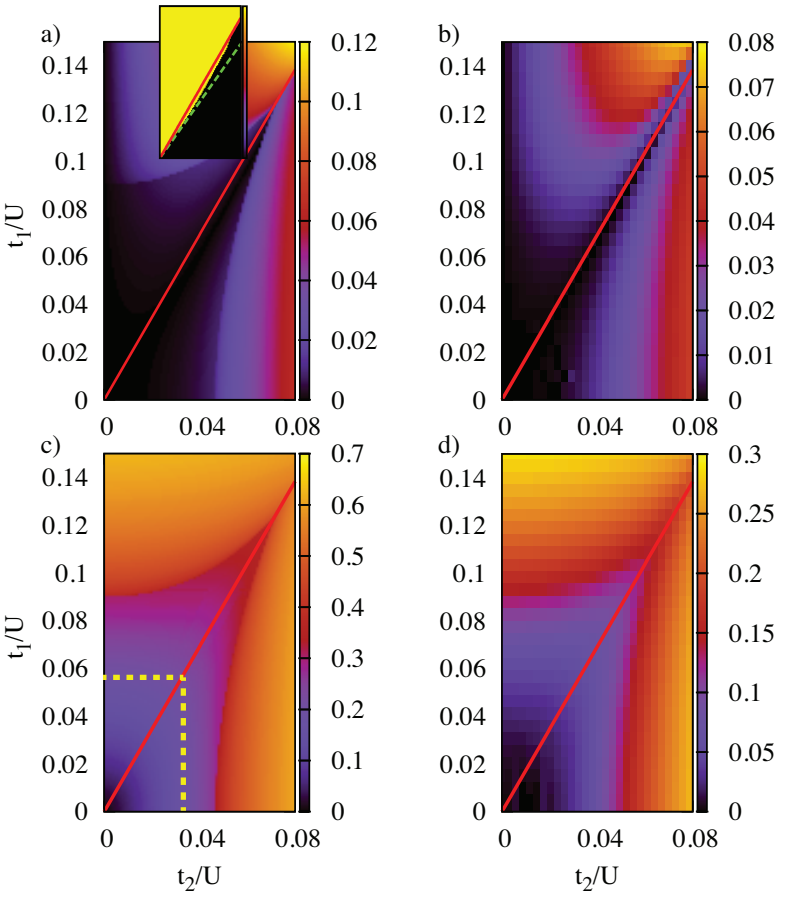

Figure 3.4: Reproduced from Ref. [70]. Comparison of DMFT, a) and c), and ED results, b) and d). $|J_{AA}|/U$ is shown in a) and b). Panels c) and d) show density fluctuations $\langle \hat{n}_i^2 \rangle - \langle \hat{n}_i \rangle^2$. The yellow dashed line in Panel c) represents the mean field theory phase boundary from (3.34). The inset in a) shows the sign of J_{AA}: In the superfluid, the sign changes for $t_1 = \sqrt{3}t_2$ (solid line), while deep in the Mott domain the boundary is given by $t_1 = \sqrt{2}t_2$ according to Eq. (3.36) (dashed line). ED results are at fixed filling $n = 1$.

tribution $n_A(\mathbf{k}) + n_B(\mathbf{k})$ is sharply peaked at the $\mathbf{\Gamma}$ point. In the *CSF* phase, $n_a(\mathbf{k})$ are peaked at $\mathbf{K}_a$, in agreement with the decoupled condensates wavefunction $|\Phi_0''\rangle$ of Eq. (3.17). In the *PMI*, $n_a(\mathbf{k})$ become more and more uniformly distributed as the hopping amplitudes t_1 and t_2 approach 0. Regarding the symmetries, we remark that lattice translation symmetry and the lattice inversion symmetry are conserved by the ground state in the $\mathbf{Q} = 0$ sector. Without breaking the discrete lattice symmetries it is impossible to obtain the coherent superposition $|\Phi'_{CSF}\rangle$.

In conclusion, we confirm by studying the exact ground state of the 3×3 lattice all the qualitative features of the DMFT phase diagram [see Figure 3.4 for a comparison]. We can distinguish between the *SF* and the *CSF* by studying

momentum distributions and currents, and determine sharply the phase boundary between the two superfluids at the critical line $t_1 = t_2\sqrt{3}$ by detecting the change in sign of the next-nearest neighbor currents J_{AA} or J_{BB}.

We stress that the results obtained in this section are for a finite sized lattice Hamiltonian obeying translation and inversion symmetries. Consequently, the finite size ground state in the $\mathbf{Q} = 0$ sector obeys these symmetries. For an infinite system obeying all symmetries, the ground state may be identified as a specific linear combination of degenerate ground states that breaks the symmetries [215]. To briefly explore this possibility, we plot the low energy spectra for each phase, as shown in Figure 3.3. In the *CSF* phase, there are two low-lying states in the $\mathbf{Q} = \mathbf{K}_A$ and $\mathbf{Q} = \mathbf{K}_B$ sectors, which may become degenerate with the ground state for an infinite system or as $U \to 0$. However, an analysis of the scaling of the gap with system size is limited by the large dimension of the Hilbert space at unit filling. Moreover, the $U \to 0$ limit cannot be rigorously explored numerically due to the necessary truncation of the bosonic Hilbert space.

3.3 Excitations of the Mott phase

In this section we study quasiparticle or quasihole excitations of the Mott insulator phase. We use the single particle Green's function $G(i\omega_n, \mathbf{k})$ to compute quasiparticle and quasihole band dispersions. We characterize transport in excited bands through band Chern numbers [11]. We have obtained $G(i\omega_n, \mathbf{k})$ from the strong coupling random phase approximation [223, 224, 225], in agreement with DMFT computations in [70].

3.3.1 Strong coupling expansion

We use the results of the strong coupling expansion with RPA introduced in Subsec. 3.2.2 to study the spectrum of quasiparticle and quasihole excitations. We extend the approach of Subsec. 3.2.2 by grouping the sites on the lattice into iden-

tically shaped nonoverlapping clusters [223, 224, 225] (*e.g.* the collection of unit cells pointing along $\mathbf{a}_1$ is a collection of 2 site clusters). Starting from the limit of decoupled clusters (intercluster hopping vanishes) we treat intercluster hopping perturbatively, summing all RPA contributions.

Let $H'_{\rm H}$ be the sum of intercluster hopping terms in $H_{\rm H}$. Let $H_{\rm I} \equiv H - H_{\rm H}$ denote the interaction part of the Hamiltonian. The Hamiltonian of decoupled clusters is

$$H_{\rm C} = H_{\rm I} + H_{\rm H} - H'_{\rm H} = \sum_j H_{{\rm C}j}. \tag{3.41}$$

The sum in the second equality is over decoupled cluster Hamiltonians $H_{{\rm C}j}$.

We now define the *local* Green's function corresponding to one decoupled cluster. Let the ground state of $H_{{\rm C}j}$ be $|\Phi_{0j}\rangle$ with ground state energy E_0. Denote sites within a cluster using Latin indices $a, b = A$ or B, such that b_{aj} annihilates a quasiparticle at the $a^{\rm th}$ site of the $j^{\rm th}$ cluster. The local Green's function becomes

$$\begin{aligned}[G^{\rm RPA}_{jj}(i\omega_n)]_{ab} &= -\langle\Phi_{0j}|b^\dagger_{bj}\frac{1}{i\omega_n - E_0 + H_{{\rm C}j}}b_{aj}|\Phi_{0j}\rangle \\ &\quad +\langle\Phi_{0j}|b_{aj}\frac{1}{i\omega_n + E_0 - H_{{\rm C}j}}b^\dagger_{bj}|\Phi_{0j}\rangle,\end{aligned} \tag{3.42}$$

for each cluster j. In what follows, we assume that clusters are identical, and therefore we will drop the cluster index denoting the local Green's function simply by $[G^{\rm RPA}(i\omega_n)]_{ab}$.

Note that Eq. (3.42) reduces to Eq. (3.30) of Subsec. 3.2.2 if we consider single-site clusters. The spectral function has a pole at $nU - \mu$ with residue $(n+1)$ and a pole at $(n-1)U - \mu$ with residue $-n$. If the cluster comprises the unit cell, hybridization from the intracluster kinetic term results in pairs of quasiparticle and quasihole poles. We commit to clusters consisting of a single unit cell. In this case, the RPA approximation to the single particle Green's function is [224, 225]

$$\left[G^{\rm RPA}(i\omega_n, \mathbf{k})\right]^{-1} = [G^{RPA}(i\omega_n)]^{-1} - H'_{\rm H}(\mathbf{k}). \tag{3.43}$$

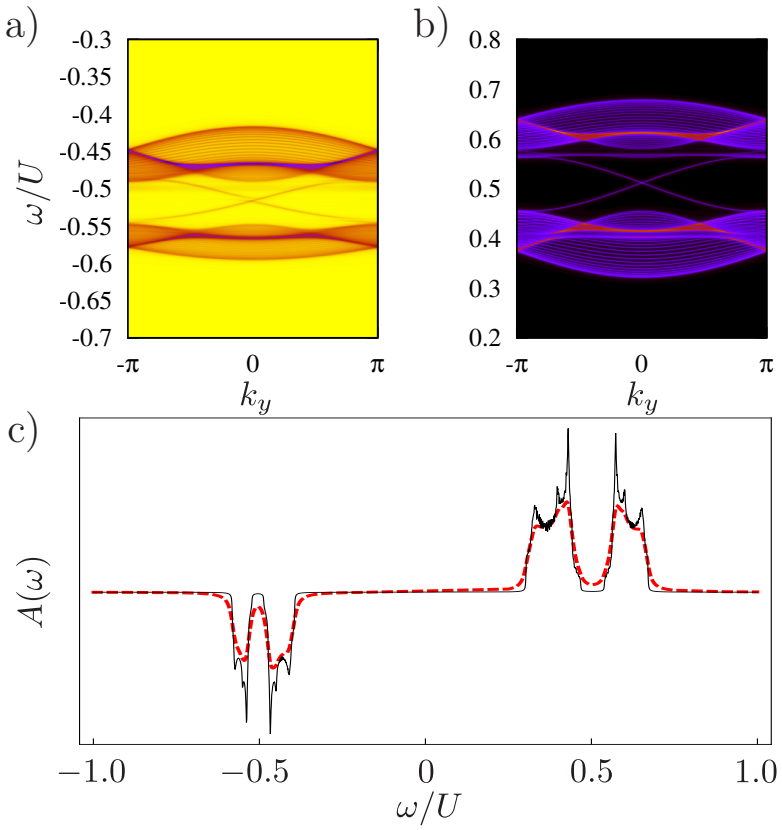

Figure 3.5: Reproduced from Ref. [70]. Typical spectral functions deep in the Mott domain, for $t_1 = 3U/100$, $t_2 = U/100$, $\mu = U/2$: **a)** and **b)** quasihole and quasiparticle branches of the spectral function obtained from DMFT for a cylinder geometry exhibiting edge modes for $\delta = U/1000$. **c)** strong–coupling expansion density of states $A(\omega)$ [in arbitrary units; according to Eq. (3.44)] for a torus geometry and for two values of δ: $U/1000$ (solid black line) and $U/100$ (thick dashed red line). Quasiparticle and quasihole bands are centered at $U - \mu$ and $-\mu$, respectively.

This is the equivalent of Eq. (3.33) in the cluster perturbation theory language. The difference is that now all three of $[G^{RPA}(i\omega_n, \mathbf{k})]_{ab}$, $[G^{RPA}(i\omega_n)]_{ab}$ and $[H'_{\rm H}(\mathbf{k})]_{ab}$ are 2×2 matrices acting on the sublattice basis. Tracing over sublattice indices in Eq. (3.43), we obtain the spectral function

$$A(\omega, \mathbf{k}) = -(1/\pi)\ \mathrm{Tr\ Im}\ G^{\rm RPA}(\omega, \mathbf{k}). \tag{3.44}$$

Since $G^{\rm RPA}(\omega, \mathbf{k})$ in Eq. (3.43) is a rational function, the spectral function $A(\omega, \mathbf{k})$ is a sum of Lorentzians. Deep in the Mott phase, the strong coupling spectral function agrees with that obtained from DMFT, plotted in Figure 3.5 a),b) for a

finite cylinder geometry. Note that the resolution of the edge states is dependent on the inverse lifetime δ. In Figure 3.5 c) we plot the density of states $A(\omega) \equiv \int d^2\mathbf{k}\ A(\omega, \mathbf{k})$ for two values of δ. The gap between quasiparticle (hole) bands disappears when the inverse lifetime approaches the bandwidth, $\delta \sim t_1$. In the opposite regime, a clear gap is present and intragap edge modes are resolved for $\delta \ll t_1$. We note finally that using larger clusters [224, 225] yields a G^{RPA} whose qualitative features are similar to those of Eq. (3.43). In particular, this approach will not yield an estimate for the quasiparticle lifetime $1/\delta$. We expect that the inverse lifetime, calculated from the strong–coupling expansion of the self–energy including two–body scattering contributions, is, to leading order, [219] $\delta \propto t_1^2/U$ which in the Mott phase is about two orders of magnitude smaller than t_1.

3.3.2 Topological particle or hole excitations

We assume that $\delta \ll t_1$, such that the $G^{\mathrm{RPA}}(\omega, \mathbf{k})$ has well defined quasiparticle and quasihole peaks. We use Greek indices $\alpha = +, -$ to denote the upper and lower subbands. We denote the quasiparticle dispersion relation as $\omega_{+,\alpha}(\mathbf{k})$ and the quasihole dispersion relation $\omega_{-,\alpha}(\mathbf{k})$. Quasiparticle and quasihole poles arise from the equation

$$\lambda\left[\omega_{\pm,\alpha}(\mathbf{k}), \mathbf{k}\right] = 0, \tag{3.45}$$

where λ denotes any one of the two eigenvalues of $[G^{\mathrm{RPA}}(\omega, \mathbf{k})]^{-1}$ obtained from Eq. (3.43). We are interested in band Chern numbers, which arise from the Ishikawa-Matsuyama formula [108] of the many-body Hall conductivity

$$\sigma_{xy} = -\int \frac{d^2\mathbf{k}d\omega}{8\pi^2}\epsilon^{ij}\mathrm{Tr}\left[\partial_0 G \partial_i G^{-1} G \partial_j G^{-1}\right]. \tag{3.46}$$

The summation over indices $i, j = 1, 2$ is implicit and ϵ^{ij} is the antisymmetric tensor defined by $\epsilon^{11} = \epsilon^{22} = 0$ and $\epsilon^{12} = -\epsilon^{21} = 1$. Integrations are performed over the Brillouin zone and over real frequencies ω. We have denoted partial derivatives as $\partial_j = \partial/\partial k_j$, where $k_0 \equiv \omega$, and $k_{1,2}$ denote momentum.

Let $\mathcal{U}(\omega, \mathbf{k})$ be the unitary transformation that diagonalizes $[G^{\mathrm{RPA}}(\omega, \mathbf{k})]^{-1}$, that is

$$[G^{\mathrm{RPA}}]^{-1}_{ab} = \sum_{\alpha\beta} \mathcal{U}_{a\alpha} \lambda_\alpha \delta_{\alpha\beta} \mathcal{U}^\dagger_{\beta b}. \tag{3.47}$$

We introduce the matrix of Berry gauge fields

$$\mathcal{A}^j_{\alpha\beta} = \sum_a i\, \mathcal{U}_{a\alpha} \partial_j \mathcal{U}^\dagger_{\beta a}, \text{ for } j = 0, 1, 2. \tag{3.48}$$

Note that the diagonal component $\mathcal{A}^j_{\alpha\alpha}$ is the Berry gauge field associated with the α^{th} band. If the Green's function has only simple poles at $\omega_{\pm,\alpha}(\mathbf{k})$, then the frequency integral of Eq. (3.46) can be performed [185, 186, 226], leading to

$$\sigma_{xy} = -\sum_{\alpha\delta} \int \frac{d^2\mathbf{k}}{2\pi}\, \epsilon^{ij} \left[\mathcal{A}^i_{\alpha\delta} \mathcal{A}^j_{\delta\alpha} + v^i_{-,\alpha} \mathcal{A}^j_{\alpha\delta} \mathcal{A}^0_{\delta\alpha} \right]_{\omega=\omega_{-,\alpha}(\mathbf{k})}. \tag{3.49}$$

The frequency integral of Eq. (3.46) amounts to evaluating the integrand of Eq. (3.49) at the two quasihole poles $\omega_{-,\alpha}(\mathbf{k})$. We have introduced band velocities

$$v^j_{-,\alpha}(\mathbf{k}) \equiv \partial_j \omega_{-,\alpha}(\mathbf{k}). \tag{3.50}$$

It turns out that we can further simplify Eq. (3.49) by introducing the *on-shell* Berry gauge field for quasihole bands as

$$\mathcal{B}^i_{h,\alpha\beta}(\mathbf{k}) = \sum_a i\, \mathcal{U}_{a\alpha} \left[\omega_{-,\alpha}(\mathbf{k}), \mathbf{k}\right] \partial_i \mathcal{U}^\dagger_{\beta a} \left[\omega_{-,\beta}(\mathbf{k}), \mathbf{k}\right]. \tag{3.51}$$

Then σ_{xy} measures the flux of the on-shell Berry field strength through the Brillouin zone and splits into a sum over quasihole bands $\sigma_{xy} = \sum_{\alpha=\pm} \nu_\alpha$, where

$$\nu_\alpha = \frac{1}{2\pi} \int d^2\mathbf{k} \left[\partial_1 \mathcal{B}^2_{h,\alpha\alpha}(\mathbf{k}) - \partial_2 \mathcal{B}^1_{h,\alpha\alpha}(\mathbf{k}) \right]. \tag{3.52}$$

Direct evaluation of Eq. (3.52) gives $\nu_\pm = \pm 1$. The total Hall conductivity of the two quasihole bands is hence $\sigma_{xy} = 0$. This corresponds to the Hall conductivity

evaluated in the Mott gap. Bulk-edge correspondence implies that edge modes exist in the gap between the two quasihole bands, which is consistent with the spectral function that was obtained numerically using DMFT in Fig. 3.5. The quasiparticle bands have $\nu_\pm = \mp 1$, which follows from an analogous calculation.

Small finite inverse lifetime δ results in a shift of quasiparticle and quasihole poles away from the real axis. The results of this subsection for ν_α remain valid as long as a gap exists between the two quasihole bands. Figure 3.5 shows that whenever the inverse lifetime δ is on the order of the kinetic energy strength t_1, the Mott gap and the two gaps between excited bands are smeared off. It is therefore necessary to require $\delta \ll t_1$ in order to resolve intra-gap edge modes from bulk states in the density of states.

3.4 Conclusions

We have investigated the Haldane Bose–Hubbard model at unit filling. We have mapped out the phase diagram as a function of the two hopping integrals and found that it consists of two competing types of superfluid and a Mott insulator supporting local plaquette currents. Using methods beyond mean–field theory, we discovered that there is a reentrant transition into the Mott insulator. We have discussed two distinct superfluid ground states, which are connected either by a first order transition in the weakly interacting regime, or via two second order transitions through an intermediate Mott insulator in the strongly interacting regime. We have differentiated these phases using observables accessible in current ultracold atom experiments, such as ground state density fluctuations and local current loops. We have shown that quasiparticle or quasihole excitations of the Mott insulator form bands with non-zero Chern numbers which predict the existence of edge states in the gaps between excited bands.

The edge modes discussed in this section should be visible either in cold–atom experiments using Bragg spectroscopy [227, 228] and photoemission spectroscopy

[229]; or in photonic systems, where a wavepacket can be prepared at an energy corresponding to the edge excitations [48]. Photon–photon interactions can be induced by coupling an off–resonant superconducting qubit to a cavity [230, 116].

These findings can be probed in the near future in ongoing experiments. The Haldane model for fermionic potassium atoms has recently been realized [41]. The required Peierls phases were obtained by modulating the position of the retroreflecting mirrors of the optical lattice. The quantum anomalous transport (see Ch. 2) was probed using band–mapping [127], which allowed for an observation of the local Berry curvature. Introducing interactions in such a lattice would open up the quest for interacting topological phases, such as the fractional Chern insulator, or other novel states, such as fractionally filled Mott insulating phases. Recent studies [231, 232, 130, 233, 234, 235] of fermions on the half–filled honeycomb lattice have identified the emergence of d-wave superconductivity close to the Mott transition, while Ref. [214] discusses a chiral spin superfluid phase of two-component bosons in a double-well potential realized on the honeycomb lattice which is related to the CSF/SF interplay discussed in this chapter.

Part II

Quasi–one dimensional topological states

Chapter 4

Chiral Phases of Ladders

In this chapter, we introduce generic models exemplifying the fact that chiral Meissner currents can persist in insulating phases of matter. Importantly, the conditions required to stabilize the states discussed here are within reach in a number of current experiments with ultracold atoms in quasi one–dimensional lattices [78, 79, 236]. The material presented in this chapter was published in Refs. [69] and [71].

On a lattice at commensurate filling, a bosonic Mott insulator [74, 237] is a state that can be adiabatically connected to an atomic insulator. In the Hamiltonian describing the atomic limit the kinetic terms providing tunneling between distinct sites are suppressed; consequently, the ground state is a product Fock state in which the variance of particle number at each site vanishes. Recent studies examine the possibility of nontrivial Mott states which, due to a broken symmetry, exhibit chiral current order and therefore quantum entanglement. Chiral Mott insulators have been shown to be closely related to short-range entangled topological phases of bosons, such as the boson topological insulator [238, 239]. The boson topological insulator is a symmetry protected topological phase [240, 241, 242, 243, 244, 15, 245], whose gapless boundary excitations are protected by bulk symmetry, but do not possess topological order.

A route in the quest for nontrivial Mott insulators is to break time-reversal

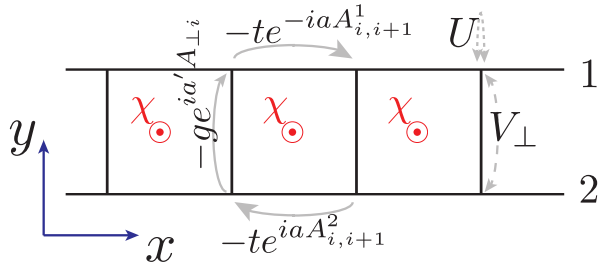

Figure 4.1: Energy scales and setup of bosonic two-leg ladder. Flux χ threads each square plaquette. Hopping integrals (*solid arrows*) t, g and repulsive interaction strengths (*dashed arrows*) $U, V_\perp$ correspond to Eq. (4.1).

symmetry manifestly by an external magnetic field. With two bosonic species on the lattice, the external field may be coupled to the pseudospin degree of freedom within a Mott phase of fixed total density [246, 247, 248, 249]. The Mott phase of spinful fermions in the time-reversal invariant Hofstadter model with additional Rashba spin-orbit coupling possesses spiral spin order [250, 251]. The unit filled bosonic Haldane model [12] of Chapter 3 sustains a Mott insulator with nontrivial plaquette currents [70].

In this chapter, we focus on a strongly interacting boson tight-binding model near half filling on a two–leg ladder in uniform flux (depicted in Fig. 4.1). The Meissner effect [252] was demonstrated on this lattice with weakly interacting ultracold ^{87}Rb atoms [78]. In Ref. [69], we showed that the Josephson effect in the pseudospin sector leads to extended Meissner currents or a vortex phase [252, 253], while the total density retains Mott insulator correlations. Repulsive interactions on a half–filled boson ladder stabilize a Mott insulator for total charge, but allow charge neutral Meissner currents in the relative density. This result was recently confirmed and extended numerically [254, 255]. In Ref. [71], we showed that given certain commensuration conditions and with nearest–neighbor repulsive interactions, the ground state corresponds to a coupled wire realization of the *Laughlin* state [8] introduced by Kane *et al.* [256]. Analogous phases are supported in spinful fermion ladders, and a duality transformation allows us to determine a distinct class of spin chiral incompressible phases for fermions.

This chapter is organized as follows. In Sec. 4.1 we derive the phase diagram

Sector	Notation	sine-Gordon term
+	*Rung Mott*	$\sqrt{8}\phi^+$
+	*Rung superfluid*	$\sqrt{8}\phi^+ + 2\pi\delta n x$
-	*Meissner*	$\sqrt{2}\theta^-$
-	*Vortex phase*	$\sqrt{2}\theta^- + \chi x$
+ & -	*Laughlin*	$\sqrt{2}\theta^- - \sqrt{8}\phi^+$

Table 4.1: Phases of the Josephson ladder appearing in the phase diagram of Fig. 4.2. The "+/−" sector denotes total/relative vertical bond (rung) density $n_i^1 + / - n_i^2$ (see Fig. 4.1). The "+" sector can be in a Mott insulator or superfluid phase, whereas the "−" sector can be in a Meissner phase or a vortex phase depending on the strength of the field. The Laughlin phase arises from a condition that mixes the two sectors.

Phase	Gapped modes per Sector	Gapless modes
Rung Mott – Meissner	1^+1^-	0
Rung Mott – Vortex phase	1^+0^-	1
Rung superfluid – Meissner	0^+1^-	1
Rung superfluid – Vortex phase	0^+0^-	2
Laughlin	$1^{+\&-}$	1

Table 4.2: Number of gapped modes in the Josephson ladder, for the phases appearing in Fig. 4.2. The only gapped phase is the *Rung Mott – Meissner* phase.

in Figure 4.2 for a bosonic ladder at or near half-odd integer filling per site. Then, Sec. 4.2 contains discussions of observables, such as currents and flux quantization, which distinguish the possible ground states. Section 4.3 contains a complementary treatment of strongly coupled bosons in the Mott insulating state. Next, we extend our results to spinful fermion ladders in Sec. 4.4. We propose in Sec. 4.5 experimental realizations in Josephson junction arrays and ultracold atoms in optical lattices with the setups of Refs. [78, 79]. Sec. 4.6 generalizes the phases found for two-leg ladders to N-leg ladders and bilayers. We summarize our results in the concluding Sec. 4.7. Technical details in the Appendices will be referred to when necessary.

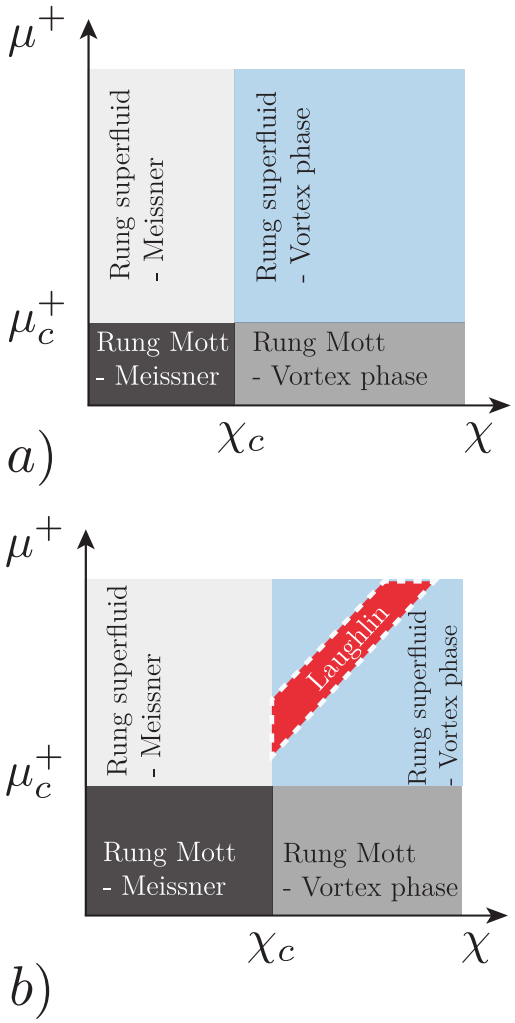

Figure 4.2: Schematic phase diagram of the Josephson ladder: a) with $V_\perp = 0$ and no other repulsive long range interaction along the chains and b) for sufficiently strong $V_\perp \neq 0$ (or for long ranged repulsion within chains), it is possible to stabilize the *Laughlin* ground state. The red region corresponds to (4.31) with the lower sign. As $V_\perp$ is increased from 0, the Mott gap and the critical flux χ_c increase. The phase notations are defined in Tables 4.1 and 4.2.

4.1 The Josephson ladder

In this section, we introduce a relatively simple insulating system exhibiting the Meissner effect [257, 258, 259]. We consider a bosonic quantum ladder with an odd number of bosons per rung (Fig. 4.1). The two-leg ladder consists of two one-dimensional chains with inter- and intrachain kinetic and interaction terms. The lattice layout is depicted in Figure 4.1, which also summarizes the terms in the Hamiltonian

$$\begin{aligned} H &= -t\sum_{\alpha,i} e^{iaA^{\alpha}_{i,i+1}} b^{\dagger}_{\alpha i} b_{\alpha,i+1} - g\sum_{i} e^{-ia'A_{\perp i}} b^{\dagger}_{2i} b_{1i} + h.c., \\ &+ \frac{U}{2}\sum_{\alpha,i} n_{\alpha i}(n_{\alpha i}-1) + V_{\perp}\sum_{i} n_{1i}n_{2i} - \mu\sum_{\alpha i} n_{\alpha i}. \end{aligned} \tag{4.1}$$

In Eq. (4.1), the operator $b^{\dagger}_{\alpha i}$ creates a boson at site i in chain $\alpha = 1, 2$. We introduced the Peierls phases $aA^{\alpha}_{i,i+1}$ acquired by a particle on chain $\alpha = 1, 2$, and $a'A_{\perp i}$ between chains. Lengths a and a' are lattice spacings along and between chains; see Fig. 4.1. The spatial indices run between $1, ..., L$, with $L + 1 \equiv 1$ for periodic boundary conditions. U and $V_{\perp}$ are repulsive on-site and "rung" interactions.

The Hamiltonian (4.1) without interactions can be realized in photonic systems (for a review see [36]). The weakly interacting limit has been realized experimentally in an ultracold atom ladder [78]. Another possibility is to realize (4.1) in Josephson junction arrays [260] or more generally quantum circuits [261, 262].

We briefly outline other results on the model in Eq. (4.1). Without gauge fields and if $V_{\perp} = 0$, and μ insuring one boson per site, the model transitions from a Mott insulator to a superfluid as g increases [263]. At arbitrary boson filling and uniform flux there is a transition from the low-field Meissner phase to a vortex phase [252] beyond some critical field strength, reminiscent of type-II superconductivity. The low-field model with $V_{\perp} = 0$ at unit filling exhibits a superfluid with Meissner currents and a Mott insulator with Meissner currents for

weak enough U [196]. The ground state for half a flux quantum per plaquette at integer filling is a chiral superfluid, a chiral Mott insulator or a Mott insulator, as argued by Dhar *et al.* [193, 194] and Tokuno and Georges [196]. The same model in the weakly interacting limit supports a staggered pattern of quantized orbital current vortices [264, 265]. The model without flux and $V_\perp = 0$ was studied for bosons with a hardcore constraint on site, $U \to \infty$ [266]. The ground state was shown to be a rung Mott insulator at half-filling. A recent numerical investigation covers the phase diagram versus filling, flux and interchain tunneling, containing a Meissner Mott insulator and a vortex phase Mott insulator at half-filling [254, 255].

In this section we will uncover the ground state of the model (4.1) at odd boson filling per rung, *i.e.* $2N + 1$ bosons for every two sites for $N \geq 0$ an integer. For $V_\perp = 0$, depending on different values of filling, flux, and interactions, we find the following low field phases: *Rung Mott – Meissner* , *Rung superfluid – Meissner* , *Rung Mott – Vortex phase* , *Rung superfluid – Vortex phase* .

While it is unnecessary for the phases listed above, the repulsive interaction $V_\perp > 0$ [or long–range repulsion within chain α, not listed in Eq. (4.1)] changes slightly the phase diagram in that it controls the size of the gap above *Rung Mott – Meissner* . In the limit of large interactions, one can draw an analogy with a spin Meissner effect [69]. Moreover, for large enough $V_\perp$, the ground state turns into a low-dimensional *Laughlin* state if flux and doping are commensurate. We note that a Hamiltonian related to (4.1) whose ground state is well approximated by the Laughlin state at $\nu = \frac{1}{2}$ has been discussed by Kalmeyer and Laughlin [267, 268], in search for a spin liquid ground state for the frustrated Heisenberg antiferromagnet. This theory was developed in succeeding work including the formulation of a Hamiltonian whose exact ground state is the Laughlin state at $\nu = \frac{1}{2}$ [269, 270]. In this work we will identify the Laughlin state by comparing the continuum form of our Hamiltonian with that of a coupled wire construction [256, 271].

The remainder of this section is structured as follows. Subsec. 4.1.1 contains a

discussion of the continuum limit and gauge invariance. Subsec. 4.1.2 discusses the *Meissner* phase. In Subsec. 4.1.3 we address the *Rung Mott* transition within the Meissner state. Subsec. 4.1.4 addresses the stability of the *Rung Mott – Meissner* phase. In Subsec. 4.1.5 we introduce the condition that favors a low dimensional form of the *Laughlin* state.

4.1.1 Continuum limit and gauge invariance

In what follows we will derive a continuum, or bosonized form [75, 272, 273] of Eq. (4.1). We will be using the conventions of Ref. [75] throughout this chapter. The resulting field theory will allow us to treat interactions nonperturbatively and determine the possible ground states of the model in Eq. (4.1). We begin by expressing the boson annihilation operator as $\psi^\alpha(x) = b_{\alpha j}/\sqrt{a}$, when $x = ja$. Then the bosonic creation operator in chain α becomes, in terms of new bosonic fields θ and ϕ

$$(\psi^\alpha)^\dagger(x) = \sqrt{n_0^\alpha}\sum_p e^{i2p(n_0^\alpha \pi x - \phi^\alpha)} e^{-i\theta^\alpha(x)}. \tag{4.2}$$

We sum over all integers p. The field $\theta^\alpha(x)$ is the phase of the boson operator, whereas $\phi^\alpha(x')$ describes deviations from the mean density: $\delta n^\alpha \equiv n^\alpha - n_0^\alpha = -\frac{1}{\pi}\nabla\phi^\alpha$. The mean densities $n_0^{1,2}$ should be taken equal in practice, $n_0^{1,2} = n_0$. However, we shall keep the dependence on $n_0^{1,2}$ explicit to obtain more general expressions. The doublet θ, ϕ satisfies the algebra

$$\left[\phi^\alpha(x), \theta^\beta(x')\right] = i\frac{\pi}{2}\delta_{\alpha\beta}\mathrm{Sign}(x' - x). \tag{4.3}$$

For the ladder Hamiltonian it is convenient to introduce rotated fields

$$\theta^\pm = (\theta^1 \pm \theta^2)/\sqrt{2},\ \phi^\pm = (\phi^1 \pm \phi^2)/\sqrt{2}. \tag{4.4}$$

These obey the same algebra in (4.3) for the new indices $\alpha = \pm$. In this basis, the model (4.1) becomes

$$\mathcal{H} = \mathcal{H}_0^+ + \mathcal{H}_0^- + \mathcal{H}_{SG}. \tag{4.5}$$

The first and second terms are Luttinger liquid Hamiltonians [75] for the symmetric and antisymmetric sectors, respectively:

$$\mathcal{H}_0^+ = \frac{v^+}{2\pi}\int dx \left[K^+(\nabla\theta^+)^2 + \frac{1}{K^+}(\nabla\phi^+)^2\right], \tag{4.6}$$

$$\mathcal{H}_0^- = \frac{v^-}{2\pi}\int dx \left[K^-(\nabla\theta^- + A_\parallel^-)^2 + \frac{1}{K^-}(\nabla\phi^-)^2\right]. \tag{4.7}$$

$A_\parallel^-$ is a gauge field component whose line integral yields A_{ij}^α. It will be discussed shortly. Note that in our geometry the artificial gauge field only couples to the antisymmetric (pseudo spin) sector. Under rotation (4.4) velocities of excitations and Luttinger parameters are expressed as:

$$\begin{aligned} v^\pm &= v\left(1 \pm \frac{V_\perp K a}{\pi v}\right)^{1/2}, \\ K^\pm &= K\left(1 \pm \frac{V_\perp K a}{\pi v}\right)^{-1/2}. \end{aligned} \tag{4.8}$$

Eqs. (4.8) are valid in the limit of weakly coupled chains $g \ll t$. Note that a weak coupling Gross-Pitaevskii approximation of the bosonic operators in Eq. (4.2), followed by a gradient expansion, would allow us to identify $v = a\sqrt{tU}$ and $K = \sqrt{t/U}$ when $n_0^\alpha = \frac{1}{2a}$. However, for general microscopic parameters in (4.1), the Luttinger parameter satisfies $1 < K$ for repulsive interactions, $K = \infty$ for free bosons, $K < 1$ for repulsive long-range interactions, and $K = 1$ for the hard core limit [75].

The third term of Eq. (4.5) is a sine-Gordon (Josephson) Hamiltonian arising from the interchain coupling. Denoting the gauge field component in the y direction by $A_\perp$, the coupling Hamiltonian reads

$$\mathcal{H}_{SG} = -2g\sqrt{n_0^1 n_0^2}\int dx \cos(-\sqrt{2}\theta^- + a' A_\perp) \times \tag{4.9}$$

$$\left[1+2\cos\left(2\pi n_0^1 x-2\phi^1\right)\right]\,\left[1+2\cos\left(2\pi n_0^2 x-2\phi^2\right)\right].$$

n_0^α represent the mean density in each chain. The values of $A_\perp$, $A_\parallel$, n_0^α determine which contributions are to be considered from $\mathcal{H}_{SG}$, based on lattice commensuration conditions.

We used in Eq. (4.7) the antisymmetric combination of gauge fields

$$A_\parallel^- = \frac{A_\parallel^1 - A_\parallel^2}{\sqrt{2}}. \tag{4.10}$$

By convention, we require that the field $A_\parallel^\alpha(x)$ is related to the lattice gauge field A_{ij}^α of Eq. (4.1) by an average over a straight line path between sites j and $j+1$ on chain α:

$$\int_{ja}^{(j+1)a} dx A_\parallel^\alpha(x) = a A_{j,j+1}^\alpha. \tag{4.11}$$

Similarly, the component $A_\perp(x)$ appearing in Eq. (4.9) is related to $A_{\perp,i}$ of Eq. (4.1):

$$\int_{\text{rung at } i} dy A_\perp(y) = a' A_{\perp i}. \tag{4.12}$$

The integral is performed over a rung at position i, starting from chain 1 and ending on chain 2.

Ground state expectation values will only depend on the curl of the gauge field

$$\text{curl}A = \nabla A_\perp(x) - \frac{A_\parallel^2(x) - A_\parallel^1(x)}{a'}. \tag{4.13}$$

The lattice curl defines the flux through the plaquette

$$\text{curl}A = \frac{\chi}{a'}. \tag{4.14}$$

This equality defines the uniform flux perpendicular to the plane of the ladder. The plaquette enclosed between the rungs j and $j+1$ is threaded by flux $a\chi = aa'\text{curl}A$.

The Hamiltonian (4.5) is invariant under the gauge transformation

$$\tilde{A}^{\alpha}_{\parallel}(x) = A^{\alpha}_{\parallel}(x) + \nabla f^{\alpha}(x), \tag{4.15}$$

$$\tilde{A}_{\perp}(x) = A_{\perp}(x) + \frac{f^2(x) - f^1(x)}{a'}, \tag{4.16}$$

$$\tilde{\theta}^{\alpha}(x) = \theta^{\alpha}(x) - f^{\alpha}(x). \tag{4.17}$$

This preserves the algebra in Eq. (4.3).

In the following treatment, it is favorable to use the gauge

$$a' A_{\perp}(x) = \chi x, \;\; A^{\alpha}_{\parallel} = 0. \tag{4.18}$$

The Hamiltonian in Eq. (4.9) becomes

$$\mathcal{H}_{SG} = -2g\sqrt{n_0^1 n_0^2}\int dx \cos(-\sqrt{2}\theta^- + \chi x) \times \tag{4.19}$$
$$\left[1 + 2\cos\left(2\pi n_0^1 x - 2\phi^1\right)\right]\,\left[1 + 2\cos\left(2\pi n_0^2 x - 2\phi^2\right)\right].$$

We summarize the notations of the phases allowed by Eq. (4.19) in Tables 4.1 and 4.2. A detailed discussion follows, but we anticipate the possible ground states here (see Figure 4.2 for phase diagrams): At infinitesimal fluxes χ, the cosine θ^- establishes Josephson phase coherence between the chains (*Meissner* phase). When the flux per plaquette is high, the phases follow the variations of the gauge field, giving way to a *Vortex phase* . Turning to the charge sector, at filling factors satisfying $n_0^1 + n_0^2 = \frac{2N+1}{a}$, where N is nonnegative and integer, the cosine potential in ϕ^+ favors an insulating ground state for total rung density, denoted *Rung Mott* . At incommensurate fillings, this turns into a *Rung superfluid* . We will introduce another state which exists if repulsive long ranged interactions are present. This state corresponds to a combined pinning of phase and charge fluctuations. We will denote it *Laughlin* since it arises from a coupled wire construction [256] of the bosonic Laughlin state at $\nu = 1/2$ [8].

4.1.2 *Meissner* phase

The description of the phase diagram follows with the application of a two step renormalization group procedure. The renormalization group equations for Eq. (4.19) are solved in more detail in [266]. Here we provide an approximate solution which captures the essential physics.

First, we follow Ref. [252] and we focus on the term in Eq. (4.19) which is the most relevant in the renormalization group sense. This is a Josephson phase pinning between the two condensate phases θ^1 and θ^2:

$$\mathcal{H}_{SG} = -2g\sqrt{n_0^1 n_0^2}\int dx\ \cos(-\sqrt{2}\theta^- + \chi x). \tag{4.20}$$

The renormalization group treatment to second order in the coupling g is detailed in App. C. We assume that $\chi a \ll 1$ such that the oscillatory argument in Eq. (4.20) is negligible. We define the dimensionless coupling constant (in units of the bandwidth) $g^- \equiv \frac{ga}{v}$. It flows to strong coupling if its bare value is nonzero and if its scaling dimension $1/(2K^-)$ is less than 2. Assuming small temperatures $T \to 0$, the renormalization of the coupling constant g^- is stopped at energy scales equal to the gap associated with the Josephson phase pinning. Inverting the RG equation for g^-, the gap has the following expression

$$\Delta^- \sim \frac{v}{a}\left(g^-\right)^{\frac{1}{2-\frac{1}{2K^-}}}. \tag{4.21}$$

Here, we have approximated that K^- renormalizes insignificantly. Therefore Eq. (4.21) contains the bare coupling constant and Luttinger parameter.

For temperatures $k_B T < \Delta^-$, the field $\theta^-(x)$ is pinned to its classical value $\langle\theta^-(x)\rangle = \chi x/\sqrt{2}$, leading to a vanishing of the interchain current and a saturation of intrachain currents [252]. Eq. (4.21) implies that Josephson phase coherence between the chains occurs as soon as a nonzero tunneling matrix element g is turned on; moreover, the gap above this ground state is a power law in the bare coupling g. We identify this as the *Meissner* state. This phase is associated

with gapped excitations of the external gauge field [274]. We illustrate this in the present situation considering the action for θ^-. This is obtained easily from the Hamiltonian (4.7) and (4.19) by a Legendre transform [75] ($\beta = 1/k_B T$):

$$\begin{aligned} \mathcal{S} &= \mathcal{S}[\theta^-] + \mathcal{S}[A] + ..., \\ \mathcal{S}[\theta^-] &= \frac{K^-}{2\pi} \int dx \int_0^\beta d\tau \left[\frac{1}{v^-} (\partial_\tau \theta^-)^2 + v^- (\nabla \theta^- + A_\parallel^-)^2 \right] \\ &\quad -2g\sqrt{n_0^1 n_0^2} \int dx \int_0^\beta d\tau \cos(-\sqrt{2}\theta^- + a' A_\perp), \\ \mathcal{S}[A] &= \int dx \int_0^\beta d\tau \left[(\mathrm{curl} A)^2 + (\partial_\tau A)^2 \right]. \end{aligned} \tag{4.22}$$

We will not require the ϕ^+-dependent part of the action, hence the ellipsis in Eq. (4.22). For the Maxwell part of the action, $\mathcal{S}[A]$, we assume that appropriate dimensionful constants are absorbed in the derivatives.

Let us assume that quantum fluctuations are suppressed, amounting to neglecting contributions in $\partial_\tau \theta^-$ or $\partial_\tau A$. This assumption is justified if the temperature is large. The saddle point of the action corresponds to the classical ground state. The saddle point condition $\delta S/\delta\theta^- = 0$ implies that the following equations hold for the relative phase field

$$\begin{aligned} \nabla \theta_{sp}^- &= -A_\parallel^- \\ \theta_{sp}^- &= \frac{1}{\sqrt{2}} a' A_\perp. \end{aligned} \tag{4.23}$$

At the saddle point A is constrained to be a (lattice) gradient of the arbitrary scalar function θ_{sp}. Next, replace everywhere in Eq. (4.22) the fluctuating field θ^- by its saddle point value θ_{sp}^-. This is justified if g and the bandwidth $v^- K^- \sim at$ are large. To obtain the resulting action for the external gauge field, perform the gauge transformation (4.15), (4.16) with scalar $f^\alpha(x) = \theta_{sp}^\alpha$ [275]. The saddle point action becomes

$$\mathcal{S} = \frac{v^- K^-}{2\pi} \beta \int dx (\tilde{A}_\parallel^-)^2 - 2g\sqrt{n_0^1 n_0^2}\beta \int dx \cos(a' \tilde{A}_\perp)$$

$$+\beta \int dx (\mathrm{curl}\tilde{A})^2. \tag{4.24}$$

The Maxwell term does not change under the gauge transformation, however the action now contains mass terms which lead to a gapped dispersion of the modes of $\tilde{A}$. This result would have been analogously obtained by integrating out the gapped θ^- field, but the approach above (see [275]) is less tedious.

Our treatment of the ladder Meissner effect in a continuum limit is reminiscent of the Meissner state due to phase coherence across a long Josephson junction [276, 277].

4.1.3 *Rung Mott*

We now address the emergence of Mott behavior in the *Meissner* state. We are interested in odd mean particle number per rung, i.e.

$$n_0^1 + n_0^2 = \frac{2N-1}{a},\ N \text{ integer } \geq 1. \tag{4.25}$$

The lowest value $N = 1$ corresponds to the half-filled boson ladder with one particle every two sites. If Eq. (4.25) holds, Eq. (4.19) becomes

$$\mathcal{H}_{SG} = -2g\sqrt{n_0^1 n_0^2} \int dx\ \cos(-\sqrt{2}\theta^- + \chi x) \left[1 + 2\cos\left(\sqrt{8}\phi^+\right)\right].$$

We summarize the results of this section: in the absence of long ranged repulsive interactions, there is a Mott ground state only in the Tonks gas limit $U \to \infty$. It is protected by a gap which is exponentially small with respect to the Josephson coupling g. Away from the Tonks limit, the Mott phase is stable if finite repulsive interactions are turned on, in which case the Josephson gap is a power law of the coupling constant g.

We now proceed to a proof of these results. Under the energy scale Δ^- we may replace θ^- by its expectation value in Eq. (4.26). Then the effective Hamiltonian

at low energies $T < \Delta^-$ is

$$\mathcal{H}_{SG} = -4g\sqrt{n_0^1 n_0^2}\int dx \cos(\sqrt{8}\phi^+). \tag{4.26}$$

This term controls the Mott transition in the total density sector. Its scaling dimension is $2K^+$. If $K^+ < 1$, then this term as well flows to strong coupling, leading to the formation of the Mott gap

$$\Delta^+ \sim \Delta^-(g^+)^{1/(2-2K^+)}. \tag{4.27}$$

We defined the dimensionless quantity $g^+ = ga/v$.

The phase appearing at $T < \Delta^+$ is the Mott insulator with Meissner currents [69], *Rung Mott – Meissner* . Importantly, note that expression (4.27) holds if $K^+ < 1$, which generally corresponds to repulsive interactions of long range. These can come from intrachain repulsions or from some value of $V_\perp > 0$. If $V_\perp = 0$ in Eq. (4.1), then $K^+ = K$ and the Luttinger parameter $K < 1$ corresponds to long range repulsion of one-dimensional bosons [75].

At the special value $K = 1$ bosons experience hard-core interactions (the infinite interaction limit of the Tonks-Girardeau gas). The sine-Gordon term $\cos(\sqrt{8}\phi^+)$ is marginal, within our approximation of renormalization group equations. Then the Mott gap turns on exponentially but is nonvanishing even if g is infinitesimal [266]

$$\Delta^+ \sim \Delta^- e^{-\alpha t/g}. \tag{4.28}$$

The Tonks-Girardeau gas has been proved experimentally [278, 279].

We have found that $\Delta^+ \ll \Delta^-$, which requires very small measurement temperature for the observation of the Mott insulator. We have also concluded that the *Rung Mott* phase exists in the Tonks limit $U \to \infty$ or if longer ranged repulsive interactions are turned on. For large $V_\perp, U \gg t, g$, the model of Eq. (4.1) maps to a gauged spin-1/2 Hamiltonian describing the Mott insulator at unit filling and

in this case formally $\Delta^+ \gg \Delta^-$, as we show in Sec. 4.3. The *Rung Mott* gap can be estimated from mean field theory, and cross checked with numerically exact density matrix renormalization group methods. For these results, the interested readers may refer to App. G.

4.1.4 *Rung Mott – Meissner* stability

Assume that the conditions are met such that *Rung Mott – Meissner* is protected by a gap $\Delta^+ < \Delta^-$. We can define critical values for flux and chemical potential beyond which the Mott insulator with Meissner currents is not stable. We perform the canonical transformation $\theta^- \to \theta^- + \frac{\chi}{\sqrt{2}}x$. The resulting form of Eq. (4.20) will have no oscillatory phase in the sine-Gordon terms. On the other hand, Eqs. (4.7) and (4.6) will contain terms of the form $-\int dx \mu^- \nabla\theta^- - \int dx \mu^+ \nabla\phi^+$. For the gapped phase to be stable, we require that $\mu^\pm$ do not exceed the gaps $\Delta^\pm$. This results in the following critical values for field and doping

$$\begin{aligned} \chi_c &= \frac{\pi\sqrt{2}\Delta^-}{v^- K^-}, \\ \mu_c^+ &= \Delta^+. \end{aligned} \tag{4.29}$$

The *Rung Mott* state is stable for $\mu^+ < \mu_c^+$. The *Meissner* state is stable for $\chi < \chi_c$. Two transitions out of this phase are possible:

1. for $\chi > \chi_c$, the sine Gordon term in θ^- is irrelevant and the system enters a *Vortex phase* [252]. The transition out of the *Meissner* phase by increasing χ is of the commensurate-incommensurate type [280, 281, 282].

2. If $\mu^+ > \mu_c^+$, it is energetically favorable to add particles to the *Rung Mott* state. Due to the incommensuration, this is the *Rung superfluid* phase. The *Rung Mott* to *Rung superfluid* transition by variation of μ is also a commensurate-incommensurate transition.

We conclude that *Rung Mott – Meissner* is stable to small flux and density variations, which leads to the finite domain depicted in Fig. 4.2. The commensurate-

incommensurate phase transition obtained here upon increasing the flux beyond χ_c resembles an experimentally probed magnetic field induced phase transition in Zeeman-coupled spin ladders [283, 284].

4.1.5 *Laughlin* state at $\nu = \frac{1}{2}$

In order to energetically favor the *Laughlin* state, density will be allowed to deviate from odd integer filling per rung. However, this deviation will be necessarily (very close to) commensurate with the flux. Let us focus on the following terms of Eq. (4.19):

$$\begin{aligned}\mathcal{H}_{SG} &= -2g\sqrt{n_0^1 n_0^2}\int dx\big[\cos(-\sqrt{2}\theta^- + \chi x) \\ &\qquad +4\cos(-\sqrt{2}\theta^- + \chi x)\cos(2\pi n_0^1 x - 2\phi^1)\cos(2\pi n_0^2 x - 2\phi^2)\big] + ... \\ &= -2g\sqrt{n_0^1 n_0^2}\int dx\Big\{\cos\Big[-\sqrt{2}\theta^- + \sqrt{8}\phi^+ + \chi x - 2\pi(n_0^1 + n_0^2)x\Big] \\ &\qquad +\cos\Big[-\sqrt{2}\theta^- - \sqrt{8}\phi^+ + \chi x + 2\pi(n_0^1 + n_0^2)x\Big]\Big\} + ...\end{aligned} \tag{4.30}$$

The ellipsis in the first row represents terms containing only one of the factors $\cos(2\phi^1 - 2\pi n_0^1 x)$, $\cos(2\phi^2 - 2\pi n_0^2 x)$, $\cos[\sqrt{8}\phi^- - 2\pi(n_0^1 - n_0^2)x]$. We assume that $n_0^1 \approx n_0^2 \approx (2N+1)/(2a)$, where the approximate equality is such that all three factors are oscillatory and can be discarded. In the second row, we assume that $\chi > \chi_c$ such that $\cos(-\sqrt{2}\theta^- + \chi x)$ can be discarded as explained in Sec. 4.1.4.

Our purpose now is to tune flux and density such that one of the two terms in Eq. (4.31) stays relevant. The oscillatory argument in the first or second term of Eq. (4.31) vanishes if the following commensuration condition holds

$$a\left[2\pi(n_0^1 + n_0^2) \pm \chi\right] = 0 \bmod 2\pi. \tag{4.31}$$

Note that if the system is gapless any change in chemical potential results in doping $\frac{v^+}{\pi K^+}\delta^+ = -\mu^+$. Therefore condition (4.31) can be attained within the gapless *Rung superfluid – Vortex phase* by continuously changing flux and chemical potential.

If we pick the lower sign for Eq. (4.31), Eq. (4.31) reduces to

$$\mathcal{H}_{SG} = -2g\sqrt{n_0^1 n_0^2}\int dx \cos(-\sqrt{2}\theta^- + m\sqrt{2}\phi^+), \quad m = 2. \tag{4.32}$$

For a general integer m, Eq. (4.32) represents the correlated hopping term in the coupled chain construction of the $\nu = \frac{1}{m}$ Laughlin state [256, 271]. Terms with $m > 2$ have larger scaling dimension. In the following, we will provide some results as a function of m for generality.

In the case $m = 2$, the scaling dimension of Eq. (4.32) is $\delta = 1/(2K^-) + 2K^+$. At $V_\perp = 0$ this term is irrelevant unless long ranged interactions along the chains are present. The coupling constant g can become relevant in the presence of sufficiently large $V_\perp > 0$. The associated energy gap is

$$\Delta \sim \frac{v}{a}\left(\frac{ga}{v}\right)^{\frac{1}{2-1/(2K^-)-2K^+}}. \tag{4.33}$$

When the coupling is marginal, the gap has an exponential dependence on g as in Eq. (4.28). To summarize, the *Laughlin* state should be observable with sufficiently strong repulsive interactions $V_\perp$ (or sufficiently long range repulsive interactions along the chains). Otherwise, when the coupling constant g is irrelevant, a gap will still be observable in finite sized systems for a sufficiently strong bare value.

The addition of a particle spoils the commensuration between mean density and flux, and therefore the term of Eq. (4.32) becomes gapless. However, a finite chemical potential is required to add an extra particle to the system. We arrive therefore at stability conditions analogous to Eqs. (4.29). A "surplus" chemical potential $\delta\mu^+$ causing deviations in mean density from the background density which satisfies Eq. (4.31) must not exceed Δ

$$\delta\mu^+ < \delta\mu_c^+ = \Delta. \tag{4.34}$$

Moreover, a "surplus" flux that causes deviations from Eq. (4.31) must obey

$$\delta\chi < \delta\chi_c = \frac{\pi\sqrt{2}\Delta}{v^- K^-}. \tag{4.35}$$

A sketch of the possible region following from the present discussion is depicted on Fig. 4.2B. However, the clear delimitation of such a region depends on the details of the microscopic Hamiltonian. Note that another possibility would be to pick the upper sign in (4.31), yielding a state related to the one discussed above by particle-hole symmetry.

4.2 Observables

In this section we discuss various observable quantities that allow us to characterize the *Rung Mott – Meissner* and *Laughlin* phases. We begin with a definition of the lattice current operators and a lattice version of the flux quantization condition obtained from a Gross-Pitaevskii approximation of the boson operator, in Sec. 4.2.1. We continue with a discussion of current operators (Sec. 4.2.2), flux quantization (Sec. 4.2.3) and Hall responses from a Laughlin argument (Sec. 4.2.4) in the *Rung Mott – Meissner* phase. The analogous discussion for the *Laughlin* phase appears in Sec. 4.2.5. We discuss the gapless effective edge model of the *Laughlin* state in 4.2.6.

4.2.1 Current operator and lattice flux quantization

The flux quantization condition for a superfluid [80] relates the winding number of the boson phase around closed loops on the lattice with current circulation and flux. We begin by fixing the definition for lattice current. Assuming a generic quadratic Hamiltonian in the form $H = \sum_{ij} |t_{ij}| e^{i\phi_{ij}} b_i^\dagger b_j$, the current operator is obtained from the Heisenberg equation of motion $\dot{n}_i = i[H, n_i] \equiv \sum_j j_{ij}$, where

$$j_{ij} = -i|t_{ij}| e^{i\phi_{ij}} b_i^\dagger b_j + \text{H.c.} \tag{4.36}$$

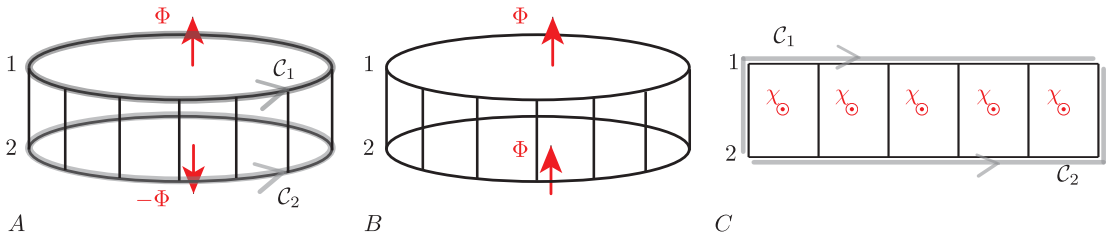

Figure 4.3: Two leg ladder. **A:** Periodic boundary conditions. Closed loops $\mathcal{C}_1$ and $\mathcal{C}_2$ traverse chains 1 and 2 in the counter-clockwise direction. $\Phi = L\chi/2$ is the net flux per chain. **B:** An Aharonov-Bohm flux through the periodic geometry. **C:** The same flux can be achieved with open boundary conditions by threading flux χ per plaquette.

For a bond $b \equiv ij$, where i and j denote sites, the current operator j_{ij} measures the number of particles per unit time flowing from site j into site i. Consider now a loop on the lattice, denoted by the sequence of bonds $\mathcal{C} = b_0, b_1, \ldots$. In a superfluid, writing boson creation operators as $b_i^\dagger \approx \sqrt{n_0} e^{-i\theta_i}$, neglecting density fluctuations, and expanding for small gauge invariant phases $-\theta_i + \theta_j + \phi_{ij}$, we obtain the following condition for any closed loop $\mathcal{C}$ on the lattice.

$$\sum_{b\in\mathcal{C}} \frac{1}{2|t_b|n_0}\langle j_b\rangle + \Phi_{\mathcal{C}} = 2\pi N_{\mathcal{C}}. \tag{4.37}$$

We have defined t_b as the hopping integral on bond b. The phase $\Phi_{\mathcal{C}} = \sum_{b\in\mathcal{C}} \phi_b$ corresponds to the line integral of the gauge field along curve $\mathcal{C}$. The winding number of the boson phase field around $\mathcal{C}$ is denoted by the integer $N_{\mathcal{C}}$. Eq. (4.37) is the flux quantization condition for a lattice, which is consistent with the continuum result [80].

4.2.2 Current operators in the *Rung Mott – Meissner* phase

We begin by computing the current expectation values in the *Rung Mott – Meissner* phase. The boson current operator is obtained from the following Heisenberg equation

$$i[\mathcal{H}, -\frac{1}{\pi}\sqrt{2}\nabla\phi^-(x)] = \frac{d}{dt}(n_1 - n_2), \tag{4.38}$$

which can be separated into interchain and intrachain current operators

$$\begin{aligned} j_\perp &= 2\frac{g}{\pi a}\sin\left(\sqrt{2}\theta^- - \chi x\right), \\ j_\parallel &= j_\parallel^1 - j_\parallel^2 = -v^- K^- \sqrt{2}\nabla\theta^-. \end{aligned} \tag{4.39}$$

Whenever the relative phase between the chain condensates is pinned, *i.e.* for energy scales below Δ^-, we find

$$\langle j_\perp(x)\rangle = 0, \tag{4.40}$$

$$\langle j_\perp(x) j_\perp(0)\rangle_{connected} = 0,$$

$$\langle j_\parallel(x)\rangle = -at\chi. \tag{4.41}$$

That is, "bulk" currents vanish, and so do their fluctuations for x larger than the correlation length associated with the Josephson gap $\xi^- = v^-/\Delta^-$. Counterflowing "edge" currents have a difference $-2ta^2 n_0 \chi$, where $n_0 = \frac{1}{2a}$ is the mean boson density per chain. We remark that the form of the current operator expectation value, Eq. (4.41), changes in the strong coupling limit $U, V_\perp \gg t, g$, where (see Ref. [69] and Sec. 4.3) at second order in perturbation theory $j_\parallel(x) = -2a(t^2/V_\perp)\chi$. In either the weak or the strong coupling regime, current $j_\parallel$ persists in the Mott phase, where the field ϕ^+ is pinned to the classical value $\langle\phi^+\rangle = 0$. In addition, this phase exhibits vanishing density fluctuations

$$\langle (n^1 + n^2)(x)(n^1 + n^2)(0)\rangle_{connected} = 0, \tag{4.42}$$

for all x greater than the correlation length $\xi^+ = v^+/\Delta^+$, as a consequence of the pinning of the field $\phi^+(x)$ in the minimum of the cosine potential [75].

4.2.3 Flux quantization in the *Rung Mott – Meissner* phase

The current expectation values obtained in Eq. (4.39) obey a flux quantization condition similar to Eq. (4.37). Consider that the loop is the boundary of the

cylinder formed by the two periodic chains. In Figure 4.3A this is $\mathcal{C} = \mathcal{C}_1 - \mathcal{C}_2$, where the minus sign means that $\mathcal{C}_2$ is traversed in reverse. Then, using Eq. (4.39) in (4.37) we obtain the following expression

$$2\pi N_{\mathcal{C}_1-\mathcal{C}_2} = \frac{1}{at}\int_0^{La} dx\langle j_\parallel^1 - j_\parallel^2\rangle + La\chi = 0. \tag{4.43}$$

The second equality follows from (4.41). The vanishing winding number of the superfluid phase is a signature of the Meissner effect.

Let us now realize flux χ per plaquette via the choice $A^1_{j,j+1} = -A^2_{j,j+1} = \chi/2$ in Eq. (4.1). With this choice, there is no net flux parallel to the axis of the cylinder, as depicted in Figure 4.3A. Writing the condition in Eq. (4.37) for each path $\mathcal{C}_1$ and $\mathcal{C}_2$ and using Eq. (4.43), we find

$$\begin{aligned} 2\pi N_{\mathcal{C}_1} &= \frac{1}{at}\int_0^{La} dx\langle j_\parallel^1\rangle + La\chi/2 \\ &= 2\pi N_{\mathcal{C}_2} = \frac{1}{at}\int_0^{La}\langle j_\parallel^2\rangle - La\chi/2. \end{aligned} \tag{4.44}$$

Eq. (4.44) represents the flux quantization condition in our setup. While Eq. (4.44) holds for periodic boundary conditions, little changes qualitatively for open boundaries, with the loop $\mathcal{C}_1 - \mathcal{C}_2$ as in Figure 4.3C. For a loop surrounding the ladder, there will be $O(1/L)$ corrections, due to rung currents appearing at the open boundaries. In general, the flux quantization provides a way to measure the winding of the phase of the boson wavefunction from current measurements, and detect the presence of vortices in the sample.

4.2.4 σ_{xy} from the Laughlin argument in the *Rung Mott – Meissner* phase

The Hall response is vanishing in the *Rung Mott – Meissner* phase. Suppose a current $j_\parallel^1 = j_\parallel^2$ is generated along the horizontal direction in Figure 4.1. A "voltage drop" to realize such a current can be realized by tilting both chains

in the same direction, or by adiabatically threading a flux quantum between the chain ends as depicted in Figure 4.3B [104, 105]. If $\sigma_{xy} \neq 0$, the response to this must be a perpendicular flow of current amounting to a quantized charge after a full period [285]. There is a converse situation, a tilt between the chains would cause a uniform $\langle j_\parallel^1 + j_\parallel^2 \rangle \neq 0$. However, since from Eq. (4.39) the commutator of operators $j_\perp$ and $j_\parallel^{1,2}$ vanishes, the Kubo formula for the conductivity implies

$$\sigma_{xy} = 0. \tag{4.45}$$

This result is expected as the *Rung Mott – Meissner* phase is fully gapped.

4.2.5 Local probes of the *Laughlin* phase

Similarly, we compute bosonic particle currents in the *Laughlin* phase. The plaquette currents of the bosonic particles are

$$\begin{aligned} j_\perp &= 2\frac{gn_0}{\pi} \sin\left(\sqrt{2}\theta^- - m\sqrt{2}\phi^+\right), \\ j_\parallel &= j_\parallel^1 - j_\parallel^2 = -v^- K^- \sqrt{2}\nabla\theta^-. \end{aligned} \tag{4.46}$$

These lead to the following expectation value in the gapped phase

$$\langle j_\perp \rangle = 0, \tag{4.47}$$

i.e. bulk currents vanish. Moreover, since charge deviations from the mean value, $-\frac{1}{\pi}\nabla\phi^+(x)$, must vanish when integrated over the entire system, equation (4.46) and the pinning condition $\langle \nabla\theta^- \rangle = m\langle \nabla\phi^+ \rangle$ imply that the circulation of current along the contour $\mathcal{C}_1 - \mathcal{C}_2$ in Figure 4.3 vanishes:

$$\frac{1}{t}\int_0^{La} dx \langle j_\parallel \rangle = \frac{1}{t}\left[\int_0^{La} dx \langle j_\parallel^1 \rangle - \int_0^{La} dx \langle j_\parallel^2 \rangle\right] = 0. \tag{4.48}$$

The contrast between Eq. (4.48) and Eq. (4.43) can be used to distinguish between the *Laughlin* and *Rung Mott – Meissner* phases. Moreover, in the vicinity of the flux and density commensurate line we expect that the current takes the following special form

$$\int_0^{La} dx\langle j_\parallel\rangle = -v^- K^- \left[\chi - 2\pi(n_0^1 + n_0^2)\right], \tag{4.49}$$

i.e. it is a linear function in flux or in mean density that vanishes at $\chi = 2\pi(n_0^1 + n_0^2)$. The observables discussed here constitute local probes which can be used to discern the *Laughlin* phase in experiment.

4.2.6 Chiral edge modes in the *Laughlin* phase

In this subsection we discuss the structure of the edge theory when the bulk term of Eq. (4.32) produces a gap. Let us define [256, 271] new chiral fields in the form

$$\phi_r^\alpha = \theta^\alpha/m + r\phi^\alpha \tag{4.50}$$

for left ($r = -1$) and right ($r = +1$) moving excitations in chain $\alpha = 1, 2$. The following commutation relations follow from the algebra in Eq. (4.3),

$$[\phi_r^\alpha(x), \phi_{r'}^\beta(x')] = ir\frac{\pi}{m}\delta_{rr'}\delta_{\alpha\beta}\mathrm{Sign}(x' - x). \tag{4.51}$$

The algebra of the chiral modes in Eq. (4.51) implies that the momentum associated with $\phi_r^\alpha(x)$ is

$$\Pi_r^\alpha(x) \equiv \frac{m}{2\pi r}\nabla\phi_r^\alpha(x). \tag{4.52}$$

Let us define new density and phase fields for the bulk, respectively:

$$\phi = (-\phi_{-1}^1 + \phi_{+1}^2)/2, \theta = (\phi_{-1}^1 + \phi_{+1}^2)/2. \tag{4.53}$$

These are related to the original fields $\theta^{\pm}, \phi^{\pm}$ through

$$\phi = -\frac{\sqrt{2}}{2m}\theta^{-} + \frac{\sqrt{2}}{2}\phi^{+},\ \theta = \frac{\sqrt{2}}{2m}\theta^{+} - \frac{\sqrt{2}}{2}\phi^{-}. \tag{4.54}$$

These fields obey the Kac-Moody algebra

$$[\phi(x), \theta(x')] = i\frac{\pi}{2m}\mathrm{Sign}(x' - x). \tag{4.55}$$

Using the new bulk variables we define the "bulk" charge density $n = -\frac{1}{\pi}\nabla\phi$, whereas the quasiparticle density is given by $n_{\mathrm{QP}} = -\frac{m}{\pi}\nabla\phi$. A kink of 2π in the field $2m\phi$ corresponds to the creation of one Laughlin quasiparticle. The correlated hopping term Eq. (4.32) pins the left chiral field of chain 1 to the right chiral field of chain 2:

$$\mathcal{H}_{SG} = -2gn_0 \int dx \cos(2m\phi). \tag{4.56}$$

The full Hamiltonian is given by

$$\mathcal{H}[\phi(x), \theta(x), \phi^{1}_{+1}(x), \phi^{2}_{-1}(x)] = \mathcal{H}_0^{+} + \mathcal{H}_0^{-} + \mathcal{H}_{SG}. \tag{4.57}$$

with $\mathcal{H}_{SG}$ specified in Eq. (4.56) and $\mathcal{H}_0^{\pm}$ as in Eqs. (4.7,4.6).

It is possible to obtain the effective low energy theory of the remaining two gapless chiral modes $\phi_{+1} \equiv \phi^{1}_{+1}$ and $\phi_{-1} \equiv \phi^{2}_{-1}$. The detailed calculation is given in App. F. The result of integrating out the massive field ϕ is a generic Luttinger liquid

$$4\pi\mathcal{L}_{edge} = \int dx \left(\dot{\phi}_r K_{rr'} \nabla\phi_{r'} - \nabla\phi_r V_{rr'} \nabla\phi_{r'}\right). \tag{4.58}$$

The matrix $K_{rr'} = m\, r\delta_{rr'}$ is determined by Eq. (4.52). It describes two counter-propagating modes on distinct edges of the Laughlin state $\nu = \frac{1}{m}$ [286, 3].

Note however that Eq. (4.58) does *not* describe a chiral Luttinger liquid. The matrix $V_{rr'}$ is nonuniversal and has nonvanishing off-diagonal elements. These

terms describe backscattering between the chiral fields. We provide the explicit form of $V_{rr'}$ in App. F. The resulting Luttinger parameter K_{edge} engenders a more complex charge fractionalization phenomenon [287, 288, 289, 290, 291]. Interestingly, when backscattering terms between the edges are suppressed, current noise between the edges probes the fractional charge of bulk quasiparticles [292]. This has been demonstrated experimentally [293, 294], in the two-dimensional electron gas. Such experiments are feasible as well in ultracold atom systems, where quantum point contacts have already been realized [295, 296, 297].

Let us consider briefly the case of N chains with the same coupling Eq. (4.32) between consecutive chains. Backscattering terms between the chiral edge modes, ϕ^1_{+1} and ϕ^N_{-1} vanish exponentially fast with N. The remaining action describes the edge degrees of freedom. It consists of a chiral Luttinger liquid

$$4\pi\mathcal{L}_{edge} = \sum_{r=\pm 1} \int dx \left[mr\dot{\phi}_r \nabla\phi_r - v(\nabla\phi_r)^2 \right]. \tag{4.59}$$

If the bulk were a continuous two dimensional manifold, this edge theory would correspond to the bulk Chern Simons theory [298]

$$4\pi S[\mathcal{A}] = \frac{1}{m} \int dxdydt\ \epsilon^{\mu\nu\rho}\delta\mathcal{A}_\mu\partial_\nu\delta\mathcal{A}_\rho \tag{4.60}$$

for the external gauge field. $\delta\mathcal{A} = \mathcal{A} - A$ is the deviation of the dynamical gauge field from the fixed background field A. $\epsilon^{\mu\nu\rho}$ is the Levi-Civita symbol. The relation between this bulk Chern-Simons theory and the edge theory is established by requiring that the action defined over a two-dimensional manifold with boundary be gauge invariant.

We stress again that the underlying assumption of this discussion was that the coupling constant in (4.32) was relevant, which occurs for sufficiently strong $V_\perp$ or sufficiently long ranged repulsive intrachain interaction. However, in finite sized systems, a gap can still be associated with (4.32) if g is larger or comparable to the energy scale of the bandwidth, set by the intrachain hopping t.

4.3 Strong coupling expansion in the *Rung Mott* phase

Let us briefly return to the treatment of the *Rung Mott – Meissner* state in Sections 4.1.3, 4.1.4 where we have determined that $\Delta^+ \ll \Delta^-$ at weak $V_\perp$. We expect, however, that for $V_\perp, U \gg t, g$ in model (4.1) there is enough repulsive interaction whenever two particles reside on the same rung of the ladder such that a Mott insulator at 1 particle per rung is protected by a significant energy gap $\Delta^+ \gg \Delta^-$. In this section we use a low–energy gauged spin-1/2 Hamiltonian describing the Mott insulator at unit filling to arrive at a phase diagram which is consistent with the one obtained so far.

A spin–$\frac{1}{2}$ model with gauge fields describes the low–energy states in the limit of strong interactions (for a derivation, see App. H). Such models have been derived previously for the fermionic Hubbard model or for the boson Hubbard model with two species [299, 300, 301, 302, 303, 304]. In our case, the particles on chains 1 and 2 are the Schwinger bosons in the representation of spin–$\frac{1}{2}$ operators. The relative density corresponds to $\sigma_i^z = b_{1i}^\dagger b_{1i} - b_{2i}^\dagger b_{2i}$. As demonstrated in boson language, σ_z fluctuates in the Mott phase. This is due to a transverse magnetic field in the $x-y$ plane, $-g\cos(a'A_{\perp i})\sigma_i^x + g\sin(a'A_{\perp i})\sigma_i^y$. (We have used $\sigma^x = b_1^\dagger b_2 + \text{H.c.}$ and $\sigma_y = -ib_1^\dagger b_2 + \text{H.c.}$). The effective Hamiltonian describing the Mott insulator at unit rung filling is:

$$H_\sigma = -\sum_{\langle ij\rangle}\left[2J_{xx}(\sigma_i^+\sigma_j^- e^{i\sqrt{2}aA_{ij}^-} + \text{H.c.}) - J_z\sigma_i^z\sigma_j^z\right] \\ -g\sum_i\left[\sigma_i^x\cos(a'A_{\perp i}) - \sigma_i^y\sin(a'A_{\perp i})\right], \tag{4.61}$$

with $J_{xx} = \frac{t^2}{V_\perp}$ and $J_z = t^2\left(-\frac{2}{U} + \frac{1}{V_\perp}\right)$, and $\sqrt{2}A_{j,j+1}^- = A_{j,j+1}^1 - A_{j,j+1}^2$. Setting $V_\perp = U/2$ or $J_z = 0$ yields the gapless XY phase of Eq. (4.61) and the Heisenberg antiferromagnetic chain is reached for $U \to +\infty$. In the absence of gauge fields, the XY term is ferromagnetic. For experimentally feasible values the Ising term

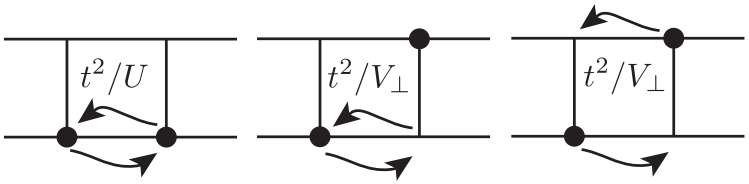

Figure 4.4: Virtual doubly occupied states leading to the spin–1/2 model (4.61). The Ising term consists of a ferromagnetic contribution proportional to t^2/U and an antiferromagnetic piece $\propto t^2/V_\perp$, whose prefactors are fixed by the possible situations of two particles on two neighboring rungs. The XY exchange term in the third panel is proportional to $t^2/V_\perp$.

is antiferromagnetic ($J_z > 0$). Equation (4.61) can be deduced from the graphic representation of virtual doubly occupied excited states in Fig. 4.4.

To bosonize (4.61) in one dimension, express the spin–$\frac{1}{2}$ operators in terms of fermion field operators via the Jordan–Wigner transformation [75] $\sigma_i^+ = c_i^\dagger e^{i\pi \sum_{j<i} c_j^\dagger c_j}$, $\sigma_z^i = 2c_i^\dagger c_i - 1$. The resulting Hamiltonian for fermions is

$$\begin{aligned} H_\sigma = \quad & -\sum_i \left[2J_{xx}(c_i^\dagger c_{i+1} e^{ia\chi} + \text{H.c.}) + 4J_z(c_i^\dagger c_i - 1/2)(c_{i+1}^\dagger c_{i+1} - 1/2) \right] \\ & -\sum_i g e^{i\pi \sum_{j<i} c_j^\dagger c_j}(c_i^\dagger + c_i). \end{aligned} \tag{4.62}$$

The free part of the Hamiltonian corresponds to dispersion relation $\epsilon_k = -4J_{xx}\cos(ka - \chi)$ and Fermi velocity $v_F = |4aJ_{xx}|$. The Fermi wavevectors are $k_F = \pm\frac{\pi}{2a} + \chi$ for the half-filled band. The Ising term for spins maps to nearest–neighbor interactions for the fermions. The low–energy spectrum is then described by a continuum bosonic theory as before. Introducing fields $\phi_\sigma, \theta_\sigma$ with commutator $[\phi_\sigma(x), \theta_\sigma(x'),] = i\frac{\pi}{2}\text{Sign}(x' - x)$, the continuum Hamiltonian is

$$\begin{aligned} H_\sigma &= \frac{1}{2\pi}\int dx \left[v_\sigma K_\sigma (\nabla\theta_\sigma - A^\sigma)^2 + \frac{v_\sigma}{K_\sigma}(\nabla\phi_\sigma)^2 \right] \\ &- \frac{2J_z}{(\pi^2 a)}\int dx \cos(4\phi_\sigma) \\ &- \frac{2g}{\sqrt{2\pi}a}\int dx \cos\left[\theta_\sigma(x) + a' A_\perp\right]\left[1 + (-1)^{\frac{x}{a}}\cos 2\phi_\sigma(x)\right]. \end{aligned} \tag{4.63}$$

The sine-Gordon term in (4.63) has been approximated by keeping only $q \sim 0$

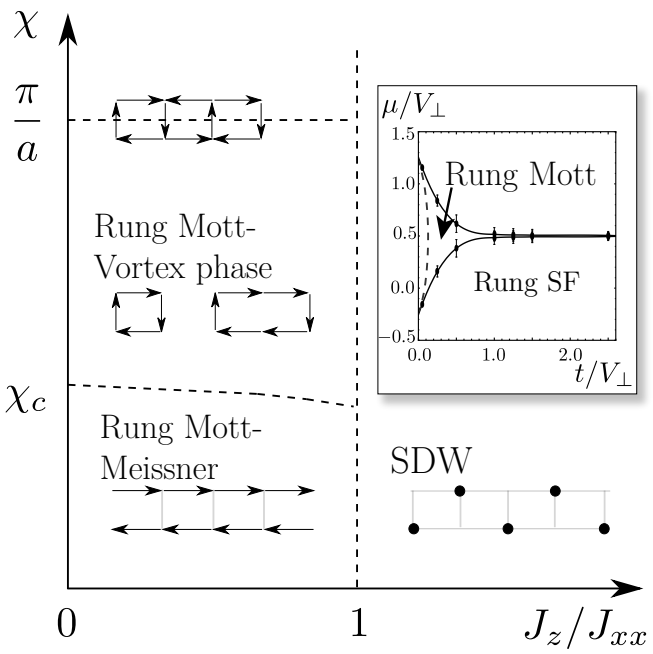

Figure 4.5: Phase diagram for the strong coupling XXZ model (4.61). In the XY limit, there is a spin–Meissner phase or a vortex phase (the direction of current patterns is shown in each phase). The inset shows the *Rung Mott* lobe at one boson per rung $n_0 = \frac{1}{2a}$, obtained using DMRG for the one–dimensional model. The dashed line is the mean-field theory result.

terms in the density operators. The speed of sound is $v_\sigma = v_F \left[1 + 16aJ_z/\pi v_F\right]^{\frac{1}{2}}$; the Luttinger parameter $K_\sigma = \left[1 + 16aJ_z/\pi v_F\right]^{-\frac{1}{2}}$ is a measure of interaction strength. $K_\sigma = 1$ for the XY limit and decreases as antiferromagnetic $J_z > 0$ is turned on.

We now turn to the phase diagram in Fig. 4.5. Whenever $J_z > J_{xx}$, dominant Ising interactions induce an antiferromagnetic spin density wave and current expectation values vanish. The corresponding inset shows a charge density wave of the bosons $b_{1,2}$, depicted as localized in the two layers. The ϕ_σ-dependent sine-Gordon term is irrelevant if $K_\sigma > \frac{1}{2}$, or $J_z < J_{xx}$. The remaining sine-Gordon term is $\propto g \cos\left(\theta_\sigma + \chi x\right)$, where we have chosen the Landau gauge with all flux on the conversion term. At small flux and for $K_\sigma > \frac{1}{8}$, g flows to strong-coupling, and it is associated with the following energy gap

$$\Delta_\sigma \sim \frac{u_\sigma}{a} \left(\frac{ga}{v_\sigma}\right)^{\frac{1}{2-\frac{1}{4K_\sigma}}} . \tag{4.64}$$

As before, Eq. (4.64) is derived in perturbation theory in $g \ll J_{xx}$ (see App. C). For nonzero fluxes χ, Δ_σ defines the critical flux χ_c at which the system undergoes a commensurate–incommensurate transition to a vortex phase. Below χ_c, the ground state is the spin–Meissner Mott state, characterized by zero interspecies current, and counterflowing intraspecies currents. The correlator $\langle \sigma^+(x)\sigma^-(0)\rangle \sim \langle e^{-i\theta_\sigma(x)} e^{+i\theta_\sigma(0)}\rangle \sim \langle e^{-i\theta_\sigma(x)}\rangle\langle e^{i\theta_\sigma(0)}\rangle$ is asymptotically constant at large distances. This situation corresponds to XY order polarized (definite $\langle\theta_\sigma\rangle$) due to the in–plane field g. The current operator expectation value in this phase can be calculated as [69],

$$\langle j_\parallel\rangle = -2J_{xx}\sin(a\chi) \approx -2J_{xx}a\chi, \tag{4.65}$$

which is to be compared with the weak–coupling result (4.41).

Above the critical field χ_c we obtain the *Rung Mott – Vortex phase* . When flux is at half the elementary flux per plaquette, $\chi = \pi/a$, the sine-Gordon term oscillates $(-1)^{\frac{x}{a}} g\cos(\theta_\sigma)$ and is naively irrelevant, but at second order in perturbation theory the oscillatory part disappears and the contribution is proportional to $-\frac{g^2}{u_\sigma}\cos(2\theta_\sigma)$ (see App. E). This pins the field θ_σ to one of two minima 0 or π resulting in the "orbital antiferromagnet" staggered current configuration $\langle j_\perp(x)\rangle \propto (-1)^{\frac{x}{a}}$.

4.4 Hybrid fermion–Cooper pair analogues

In this section we prove that spinful fermions on the lattice of Fig. 4.1 have ground states analogous to those of bosons presented in Sec. 4.1. This model, in the absence of gauge fields, was introduced in Ref. [305] to qualitatively describe the pseudo-gap phase of high-Tc superconductors [modeled as "hot spots" with preformed Cooper pairs and "cold spot" Fermi arcs [306, 307, 308, 309, 310, 311, 312, 313, 314] as shown in Fig. 4.7b)]. We note that recently novel features in high-Tc superconductors with magnetic fields or in relation with density wave order have been discussed [315, 316, 317, 318, 319, 320, 321, 322].

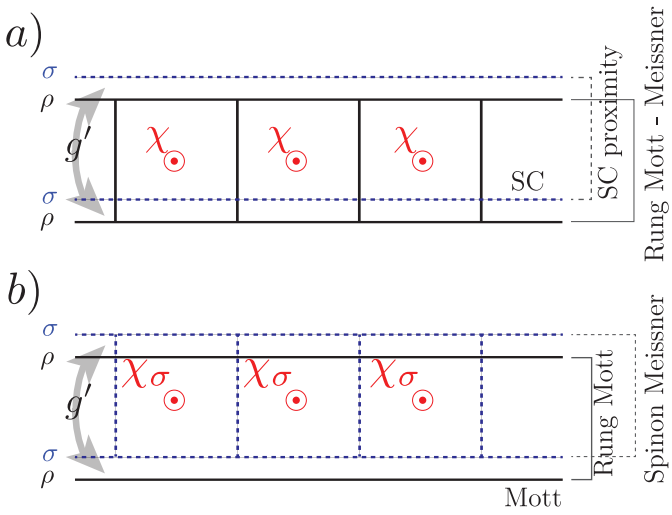

Figure 4.6: Possible coupling schemes for a fermion ladder: a) The Cooper pair *Rung Mott – Meissner* state is realized by starting with superconductivity in 1. The proximity effect induces superconductivity in chain 2, via a term labeled *SC proximity effect* (see Table 4.3). At lower energy scales, the *Rung Mott – Meissner* (or depending on filling and flux any other state of Table 4.3) forms. b) Dual model: Starting with MI in chain 1, the proximity effect makes chain 2 insulating, via a *Rung Mott* term. At lower energy scales, the spin sector is in the *Spinon Meissner* phase.

Sector	Notation	Phase description sine-Gordon term
ρ,+	*Rung Mott*	$2\phi_\rho^+$
ρ,+	*Rung superfluid*	$2\phi_\rho^+ + 2(k_F^1 + k_F^2)x$
ρ,-	*Meissner*	$2\theta_\rho^-$
ρ,-	*Vortex phase*	$2\theta_\rho^- - 2\chi x$
ρ,+& -	*Laughlin*	$2\theta_\rho^- - 2\phi_\rho^+$
σ,+	*SC proximity effect*	$2\phi_\sigma^+$
σ,-	*Spinon Meissner*	$2\theta_\sigma^-$
σ,+&-	*Laughlin*	$2\theta_\sigma^- - 2\phi_\sigma^+$

Table 4.3: The analogue of Table 4.1 listing the ordering tendencies of the hybrid fermion–Cooper pair ladder and the corresponding sine–Gordon terms generating gaps in each sector.

There exists a rich literature on the topic of two-leg fermion ladders [323]. For spinless fermions, a striking phenomenon in the presence of magnetic field is the existence of the orbital antiferromagnetic phase, (also called d–density wave [324], or staggered flux phase of the mean-field Hamiltonian proposed by Affleck and Marston [325, 326] introduced in the context of high-T_c superconductivity) coexisiting with the bond-density wave [327, 323, 328]. Carr and Tsvelik [329] studied the model of spin-gapped chains coupled by Josephson terms in magnetic fields and found competing charge density wave and superconducting correlations. Roux *et al.* [330] have studied the magnetic orbital effect in doped two-leg spinful fermionic ladders and found a reentrant transition into a spin gapped phase at high magnetic flux. More recently, it was argued that the ground state of a ladder of spinful fermions with ring exchange interaction has a d-wave metal ground state, which is analogous to the composite Fermi-liquid description of the half-filled Landau level [331].

We summarize the main results in this section: If superconducting correlations dominate, ground states analogous to those of Sec. 4.1 occur. The Cooper pair *Rung Mott – Meissner* ground state is separated by a finite gap from the rest of the spectrum. This gap depends on the interchain coupling g like a power law even when long range repulsive interactions are off. If charge density wave correlations dominate, as happens when each chain is at half filling, then superfluidity and the Meissner effect can occur in the spinon sector. To aid throughout the discussion, Table 4.3 lists the phases encountered in this section, along with the relevant charge or spin sector, and terms in the Hamiltonian inducing the particular order.

We start with a microscopic tight-binding model of spinful fermions with Hubbard interactions on the same ladder lattice of Fig. 4.1.

$$\begin{aligned} H &= H_1 + H_2 + H_\perp \\ H_\alpha &= \sum_{\sigma i} \left[-t c^\dagger_{\alpha\sigma}(i) c_{\alpha\sigma}(i+1) + \text{H.c.} \right] \\ &\quad + \sum_i U_\alpha n_{\alpha\uparrow}(i) n_{\alpha\downarrow}(i) \end{aligned}$$

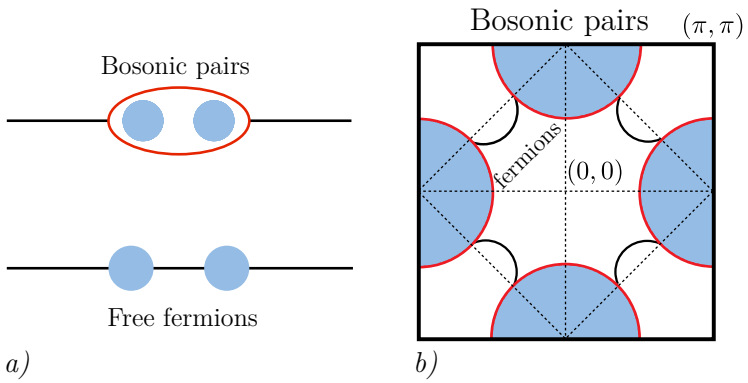

Figure 4.7: Hybrid two-leg ladder system introduced in Ref. [305] with preformed Cooper pairs in one chain and repulsive fermions in the other chain. Here, we extend the model by discussing magnetic field effects.

$$H_\perp = \sum_{\sigma i} \left[-g e^{ia' A_{\perp i}} c^\dagger_{1\sigma}(i) c_{2\sigma}(i) + \text{H.c.} \right]. \tag{4.66}$$

The operator $c^\dagger_{\alpha\sigma}(i)$ creates a fermion of spin $\sigma =\uparrow$ or $\downarrow$ on chain $\alpha = 1$ or 2 at site i, and $n_{\alpha\sigma}(i) = c^\dagger_{\alpha\sigma}(i) c_{\alpha\sigma}(i)$ is the fermion number operator. In Eq. (4.66) we consider periodic boundary conditions, so the summations run from $i = 1$ to L with $L + 1 \equiv 1$.

To study the possible phases of this system it is again convenient to use bosonization. We assume that interchain coupling is small. The basis suitable for expressing the continuum Hamiltonian consists of field operators $\psi^\alpha_\sigma(x) = c_{\alpha\sigma}(j)/\sqrt{a}$. In the free particle model, we assume that Fermi momenta k^α_F, the coupling g, and the flux per plaquette χ are chosen such that the Fermi surface contains two points. We approximate the spin s fermion field operator as a sum over right-moving and left-moving contributions at the two Fermi points,

$$\psi^\alpha_s(x) = \psi^\alpha_{+,s}(x) + \psi^\alpha_{-,s}(x), \tag{4.67}$$

with $s = \pm 1$ denoting the two spin species. Next, it is necessary to introduce bosonic fields describing charge degrees of freedom, $\phi^\alpha_\rho(x)$, $\theta^\alpha_\rho(x)$; and spin degrees of freedom, $\phi^\alpha_\sigma(x)$, $\theta^\alpha_\sigma(x)$. Each pair of operators obeys the algebra in Eq. (4.3), and either one of the ρ fields commutes with the σ fields. The chiral fermion

operators in Eq. (4.67) are [75]:

$$\psi^{\alpha}_{r,s}(x) = \frac{U^{\alpha}_{r,s}}{\sqrt{2\pi a}} e^{irk^{\alpha}_F x} e^{-\frac{i}{\sqrt{2}}\left[r\phi^{\alpha}_{\rho}(x) - \theta^{\alpha}_{\rho}(x) + s(r\phi^{\alpha}_{\sigma}(x) - \theta^{\alpha}_{\sigma})\right]} \tag{4.68}$$

for $\alpha = 1, 2$, $r = \pm 1$. $U_{r,s}$ are Klein factors enforcing Fermi statistics. For our purposes it is sufficient to neglect their contribution and replace them by unity. We have denoted the Fermi momentum in chain α by k^{α}_F. The continuum limit Hamiltonian corresponding to Eq. (4.66) is

$$\begin{aligned} \mathcal{H} &= \mathcal{H}_1 + \mathcal{H}_2 + \mathcal{H}^I_{\perp} \\ \mathcal{H}_{\alpha} &= \mathcal{H}^{\alpha}_{0\rho} + \mathcal{H}^{\alpha}_{0\sigma} + \frac{U_{\alpha}}{2\pi^2 a} \int dx \cos(\sqrt{8}\phi^{\alpha}_{\sigma}). \end{aligned} \tag{4.69}$$

The Hamiltonians $\mathcal{H}^{\alpha}_{0\rho}$ and $\mathcal{H}^{\alpha}_{0\sigma}$ represent Luttinger liquids [see Eq. (4.6)] with sound velocities and Luttinger parameters given by [75]:

$$\begin{aligned} K^{\alpha}_{\rho} = 1/\sqrt{1 + \frac{U_{\alpha} a}{\pi v^{\alpha}_F}} \quad , \quad K^{\alpha}_{\sigma} = 1/\sqrt{1 - \frac{U_{\alpha} a}{\pi v^{\alpha}_F}}, \\ v^{\alpha}_{\rho} = v^{\alpha}_F \sqrt{1 + \frac{U_{\alpha} a}{\pi v^{\alpha}_F}} \quad , \quad v^{\alpha}_{\sigma} = v^{\alpha}_F \sqrt{1 - \frac{U_{\alpha} a}{\pi v^{\alpha}_F}}. \end{aligned} \tag{4.70}$$

The tunneling term $\mathcal{H}^I_{\perp}$ in Eq. (4.69) is given explicitly in App. D, Eq. (D.1). The essential property is that $\mathcal{H}^I_{\perp}$ contains terms $\propto \exp(i\theta^{1,2}_{\sigma})$ and is therefore irrelevant if a spin gap is open in chain 1 or 2 via the sine-Gordon potentials in Eq. (4.69). Note that since the tunneling term also contains terms $\propto e^{i\theta^{\alpha}_{\rho}}$, the development of a charge gap due to umklapp terms would also make the tunneling term irrelevant. For the moment, let us assume that the fermions are at half-filling, $k^1_F + k^2_F = \frac{\pi}{a}$, but that this condition is fulfilled while each chain is away from half-filling, such that *umklapp* terms are irrelevant.

The sine-Gordon terms U_{α} are responsible for opening a spin gap Δ^{α}_{σ} in chain α whenever $U_{\alpha} < 0$. Let us assume that the interactions in chain 1 are attractive, such that the associated coupling $g^1_{1\perp} = U_1$ flows to strong coupling and a

spin gap Δ_σ^1 opens. This phase is the Luther–Emery liquid [332]. We moreover assume that interactions in chain 2 are repulsive, such that there is no spin gap. Then the effective theory of chain 2 is described by a fixed point Luttinger liquid Hamiltonian with parameter $(K_\sigma^2)^* = 1$. For energy scales under Δ_σ^1, interchain hopping terms $\mathcal{H}_\perp^I$ are irrelevant, and the coupling between the chains is given by terms obtained at second order in perturbation theory. Karyn Le Hur has shown that superconductivity is induced in chain 2 from the proximity with chain 1 of preformed pairs [305].

The Hamiltonian at second order in g is (see Appendices D and E)

$$\begin{aligned}\mathcal{H}_\perp^{II} &= -\frac{g'}{a}\int dx \cos\left[\sqrt{2}\phi_\sigma^2\right]\left\{\cos\left[2(k_F^1+k_F^2)x-2\phi_\rho^+\right]\right. \\ &\qquad \left. +2\cos\left[2\chi x-2\theta_\rho^-\right]\right\} \\ &\quad -\frac{g'}{a}\int dx \cos\left[2\chi x-2\theta_\rho^-\right]\cos\left[2(k_F^1+k_F^2)x-2\phi_\rho^+\right],\end{aligned} \tag{4.71}$$

where

$$\frac{g'}{a} = \frac{2g^2}{\Delta_\sigma^1}\frac{1}{\pi a}, \tag{4.72}$$

$$2\chi x = a' A_{\perp\downarrow} + a' A_{\perp\uparrow}, \tag{4.73}$$

with infinitesimal χ representing the flux per plaquette per spin species.

Note that the first two of the three terms in Eq. (4.71) gap the field ϕ_σ^2, triggering the formation of Cooper pairs in the second chain [305]. We mark the opening of the superconducting gap in the second chain by *SC proximity effect* on Figure 4.6a). The coupling is represented between the blue dashed lines since it occurs in the σ sector.

The first term of Eq. (4.71) is a spin conserving backscattering term

$$(\psi_{-r,\sigma}^1)^\dagger \psi_{+r,\sigma}^2 (\psi_{-r,\sigma}^2)^\dagger \psi_{+r,\sigma}^1 + \text{H.c.} \tag{4.74}$$

It favors a charge density wave. Its scaling dimension is

$$\delta_1 = \frac{1}{2} + \frac{K_\rho^1}{2} + \frac{K_\rho^2}{2}. \tag{4.75}$$

The second term of Eq. (4.71) corresponds to the tunneling of Cooper pairs

$$(\psi^1_{-r,\sigma})^\dagger \psi^2_{+r,\sigma} (\psi^1_{+r,-\sigma})^\dagger \psi^2_{-r,-\sigma} e^{ia'(A_{\perp\sigma}+A_{\perp-\sigma})} + \text{H.c.} \tag{4.76}$$

Due to this term, there is Josephson phase coherence between the Cooper pair condensates. The scaling dimension associated to this is

$$\delta_2 = \frac{1}{2} + \frac{1}{2K_\rho^1} + \frac{1}{2K_\rho^2}. \tag{4.77}$$

The third contribution in Eq. (4.71) corresponds to the operator

$$(\psi^1_{-r,\sigma})^\dagger \psi^2_{+r,\sigma} (\psi^1_{-r,\sigma'})^\dagger \psi^2_{+r,\sigma'} e^{ia'(A_{\perp\sigma}+A_{\perp\sigma'})} + \text{H.c.} \tag{4.78}$$

It is a correlated hopping term that is irrelevant without longer ranged repulsive interactions

$$\delta_3 = \frac{1}{2}\left(K_\rho^1 + K_\rho^2 + \frac{1}{K_\rho^1} + \frac{1}{K_\rho^2}\right) > 2. \tag{4.79}$$

We will return to this term in Subsec. 4.4.2. It favors the Cooper pair *Laughlin* ground state.

4.4.1 Cooper pair *Rung Mott – Meissner* phase

To realize the *Rung Mott – Meissner* phase, take $U_1 < 0$ and $U_2 > 0$ on the order of the bandwidth $4t$, such that $K_\rho^1 = 2$ and $K_\rho^2 = 1/2$. Then $\delta \equiv \delta_1 = \delta_2 = 7/4$, showing that it is possible to achieve an energy scale

$$\Delta^* \sim \Delta_\sigma^1 \left(\frac{g'a}{v_F}\right)^{\frac{1}{2-\delta}}, \tag{4.80}$$

under which Mott insulating behavior and Meissner currents coexist. Note that the *Rung Mott – Meissner* gap lies in general below the spin gap in chain 1, *i.e.* $\Delta^* < \Delta_\sigma^1$. We have let v_F be a velocity close to the Fermi velocities of the two chains. Remark the difference from the bosonic case, Subsec. 4.1.2. The Cooper pair *Rung Mott – Meissner* gap has a power law dependence on the tunneling between chains. We denote this phase by *Rung Mott – Meissner* between the ρ sectors of chains 1 and 2 on Figure 4.6a) .

To characterize *Rung Mott – Meissner* , let us consider the relative charge current

$$i[\mathcal{H}, -\frac{1}{\pi}\sqrt{2}\nabla\phi_\rho^-] = \frac{d}{dt}(n_1 - n_2)$$

which splits as before into two components

$$j_\perp = \frac{4g'}{a}\langle\cos(\sqrt{2}\phi_\sigma^2)\rangle \sin(-2\chi x + 2\theta_\rho^-), \tag{4.81}$$

$$j_\parallel = -v_\rho^1 K_\rho^1 \nabla\theta_\rho^1 + v_\rho^2 K_\rho^2 \nabla\theta_\rho^2 = -v_F\sqrt{2}\nabla\theta_\rho^-. \tag{4.82}$$

These operators are the analogues of Eqs. (4.39). For energy scales smaller than Δ^*, they have the following expectation values

$$\langle j_\perp\rangle = 0,\ \langle j_\parallel\rangle = -\sqrt{2}v_F\chi = -2\sqrt{2}at\chi. \tag{4.83}$$

The new factor in the second equation comes from the fact that we are considering Cooper pairs (hence a $\sqrt{2}$) with magnetic flux χ per spin (hence the 2).

4.4.2 Cooper pair *Laughlin* phase

The third term in Eq. (4.71) produces a Laughlin state at $\nu = \frac{1}{2}$ for the Cooper pairs. It can be made relevant by the addition of an interchain repulsive interaction.

Let us assume that the two chains are identical $K_\rho = K_\rho^1 = K_\rho^2$ and $v_\rho = v_\rho^1 =$

v_ρ^2; further we assume that they have attractive interactions and that ϕ_σ^1 and ϕ_σ^2 are both gapped.

To make the third term of Eq. (4.71) relevant, it is sufficient to add an interchain interaction

$$\mathcal{V} = \frac{aV_\perp}{\pi^2} \int dx (\nabla\phi_\rho^1)(\nabla\phi_\rho^2). \tag{4.84}$$

We need to reexpress the Luttinger liquid Hamiltonian describing the density sector $\mathcal{H}_{0\rho}^1 + \mathcal{H}_{0\rho}^2 + \mathcal{V} = \mathcal{H}_{0\rho}^+ + \mathcal{H}_{0\rho}^-$. The new Luttinger liquid Hamiltonians are characterized by parameters

$$v_\rho^\pm K_\rho^\pm = v_\rho K_\rho, v_\rho^\pm / K_\rho^\pm = \frac{v_\rho}{K_\rho} \pm \frac{aV_\perp}{\pi}, \tag{4.85}$$

from which $K_\rho^\pm = (1 - u \pm v_\perp)^{-\frac{1}{2}}$, where $u = |U|a/(\pi v_F)$ and $v_\perp = V_\perp a/(\pi v_F)$ obey $0 < u, v_\perp < 1$. Then the scaling dimension $\delta_3 = (1-u-v_\perp)^{\frac{1}{2}} + (1-u+v_\perp)^{-\frac{1}{2}}$. For small u, we find that $\delta_3 < 2$ for large enough repulsive interactions $V_\perp$ between the chains.

By imposing the following constraint on the flux and density,

$$2(k_F^1 + k_F^2) \pm 2\chi = 0 \mod 2\pi, \tag{4.86}$$

the effective sine-Gordon Hamiltonian from Eq. (4.71) is

$$\mathcal{H}_\perp^{II} = -\frac{g'}{a} \int dx \cos\left[\sqrt{2}(\theta_\rho^1 - \theta_\rho^2) \pm \sqrt{2}(\phi_\rho^1 + \phi_\rho^2)\right]. \tag{4.87}$$

Upper and lower signs correspond to the constraint in Eq. (4.86). The canonical transformation

$$(1/\sqrt{2})\Theta_\rho^\alpha = \theta_\rho^\alpha, \sqrt{2}\Phi_\rho^\alpha = \phi_\rho^\alpha \tag{4.88}$$

performed for each chain α yields the interchain coupling

$$\mathcal{H}_\perp^{II} = -\frac{g'}{a} \int dx \cos\left[\Theta_\rho^1 - \Theta_\rho^2 \pm 2(\Phi_\rho^1 + \Phi_\rho^2)\right]. \tag{4.89}$$

Equation (4.89) is formally identical to Eq. (4.32) and describes the Laughlin state at filling $\nu = \frac{1}{2}$ for Cooper pairs, which are created by the operator $(\psi^{\alpha}_{-r,\uparrow}\psi^{\alpha}_{r,\downarrow})^{\dagger} \sim e^{i\Theta^{\alpha}_{\rho}}$. The discussion of observables in this phase is analogous to the one in Subsec. 4.1.5.

4.4.3 Dual phase: fermionic Mott insulator with spinon currents

In this section we present a phase that is in some sense dual to the *Rung Mott – Meissner* phase. That state involved inducing superconductivity through the proximity effect, *SC proximity effect* , and the development of the *Rung Mott – Meissner* state gaps in the density, or "ρ", sector. The dual to this occurs at half-filling in each chain $k^1_F = k^2_F = \frac{\pi}{2a}$, when it is necessary to include the *umklapp terms* in Eq. (4.69)

$$\sum_{\alpha} \frac{U_{\alpha}}{2\pi a} \int dx \cos(\sqrt{8}\phi^{\alpha}_{\rho}). \tag{4.90}$$

The resulting phase will be the *Rung Mott* phase. In this Mott phase, a *Spinon Meissner* phase will develop, which we summarize in Figure 4.6b).

To obtain the dual phase, assume that in both chains there are repulsive interactions $U \equiv U_1 = U_2 > 0$ and that $K_{\rho} = K^1_{\rho} = K^2_{\rho}$. Assume in addition that $K^{1,2}_{\sigma} = K_{\sigma} \geq 1$, which makes terms generating a spin gap in (4.69) irrelevant. For this, it is necessary that the repulsion U be on the order of the bandwidth. The Mott gap has the asymptotic power law form,

$$\Delta_{\rho} \sim \frac{v_F}{a}\left(\frac{Ua}{v_F}\right)^{1/(2-2K_{\rho})}. \tag{4.91}$$

Then the tunneling term $\mathcal{H}^I_{\perp}$ is irrelevant, and we can proceed to obtain a Hamiltonian at second order in perturbation theory. The derivation of this Hamiltonian can be found in App. D. We obtain

$$\mathcal{H}^{II}_{\perp} = -\frac{g'}{a}\int dx \cos\left(2\theta^{-}_{\sigma} - 2\chi_{\sigma}x\right)\langle\cos(\sqrt{2}\phi^1_{\rho})\cos(\sqrt{2}\phi^2_{\rho})\rangle.$$

(4.92)

The expectation value is order 1 for energy scales under Δ_ρ. We introduced

$$\frac{g'}{a} = 4\frac{g^2}{\Delta_\rho}\frac{1}{\pi a}, \tag{4.93}$$

$$2\chi_\sigma x = -a' A_{\perp\downarrow} + a' A_{\perp\uparrow}. \tag{4.94}$$

For the second equation, we require that the two spin species have different charges with respect to the gauge field. This results in a flux coupling to spin, denoted χ_σ.

It is now easy to see that a spinon Meissner phase can arise. Under the Mott gap, the effective scaling dimension of Eq. (4.92), which represents a Josephson term for the spinon phase, is $1/K_\sigma$. As before, we consider the low χ_σ limit, so the oscillatory argument of the sine-Gordon term can be neglected in the renormalization group flow equations. Therefore we introduce a new energy scale

$$\Delta \sim \Delta_\rho \left(\frac{g'a}{v_F}\right)^{\frac{1}{2-\frac{1}{K_\sigma}}}. \tag{4.95}$$

This energy scale is under the Mott gap and characterizes the onset of spinon Josephson phase pinning. In analogy to the situation studied before, Meissner spinon currents are allowed in this phase

$$\langle j_\perp^\sigma \rangle = 0, \langle j_\parallel^\sigma \rangle = -2\sqrt{2} a t \chi_\sigma, \tag{4.96}$$

as obtained from the time derivative of the relative spin density $-\frac{1}{\pi}\nabla\phi_\sigma^-(x)$. The $\sqrt{2}$ comes from the definition of the spinon field $(\psi^\alpha)^\dagger_{r,\uparrow}\psi^\alpha_{-r,\downarrow} \sim e^{-i2rk_F x}e^{-i\sqrt{2}\theta^\alpha_\sigma}$, and the factor of 2 comes from (4.94).

4.5 Experimental realizations

In this section we propose experimental realizations of Eq. (4.1) with ultracold atoms in optical lattices (Subsec. 4.5.1) and with quantum circuits (Subsec. 4.5.2).

4.5.1 Ultracold atom implementation

Ladder implementation

Several aspects related to our model have been proven experimentally. The Abrikosov vortex lattice was observed in rotating traps [333, 334]. The Josephson effect was demonstrated with spatially separated Bose-Einstein condensates [335, 336]. A recent experiment [78] demonstrates the Meissner effect in a ladder optical lattice of about 40 rungs filled with approximately 5×10^4 ^{87}Rb atoms. For the purposes of this subsection, we will use the notation of Ref. [78] and define hopping matrix elements J_x and J_y. The square lattice is defined by translation vectors $\mathbf{d}_{x,y}$. The tunneling along the x direction can be suppressed by means of an inhomogenous electric field inducing a tilt $\Delta_{tilt} \gg J_x$ between neighboring minima of the optical lattice. The tunneling can be restored resonantly by a pair of far-detuned Raman running-wave beams $(\mathbf{k}_1, \Omega_1)$ and $(\mathbf{k}_2, \Omega_2)$. The frequency detuning $\omega = |\Omega_1 - \Omega_2|$ is matched to the tilt Δ_{tilt}. This driving scheme gives a spatially modulated and time-dependent potential energy at every site, $V_{m,n} = V_K^0 \cos^2 [\mathbf{q} \cdot (m\mathbf{d}_x + n\mathbf{d}_y)/2 + \omega t/2]$. Then the wavevector $\mathbf{q} = \mathbf{k}_1 - \mathbf{k}_2$ induces a phase $\Phi_{m,n} = \mathbf{q} \cdot (m\mathbf{d}_x + n\mathbf{d}_y)$ for hops from site (m, n) to site $(m+1, n)$ (see also Ref. [337]). The effective Hamiltonian is

$$H = -\sum_{m,n} \left(K e^{i\Phi_{m,n}} a^\dagger_{m+1,n} a_{m,n} + J a^\dagger_{m,n+1} a_{m,n} \right). \tag{4.97}$$

For large tilts $\Delta_{tilt} \gg V_K^0$, the renormalized hopping strengths are $K = J_x V_K^0/(2\sqrt{2}\Delta_{tilt})$, and $J \approx J_y$. The experiment for the realization of the Meissner effect in a ladder started with a finite value of the flux and increased the coupling between the

wires J [g in the notation of our Eq. (4.1)] in order to obtain a Meissner phase. Decreasing J allowed a transition into a vortex phase below some critical rung hopping matrix element J^c.

In the experiment of Ref. [78] one can, in principle, control the lattice filling such that on average an *odd number of bosons per rung* is achieved. The charge gap of the Mott insulator can be probed by implementing an additional tilt of the ladder lattice in the x direction. That is, Δ^+ can be determined from the particle-hole excitation probability in the total density sector under the tilt, as exemplified in the classic experiment by Greiner *et al* [237].

Alternative implementation: Spin-orbit coupling of hyperfine states

Let us briefly discuss an alternative implementation in the setup of Ref. [38]. It is possible to formally map the chains 1 and 2 into two internal degrees of freedom of atoms in a single one-dimensional optical lattice. Coherent transport and splitting of atomic wavepackets for different Zeeman states has been demonstrated [338]. As a concrete example, for ^{87}Rb atoms, the Zeeman states with opposite magnetic moments $|1\rangle = |F = 1, m_F = -1\rangle$ and $|2\rangle = |F = 2, m_F = -1\rangle$ experience opposite Peierls phases in the presence of laser assisted tunneling [38]. This amounts to a spin-orbit coupling term for the spinor Bose gas in one dimension.

The Josephson term couples the two Zeeman states, taking the form

$$-g|1\rangle_i\langle 2|_i - g|2\rangle_i\langle 1|_i$$

for an atom at site i. The Peierls phase corresponds to the transport of an atom from site i to site $i+1$, $-te^{iaA^\alpha_{i,i+1}}|\alpha\rangle_i\langle\alpha|_{i+1} + \text{H.c.}$, where $\alpha = 1, 2$ and $A^1_{i,i+1} = -A^2_{i,i+1}$. Importantly, the odd integer filling condition (4.25) becomes a simple condition on the *parity of the atom number at each site*:

$$\left\langle\, |1\rangle_i\langle 1|_i + |2\rangle_i\langle 2|_i \,\right\rangle \equiv 1 \bmod 2. \tag{4.98}$$

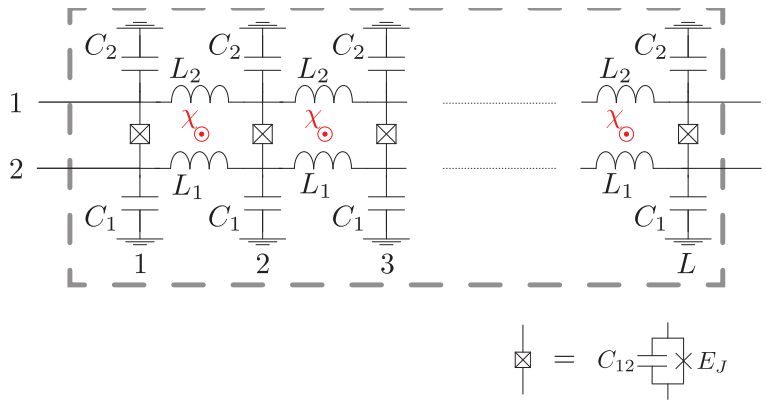

Figure 4.8: Two-leg ladder as quantum circuit, with Josephson junction components on the rungs.

The odd–integer filled *Rung Mott* state can then be probed since atom number parity can be imaged with current technology [339, 340]. The *Rung Mott – Meissner* state can be obtained by preparing an odd filling Mott insulator, then tuning the population of $|1\rangle$ versus $|2\rangle$ by the application of microwave fields and a magnetic field to realize a Landau Zener sweep [38].

The *Laughlin* phase becomes possible for a finite value of $V_\perp > 0$. Interactions between distinct spin species [341] can be tuned by magnetic Feshbach resonances [342], which is a possible pathway towards stabilizing the *Laughlin* phase. In the *Laughlin* phase, a lattice tilt would yield spin flip current.

More generally, long ranged repulsion between next-neighbor atoms can be achieved with the dipole-dipole interactions of Rydberg atoms [343, 344, 345]. Dipolar molecule interactions can be used as well [346, 347]. We have argued previously that free fermions interacting repulsively with the bosons give rise to effective repulsive interactions between the bosons [69].

4.5.2 Quantum circuit implementation

It has long been known that the *Meissner* and the *Vortex phase* can be realized in Josephson junction arrays [253, 348, 349]. When the Josephson coupling energy is comparable to the capacitive charging energy of the superconducting islands, such systems present a magnetic field tuned superconductor – insulator transition [350,

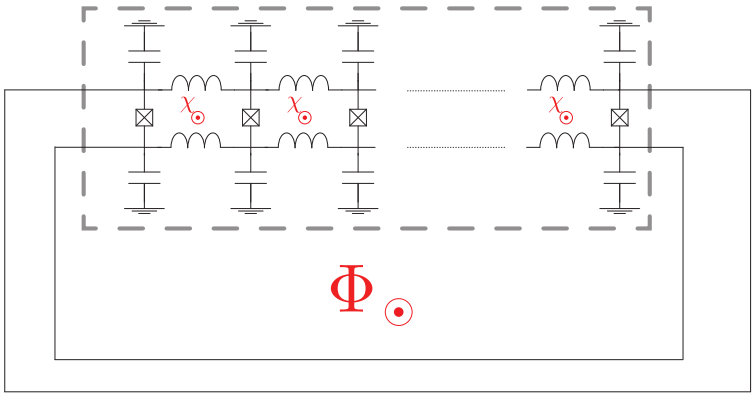

Figure 4.9: Setup that allows threading of Aharonov Bohm flux, denoted Φ, through the ladder.

351]. At small Josephson energy, the dynamics of the system is described in terms of charges, whereas the large Josephson energy limit gives way to a description in terms of vortices. The field tuned superconductor–insulator transition is a vortex delocalization transition, proposed by Fisher [352]. Moreover, quantum Hall states have been theoretically predicted for Josephson junction arrays: quantum Hall phases of vortices stabilized by inherent long ranged interactions [353, 354]; and, directly relevant to our discussion, a fractional quantum Hall state at $\nu = \frac{1}{2}$ was predicted in Josephson arrays by Odintsov and Nazarov [355].

We propose here a quantum circuit [261, 262] realization of the Hamiltonian in Eq. (4.1). In this circuit, the various energy scales are tuned to agree with the effective continuum theory (4.5). We associate to the capacitive, inductive and Josephson junction circuit components energy scales

$$E_C = \frac{e^2}{2C}, \; E_J = \frac{I_c}{\phi_0}, \; E_L = \frac{\phi_0^2}{L}. \tag{4.99}$$

Here $\phi_0 = \hbar/(2e)$ is the reduced flux quantum. The critical current I_c of the Josephson junction is in the nA-μA range. Typical capacitances C are in the fF to pF range. Inductances L can be in the nH range.

To define the quantum circuit Hamiltonian, we define node fluxes [261] $\theta_i^{1,2}$ on the circuit in Figure 4.8. Josephson junctions connecting the chains 1 and 2

correspond to cosine terms in the circuit Hamiltonian

$$-\sum_{i=1}^{L} E_J^{12}\cos(\theta_i^1 - \theta_i^2 + a' A_{\perp i}). \tag{4.100}$$

In addition to this, the mutual capacitance C_{12} between the chains leads to a charging term

$$\sum_{i=1}^{L} E_C^{12}(n_{1i} - n_{1i}^0)(n_{2i} - n_{2i}^0). \tag{4.101}$$

The offset charges on each superconducting island are denoted $n_{\alpha i}^0$.

We turn now to terms corresponding to individual chains. There is a charging energy at the i^{th} site in chain α due to the capacitive coupling C_α

$$\sum_{i=1}^{L} E_C^{\alpha}(n_{\alpha i} - n_{\alpha i}^0)^2. \tag{4.102}$$

Additionally, we have assumed that the Josephson energy associated with a junction between sites i and $i+1$ is large compared to the charging energy $E_J^\alpha \gg E_C^\alpha$. Then Josephson terms in each chain are replaced by inductive contributions

$$\sum_{i=1}^{L-1} \frac{E_J^\alpha}{2}\left(\theta_i^\alpha - \theta_{i+1}^\alpha + aA_{i,i+1}^\alpha\right)^2. \tag{4.103}$$

The Hamiltonian is the sum of Eqs. (4.100, 4.101, 4.102, 4.103). We now estimate the involved energy scales. The chain Josephson energy scales must be set large $E_J^{1,2}/h \approx 10$ GHz, compared to charging energy $E_C^{1,2}/h \approx E_J^{12}/h \approx 2$ GHz. These values are commonly achieved in experiments [356, 357]. Note that typical temperatures are 20 mK corresponding to frequencies of 0.4 GHz. This is well below the superconducting gap of aluminum, about 2 K. Returning to the notation of the original Hamiltonian in Eq. (4.1),

$$t \sim E_J^\alpha,\ U = E_C^\alpha,\ g = E_J^{12},\ V_\perp = E_C^{12}. \tag{4.104}$$

The Luttinger parameter in each chain is very large if E_C^α is negligible and the

Tonks limit would be achieved in a limit where the intra-chain charging energy would formally become infinite.

One shared characteristic of Josephson junction array experiments is the presence of offset charge noise [262], which becomes difficult to control over large arrays [351]. Control of offset charge is crucial for the realization of the *Rung Mott* phase. Offset charges can in principle be tuned by voltage terms $-V_i^{\alpha}(2e)n_{\alpha i}$. With the aid of these terms and tuning the mutual capacitance C_{12}, it is possible to achieve a stable state with an odd number of Cooper pairs on each rung. This was shown in the context of a pair of superconducting islands [357, 358]. While control of offset charge over a large array is hard experimentally, signatures of the phases proposed here should in principle appear in arrays of *several* junctions. The charge gap Δ^+ can be probed by showing the absence of current when flux is threaded through the cylinder of the ladder, as argued in Sec. 4.2.4. Experimentally this is achieved by threading flux through two large external loops that wrap around the cylinder (Figure 4.9). In the *Laughlin* phase, current through the rungs should be observed while adiabatically threading AB flux through the ladder.

4.6 Two-dimensional generalizations

In this section we generalize the 2-chain ladder models of Sec. 4.1 to N-leg ladders. We find that the *Rung Mott – Meissner* phase cannot be stable for $N > 2$ if we keep the same average filling per chain $n_0 = \frac{1}{2a}$. However, regardless of filling, Josephson phase pinning terms are present and allow us to generalize the *Meissner* phase in N-leg ladders. This is detailed in Sec. 4.6.1. We find that the *Rung Mott – Meissner* can be actually stabilized if the ladder has $(N-1)$ bosons per unit cell. In this case, a Mott phase can be stabilized on the inner chains of the ladder, whereas *Rung Mott – Meissner* occurs on the outer chains. This is presented in Sec. 4.6.2. Finally, we dedicate Subsec. 4.6.4 to two-dimensional generalizations which involve bilayers formed by juxtaposing ladders.

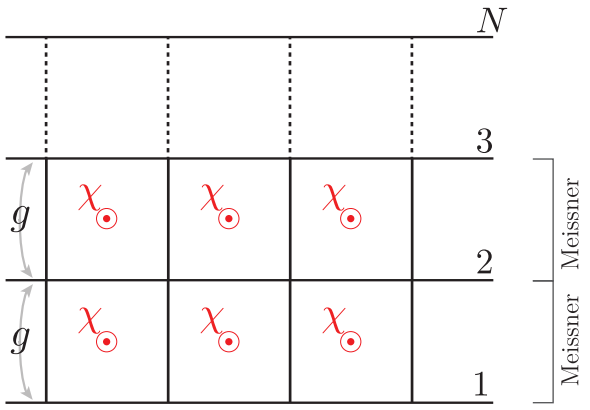

Figure 4.10: Planar array of N chains obeying Eq. (4.105). In the strong coupling phase, only edge bonds in chains 1 and N carry nonvanishing current.

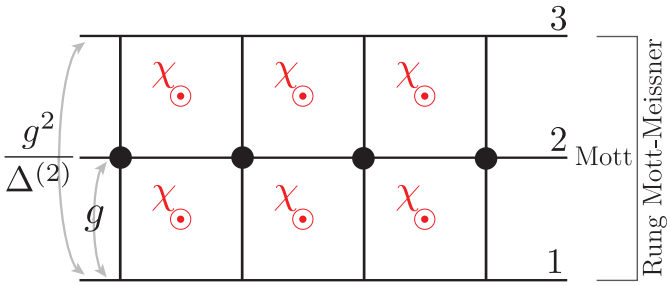

Figure 4.11: Three leg ladder construction for the *Rung Mott – Meissner* state. There is Mott insulator of average filling $n_0^2 = 1/a$ on wire 2. The Josephson coupling between chains 1 and 3 appears at second order in perturbation theory.

4.6.1 N-chain construction for the Meissner phase

Consider N identical bosonic chains (Figure 4.10) described by Luttinger liquid Hamiltonians as in Eq. (4.6,4.7): the fields corresponding to the J^{th} chain are $\theta^J(x)$ and $\phi^J(x)$. Their commutation relation is $[\phi^J(x), \theta^{J'}(x')] = i\frac{\pi}{2}\delta_{JJ'}\mathrm{Sign}(x'-x)$. Under the assumptions of Subsec. 4.1.2 for density and flux, we obtain the following coupling Hamiltonian

$$\begin{aligned} \mathcal{H}_\perp^{\mathrm{2D}} &= \sum_{J=1}^{N-1} \mathcal{H}_\perp^{J,J+1} \\ \mathcal{H}_\perp^{J,J+1} &= -\frac{g}{a}\int dx \cos(\theta^{J+1} - \theta^J - \chi x) \times \\ &\qquad \left(1 + 2\cos\left[2(\phi^J + \phi^{J+1})\right]\right). \end{aligned} \tag{4.105}$$

Under the energy scale Δ^- of Eq. (4.21), the phase fields $\theta^{J+1} - \theta^J$ are pinned to the classical value $\langle \theta^{J+1} - \theta^J \rangle = -\chi x$. The following Meissner currents result

$$\begin{aligned} j_\perp &= 0, \\ j_\parallel^J &= 0, \ J = 2, ..., N-1 \\ j_\parallel^1 - j_\parallel^N &= -(N-1)at\chi. \end{aligned} \tag{4.106}$$

Concerning the possibility of a Mott transition, the $N-1$ fields $\phi^1 + \phi^2$, ..., $\phi^{N-1} + \phi^N$ cannot be pinned, since they are not independent from the fields $\theta^1 - \theta^2$, ..., $\theta^{N-1} - \theta^N$. This is because there is a nonzero commutation relation:

$$\begin{aligned} [\phi^J(x) + \phi^{J+1}(x), \theta^J(x') - \theta^{J-1}(x')] &= [\phi^J(x), \theta^J(x')] \\ &= i\frac{\pi}{2}\mathrm{Sign}(x' - x). \end{aligned}$$

The field $\phi^\rho = \frac{1}{\sqrt{N}} \sum_{j=1}^N \phi^j$ describing fluctuations of the total density remains gapless, leading to a power law density–density correlation function. In conclusion, the N-leg ladder leads to a Meissner effect with vanishing bulk current expectation values. The Mott phase is unstable for $N > 2$. The Mott phase described by a finite correlation length discussed for $N = 2$ is replaced by algebraic density–density correlation functions for $N \geq 3$.

If the flux and density are changed to satisfy $\nu = \frac{1}{2}$ filling, the coupled chain construction of the bosonic Laughlin state is obtained. For $N \geq 3$, it is possible to form a closed loop contained entirely in the bulk, at each point on the loop having one vertical bond (rung). Fractional statistics are manifest in the phase acquired by bulk quasiparticles around such a closed loop [271].

4.6.2 3-leg construction for the boson Mott insulator with Meissner current

Let us return to the possibility of realizing the *Rung Mott – Meissner* phase in an N-leg ladder. In order to achieve this phase, the densities need to be changed from half-filling. In the simplest instance, it is possible to realize a Mott insulator with Meissner current at the edges in a 3-leg ladder (see Fig. 4.11). Consider the Hamiltonian of Eq. (4.1), with $\alpha = 1, 2, 3$ denoting the three chains. Let $n_0^2 = \frac{1}{a} = n_0^1 + n_0^3$. Then the bosonized form of the chain number 2 is:

$$\begin{aligned} \mathcal{H}^2 &= \frac{v^2}{2\pi}\int dx \left[K^2(\nabla\theta^2)^2 + \frac{1}{K^2}(\nabla\phi^2)^2\right] \\ &\quad + \frac{U_2}{a}\int dx \cos\left(2\phi^2\right). \end{aligned} \tag{4.107}$$

Assuming $K^2 < 2$ and $U_2 > U_{1,3}$, the middle chain undergoes a Mott transition characterized by the energy scale

$$\Delta^{(2)} \sim \frac{v^2}{a}\left(\frac{aU_2}{v^2}\right)^{\frac{1}{2-K^2}}. \tag{4.108}$$

The Josephson coupling terms are analogous to Eq. (4.19). For $T < \Delta^{(2)}$, where θ^2 is disordered, the effective Josephson coupling between chains 1 and 3 appears at order $\frac{g^2}{\Delta^{(2)}}$:

$$\begin{aligned} \mathcal{H}_{SG} &= -\frac{4g^2}{a\Delta^{(2)}}\int dx \cos(-\theta^1+\theta^2+\chi x)\cos(-\theta^2+\theta^3+\chi x)\times \qquad (4.109) \\ &\qquad \left[1+2\cos\left(2\pi n_0^1 x - 2\phi^1\right)\right]\left[1+2\cos\left(2\pi n_0^3 x - 2\phi^3\right)\right] \\ &= -\frac{2g^2}{a\Delta^{(2)}}\int dx \cos(-\theta^1+\theta^3+2\chi x)\left[1+2\cos\left(2\phi^1+2\phi^3\right)\right] + \ldots \qquad (4.110) \end{aligned}$$

The ellipsis contains a term proportional to $\cos(-\theta^1 - \theta^3 + 2\theta^2)$, which is less relevant. The remaining contribution is identical to Eq. (4.19), provided that the following changes are made: field ϕ^2 becomes ϕ^3, $\theta^2 \to \theta^3$, and $\chi \to 2\chi$. The transport observables are obtained from Subsec. 4.1.2 with the substitutions

described in this paragraph.

The description of the phase for temperatures below $\Delta^{(2)}$ is analogous to that of the two chain ladder with double the flux, and a suppressed Josephson coupling $\propto g^2/\Delta^{(2)}$. The Josephson phase pinning gap Δ^- is modified to account for the fact that the renormalization group flow begins at the Mott energy scale of the middle chain, $\Delta^{(2)}$:

$$\Delta^- = \Delta^{(2)} \left(\frac{g^2}{\Delta^{(2)}} \frac{a}{v} \right)^{\left(2-\frac{1}{2K^-}\right)^{-1}}, \tag{4.111}$$

with K^- as given in Subsec. 4.1.2 in Eq. (4.8). From here, Δ^+ is obtained via Eq. (4.27). Then we expect the following hierarchy

$$\Delta^+ < \Delta^- < \Delta^{(2)}. \tag{4.112}$$

The large Mott gap in the middle chain, $\Delta^{(2)}$, implies that an added particle will go to one of the outer chains 1 or 3. This causes the *Rung Mott* phase to transition to the *Rung superfluid* phase. Therefore doping leads to the phase *Rung superfluid – Meissner* , along with a Mott insulator at unit filling in chain 2. This situation is reminiscent of the d–Mott phase of spinful fermion ladders, where a hierarchy of gaps leads to similar behavior [359, 360, 361].

The presence of the unit filled Mott insulating chain 2 induces Josephson coupling between chains 1 and 3 at order $g^2/\Delta^{(2)}$. To generalize, assume that the ladder consisted of $N+2$ chains, N of which were at unit filling in a Mott phase, making up the bulk. The Josephson term between chains 1 and $N+2$ would appear at order $g^{N+1}/(\Delta^{(2)})^N$ in perturbation theory. This is the exponential suppression of the tunneling term between the edge chains 1 and $N+2$ due to the insulating bulk.

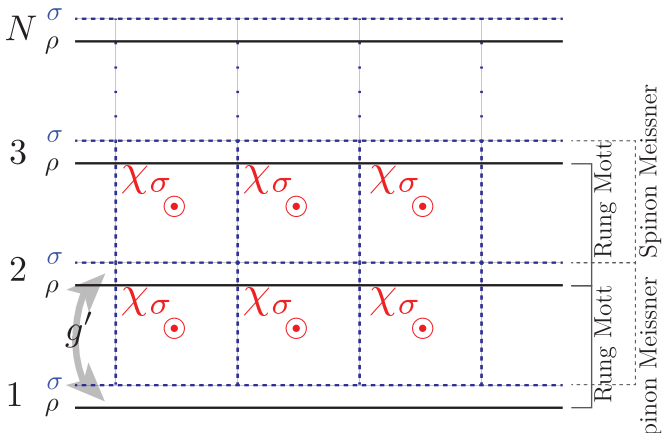

Figure 4.12: The couplings responsible for the two–dimensional *Rung Mott – Spinon Meissner* state, obtained from Eq. (4.113)

4.6.3 2D construction for fermionic Mott insulator with spinon currents

The coupling Hamiltonian of Eq. (4.92) can be generalized to N identical chains [see Fig. 4.12]

$$\begin{aligned} \mathcal{H}_{\perp}^{2D} &= \sum_{J} \mathcal{H}_{\perp}^{J,J+1} \\ \mathcal{H}_{\perp}^{J,J+1} &= -\frac{g'}{a} \int dx \cos\left(\sqrt{2}\phi_{\rho}^{J}\right) \cos\left(\sqrt{2}\phi_{\rho}^{J+1}\right) \times \\ &\qquad \cos\left[-2\chi_{\sigma}x + \sqrt{2}(\theta_{\sigma}^{J} - \theta_{\sigma}^{J+1})\right]. \end{aligned} \tag{4.113}$$

Here $1 \leq J \leq N-1$, and $\mathcal{H}_{\perp}^{J,J+1}$ is the same as $\mathcal{H}_{\perp}^{II}$ of Eq. (4.92) only for fields corresponding to chains J and $J+1$ instead of 1 and 2. The scaling dimension of the sine-Gordon operator is the one calculated in Subsec. 4.4.3. Assuming that only the field ϕ_{ρ}^{1} is pinned to its classical value, the sine-Gordon terms pin the density fields ϕ_{ρ}^{J}, for all remaining chains $J \geq 2$, inducing a Mott transition in each chain. In addition, terms dependent on the spinon field phase differences $\theta_{\sigma}^{J} - \theta_{\sigma}^{J+1}$ cause a Meissner effect. Current vanishes on all "bulk" chains $2 \leq J \leq N-1$ and on all vertical bonds (between chains 1 and 2,..., $N-1$ and N). The Meissner current at the edge is $\langle j_{N}^{\sigma} - j_{1}^{\sigma} \rangle = -2\sqrt{2}(N-1)at\chi_{\sigma}$, as found in Sec. 4.4.3 for $N = 2$.

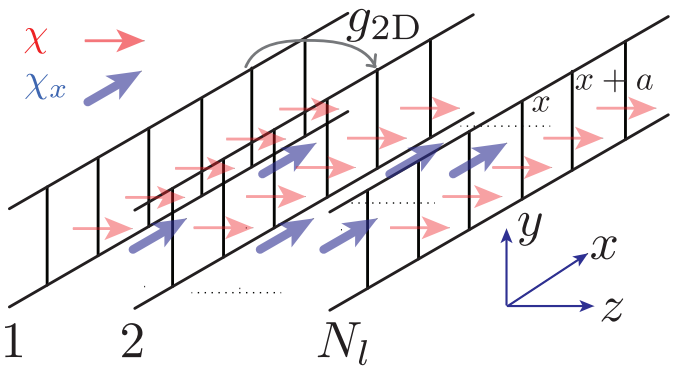

Figure 4.13: Bilayer formed by an array of N_l two leg ladders. The χ flux [see Eq. (4.19)] is produced by a magnetic field in the z direction (thin red arrows). A magnetic field in the x direction (thick blue arrows) has flux χ_x through the vertical square plaquettes lying parallel to the yz plane.

4.6.4 Coupled planes

It is possible to generalize the models of Sections 4.1 and 4.4 by Josephson coupling more ladders to form bilayers. In the bilayer geometry, different magnetic field orientations highlight the Meissner effect. The two–dimensional extension of the *Rung Mott – Meissner* state is a stack of ladders in the *Rung Mott – Meissner* phase; nonetheless, the ground state has spinon superfluidity and Meissner currents between any two consecutive ladders. The two-dimensional extension of *Laughlin* is a stack of ladders in the *Laughlin* state; however, a nontrivial feature of the bilayer ground state is that the charge fluctuations of the ladders are pinned to each other.

We start with an array of two chain ladders such that the $\alpha = 1, 2$ wire of the I^{th} ladder lies in the α^{th} plane of the bilayer (Figure 4.13). Let the fields in the I^{th} ladder be $\theta^{1I}, \phi^{1I}, \theta^{2I}, \phi^{2I}$. We replace $\theta^{1,2}, \phi^{1,2}$ by these fields in Eqs. (4.5)-(4.7) and (4.19) (*Rung Mott – Meissner*) or (4.32) (*Laughlin*) to obtain the Hamiltonian for the I^{th} ladder. In addition, we assume that the Luttinger parameter K and the velocity of excitations v are independent of the ladder index I.

Let us assume that hopping terms across ladders, which are characterized by the hopping strength g_{2D} along the z direction, contain a Peierls phase $aA^{\alpha}_{I,I+1}$. This is given by a magnetic field parallel to the x direction in Figure 4.13. We

will pick a gauge such that the inter–ladder coupling is

$$\mathcal{H}_{\rm 2D} = -\frac{g_{\rm 2D}}{a}\sum_{\alpha=1,2}\sum_{I=1}^{N_l-1}\int dx\cos(\theta^{\alpha I}-\theta^{\alpha,I+1}-aA^{\alpha}_{I,I+1}), \tag{4.114}$$

where N_l is the number of ladders forming the planar bilayer. Equation (4.114) is the Josephson coupling within each layer of our bilayer. The flux through a plaquette parallel to the yz plane is

$$\chi_x = -aA^1_{I,I+1} + aA^2_{I,I+1}. \tag{4.115}$$

To study the relevance of the hopping term in Eq. (4.114), we rewrite the sum over α in terms of $\theta^{-,I}$ and $\theta^{+,I}$

$$\begin{aligned}\mathcal{H}_{\rm 2D} = -2\frac{g_{\rm 2D}}{a}\sum_{I=1}^{N_l-1}\int dx\cos\left(\frac{\theta^{-,I}-\theta^{-,I+1}}{\sqrt{2}}+\frac{\chi_x}{2}\right) \\ \times\cos\left(\frac{\theta^{+,I}-\theta^{+,I+1}}{\sqrt{2}}-\frac{aA^1_{I,I+1}+aA_{I,I+1}}{2}\right).\end{aligned} \tag{4.116}$$

Phase locking in an array of ladders

If the identical ladders are either in the *Rung Mott – Meissner* state or in the *Laughlin* state, the term (4.116) is irrelevant due to the second cosine factor of the integrand. We can check this by inspecting the ordered fields in either of the two phases [described by (4.26) or (4.32)], and using the fact that $[\phi^{+,I},\theta^{+,I}]\neq 0$. Nonetheless a contribution at second order in perturbation theory is relevant (see App. E). To derive this contribution we need to determine the relevant energy gap that determines the correlation length. This gap is Δ^+ for *Rung Mott – Meissner* [see Eq. (4.27)] or Δ for *Laughlin* [see Eq. (4.33)]. For generality we denote the gap by Δ^{ladder}. Unless mentioned otherwise, the results below hold regardless of the phase of the individual ladders.

The effective Hamiltonian at second order in perturbation theory in $g_{2\mathrm{D}}$ is:

$$\mathcal{H}_{2\mathrm{D}} = -\frac{g_{2\mathrm{D}}^2}{a\Delta^{ladder}} \int dx \cos(\sqrt{2}\theta^{-,I} - \sqrt{2}\theta^{-,I+1} + \chi_x). \tag{4.117}$$

We have obtained a planar Meissner phase formally equivalent to the one produced by the Josephson term in Eq. (4.105). Note however that the bosons have been replaced by (pseudo-)spinons $b_{2I}^\dagger b_{1I} \propto e^{-i\sqrt{2}\theta^{-,I}}$. The spinon corresponds to interwire hopping inside the I^{th} ladder. The oscillatory argument of the cosine [χx in Eq. (4.105)] is absent in Eq. (4.117). Therefore, the spinon Hamiltonian has no effective magnetic field. With this, the phase pinning condition Eq. (4.117) implies that

$$\langle\theta^{-,I}\rangle = \langle\theta^{-,I+1}\rangle - \frac{1}{\sqrt{2}}\chi_x. \tag{4.118}$$

Using Eq. (4.39) for current operators in the I^{th} ladder, we obtain

$$j_\parallel^I = j_\parallel^{1,I} - j_\parallel^{2,I} = -v^- K^- \sqrt{2}\nabla\theta^{-,I}. \tag{4.119}$$

Then, using Eq. (4.118), we find that expectation values of currents in adjacent ladders obey

$$\langle j_\parallel^I\rangle = \langle j_\parallel^{I+1}\rangle. \tag{4.120}$$

The current flows are pinned to each other.

Drag effects in bilayer geometry

We obtain here a Hamiltonian that manifests drag between Luttinger liquids [362, 363, 364] due to the Josephson coupling in Eq. (4.114). Start with many ladders coupled with Eq. (4.114). Assume that there are Laughlin terms of the form (4.32) in each ladder:

$$-2gn_0 \int dx \cos\left[-(\theta^{I1} - \theta^{I2}) + m(\phi^{I1} + \phi^{I2})\right]. \tag{4.121}$$

Assume, as opposed to the previous subsection, that the intralayer coupling Eq. (4.114) is the most relevant term. Eq. (4.114) realizes the phase pinning

$$\langle \theta^{\alpha I} - \theta^{\alpha, I+1} \rangle - a A^{\alpha}_{I,I+1} = 0, \ \alpha = 1, 2. \tag{4.122}$$

Then the Laughlin terms (4.121) are irrelevant at first order in perturbation theory but give a contribution at second order:

$$- \cos(-m\sqrt{2}\phi^{+,I} + m\sqrt{2}\phi^{+,I+1}). \tag{4.123}$$

This term could have interesting consequences for transport. For example, this is the form studied in the context of Coulomb drag between two (electron-like) Luttinger liquids [Eq. (4) of Ref. [362]]. In that case, drag resistivity is defined as $\rho_{I,I+1,d} = -\frac{V^{I+1}}{j^I L}$, where ladder I is the active channel, where a drive current is applied, and ladder $I+1$ is the passive channel (not connected to any reservoirs) where a voltage V^{I+1} is measured. The results known from that problem [362, 363, 365, 364] can be used here to describe the response at finite temperature. Importantly, in our setup, the drag is not necessarily brought about by Coulomb interactions between the ladders, but by the intralayer Josephson coupling Eq. (4.105). Note that drag responses have been recently measured in pairs of quantum wires separated by a small barrier [366]. There has been as well recent work on topologically ordered states of bosons in bilayers [367, 368].

4.7 Conclusions

To conclude, we have presented tight-binding models of bosons and fermions on quasi one-dimensional lattices whose ground states are incompressible states with correlations illustrating chiral order. In particular, we have shown that a Mott insulating phase with pseudospin Meissner effect [69] can be observed in current experiments with ultracold atoms and Josephson junction arrays, and provided

concrete experimental proposals for both setups. Moreover, we have argued that in the presence of repulsive interactions this phase will transition into a low dimensional precursor of the Laughlin state, and enumerated observables that can be used to detect this transition. The model presented here is not restricted to bosons, and we have argued that a larger variety of phases can be obtained in a spinful fermion ladder at or near half-filling. Finally, we have derived extensions of the phases found on the ladder to two-dimensional lattices, either single-layered or bilayers. The phase diagram that was presented here should be robust to small amounts of disorder [74, 75, 369, 370, 371, 372].

We remark that a recent proposal appeared for the realization of the infinitely thin cylinder limit of the Laughlin state [373], with the same filling factor but periodic boundary conditions in the y direction. Refs. [254, 255] contain an extensive DMRG treatment complemented by bosonization which yields the phase diagram as a function of boson filling factor, on-site interaction U and flux; where regimes coincide, our results agree. Connections between our results and phases obtained from the interplay of band topology and Mott physics, such as topological insulators with Hubbard interactions [182, 183], topological Mott insulators [184], or chiral $d + id$ superconductors formed upon doping a Mott state, [233, 374, 235] will be explored in future work.

Chapter 5

Conclusions and Outlook

In this thesis we have explored tight–binding Hamiltonians which host topological phases. In Part I, we have dealt with two–dimensional lattice models. Starting with topological bandstructures, we explored the effects of band topology on the correlated many–body ground states arising from the interplay of strong interactions (the Bose–Hubbard model) and the kinetic energy. We have shown that topological properties at the single–particle level find their way in the many–body physics: The quasiparticles of a Mott insulator, at strong repulsive Hubbard interactions [Chapter 3], or Bogoliubov quasiparticles in a superfluid, at weak interactions [Chapter 2], inherit the topology of the underlying Chern insulator bandstructure. Since such quasiparticles are expected to have a long lifetime, we predict that their topologically protected edge modes or bulk bands can be probed in current experiments. Moreover, we have encountered a situation where the kinetic terms are frustrated, which leads to novel superfluid states that break a discrete symmetry, such as the chiral superfluid. The unit filling plaquette Mott insulator of Ch. 3 is an example of a nontrivial Mott phase with quantum entanglement brought about by local current loops.

We should like to enumerate some questions that follow naturally from Part I. 1. It is now known that topologically ordered states, such as the fractional Chern insulators [27, 28, 29, 30, 31], are realizable when the bandstructure is altered

such that a topological band is flat enough compared to the band gap to enhance the effects of interactions. While engineering a flat band with nonzero Chern number remains a daunting task, an alternate route to the fractional quantum Hall effect can be achieved in synthetic dimensions, such as the internal degrees of freedom (for example, distinct Zeeman states playing the role of distinct sites in the synthetic direction) of atoms trapped in one dimensional real space lattices [375, 376, 236, 377], where boundary conditions, magnetic fields, the range of hopping terms and interactions are tunable. 2. symmetry protected topological phases in 2D, such as the boson topological insulator, have a field–theoretic description [378], but the construction of microscopic Hamiltonians supporting such a phase is still an open problem (for a recent proposal, see Ref. [239]). 3. inspired by Mott insulating phases with some minimal amount of entanglement, we may wonder what other kinds of Mott insulators may exist in two–dimensional lattices. An intriguing phase is that of a fractionally filled, singly degenerate, insulating ground state, a featureless bosonic Mott insulator (proposed for the Kagomé lattice at 1/3 filling [379] and honeycomb lattices at half–filling [380]), which is neither described by a broken symmetry nor by topological order.

In Part II, we have shifted focus toward quasi one–dimensional systems. There is a rich classification of symmetry protected topological phases in one dimension [381, 382, 244], including the ground states of models such as the Su–Schrieffer–Heeger model for polyacetylene [383], the Haldane spin 1 chain [240], or the Affleck–Kennedy–Lieb–Tasaki model [241]. We have looked at *quasi* one dimensional systems, such as ladders, whose advantage is that they often allow us to make inferences about the properties of the thermodynamic limit of two–dimensional systems [359, 256, 271], while at the same time being amenable to exact treatment, numerically through density matrix renormalization group methods [76, 77] and analytically via bosonization [75]. Looking at ladders in a uniform magnetic field, which have been realized in a variety of current experiments [79, 78, 377], we have uncovered rich phase diagrams of Mott insulators with

chiral currents, as well as low–dimensional precursors of Laughlin's state for the $\nu = 1/m$ fractional quantum Hall effect, which in this one–dimensional limit turn out to be topological phases protected by inversion symmetry [373]. In view of current experimental progress, we have proposed a series of local observables that discriminate between the "topological" and non-"topological" states of quantum ladders.

A number of pending questions remain on the topics of Part II: 1. the study of the phase diagram can be carried out in an exact fashion using numerical techniques, from which the energy scales required for the experimental realization can be extracted. 2. It is known that topological order does not survive in one dimension [244], and that the topologically degenerate Laughlin state reduces to a charge density wave in when the bulk of the sample becomes thin [384, 385]. The determination of the minimal size of the bulk for which the fractional quantum Hall state still survives is also a problem amenable to numerical treatment. 3. For such one–dimensional topological phases, what are the order parameters that distinguish them from nontopological states (for some proposals, see Ref. [386]), and to what extent are local observables sufficient (apart from our recent proposals in [71], see Ref. [387])? We would like to end with one last wrinkle to the variety of questions on topological phases. Topological classifications go beyond the band theory of solids, or of two–dimensional correlated gases. In a recent experiment Roushan *et al.* [120] have observed a topological transition by mapping the Brillouin zone of a Chern insulator [12] to the parameter space of single qubit system, and went on to explore two–qubit systems and their interaction induced topological transitions. This experiment offers a glimpse into the exciting world of topological phases in controllable quantum systems with a small number of degrees of freedom.

Appendix A

Realization of a synthetic gauge field

We discuss here how to simulate the effect of a magnetic field in a system of neutral particles. Such artificial magnetic fields, including frustrated or staggered configurations, have been actively studied in recent years. In what follows, we follow the line of thought of Kolovsky [337]. The method relies on adjusting the potential terms individually for each site in the trapping optical lattice of the cold atom system. In cQED systems, this is equivalent to adjusting the frequency of each resonator individually and time–dependently, which has become experimentally possible [159, 388, 389, 390]. The authors of Ref. [159] have already proposed a means of realizing a synthetic gauge field in a square lattice array of coupled photonic cavities.

A.1 Magnetic field from lattice modulation

Consider the time-dependent Hamiltonian

$$H_\tau = H + \sum_{\mathbf{m}} \left[\hbar\omega + \hbar\omega_0 \cos\left(\Omega\tau + m_2\theta\right) m_1\right] a^\dagger_{\mathbf{m}} a_{\mathbf{m}}. \tag{A.1}$$

We construct the solution to the Schrödinger equation as follows. If the hopping is suppressed, $|t| = 0$, then the following function solves the time-dependent Schrödinger equation:

$$\begin{aligned} |\psi\rangle &= \sum_{\mathbf{m}} e^{i\phi_{\mathbf{m}}} |\mathbf{m}\rangle, \\ \phi_{\mathbf{m}}(\tau) &= -\omega\tau - \frac{\omega_0}{\Omega} \sin\left(\Omega\tau + \theta m_2\right) m_1. \end{aligned} \tag{A.2}$$

The solution for $|t| \neq 0$ is constructed from this as

$$|\psi\rangle = \sum_{\mathbf{m}} d_{\mathbf{m}} e^{i\phi_{\mathbf{m}}} |\mathbf{m}\rangle, \tag{A.3}$$

where the $d_{\mathbf{m}}$ must now obey the following differential equation

$$i\hbar \dot{d}_{\mathbf{m}} = \sum_{\mathbf{n}} t_{\mathbf{m},\mathbf{n}} e^{i(\phi_{\mathbf{m}} - \phi_{\mathbf{n}})} d_{\mathbf{n}}. \tag{A.4}$$

In this last equation, the $t_{\mathbf{m},\mathbf{n}}$ is the tight-binding hopping integral, which takes the value $|t|e^{\pm i\phi}$ for nearest-neighbors and zero otherwise, and $\phi_{\mathbf{m}}$ are the phases computed in Eq. (A.2). The perturbation has induced a time-dependent phase factor $e^{i(\phi_{\mathbf{m}} - \phi_{\mathbf{n}})}$ which we will now simplify by keeping only those parts that oscillate very slowly (rotating wave approximation). We use the following expansion [166]

$$e^{iz\sin\alpha} = \sum_{l=-\infty}^{+\infty} e^{il\alpha} \mathcal{J}_l(z), \tag{A.5}$$

where $\mathcal{J}_l(z)$ are the Bessel functions of the first kind. Upon inspection of the expansion in Eq. (A.5) and of the phase $\phi_{\mathbf{m}}$ in Eq. (A.2) we find that, in general, one must have the driving frequency Ω be an integer multiple of the on–site frequency ω, i.e. $l\omega$, in order to obtain at least one time-independent term in the expansion. The largest contribution is obtained if we take $\Omega = \omega$. We obtain the

following effective changes to the hopping amplitudes

$$\begin{aligned}
&\text{bond} \parallel \hat{\mathbf{\Delta}}_1 : \quad |t|e^{-i\phi} \rightarrow |t|e^{-i\phi} \cdot \mathcal{J}_{-1}\left(\frac{\omega_0}{\Omega}\right) e^{-im_2\theta}, \\
&\text{bond} \parallel \hat{\mathbf{\Delta}}_2 : \quad |t|e^{-i\phi} \rightarrow |t|e^{-i\phi}, \\
&\text{bond} \parallel \left(\hat{\mathbf{\Delta}}_2 - \hat{\mathbf{\Delta}}_1\right) : |t|e^{-i\phi} \rightarrow |t|e^{-i\phi} \cdot \left[\mathcal{J}_{-1}\left(\frac{\omega_0}{\Omega}(m_1+1)\right) e^{-i\theta m_2} + \right. \\
&\qquad\qquad \left. \mathcal{J}_{-1}\left(-\frac{\omega_0}{\Omega}m_1\right) e^{-i\theta(m_2+1)}\right].
\end{aligned} \tag{A.6}$$

The ratio $\frac{\omega_0}{\Omega}$ provides an additional experimental parameter to tune the hopping strength via the Bessel functions of the first kind $\mathcal{J}_{-1}$.

The time–dependent perturbation induces spatially dependent phases and a dressing of the hopping integral $|t|$. These spatially dependent phases mimic the phases that would be produced by a gauge field in the minimal substitution. The fact that an additional phase is acquired along oblique bonds parallel to $\hat{\mathbf{\Delta}}_2 - \hat{\mathbf{\Delta}}_1$ implies that at the level of each unit cell the phases will correspond to a field that is non–uniform across the unit cell. However, the total phase acquired by a photon traversing around a parallelogram unit cell of area $|\mathbf{\Delta}_1 \times \mathbf{\Delta}_2|$, see Fig. 2.1, is going to be a constant equal to $f = 2\theta$. Since the uniformity of the field at the level of the unit cell can be recovered by a gauge transformation, we perform all of our calculations (App. A.2) for a uniform field.

A.2 Spectrum in a magnetic field

In this appendix we show the detailed calculations for the spectrum of the Kagomé system placed in a uniform magnetic field $\mathbf{B}$. The phase acquired by a particle along an elementary parallelogram unit cell of the Kagomé lattice (see Fig. 2.1) is $f \equiv \frac{|\mathbf{B}|a^2\sqrt{3}}{2} \equiv 8\pi f \equiv \sqrt{3}ba$, where f is dimensionless, and b has units of inverse length. The phase acquired by a photon around the unit cell is eight times the phase acquired on a counter-clockwise loop around a triangular plaquette. Let us

for simplicity pick the following gauge field in the Landau gauge, $\mathbf{A} = (-|\mathbf{B}|y, 0)$, where the two components are cartesian. Due to the presence of a magnetic field, the Hamiltonian will couple k_y to $k_y \pm \frac{b}{2}$ and to $k_y \pm b$. Without loss of generality, we take $\hbar\omega = 0$. The Hamiltonian reads

$$\begin{aligned} H &= |t|e^{i\phi}\sum_{\mathbf{k}} e^{i\mathbf{k}.\boldsymbol{\Delta}_1} a^{\dagger}_{Ak_x,k_y} a_{Bk_x,k_y+b} + a^{\dagger}_{Ak_x,k_y} a_{Bk_x,k_y-b} \\ &\quad + e^{i\frac{f}{16}}\left(e^{-i\mathbf{k}.\boldsymbol{\Delta}_2} a^{\dagger}_{C,k_x,k_y} a_{B,k_x,k_y+\frac{b}{2}} + a^{\dagger}_{C,k_x,k_y} a_{B,k_x,k_y-\frac{b}{2}}\right) \\ &\quad + e^{-i\frac{f}{16}}\left(e^{-i\mathbf{k}.(\boldsymbol{\Delta}_1-\boldsymbol{\Delta}_2)-i\frac{ba\sqrt{3}}{8}} a^{\dagger}_{A,k_x,k_y} a_{C,k_x,k_y+\frac{b}{2}}\right. \\ &\quad \left. + e^{i\frac{ba\sqrt{3}}{8}} a^{\dagger}_{A,k_x,k_y} a_{C,k_x,k_y-\frac{b}{2}}\right) + \text{H.c.} \end{aligned} \tag{A.7}$$

For rational values of $f = \frac{p}{q}$, where p, q are relatively prime integers, one can reduce the Brillouin zone from the original $\left[0, \frac{2\pi}{a}\right] \times \left[0, \frac{4\pi}{a\sqrt{3}}\right]$ to the magnetic Brillouin zone $\left[0, \frac{2\pi}{qa}\right] \times \left[0, \frac{4\pi}{a\sqrt{3}}\right]$. The couplings between different momenta disappear and we have replaced the original problem with that of a periodic one–dimensional chain of $3q$ sites. Let us take a generic wavefunction to be

$$|\psi\rangle = \sum_{n=0,\alpha=A,B,C}^{q-1} \psi_{\alpha n} a^{\dagger}_{\alpha k_x, k_y^0+n\frac{b}{2}}|0\rangle, \tag{A.8}$$

where $a^{\dagger}_{\alpha k_x,k_y^0+n\frac{b}{2}}$ creates a photon on sublattice α at a given momentum. Then the Schrödinger equation is equivalent to the following set of three Harper equations

$$\begin{aligned} E_{k_x,k_y^0}\psi_{Am} &= |t|e^{i\phi-i\frac{f}{16}}\left(e^{+i\frac{b\sqrt{3}}{2}}\psi_{C,m-1} + e^{-i\left(k_x,k_y^0+m\frac{b}{2}\right).(\boldsymbol{\Delta}_1-\boldsymbol{\Delta}_2)}\psi_{C,m+1}\right) \\ &\quad + |t|e^{-i\phi}\left(e^{-i\left(k_x,k_y^0+m\frac{b}{2}\right).\boldsymbol{\Delta}_1}\psi_{B,m+2} + \psi_{B,m-2}\right) \\ E_{k_x,k_y^0}\psi_{Bm} &= |t|e^{i\phi}\left(e^{i\left(k_x,k_y^0+(m-2)\frac{b}{2}\right).\boldsymbol{\Delta}_1}\psi_{A,m-2} + \psi_{A,m+2}\right) \\ &\quad + |t|e^{-i\phi-\frac{f}{16}}\left(e^{i\left(k_x,k_y^0+(m-1)\frac{b}{2}\right).\boldsymbol{\Delta}_2}\psi_{C,m-1} + \psi_{C,m+1}\right) \\ E_{k_x,k_y^0}\psi_{Cm} &= |t|e^{i\phi+i\frac{f}{16}}\left(e^{-i\left(k_x,k_y^0+m\frac{b}{2}\right).\boldsymbol{\Delta}_2}\psi_{B,m+1} + \psi_{B,m-1}\right) \\ &\quad + |t|e^{-i\phi+i\frac{f}{16}}\left(e^{i\left(k_x,k_y^0+(m-1)\frac{b}{2}\right).(\boldsymbol{\Delta}_1-\boldsymbol{\Delta}_2)+i\frac{ba\sqrt{3}}{8}}\psi_{A,m-1} + e^{-i\frac{ba\sqrt{3}}{8}}\psi_{A,m+1}\right). \end{aligned}$$

(A.9)

The solution to these equations gives the spectrum of the system for every rational flux $f = p/q$, and the pattern of splittings into magnetic subbands is known as the Hofstadter butterfly [37]. The spectrum of the problem is periodic in f of period 2, for example $f = 0$ and $f = 2$ systems have the same spectrum etc.

Appendix B

Bogoliubov transformation

This appendix contains the diagonalization of (2.45). The Hamiltonian matrix can be written in the following basis

$$\Phi_{\mathbf{k}}^{\dagger} = \left(b_{A,\mathbf{k}} b_{A,-\mathbf{k}}^{\dagger} b_{B,\mathbf{k}} b_{B,-\mathbf{k}}^{\dagger} b_{C,\mathbf{k}} b_{C,-\mathbf{k}}^{\dagger} \right). \tag{B.1}$$

Then

$$H_t = \sum_{\mathbf{k}\in \mathrm{BZ}} \Phi_{\mathbf{k}}^{\dagger} H_t(\mathbf{k}) \Phi_{\mathbf{k}}, \tag{B.2}$$

where the Bogoliubov Hamiltonian may be expressed as

$$H_t(\mathbf{k}) = \begin{pmatrix} H_{AA}(\mathbf{k}) & H_{AB}(\mathbf{k}) & H_{AC}(\mathbf{k}) \\ H_{BA}(\mathbf{k}) & H_{BB}(\mathbf{k}) & H_{BC}(\mathbf{k}) \\ H_{CA}(\mathbf{k}) & H_{CB}(\mathbf{k}) & H_{CC}(\mathbf{k}) \end{pmatrix}, \tag{B.3}$$

whose elements are 2×2 matrices defined as

$$\begin{aligned} H_{\alpha\alpha}(\mathbf{k}) &= \begin{pmatrix} \frac{h^{\alpha\alpha}(\mathbf{k})}{2} - \frac{E_0}{2} + \frac{Un_0}{2} & \frac{Un_0}{2} \\ \frac{Un_0}{2} & \frac{[h^{\alpha\alpha}(-\mathbf{k})]^*}{2} - \frac{E_0}{2} + \frac{Un_0}{2} \end{pmatrix}, \\ H_{\alpha\neq\beta}(\mathbf{k}) &= \begin{pmatrix} \frac{h^{\beta\alpha}(\mathbf{k})}{2} & 0 \\ 0 & \frac{\left[h^{\alpha\beta}(-\mathbf{k})\right]^*}{2} \end{pmatrix}. \end{aligned} \tag{B.4}$$

Recall that E_0 is the energy of the minimum of the lowest band in the single–particle spectrum, obtained from the matrix $h(\mathbf{k})$, expressed in the sublattice basis as in (2.4). The b operators can be transformed to quasiparticle operators $\tilde{b}$ via a canonical transformation

$$\Phi_{\mathbf{k}} = B(\mathbf{k})\tilde{\Phi}_{\mathbf{k}}, \tag{B.5}$$

with $\tilde{\Phi}$ defined as in (B.1) with $\tilde{b}$ replacing b. The conditions for $B(\mathbf{k})$ to preserve the bosonic commutation relations between the $\tilde{b}$ operators, $[\tilde{b}_{\alpha\mathbf{k}}, \tilde{b}^{\dagger}_{\beta\mathbf{k}'}] = \delta_{\alpha\beta}\delta_{\mathbf{k}\mathbf{k}'}$ and $[\tilde{b}_{\alpha\mathbf{k}}, \tilde{b}_{\beta\mathbf{k}'}] = 0$, are equivalent to the following pseudo–unitarity condition [391]

$$B(\mathbf{k})\Sigma B^{\dagger}(\mathbf{k}) = \Sigma,\ B^{\dagger}(\mathbf{k})\Sigma B(\mathbf{k}) = \Sigma,\ \text{where } \Sigma = \mathrm{id}_{3\times 3} \otimes \sigma_3, \tag{B.6}$$

where $\mathrm{id}_{3\times 3}$ is the identity acting on sublattice space and σ_3 is the third Pauli matrix. $B(\mathbf{k})$ must diagonalize the Bogoliubov Hamiltonian of Eq. (B.3); denote the diagonalized matrix by K:

$$B(\mathbf{k})^{\dagger} H_t(\mathbf{k}) B(\mathbf{k}) = K(\mathbf{k}). \tag{B.7}$$

From the condition in (B.6) one can reexpress this as

$$\Sigma B^{\dagger}(\mathbf{k})\Sigma\Sigma H_t(\mathbf{k})B(\mathbf{k}) = B^{-1}(\mathbf{k})\Sigma H_t(\mathbf{k})B(\mathbf{k}) = \Sigma K(\mathbf{k}), \tag{B.8}$$

whence the matrices ΣK and ΣH_t are similar and it suffices to diagonalize ΣH_t to determine the spectrum of Bogoliubov quasiparticles.

In fact, the eigenvectors of the diagonalization above can be constructed explicitly. By definition, $H_t(\mathbf{k})$ is Hermitian and positive definite (note the $-E_0/2$ subtraction of the band minimum). Then there exists a Cholesky decomposition for $H_t(\mathbf{k})$ [189, 391]: $H_t(\mathbf{k}) = C^{\dagger}(\mathbf{k})C(\mathbf{k})$, where $C(\mathbf{k})$ is upper triangular, and invertible. Now construct the matrix $W(\mathbf{k}) = C(\mathbf{k})\Sigma C^{\dagger}(\mathbf{k})$. It has the property that it contains the spectrum of quasiparticles and quasiholes: there exists a unitary

matrix $U(\mathbf{k})$ such that $U^\dagger(\mathbf{k})W(\mathbf{k})U(\mathbf{k}) = \mathrm{diag}(\xi_1(\mathbf{k}), -\xi_1(-\mathbf{k}), ...)$. Then let

$$B(\mathbf{k}) \equiv C^{-1}(\mathbf{k})U(\mathbf{k})\mathrm{diag}(\xi_1^{1/2}(\mathbf{k}), \xi_1^{1/2}(-\mathbf{k}), ...), \tag{B.9}$$

which is a pseudounitary matrix [cf. (B.6)] that satisfies

$$H_t(\mathbf{k})B(\mathbf{k}) = \Sigma B(\mathbf{k})\mathrm{diag}(\xi_1(\mathbf{k}), -\xi_1(-\mathbf{k}), ...). \tag{B.10}$$

By application of (B.6), this gives the diagonalization of $H_t(\mathbf{k})$ into a positive definite diagonal matrix

$$B^\dagger H_t(\mathbf{k})B(\mathbf{k}) = (\xi_1(\mathbf{k}), \xi_1(-\mathbf{k}), ...) = K(\mathbf{k}). \tag{B.11}$$

The Avron–Seiler–Simon formula [103] can be applied to obtain Chern numbers of the Bogoliubov quasiparticle bands with the following band projector [189]:

$$P_j(\mathbf{k}) = B(\mathbf{k})\Gamma_j\Sigma B^\dagger(\mathbf{k})\Sigma, \tag{B.12}$$

where Γ_j is a matrix with all entries zero except for the j^{th} entry on its diagonal, which is 1. Then the Chern number can be computed using:

$$\nu_j = \frac{i}{2\pi}\int_{BZ} d^2\mathbf{k}\mathrm{Tr}\left\{[1 - P_j(\mathbf{k})]\left[\frac{\partial P_j(\mathbf{k})}{\partial k_1}, \frac{\partial P_j(\mathbf{k})}{\partial k_2}\right]\right\}, \tag{B.13}$$

with the trace over the 6 quasiparticle and quasihole bands.

In the numerical implementation of Eq. (B.13), care must be taken that the matrix $U(\mathbf{k})$, obtained from a numerical diagonalization of the matrix $W(\mathbf{k})$, is expressed in a consistent basis when $\mathbf{k}$ is varied across the Brillouin zone. One consistent choice of basis is to enforce that

$$U^\dagger(\mathbf{k})W(\mathbf{k})U(\mathbf{k}) = \mathrm{diag}(\xi_1(\mathbf{k}), -\xi_1(-\mathbf{k}), \xi_2(\mathbf{k}), -\xi_2(-\mathbf{k}), \xi_3(\mathbf{k}), -\xi_3(-\mathbf{k})), \tag{B.14}$$

with $\xi_1(\mathbf{k}) > \xi_2(\mathbf{k}) > \xi_3(\mathbf{k}) \geq 0$. This involves a permutation of the ordered band basis contained in $U(\mathbf{k})$ and is consistent with the pseudounitary metric Σ chosen above.

Appendix C

RG equations for sine–Gordon models

We consider a generic sine–Gordon Hamiltonian

$$H = \frac{1}{2\pi}\int dx \left[uK(\nabla\theta)^2 + \frac{u}{K}(\nabla\phi)^2\right] + \frac{g}{a}\int dx \cos\left(\beta\phi\right), \tag{C.1}$$

for which we derive the renormalization group equations for g and K to second order in the perturbation g. We will finally use a duality relation to derive the renormalization-group equations for $g\int dx \cos(\beta\theta(x))$. The dimensionless β is related to the scaling dimension via $\delta = \beta^2/4$.

Following Ref. [75], we require that the two–point correlation function remain invariant under a change of the low distance cutoff. We expand the interacting theory zero temperature two–point correlation function

$$R(r_1 - r_2) = \langle e^{i\phi(r_1)} e^{-i\phi(r_2)}\rangle \tag{C.2}$$

to second order in g.

The expansion of the correlation function (equivalently, of the partition func-

tion) to second order in the coupling g is

$$R(r_1 - r_2) = \langle e^{i\phi_1} e^{-i\phi_2} \rangle_0 + \frac{1}{2^3} \left(\frac{g}{ua}\right)^2 \sum_{\epsilon',\epsilon''=\pm 1} \int d^2r' d^2r'' \langle e^{i\phi_1} e^{-i\phi_2} e^{i\epsilon'\beta\phi'} e^{-i\epsilon''\beta\phi''} \rangle_{0,\mathrm{c}} \tag{C.3}$$

For brevity, we denote $\phi_1 = \phi(r_1)$ etc. Integrals $\int d^2r \equiv u \int_0^\infty dx \int_0^\infty d\tau$. The connected correlation function means

$$\langle e^{i\phi_1} e^{-i\phi_2} e^{i\epsilon'\beta\phi'} e^{-i\epsilon''\beta\phi''} \rangle_0 - \langle e^{i\phi_1} e^{-i\phi_2} \rangle_0 \langle e^{i\epsilon'\beta\phi'} e^{-i\epsilon''\beta\phi''} \rangle_0 \tag{C.4}$$

In the gaussian theory correlation functions of products of exponentials are power laws:

$$\left\langle \prod_j e^{iA_j\phi_j} \right\rangle_0 = \delta\left(\sum_j A_j\right) e^{-\frac{K}{2}\sum_{i<j} A_i A_j F(r_i - r_j)}, \tag{C.5}$$

where $F(r_i - r_j) \equiv \log|r_1 - r_2|/a$ and the length a is the small distance cutoff. The simplest of these correlation functions is the two-point correlation function $R_0(r_1 - r_2) = (a/|r_1 - r_2|)^{\frac{K}{2}}$.

The double integral in Eq. (C.3) is dominated by contributions from nearby terms $r' \approx r''$. Expanding in the small parameter $r = r' - r''$, we arrive at:

$$R(r_1 - r_2) = R_0(r_1 - r_2)\Big(1 + \frac{y^2\beta^2K^2}{2^5} F(r_1 - r_2) \int_{r>a} \frac{dr}{a} \left(\frac{r}{a}\right)^{3-\frac{\beta^2}{2}K}\Big).$$

We have introduced the dimensionless coupling constant $y = \frac{ga}{u}$. Approximating the parenthesis by an exponential function yields

$$R(r_1 - r_2) \approx e^{-\frac{K}{2}F(r_1-r_2)} e^{\frac{y^2\beta^2K^2}{2^5}F(r_1-r_2)\int_{r>a}\frac{dr}{a}\left(\frac{r}{a}\right)^{3-\frac{\beta^2}{2}K}}. \tag{C.6}$$

We express the two-point correlator as

$$R(r_1 - r_2) = e^{-\frac{K_{eff}}{2}F(r_1-r_2)}, \tag{C.7}$$

with

$$K_{\mathit{eff}}(a) = K - \frac{\beta^2 y^2 K^2}{2^4} \int_a^\infty \frac{dr}{a} \left(\frac{r}{a}\right)^{3-\frac{\beta^2}{2}K}. \tag{C.8}$$

The renormalization group equations arise by requiring that $R(r_1 - r_2)$, or equivalently K_{eff}, be invariant under a change of the low distance cutoff. We may rewrite the equation above as

$$\begin{aligned} K_{\mathit{eff}}(a) &= K - \frac{\beta^2 y^2 K^2}{2^4} \left(\int_a^{a+da} + \int_{a+da}^\infty \right) \frac{dr}{a} \left(\frac{r}{a}\right)^{3-\frac{\beta^2}{2}K} \\ &= K - \frac{\beta^2 y^2 K^2}{2^4} \frac{da}{a} - \frac{\beta^2 y^2 K^2}{2^4} \int_{a+da}^\infty \frac{dr}{a} \left(\frac{r}{a}\right)^{3-\frac{\beta^2}{2}K} + ... \end{aligned}$$

The ellipsis denotes higher order terms in $\frac{da}{a}$. K_{eff} must remain constant with respect to changes in the low energy scale $a \to a + da$. The Luttinger parameter K and the coupling y must flow to accommodate these changes:

$$K(a + da) = K(a) - \frac{\beta^2 y^2 K^2}{2^4} \frac{da}{a}. \tag{C.9}$$

The rescaling of the integrand yields the equation for y

$$y^2(a + da) = y^2(a) \left(\frac{a + da}{a}\right)^{4-\frac{\beta^2}{2}K(a)}. \tag{C.10}$$

Changing variable such that $a(l) = ae^l$ yields the following equations

$$\frac{dK}{dl} = -\frac{\beta^2}{2^4} y^2 K^2, \quad \frac{dy}{dl} = \left(2 - \frac{\beta^2}{4}K\right) y. \tag{C.11}$$

In the weak-coupling limit we approximate $K(l) \approx K(l = 0)$ and the second equation can be integrated to leading order in y. To obtain the analogous equations for $\cos[\beta\theta(x)]$, one needs to simply map $K \to K^{-1}$ in all equations.

As the sine–Gordon term flows to strong coupling, the spectrum will acquire a gap Δ, determined as follows. We define the parameter l^* at which y flows to

strong coupling:

$$y(l^*) = 1 = \frac{ga}{u} e^{\left(2-\frac{\beta^2}{4}K\right)l^*}. \tag{C.12}$$

Then, we use the fact that within our notations the gap is defined as:

$$l^* = \ln\left(\frac{u}{\Delta a}\right). \tag{C.13}$$

The asymptotic form for the gap Δ follows from the previous equation:

$$\Delta \sim \frac{u}{a} y^{\frac{1}{2-\frac{\beta^2}{4}K}}. \tag{C.14}$$

If the sine–Gordon term was instead $\int dx \cos(\beta\theta)$, then this would be modified by replacing $K \to K^{-1}$.

Appendix D

Hamiltonian for spinful fermion ladders

This appendix contains the derivation of Eqs. (4.71) and (4.92). For brevity, we omit from the equations containing Hamiltonians the spatial integrals $\int dx...$, i.e. all equations in this appendix represent Hamiltonian densities. Using Eq. (4.68) we write the hopping term $H_\perp$ in Eq. (4.66) in the continuum limit as

$$\begin{aligned}\mathcal{H}_\perp^I &= -ga\sum_\sigma\sum_{r,r'}\left[(\psi^1_{r,\sigma})^\dagger\psi^2_{r',\sigma}e^{ia'A_{\perp\sigma}}+\text{H.c.}\right] \qquad \text{(D.1)}\\ &= -\frac{g}{2\pi}\sum_\sigma e^{ia'A_{\perp\sigma}}\times\Big\{e^{i\left[-\phi_\rho^- -\theta_\rho^- +\sigma\left(-\phi_\sigma^- -\theta_\sigma^-\right)\right]}e^{i(k_F^1-k_F^2)x}+e^{i\left[-\phi_\rho^+ -\theta_\rho^- +\sigma\left(-\phi_\sigma^+ -\theta_\sigma^-\right)\right]}e^{i(k_F^1+k_F^2)x}\\ &\qquad +e^{i\left[+\phi_\rho^+ -\theta_\rho^- +\sigma\left(\phi_\sigma^+ -\theta_\sigma^-\right)\right]}e^{-i(k_F^1+k_F^2)x}+e^{i\left[+\phi_\rho^- -\theta_\rho^- +\sigma\left(+\phi_\sigma^- -\theta_\sigma^-\right)\right]}e^{-i(k_F^1-k_F^2)x}\Big\}+\text{H.c.}\end{aligned}$$

Note that this part of the Hamiltonian is irrelevant if either one of the four fields $\phi_\sigma^{1,2}$ or $\phi_\rho^{1,2}$ is gapped (either a spin gap or a charge gap develops in one of the chains). However, relevant contributions in Eq. (D.1) give rise to nonzero terms at second order in perturbation theory. The effective Hamiltonian density corresponding to order $\frac{g^2}{\Delta_\sigma^1}$ is [see the derivation in App. E], assuming that a spin gap Δ_σ^1 has developed in chain 1:

$$\mathcal{H}_\perp^{II,hf}=-\frac{\pi a}{\Delta_\sigma^1}g^2\left\{\sum_\sigma\left[(\psi^1_{-,\sigma})^\dagger\psi^2_{-,\sigma}+(\psi^1_{+,\sigma})^\dagger\psi^2_{+,\sigma}\right]e^{ia'A_{\perp,\sigma}}+\text{H.c.}\right\}^2 \qquad \text{(D.2)}$$

$$-\frac{\pi a}{\Delta_\sigma^1} g^2 \left\{ \sum_\sigma \left[(\psi_{-,\sigma}^1)^\dagger \psi_{+,\sigma}^2 + (\psi_{+,\sigma}^1)^\dagger \psi_{-,\sigma}^2 \right] e^{ia' A_{\perp,\sigma}} + \text{H.c.} \right\}^2 .$$

The square of Eq. (D.1) contains as well a set of contributions which are proportional to $\exp(\pm 2ik_F^\alpha x)$. We have dropped these contributions from Eq. (D.2), since they are oscillatory at or near half-filling in each chain, $k_F^\alpha \approx \frac{\pi}{2a}$. The first term of (D.2) contains terms which are proportional to $\exp\left[\pm 2i(k_F^1 - k_F^2)x\right]$, whereas the second term contains contributions proportional to $\exp\left[\pm 2i(k_F^1 + k_F^2)x\right]$. Each of the two terms contains nonoscillatory contributions in addition to the ones mentioned.

From (D.2) we derive the effective Hamiltonian (4.71) of Sec. 4.4, corresponding to the case $k_F^1 + k_F^2 = \frac{\pi}{a}$, with $k_F^1 \neq k_F^2$ so as to make umklapp terms irrelevant in each chain. In addition, assuming a spin gap in chain 1, Δ_σ^1, terms proportional to $\exp(i\theta_\sigma^1)$ are irrelevant. The resulting Hamiltonian at second order in perturbation theory is

$$\begin{aligned} \mathcal{H}_\perp^{II} = -\frac{g^2}{\Delta_\sigma^1} \frac{1}{\pi a} \Big\{ 4 \quad &+ \quad 4\cos(\sqrt{2}\phi_\sigma^1)\cos(\sqrt{2}\phi_\sigma^2)\cos(-2\theta_\rho^- + a'A_{\perp,\uparrow} + a'A_{\perp,\downarrow}) \\ &+ \quad 2\cos(\sqrt{2}\phi_\sigma^1 + \sqrt{2}\phi_\sigma^2)\cos\left[-2\phi_\rho^+ + 2x(k_F^1 + k_F^2)\right] \\ &+ \quad \cos\left[a'A_{\perp,\downarrow} + a'A_{\perp,\uparrow} + 2x(k_F^1 + k_F^2) - 2\theta_\rho^- - 2\phi_\rho^+\right] \\ &+ \quad \cos\left[a'A_{\perp,\downarrow} + a'A_{\perp,\uparrow} - 2x(k_F^1 + k_F^2) - 2\theta_\rho^- + 2\phi_\rho^+\right] \Big\}. \end{aligned} \tag{D.3}$$

Note that we have made explicit the oscillatory arguments $2x(k_F^1 + k_F^2)$. At half-filling $k_F^1 + k_F^2 = \frac{\pi}{a}$ these are multiples of 2π, but we will be concerned in Sec. 4.4.2 with slight deviations from half filling.

From the analogue of (D.2) in the case of a charge gap ($\Delta_\sigma^1 \to \Delta_\rho^1$) we derive the effective Hamiltonian (4.92) of Sec. 4.4.3, corresponding to the case $k_F^1 + k_F^2 = \frac{\pi}{a}$, with $k_F^1 = k_F^2$ so as to make umklapp terms relevant in each chain. In addition, assuming a charge gap Δ_ρ^1, all terms containing $\exp(i\theta_\rho^1)$ are irrelevant.

The resulting Hamiltonian at second order in perturbation theory is

$$\begin{aligned}\mathcal{H}_{\perp}^{II} = -\frac{g^2}{\Delta_\rho^1}\frac{1}{\pi a}\Big[4 \;&+\; 4\cos(\sqrt{2}\phi_\sigma^1)\cos(\sqrt{2}\phi_\sigma^2)\cos(a'A_{\perp,\downarrow} - a'A_{\perp,\uparrow} + 2\theta_\sigma^-) \\ &+\; 2\cos(2\phi_\sigma^-)\cos(2\phi_\rho^-) + 2\cos(2\phi_\sigma^+)\cos(2\phi_\rho^+) \\ &+\; 4\cos(a'A_{\perp,\downarrow} - a'A_{\perp,\uparrow} + 2\theta_\sigma^-)\cos(\sqrt{2}\phi_\rho^1)\cos(\sqrt{2}\phi_\rho^2)\Big] \end{aligned} \quad \text{(D.4)}$$

In Sec. 4.4.3 we will assume that K_σ is large enough such that the terms favoring the formation of a spin gap are irrelevant, and then the simpler form remains

$$\mathcal{H}_{\perp}^{II} = -\frac{g^2}{\Delta_\rho^1}\frac{1}{\pi a}\left[4 + 4\cos\left(a'A_{\perp,\downarrow} - a'A_{\perp,\uparrow} + 2\theta_\sigma^-\right)\cos(\sqrt{2}\phi_\rho^1)\cos(\sqrt{2}\phi_\rho^2)\right]. \quad \text{(D.5)}$$

Apart from an additive constant, this is Eq. (4.92) in the main text.

Appendix E

Effective Hamiltonian at second order in perturbation theory

In this appendix we derive Eq. (D.2). The general result can be summarized as follows. Let us consider a generic gapped (Δ) unperturbed Hamiltonian and a sine-Gordon perturbation $\mathcal{T}$. Assuming that correlation functions of the perturbation are cut off at separation larger than the correlation length $\xi = u/\Delta$ associated with the gap, an effective sine-Gordon term of order $\mathcal{T}^2/\Delta$ can approximate expectation values of arbitrary observables at second order in $\mathcal{T}$.

Let the gapped Hamiltonian density be

$$\mathcal{H}(x) = \mathcal{H}_0[\vartheta(x), \varphi(x)] - \frac{g}{a}\cos(\alpha\vartheta(x)) + \mathcal{H}_0'[\vartheta'(x), \varphi'(x)] \tag{E.1}$$

where $\mathcal{H}_0(x)$ ($\mathcal{H}_0'(x)$) is the Luttinger liquid Hamiltonian for conjugate fields ϑ, φ (ϑ', φ'). Let $\Delta = u/\xi$ be the gap associated with the ordering of ϑ due to the cosine potential, where u is the velocity of excitations characterizing $\mathcal{H}_0$.

Let $\mathcal{T}(x)$ be a sum of sine-Gordon terms added as perturbations to $\mathcal{H}(x)$:

$$\mathcal{T}(x) = -\frac{t}{a}\left[\cos(\varphi'(x) - \varphi(x)) + \cos(\varphi'(x) + \varphi(x))\right]. \tag{E.2}$$

Importantly, the fields that $\mathcal{T}$ would pin do not commute with ϑ pinned by $\mathcal{H}$, and

are therefore irrelevant. However, the term $\cos(2\varphi'(x))$ that appears in $\mathcal{T}^2(x)$, can order φ', which commutes with ϑ. At second order in perturbation theory in $\mathcal{T}$ there appear terms which are relevant in the renormalization group sense, although $\mathcal{T}$ itself is irrelevant.

The addition of $\mathcal{T}$ leads to the effective Hamiltonian density:

$$\mathcal{H}_{\mathit{eff}} = \mathcal{H} - \frac{\pi a}{\Delta}\mathcal{T}(x)^2. \tag{E.3}$$

For any observable A, the expectation values with respect to $\mathcal{H}+\mathcal{T}$ and with respect to $\mathcal{H}_{\mathit{eff}}$ are equal up to order $\mathcal{T}^2$

$$\langle A\rangle_{\mathcal{H}+\mathcal{T}} = \langle A\rangle_{\mathcal{H}_{\mathit{eff}}}. \tag{E.4}$$

In the remainder of this section we argue that this follows from an expansion of the partition function.

Let us denote $\int \mathcal{T} \equiv \int dx d\tau \mathcal{T}(x,\tau)$. The proof of Eq. (E.3) follows from expanding an arbitrary expectation value to second order in $\mathcal{T}$

$$\begin{aligned}
\langle A\rangle_{\mathcal{H}+\mathcal{T}} &= \frac{\mathrm{Tr}\left\{e^{-\int dx d\tau(\mathcal{H}+\mathcal{T})}A\right\}}{\mathrm{Tr}\left\{e^{-\int dx d\tau(\mathcal{H}+\mathcal{T})}\right\}} \\
&= \left[\langle A\rangle_{\mathcal{H}} - \langle(\int \mathcal{T})A\rangle_{\mathcal{H}} + \frac{1}{2}\langle(\int \mathcal{T})^2 A\rangle_{\mathcal{H}}\right] \\
&\quad \times \left[1 + \langle\int \mathcal{T}\rangle_{\mathcal{H}} - \frac{1}{2}\langle(\int \mathcal{T})^2\rangle_{\mathcal{H}} + \langle\int \mathcal{T}\rangle^2_{\mathcal{H}}\right] + O\left[(\int \mathcal{T})^3\right] \\
&= \langle A\rangle_{\mathcal{H}} + \frac{1}{2}\left[\langle(\int \mathcal{T})^2 A\rangle_{\mathcal{H}} - \langle(\int \mathcal{T})^2\rangle_{\mathcal{H}}\langle A\rangle_{\mathcal{H}}\right] + O\left[(\int \mathcal{T})^3\right]
\end{aligned} \tag{E.5}$$

In the last equality we have dropped all contributions at first order in $\mathcal{T}$. These contain the disordered field φ.

Now, let

$$d_{12} = \sqrt{(x_1-x_2)^2 + u^2(\tau_1-\tau_2)^2} \tag{E.6}$$

and let $\mathcal{T}_1 \equiv \mathcal{T}(x_1, \tau_1)$. Consider the following $\mathcal{T}\mathcal{T}$ correlation functions

$$\begin{aligned} \langle (\int \mathcal{T})^2 \rangle &= \int dx_1 d\tau_1 dx_2 d\tau_2 \langle \mathcal{T}_1 \mathcal{T}_2 \rangle_{\mathcal{H}} \\ &= \int dx_1 d\tau_1 dx_2 d\tau_2 R(d_{12}) \exp(-d_{12}/\xi), \end{aligned} \tag{E.7}$$

where $R(d_{12})$ is a power law and ξ is the correlation length associated with the gapped mode ϑ. Switching to relative and center of mass coordinates, and assuming $\beta \gg 0$, we obtain the approximate form

$$\begin{aligned} \text{Eq. (E.7)} &= 2\pi \int dX d\eta \int d(d_{12})\, d_{12} R(d_{12}) \exp(-d_{12}/\xi) \\ &\approx 2\pi(\xi - a) R(a) \int dX d\eta\, 1 \approx 2\pi \xi R(a)\, (L\beta). \end{aligned}$$

Then we may approximate

$$\begin{aligned} (\int \mathcal{T})^2 &= \int dx_1 d\tau_1 dx_2 d\tau_2 \mathcal{T}_1 \mathcal{T}_2 \\ &\approx \frac{2\pi\xi a}{u} \int dX d\eta\, \mathcal{T}(X, \eta) \mathcal{T}(X + a, \eta) \\ &= \frac{2\pi a}{\Delta} \int dX d\eta\, \mathcal{T}(X, \eta) \mathcal{T}(X + a, \eta) \\ &= \frac{2\pi a}{\Delta} \int \mathcal{T}^2. \end{aligned} \tag{E.8}$$

By replacing $(\int \mathcal{T})^2 \approx \frac{2\pi a}{\Delta} \int \mathcal{T}^2$ in Eq. (E.5), we obtain the lowest order contribution, of order $\mathcal{T}^2$, to the expectation value computed with respect to $\mathcal{H}_{\mathit{eff}}$. This proves Eq. (E.3).

Appendix F

Effective edge Hamiltonian

In this appendix, we derive the effective edge theory summarized in Sec. 4.2.6. The Hamiltonian is expressed in Eq. (4.57), which we reproduce here

$$\begin{aligned}\mathcal{H} = \frac{v}{2\pi}\sum_{\alpha}\int dx\left[K(\nabla\theta^{\alpha})^2+\frac{1}{K}(\nabla\phi^{\alpha})^2\right]\\ +\frac{V_{\perp}a}{\pi^2}\int dx(\nabla\phi^1)(\nabla\phi^2)\\ -2gn_0\int dx\cos(\theta^1-\theta^2-m\phi^1-m\phi^2).\end{aligned} \tag{F.1}$$

To obtain the effective gapless Hamiltonian describing the edge chiral fields $\phi_{-1}\equiv\phi^2_{-1}$ and $\phi_{+1}\equiv\phi^1_{+1}$, we integrate out the gapped degrees of freedom in (F.1). Importantly, this relies on the assumption that the coupling constant g is relevant, which assumes strong enough $V_{\perp}$ (or long ranged intrachain repulsion), as explained in the main text.

Readers may wish to skip the detailed calculation and go directly to Eq. (F.10), for the effective Hamiltonian $\mathcal{H}_{edge}$, and the discussion thereafter.

We recall here the linear transformations of fields in Eqs. (4.50) and (4.53):

$$\begin{aligned}\phi^{\alpha}_{r} &= \theta^{\alpha}/m + r\phi^{\alpha}, \alpha = 1,2, r = \pm 1,\\ \phi &= (-\phi^1_{-1}+\phi^2_{+1})/2, \theta = (\phi^1_{-1}+\phi^2_{+1})/2.\end{aligned} \tag{F.2}$$

The bulk fields obey the following algebra:

$$[\phi(x), \theta(x')] = i\frac{\pi}{2m}\text{Sign}(x' - x), \tag{F.3}$$

therefore the momentum associated to ϕ is $\Pi_\phi = \frac{m}{\pi}\nabla\theta$. The chiral fields obey:

$$[\phi_r^\alpha(x), \phi_p^\beta(x')] = ir\delta_{\alpha\beta}\delta_{rp}\frac{\pi}{m}\text{Sign}(x' - x). \tag{F.4}$$

The inverse transformations are

$$\begin{aligned}
\theta^\alpha &= \frac{m}{2}\left(\phi_{+1}^\alpha + \phi_{-1}^\alpha\right), \\
\phi^\alpha &= \frac{1}{2}\left(\phi_{+1}^\alpha - \phi_{-1}^\alpha\right), \\
\phi_{+1}^2 &= \phi + \theta, \\
\phi_{-1}^1 &= -\phi + \theta.
\end{aligned} \tag{F.5}$$

for $\alpha = 1, 2$.

In terms of these variables, the sine-Gordon term is $-2gn_0\int dx\cos(2m\phi)$. Let us assume that g is a large energy scale, so that we can approximate the sine Gordon term by the quadratic contribution, i.e.

$$-2gn_0\int dx\cos(2m\phi) \approx 4m^2gn_0\phi^2 + \text{const.} \tag{F.6}$$

In terms of $\phi, \theta, \phi_{+1} \equiv \phi_{+1}^1, \phi_{-1} \equiv \phi_{-1}^2$, the various contributions to Eq. (F.1) are

$$\begin{aligned}
\sum_\alpha(\nabla\theta^\alpha)^2 = \frac{m^2}{2}\left[(\nabla\phi)^2 + (\nabla\theta)^2\right] + \frac{m^2}{2}\left[(-\nabla\phi_{+1} + \nabla\phi_{-1})(\nabla\phi) + (\nabla\phi_{+1} + \nabla\phi_{-1})(\nabla\theta)\right] \\
+\frac{m^2}{4}\left[(\nabla\phi_{-1})^2 + (\nabla\phi_{+1})^2\right], \\
\sum_\alpha(\nabla\phi^\alpha)^2 = \frac{1}{2}\left[(\nabla\phi)^2 + (\nabla\theta)^2\right] - \frac{1}{2}\left[(-\nabla\phi_{+1} + \nabla\phi_{-1})(\nabla\phi) + (\nabla\phi_{+1} + \nabla\phi_{-1})(\nabla\theta)\right] \\
+\frac{1}{4}\left[(\nabla\phi_{-1})^2 + (\nabla\phi_{+1})^2\right],
\end{aligned}$$

$$(\nabla\phi^1)(\nabla\phi^2) = \frac{1}{4}(\nabla\phi_{+1} + \nabla\phi)(\nabla\phi - \nabla\phi_{-1}) + \frac{1}{4}\nabla\theta(\nabla\phi_{-1} + \nabla\phi_{+1}) - \frac{1}{4}(\nabla\theta)^2.$$

To obtain the effective Hamiltonian for the fields ϕ_{-1} and ϕ_{+1}, we integrate out θ, then the gapped mode ϕ. This integration is easily performed in Fourier space. We use the Fourier transform convention

$$f(r) = \frac{1}{\beta L}\sum_q f_q e^{iqr}, \tag{F.7}$$

where $r = (x, v\tau)$, $q = (k, \omega_n/v)$, $qr = kx - \omega_n\tau$, and the Matsubara frequencies are $\omega_n = \frac{2\pi n}{\beta}$ for all integer n. The part of the action that depends on θ is

$$\beta L S_\theta = \sum_q \frac{imk\omega_n}{\pi}\phi_k\theta_k^* + \sum_q k^2\theta_k F_k^* + \sum_q G_k\theta_k^*\theta_k. \tag{F.8}$$

We defined

$$\begin{aligned} F_k &= \left[\frac{V_\perp a}{4\pi^2} + \frac{v}{4\pi}\left(Km^2 - \frac{1}{K}\right)\right](\phi_{+1,k} + \phi_{-1,k}) \\ G_k &= -\frac{V_\perp a}{4\pi^2} + \frac{v}{4\pi}\left(Km^2 + \frac{1}{K}\right). \end{aligned} \tag{F.9}$$

For any field f that is a real-valued function of the coordinate x, the Fourier transform has the property $f_q = f_{-q}^*$. The θ integral is gaussian. We remark that the ϕ integral introduces terms of order $1/g$. We make the assumption that g is large, and find that all contributions from the ϕ integral contain terms quartic in derivatives, which we drop. Fourier transforming back to real space, the remaining effective action yields the following Hamiltonian for the "edge" degrees of freedom

$$\mathcal{H}_{edge} = \int dx \left\{A\left[(\nabla\phi_{+1})^2 + (\nabla\phi_{-1})^2\right] + B(\nabla\phi_{+1})(\nabla\phi_{-1})\right\} \tag{F.10}$$

where the coefficients are given by

$$
\begin{aligned}
A &= \frac{v}{8\pi}\left(Km^2+\frac{1}{K}\right)+\bar{A} \\
B &= \frac{V_\perp a}{2\pi^2}+\bar{A} \\
\bar{A} &= \frac{1}{4\pi}\frac{\left[\frac{V_\perp a}{\pi}+v(Km^2-1/K)\right]^2}{-\frac{V_\perp a}{\pi}+v(Km^2+1/K)}.
\end{aligned}
\tag{F.11}
$$

Equivalently, these describe a Luttinger liquid with effective velocity of excitations and Luttinger parameter

$$
v_{\mathit{eff}}^2=(A-B)(A+B),\ K_{\mathit{eff}}^2=(A-B)/(A+B). \tag{F.12}
$$

It is instructive to consider a simple case. In the limit $K=1/m$, there must be no backscattering term in chain α of the form $(\nabla\phi_{+1}^{\alpha})(\nabla\phi_{-1}^{\alpha})$. Note as well that this value corresponds to long ranged repulsive interactions in each of the bosonic chains [75]. Let us assume that $V_\perp$ is small while the sine-Gordon term in (F.1) is relevant in the renormalization group flow. For small enough $V_\perp$, we approximate

$$
A\approx\frac{mv}{4\pi},\ B\approx\frac{V_\perp a}{2\pi^2},\ \bar{A}=O(V_\perp^2). \tag{F.13}
$$

That is, all backscattering terms in the effective Hamiltonian arise from $V_\perp$. The resulting Luttinger liquid Hamiltonian is characterized by the following velocity and Luttinger parameter

$$
\begin{aligned}
v_{\mathit{edge}}^2 &= (\pi mv-2V_\perp a)(\pi mv+2V_\perp a), \\
K_{\mathit{edge}}^2 &= \frac{\pi mv-2V_\perp a}{\pi mv+2V_\perp a}.
\end{aligned}
\tag{F.14}
$$

A useful check is to set $V_\perp=0$. In this limit all backscattering terms between the remaining gapless chiral fields must be absent, and the edge is described by the

chiral Luttinger liquid Hamiltonian,

$$\mathcal{H}_{edge} = \frac{mv}{4\pi} \int dx \left[(\nabla \phi_{+1})^2 + (\nabla \phi_{-1})^2 \right]. \tag{F.15}$$

Appendix G

Rung Mott – Rung superfluid phase boundary

G.1 Atomic limit

The atomic limit serves to determine the boundaries of the *Rung Mott* phase as a function of μ in the limit of vanishing hopping.

Consider the Hamiltonian of (4.1), suppressing gauge fields. We use the Fock states of an isolated rung $|n_1 n_2\rangle$, with $n_{1,2}$ denoting the occupancy of each species. The atomic limit Hamiltonian for the $U(1)$ block acting over the subspace spanned by the ordered basis $|1,0\rangle,\ |0,1\rangle$ is

$$H(1/2) = \begin{pmatrix} -\mu & -g \\ -g & -\mu \end{pmatrix}, \tag{G.1}$$

whose eigenvalues are $-\mu \pm g$. Next, the block corresponding to two particles per rung, acting on the subspace spanned by the ordered basis $|2,0\rangle, |1,1\rangle, |0,2\rangle$, is

$$H(1) = \begin{pmatrix} U-2\mu & -\sqrt{2}g & 0 \\ -\sqrt{2}g & V_\perp - 2\mu & -\sqrt{2}g \\ 0 & -\sqrt{2}g & U-2\mu \end{pmatrix}. \tag{G.2}$$

The eigenvalues in this block are

$$U - 2\mu, \;\; \frac{1}{2}\left(U \pm \sqrt{16g^2 + (U - V_\perp)^2} + V_\perp - 4\mu\right). \tag{G.3}$$

For $U \to \infty$ the atomic ground state is the half filled ground state if $V_\perp + g > \mu > -g$; for $\mu < -g$, the ground state is the vacuum; for $\mu > V_\perp + g$, the ground state consists of 2 bosons per rung. For $\mu = -g$ and $\mu = V_\perp + g$ the atomic ground state is degenerate. Next, we consider the effect of the kinetic term.

G.2 Phase diagram from mean-field theory

We obtain the boundary between the Mott phase half-filling and the superfluid phase from a variational wavefunction which accounts for fluctuations by ± 1 in the total rung density around 1 boson per rung:

$$|\psi\rangle = \prod_i (n_i|00\rangle_i + a_i|10\rangle_i + b_i|01\rangle_i + x_i|20\rangle_i + y_i|11\rangle_i + z_i|02\rangle_i). \tag{G.4}$$

We have let $|n_1 n_2\rangle_i$ be the Fock state for the i^{th} rung. We assume that the coefficients are independent of the coordinate i, and therefore the normalization condition is $|n|^2+|a|^2+|b|^2+|x|^2+|y|^2+|z|^2 = 1$. These coefficients are determined from the minimization of the variational energy $\langle\psi|H|\psi\rangle$. The variational energy per site is

$$\begin{aligned} E_{var} &= U(|x|^2 + |z|^2) + V_\perp|y|^2 - \mu\langle b_1^\dagger b_1 + b_2^\dagger b_2\rangle \\ &\quad -g\langle b_1^\dagger b_2 + b_2^\dagger b_1\rangle - tZ\big(\langle b_1^\dagger\rangle\langle b_1\rangle + \langle b_2^\dagger\rangle\langle b_2\rangle\big). \end{aligned} \tag{G.5}$$

The first row and the first term on the second row are obtained from the atomic part of the Hamiltonian. In the kinetic part, $Z = 3$ is the number of near-neighbors on the ladder.

The order parameters depend on the coefficients in the variational wavefunction:

$$\begin{aligned}
\langle b_1^\dagger \rangle &= \sqrt{2}x^* a + y^* b + a^* n, \\
\langle b_2^\dagger \rangle &= y^* a + \sqrt{2}z^* b + b^* n, \\
\langle b_1^\dagger b_2 \rangle &= a^* b + \sqrt{2}x^* y + \sqrt{2}y^* z, \\
\langle b_2^\dagger b_1 \rangle &= b^* a + \sqrt{2}y^* x + \sqrt{2}z^* y, \\
\langle b_1^\dagger b_1 \rangle &= |a|^2 + 2|x|^2 + |y|^2, \\
\langle b_2^\dagger b_2 \rangle &= |b|^2 + 2|z|^2 + |y|^2.
\end{aligned} \tag{G.6}$$

The order parameters determine the two phases of interest, *Rung Mott* and *Rung superfluid* , based on the following classification: $\langle b_{1,2}^\dagger \rangle = 0$ and $\langle b_1^\dagger b_2 \rangle = 0$ in *Rung Mott* , whereas $\langle b_1^\dagger b_1 + b_2^\dagger b_2 \rangle \neq 1$ in the superfluid phase with the exception of a special line that starts at the tip of the Mott lobe.

In the inset of Figure 4.5 of the main text, we have plotted the mean-field phase diagram of hard core bosons at finite $V_\perp$ with dashed lines. The hard core constraint is implemented requiring $|x| = |z| = 0$. The boundaries of the Mott lobe $\mu = -g$ and $\mu = V_\perp + g$ are consistent with the calculation in the atomic limit. Remark that Josephson coupling itself is enough for the *Rung Mott* to exist: In the limit $V_\perp \to 0$, the *Rung Mott* phase is located between $\mu = \pm g$.

G.3 DMRG phase diagram

We use the density matrix renormalization group implementation of Ref. [221] to draw the phase diagram for a one-dimensional system. We determine the ground state at fixed particle number (setting $\mu = 0$). For N particles on a finite ladder of length L with open boundary conditions, half filling corresponds to $N = L$.

With respect to the reference ground state energy at half filling, the particle

and hole excitation energies are

$$\pm\,\mu^{\pm} = E(N = L \pm 1) - E(N = L), \tag{G.7}$$

and the Mott gap is defined as $\Delta^{+} \equiv \mu^{+} - \mu^{-}$. The particle and hole excitation energies determine the boundaries of the Mott lobe. These phase boundaries can be plotted in the t (hopping along the chains) and μ plane. The Mott phase has a finite gap Δ^{+}, which is expected to scale with the finite size of the system, L [392],

$$\begin{aligned} \mu^{\mathrm{MI}} &\sim A_0 + A_1\frac{1}{L} + A_2\frac{1}{L^2}, \\ \mu^{\mathrm{SF}} &\sim B_0 + B_1\frac{1}{L}. \end{aligned} \tag{G.8}$$

The corrected phase boundaries $\mu^{\pm}$ are determined from extrapolations to the thermodynamic limit $1/L \to \infty$ from a polynomial fit. In the inset of Figure 4.5, we show the results for finite-size extrapolation from $L = 24, 36, 48, 64, 80$, for hardcore bosons with $V_{\perp} = 1.0$ and $g = 0.25$. The top and bottom curves represent μ^{+} and μ^{-}, respectively. The error bars from linear fits of $\mu^{\pm}(1/L)$ are magnified by a factor of 10^2. The lines going through the points are guides to the eye. The DMRG routine of Ref. [221] was run with 2 sweeps, a maximum of 60 states in the truncated space, and 20 warm-up states.

Appendix H

Strong coupling expansion for the *Rung Mott* phase

In this appendix we derive the spin chain Hamiltonian of Sec. 4.3. For brevity, we present a derivation where gauge fields are set to zero, and restore them at the very end. We are interested in the Hamiltonian connecting states with only singly occupied rungs, via doubly occupied virtual states which have higher energy (of linear order in $U, V_\perp$). This Hamiltonian can be expressed as [303]

$$(H_\sigma)_{\alpha\beta} = -\sum_{\langle ij\rangle}\sum_{\gamma} \frac{(T_{ij})_{\alpha\gamma}(T_{ij})_{\gamma\alpha}}{E_\gamma - \frac{1}{2}(E_\alpha + E_\beta)}, \tag{H.1}$$

where $\langle ij\rangle$ represent two nearest–neighbors on the lattice and T_{ij} is the kinetic term corresponding to these two sites in (4.1). The states denoted by α and β denote the unperturbed half-filled states,

$$\alpha: \ |n_1 n_2\rangle_i |n_1 n_2\rangle_j \in \ \{ \ \ |10\rangle_i|10\rangle_j, |10\rangle_i|01\rangle_j,$$
$$|01\rangle_i|10\rangle_j, |01\rangle_i|01\rangle_j\}.$$

The γ states are the excited states produced by a single application of the operator T_{ij}

$$\gamma:\ |n_1n_2\rangle_i|n_1n_2\rangle_j \in \{\quad |20\rangle_i|00\rangle_j, |11\rangle_i|00\rangle_j, |02\rangle_i|00\rangle_j,$$
$$|00\rangle_i|20\rangle_j, |00\rangle_i|11\rangle_j, |00\rangle_i|02\rangle_j\}.$$

The spin Hamiltonian becomes apparent through the identification $|\uparrow\rangle \equiv |10\rangle$ and $|\downarrow\rangle \equiv |01\rangle$. Our original bosons correspond to the Schwinger boson representation of spin: $\sigma_x = b_1^\dagger b_2 + b_2^\dagger b_1$, $\sigma_y = -ib_1^\dagger b_2 + ib_2^\dagger b_1$, and $\sigma_z = b_1^\dagger b_1 - b_2^\dagger b_2$. In the ordered basis $\{|\uparrow\rangle, |\downarrow\rangle\} \otimes \{|\uparrow\rangle, |\downarrow\rangle\}$, the Hamiltonian reads

$$H_\sigma = \begin{pmatrix} -\frac{4t^2}{U} & 0 & 0 & 0 \\ 0 & -\frac{2t^2}{V_\perp} & -\frac{2t^2}{V_\perp} & 0 \\ 0 & -\frac{2t^2}{V_\perp} & -\frac{2t^2}{V_\perp} & 0 \\ 0 & 0 & 0 & -\frac{4t^2}{U} \end{pmatrix}, \tag{H.2}$$

or, more compactly in terms of Pauli matrices

$$H_\sigma = -\sum_{\langle ij\rangle} \left(2J_{xx}(\sigma_i^+\sigma_j^- + \text{H.c.}) - J_z\sigma_i^z\sigma_j^z\right) - g\sum_i \sigma_i^x,$$
$$J_{xx} = \frac{t^2}{V_\perp},\ \ J_z = t^2\left(-\frac{2}{U} + \frac{1}{V_\perp}\right). \tag{H.3}$$

Above, we have used $\sigma_i^\pm = \frac{1}{2}(\sigma_i^x \pm \sigma_i^y)$. The conversion term g, or the spin-flip operator, does not create doubly-occupied states when acting on singly occupied rungs. We have left out a constant term in the Hamiltonian equal to $-t^2\,(2/U + 1/V_\perp)$, which does not affect the dynamics. Finally, gauge fields will appear in all terms but the Ising term, which is related to the boson density and therefore does not retain a Peierls phase. Restoring these to their nonzero values, we obtain (4.61).

Bibliography

[1] On the theory of superconductivity. In Haar, D. Ter, editor, *Collected Papers of L.D. Landau*, pages 546 – 568. Pergamon, 1965.

[2] X. G. Wen. Topological orders in rigid states. *International Journal of Modern Physics B*, 04(02):239–271, 1990.

[3] Xiao-Gang Wen. Topological orders and edge excitations in fractional quantum Hall states. *Advances in Physics*, 44(5):405–473, 1995.

[4] S. M. Girvin and A. H. MacDonald. Off-diagonal long-range order, oblique confinement, and the fractional quantum Hall effect. *Phys. Rev. Lett.*, 58:1252–1255, Mar 1987.

[5] S. C. Zhang, T. H. Hansson, and S. Kivelson. Effective-Field-Theory Model for the Fractional Quantum Hall Effect. *Phys. Rev. Lett.*, 62:82–85, Jan 1989.

[6] N. Read. Order Parameter and Ginzburg-Landau Theory for the Fractional Quantum Hall Effect. *Phys. Rev. Lett.*, 62:86–89, Jan 1989.

[7] Z. F. Ezawa and A. Iwazaki. Chern-Simons gauge theories for the fractional-quantum-Hall-effect hierarchy and anyon superconductivity. *Phys. Rev. B*, 43:2637–2641, Feb 1991.

[8] R. B. Laughlin. Anomalous Quantum Hall Effect: An Incompressible Quantum Fluid with Fractionally Charged Excitations. *Phys. Rev. Lett.*, 50:1395–1398, May 1983.

[9] D. C. Tsui, H. L. Störmer, and A. C. Gossard. Two-Dimensional Magnetotransport in the Extreme Quantum Limit. *Phys. Rev. Lett.*, 48:1559–1562, May 1982.

[10] K. v. Klitzing, G. Dorda, and M. Pepper. New Method for High-Accuracy Determination of the Fine-Structure Constant Based on Quantized Hall Resistance. *Phys. Rev. Lett.*, 45:494–497, Aug 1980.

[11] D. J. Thouless, M. Kohmoto, M. P. Nightingale, and M. den Nijs. Quantized Hall Conductance in a Two-Dimensional Periodic Potential. *Phys. Rev. Lett.*, 49:405–408, Aug 1982.

[12] F. D. M. Haldane. Model for a Quantum Hall Effect without Landau Levels: Condensed-Matter Realization of the "Parity Anomaly". *Phys. Rev. Lett.*, 61:2015–2018, Oct 1988.

[13] Hasan, M. Z. and Kane, C. L. *Colloquium* : Topological insulators. *Rev. Mod. Phys.*, 82:3045–3067, Nov 2010.

[14] Xiao-Liang Qi and Shou-Cheng Zhang. Topological insulators and superconductors. *Rev. Mod. Phys.*, 83:1057–1110, Oct 2011.

[15] T. Senthil. Symmetry Protected Topological phases of Quantum Matter. *ArXiv e-prints*, May 2014.

[16] Xiao-Liang Qi. Symmetry Meets Topology. *Science*, 338(6114):1550–1551, 2012.

[17] C. L. Kane and E. J. Mele. Quantum Spin Hall Effect in Graphene. *Phys. Rev. Lett.*, 95:226801, Nov 2005.

[18] Markus Büttiker. Edge-State Physics Without Magnetic Fields. *Science*, 325(5938):278–279, 2009.

[19] C.W.J. Beenakker. Search for Majorana Fermions in Superconductors. *Annual Review of Condensed Matter Physics*, 4(1):113–136, 2013.

[20] Xiao-Liang Qi, Taylor L. Hughes, and Shou-Cheng Zhang. Topological field theory of time-reversal invariant insulators. *Phys. Rev. B*, 78:195424, Nov 2008.

[21] Qi, Xiao-Liang and Zhang, Shou-Cheng. The quantum spin Hall effect and topological insulators. *Physics Today*, January 2010:33.

[22] Frank Wilczek. Quantum Mechanics of Fractional-Spin Particles. *Phys. Rev. Lett.*, 49:957–959, Oct 1982.

[23] Ady Stern. Anyons and the quantum Hall effect a pedagogical review. *Annals of Physics*, 323(1):204 – 249, 2008. January Special Issue 2008.

[24] A. Y. Kitaev. Fault-tolerant quantum computation by anyons. *Annals of Physics*, 303:2–30, January 2003.

[25] R. Walter Ogburn and John Preskill. Topological Quantum Computation. In C P Williams, editor, *Quantum Computing and Quantum Communications*, volume 1509 of *Lecture Notes in Computer Science*, pages 341–356. Springer Berlin Heidelberg, 1999.

[26] Chetan Nayak, Steven H. Simon, Ady Stern, Michael Freedman, and Sankar Das Sarma. Non-Abelian anyons and topological quantum computation. *Rev. Mod. Phys.*, 80:1083–1159, Sep 2008.

[27] Rahul Roy and Shivaji Sondhi. Fractional quantum Hall effect without Landau levels. *Physics*, 4:46, Jun 2011.

[28] N. Regnault and B. Andrei Bernevig. Fractional Chern Insulator. *Phys. Rev. X*, 1:021014, Dec 2011.

[29] Titus Neupert, Luiz Santos, Claudio Chamon, and Christopher Mudry. Fractional Quantum Hall States at Zero Magnetic Field. *Phys. Rev. Lett.*, 106:236804, Jun 2011.

[30] Evelyn Tang, Jia-Wei Mei, and Xiao-Gang Wen. High-Temperature Fractional Quantum Hall States. *Phys. Rev. Lett.*, 106:236802, Jun 2011.

[31] D. N. Sheng, Zheng-Cheng Gu, Kai Sun, and L. Sheng. Fractional quantum Hall effect in the absence of Landau levels. *Nature Communications*, 2:389, 2011.

[32] M. Levin and A. Stern. Fractional Topological Insulators. *Physical Review Letters*, 103(19):196803, November 2009.

[33] R. P. Feynman. Simulating physics with computers. *International Journal of Theoretical Physics*, 21(6-7):467–488, 1982.

[34] Jean Dalibard, Fabrice Gerbier, Gediminas Juzeliūnas, and Patrik Öhberg. Colloquium: Artificial gauge potentials for neutral atoms. *Rev. Mod. Phys.*, 83:1523–1543, Nov 2011.

[35] N Goldman, G Juzeliunas, P Öhberg, and I B Spielman. Light-induced gauge fields for ultracold atoms. *Reports on Progress in Physics*, 77(12):126401, 2014.

[36] L. Lu, J. D. Joannopoulos, and M. Soljačić. Topological photonics. *Nature Photon.*, 8:821–829, November 2014.

[37] Douglas R. Hofstadter. Energy levels and wave functions of Bloch electrons in rational and irrational magnetic fields. *Phys. Rev. B*, 14:2239–2249, Sep 1976.

[38] M. Aidelsburger, M. Atala, M. Lohse, J. T. Barreiro, B. Paredes, and I. Bloch. Realization of the Hofstadter Hamiltonian with Ultracold Atoms in Optical Lattices. *Phys. Rev. Lett.*, 111:185301, Oct 2013.

[39] M. Aidelsburger, M. Lohse, C. Schweizer, M. Atala, J. T. Barreiro, S. Nascimbène, N. R. Cooper, I. Bloch, and N. Goldman. Measuring the

Chern number of Hofstadter bands with ultracold bosonic atoms. *Nature Physics*, 11:162–166, February 2015.

[40] Hirokazu Miyake, Georgios A. Siviloglou, Colin J. Kennedy, William Cody Burton, and Wolfgang Ketterle. Realizing the Harper Hamiltonian with Laser-Assisted Tunneling in Optical Lattices. *Phys. Rev. Lett.*, 111:185302, Oct 2013.

[41] G. Jotzu, M. Messer, R. Desbuquois, M. Lebrat, T. Uehlinger, D. Greif, and T. Esslinger. Experimental realisation of the topological Haldane model. *Nature*, 515:237–240, Nov 2014.

[42] K. Jimenez-Garcia, L. J. LeBlanc, R. A. Williams, M. C. Beeler, A. R. Perry, and I. B. Spielman. Peierls Substitution in an Engineered Lattice Potential. *Phys. Rev. Lett.*, 108:225303, May 2012.

[43] J. Struck, C. Ölschläger, M. Weinberg, P. Hauke, J. Simonet, A. Eckardt, M. Lewenstein, K. Sengstock, and P. Windpassinger. Tunable Gauge Potential for Neutral and Spinless Particles in Driven Optical Lattices. *Phys. Rev. Lett.*, 108:225304, May 2012.

[44] F. D. M. Haldane and S. Raghu. Possible Realization of Directional Optical Waveguides in Photonic Crystals with Broken Time-Reversal Symmetry. *Phys. Rev. Lett.*, 100:013904, Jan 2008.

[45] S. Raghu and F. D. M. Haldane. Analogs of quantum-Hall-effect edge states in photonic crystals. *Phys. Rev. A*, 78:033834, Sep 2008.

[46] Zheng Wang, Yidong Chong, J. D. Joannopoulos, and Marin Soljacic. Observation of unidirectional backscattering-immune topological electromagnetic states. *Nature*, 461:772–775, 2009.

[47] M. Hafezi, Eugene A. Demler, Mikhail D. Lukin, and Jacob M. Taylor. Robust optical delay lines with topological protection. *Nat. Phys.*, 7:907–912, 2011.

[48] M. Hafezi, S. Mittal, J. Fan, A. Migdall, and J. M. Taylor. Imaging topological edge states in silicon photonics. *Nature Photon.*, 7:1001–1005, December 2013.

[49] S. Mittal, J. Fan, S. Faez, A. Migdall, J. M. Taylor, and M. Hafezi. Topologically Robust Transport of Photons in a Synthetic Gauge Field. *Phys. Rev. Lett.*, 113:087403, Aug 2014.

[50] Alexander B. Khanikaev, S. Hossein Mousavi, Wang-Kong Tse, Mehdi Kargarian, Allan H. MacDonald, and Gennady Shvets. Photonic topological insulators. *Nat. Mater.*, 12:233–239, 2013.

[51] M. C. Rechtsman, J. M. Zeuner, Y. Plotnik, Y. Lumer, D. Podolsky, F. Dreisow, S. Nolte, M. Segev, and A. Szameit. Photonic Floquet topological insulators. *Nature*, 496:196–200, April 2013.

[52] V. G. Sala, D. D. Solnyshkov, I. Carusotto, T. Jacqmin, A. Lemaître, H. Terças, A. Nalitov, M. Abbarchi, E. Galopin, I. Sagnes, J. Bloch, G. Malpuech, and A. Amo. Spin-Orbit Coupling for Photons and Polaritons in Microstructures. *Phys. Rev. X*, 5:011034, Mar 2015.

[53] M. Schmidt, V. Peano, and F. Marquardt. Optomechanical Metamaterials: Dirac polaritons, Gauge fields, and Instabilities. *ArXiv e-prints*, November 2013.

[54] Jia Ningyuan, Clai Owens, Ariel Sommer, David Schuster, and Jonathan Simon. Time- and Site-Resolved Dynamics in a Topological Circuit. *Phys. Rev. X*, 5:021031, Jun 2015.

[55] Victor V. Albert, Leonid I. Glazman, and Liang Jiang. Topological properties of linear circuit lattices. *Phys. Rev. Lett.*, 114:173902, Apr 2015.

[56] Roman Süsstrunk and Sebastian D. Huber. Observation of phononic helical edge states in a mechanical topological insulator. *Science*, 349(6243):47–50, 2015.

[57] Jens Koch, Andrew A. Houck, Karyn Le Hur, and S. M. Girvin. Time-reversal-symmetry breaking in circuit-QED-based photon lattices. *Phys. Rev. A*, 82:043811, Oct 2010.

[58] Alexandru Petrescu, Andrew A. Houck, and Karyn Le Hur. Anomalous Hall effects of light and chiral edge modes on the Kagomé lattice. *Phys. Rev. A*, 86:053804, Nov 2012.

[59] Leon Balents. Spin liquids in frustrated magnets. *Nature*, 464:199, 2010.

[60] Anders S. Sørensen, Eugene Demler, and Mikhail D. Lukin. Fractional Quantum Hall States of Atoms in Optical Lattices. *Phys. Rev. Lett.*, 94:086803, Mar 2005.

[61] M. Hafezi, A. S. Sørensen, E. Demler, and M. D. Lukin. Fractional quantum Hall effect in optical lattices. *Phys. Rev. A*, 76:023613, Aug 2007.

[62] L. Hormozi, G. Möller, and S. H. Simon. Fractional Quantum Hall Effect of Lattice Bosons Near Commensurate Flux. *Phys. Rev. Lett.*, 108:256809, Jun 2012.

[63] R. N. Palmer and D. Jaksch. High-Field Fractional Quantum Hall Effect in Optical Lattices. *Phys. Rev. Lett.*, 96:180407, 2003.

[64] Nigel R. Cooper and Jean Dalibard. Reaching Fractional Quantum Hall States with Optical Flux Lattices. *Phys. Rev. Lett.*, 110:185301, Apr 2013.

[65] N. Y. Yao, A. V. Gorshkov, C. R. Laumann, A. M. Läuchli, J. Ye, and M. D. Lukin. Realizing Fractional Chern Insulators in Dipolar Spin Systems. *Phys. Rev. Lett.*, 110:185302, Apr 2013.

[66] A. Sterdyniak, B. Andrei Bernevig, Nigel R. Cooper, and N. Regnault. Interacting bosons in topological optical flux lattices. *Phys. Rev. B*, 91:035115, Jan 2015.

[67] Mohammad Hafezi, Mikhail D Lukin, and Jacob M Taylor. Non-equilibrium fractional quantum Hall state of light. *New Journal of Physics*, 15(6):063001, 2013.

[68] Eliot Kapit, Mohammad Hafezi, and Steven H. Simon. Induced Self-Stabilization in Fractional Quantum Hall States of Light. *Phys. Rev. X*, 4:031039, Sep 2014.

[69] Alexandru Petrescu and Karyn Le Hur. Bosonic Mott Insulator with Meissner Currents. *Phys. Rev. Lett.*, 111:150601, Oct 2013.

[70] Ivana Vasić, Alexandru Petrescu, Karyn Le Hur, and Walter Hofstetter. Chiral bosonic phases on the Haldane honeycomb lattice. *Phys. Rev. B*, 91:094502, Mar 2015.

[71] A. Petrescu and K. Le Hur. Chiral Mott insulators, Meissner effect, and Laughlin states in quantum ladders. *Phys. Rev. B*, 91(5):054520, February 2015.

[72] A. H. Castro Neto, F. Guinea, N. M. R. Peres, K. S. Novoselov, and A. K. Geim. The electronic properties of graphene. *Rev. Mod. Phys.*, 81:109–162, Jan 2009.

[73] D. L. Underwood, W. E. Shanks, Jens Koch, and A. A. Houck. Low-disorder microwave cavity lattices for quantum simulation with photons. *Phys. Rev. A*, 86:023837, Aug 2012.

[74] Matthew P. A. Fisher, Peter B. Weichman, G. Grinstein, and Daniel S. Fisher. Boson localization and the superfluid-insulator transition. *Phys. Rev. B*, 40:546–570, Jul 1989.

[75] Thierry Giamarchi. *Quantum Physics in One Dimension*. Clarendon Press, Oxford, 2003.

[76] Steven R. White. Density matrix formulation for quantum renormalization groups. *Phys. Rev. Lett.*, 69:2863–2866, Nov 1992.

[77] Steven R. White. Density-matrix algorithms for quantum renormalization groups. *Phys. Rev. B*, 48:10345–10356, Oct 1993.

[78] M. Atala, M. Aidelsburger, M. Lohse, J. T. Barreiro, B. Paredes, and I. Bloch. Observation of chiral currents with ultracold atoms in bosonic ladders. *Nature Physics*, 10:588–593, August 2014.

[79] B. K. Stuhl, H.-I Lu, L. M. Aycock, D. Genkina, and I. B. Spielman. Visualizing edge states with an atomic Bose gas in the quantum Hall regime. *ArXiv e-prints*, February 2015.

[80] David J. Thouless. *Topological Quantum Numbers in Nonrelativistic Physics*. World Scientific, 1998.

[81] Grigory Volovik. *The Universe in a Helium Droplet*. Clarendon Press, Oxford, 2003.

[82] Mikio Nakahara. *Geometry, topology and physics*. IoP – Institute of Physics Publishing, 2003.

[83] N. D. Mermin. The topological theory of defects in ordered media. *Rev. Mod. Phys.*, 51:591–648, Jul 1979.

[84] S. M. Girvin. Course 2: The Quantum Hall Effect: Novel Excitations and Broken Symmetries. In A. Comtet, T. Jolicoeur, S. Ouvry, and F. David, editors, *Topological Aspects of Low Dimensional Systems*, page 53, 1999.

[85] M. Z. Hasan and J. E. Moore. Three-Dimensional Topological Insulators. *Annual Review of Condensed Matter Physics*, 2:55–78, March 2011.

[86] M. V. Berry. Quantal phase factors accompanying adiabatic changes. *Proc. R. Soc. Lond. A*, 392:45–57, 1984.

[87] A. Messiah. *Quantum Mechanics. Volume 2.* North–Holland Publishing Company. Amsterdam., 1962.

[88] S. Pancharatnam. Generalized theory of interference, and its applications. *Proceedings of the Indian Academy of Sciences - Section A*, 44(5):247–262, 1956.

[89] Barry Simon. Holonomy, the Quantum Adiabatic Theorem, and Berry's Phase. *Phys. Rev. Lett.*, 51:2167–2170, Dec 1983.

[90] J. Zak. Berry's phase for energy bands in solids. *Phys. Rev. Lett.*, 62:2747–2750, Jun 1989.

[91] Y. Aharonov and D. Bohm. Significance of Electromagnetic Potentials in the Quantum Theory. *Phys. Rev.*, 115:485–491, Aug 1959.

[92] J.J. Sakurai. *Modern Quantum Mechanics.* Addison Wesley, 1993.

[93] Marder, Michael P. *Condensed Matter Physics.* John Wiley & Sons, 2010.

[94] Gregory H. Wannier. Dynamics of Band Electrons in Electric and Magnetic Fields. *Rev. Mod. Phys.*, 34:645–655, Oct 1962.

[95] Nicola Marzari and David Vanderbilt. Maximally localized generalized Wannier functions for composite energy bands. *Phys. Rev. B*, 56:12847–12865, Nov 1997.

[96] E.I. Blount. Formalisms of band theory. volume 13 of *Solid State Physics*, pages 305 – 373. Academic Press, 1962.

[97] W. Kohn. Analytic Properties of Bloch Waves and Wannier Functions. *Phys. Rev.*, 115:809–821, Aug 1959.

[98] R. D. King-Smith and David Vanderbilt. Theory of polarization of crystalline solids. *Phys. Rev. B*, 47:1651–1654, Jan 1993.

[99] D J Thouless. Wannier functions for magnetic sub-bands. *Journal of Physics C: Solid State Physics*, 17(12):L325, 1984.

[100] Christian Brouder, Gianluca Panati, Matteo Calandra, Christophe Mourougane, and Nicola Marzari. Exponential Localization of Wannier Functions in Insulators. *Phys. Rev. Lett.*, 98:046402, Jan 2007.

[101] G. Panati. Triviality of Bloch and Bloch-Dirac Bundles. *Annales Henri Poincaré*, 8:995–1011, July 2007.

[102] Mahito Kohmoto. Topological invariant and the quantization of the hall conductance. *Annals of Physics*, 160(2):343 – 354, 1985.

[103] J. E. Avron, R. Seiler, and B. Simon. Homotopy and Quantization in Condensed Matter Physics. *Phys. Rev. Lett.*, 51:51–53, Jul 1983.

[104] R. B. Laughlin. Quantized Hall conductivity in two dimensions. *Phys. Rev. B*, 23:5632–5633, May 1981.

[105] B. I. Halperin. Quantized Hall conductance, current-carrying edge states, and the existence of extended states in a two-dimensional disordered potential. *Phys. Rev. B*, 25:2185–2190, Feb 1982.

[106] Qian Niu, D. J. Thouless, and Yong-Shi Wu. Quantized Hall conductance as a topological invariant. *Phys. Rev. B*, 31:3372–3377, Mar 1985.

[107] Gordon W. Semenoff. Condensed-Matter Simulation of a Three-Dimensional Anomaly. *Phys. Rev. Lett.*, 53:2449–2452, Dec 1984.

[108] Kenzo Ishikawa and Toyoki Matsuyama. A microscopic theory of the quantum Hall effect. *Nucl. Phys. B*, 280:523–548, 1987.

[109] C. L. Kane and E. J. Mele. Z_2 Topological Order and the Quantum Spin Hall Effect. *Phys. Rev. Lett.*, 95:146802, Sep 2005.

[110] B. Andrei Bernevig and Shou-Cheng Zhang. Quantum Spin Hall Effect. *Phys. Rev. Lett.*, 96:106802, Mar 2006.

[111] B. Andrei Bernevig, Taylor L. Hughes, and Shou-Cheng Zhang. Quantum Spin Hall Effect and Topological Phase Transition in HgTe Quantum Wells. *Science*, 314(5806):1757–1761, 2006.

[112] Markus Knig, Steffen Wiedmann, Christoph Brne, Andreas Roth, Hartmut Buhmann, Laurens W. Molenkamp, Xiao-Liang Qi, and Shou-Cheng Zhang. Quantum Spin Hall Insulator State in HgTe Quantum Wells. *Science*, 318(5851):766–770, 2007.

[113] Andreas Roth, Christoph Brne, Hartmut Buhmann, Laurens W. Molenkamp, Joseph Maciejko, Xiao-Liang Qi, and Shou-Cheng Zhang. Nonlocal Transport in the Quantum Spin Hall State. *Science*, 325(5938):294–297, 2009.

[114] Cui-Zu Chang, Jinsong Zhang, Xiao Feng, Jie Shen, Zuocheng Zhang, Minghua Guo, Kang Li, Yunbo Ou, Pang Wei, Li-Li Wang, Zhong-Qing Ji, Yang Feng, Shuaihua Ji, Xi Chen, Jinfeng Jia, Xi Dai, Zhong Fang, Shou-Cheng Zhang, Ke He, Yayu Wang, Li Lu, Xu-Cun Ma, and Qi-Kun Xue. Experimental Observation of the Quantum Anomalous Hall Effect in a Magnetic Topological Insulator. *Science*, 340(6129):167–170, 2013.

[115] Z. Wang, Y. D. Chong, J. D. Joannopoulos, and M. Soljačić. Reflection-Free One-Way Edge Modes in a Gyromagnetic Photonic Crystal. *Physical Review Letters*, 100(1):013905, January 2008.

[116] Iacopo Carusotto and Cristiano Ciuti. Quantum fluids of light. *Rev. Mod. Phys.*, 85:299–366, Feb 2013.

[117] R. O. Umucalilar and I. Carusotto. Artificial gauge field for photons in coupled cavity arrays. *Phys. Rev. A*, 84:043804, Oct 2011.

[118] Tomoki Ozawa and Iacopo Carusotto. Anomalous and Quantum Hall Effects in Lossy Photonic Lattices. *Phys. Rev. Lett.*, 112:133902, Apr 2014.

[119] Mohammad Hafezi. Measuring Topological Invariants in Photonic Systems. *Phys. Rev. Lett.*, 112:210405, May 2014.

[120] P. Roushan, C. Neill, Y. Chen, M. Kolodrubetz, C. Quintana, N. Leung, M. Fang, R. Barends, B. Campbell, Z. Chen, B. Chiaro, A. Dunsworth, E. Jeffrey, J. Kelly, A. Megrant, J. Mutus, P. O'Malley, D. Sank, A. Vainsencher, J. Wenner, T. White, A. Polkovnikov, A. N. Cleland, and J. M. Martinis. Observation of topological transitions in interacting quantum circuits. *Nature*, 515:241–244, Nov 2014.

[121] N. H. Lindner, G. Refael, and V. Galitski. Floquet topological insulator in semiconductor quantum wells. *Nat. Phys.* , 7:490–495, June 2011.

[122] Takuya Kitagawa, Erez Berg, Mark Rudner, and Eugene Demler. Topological characterization of periodically driven quantum systems. *Phys. Rev. B*, 82:235114, Dec 2010.

[123] J. Cayssol. Introduction to Dirac materials and topological insulators. *Comptes Rendus Physique*, 14:760–778, November 2013.

[124] Mark S. Rudner, Netanel H. Lindner, Erez Berg, and Michael Levin. Anomalous Edge States and the Bulk-Edge Correspondence for Periodically Driven Two-Dimensional Systems. *Phys. Rev. X*, 3:031005, Jul 2013.

[125] David Carpentier, Pierre Delplace, Michel Fruchart, and Krzysztof Gawędzki. Topological index for periodically driven time-reversal invariant 2d systems. *Phys. Rev. Lett.*, 114:106806, Mar 2015.

[126] Hossein Dehghani, Takashi Oka, and Aditi Mitra. Dissipative Floquet topological systems. *Phys. Rev. B*, 90:195429, Nov 2014.

[127] L. Tarruell, D. Greif, T. Uehlinger, G. Jotzu, and T. Esslinger. Creating, moving and merging Dirac points with a Fermi gas in a tunable honeycomb lattice. *Nature*, 483:302–305, March 2012.

[128] D. A. Abanin, T. Kitagawa, I. Bloch, and E. Demler. Interferometric Approach to Measuring Band Topology in 2D Optical Lattices. *Physical Review Letters*, 110(16):165304, April 2013.

[129] L. Duca, T. Li, M. Reitter, I. Bloch, M. Schleier-Smith, and U. Schneider. An Aharonov-Bohm interferometer for determining Bloch band topology. *Science*, 347:288–292, January 2015.

[130] Yi-Fei Wang, Zheng-Cheng Gu, Chang-De Gong, and D. N. Sheng. Fractional Quantum Hall Effect of Hard-Core Bosons in Topological Flat Bands. *Phys. Rev. Lett.*, 107:146803, Sep 2011.

[131] N. Regnault and B. Bernevig. Fractional Chern Insulator. *Phys. Rev. X*, 1:021014, Dec 2011.

[132] B. A. Bernevig and N. Regnault. Emergent many-body translational symmetries of Abelian and non-Abelian fractionally filled topological insulators. *Phys. Rev. B*, 85(7):075128, February 2012.

[133] Yi-Fei Wang, Hong Yao, Zheng-Cheng Gu, Chang-De Gong, and D. Sheng. Non-Abelian Quantum Hall Effect in Topological Flat Bands. *Phys. Rev. Lett.*, 108:126805, Mar 2012.

[134] M. O. Goerbig. From fractional Chern insulators to a fractional quantum spin hall effect. *European Physical Journal B*, 85:15, January 2012.

[135] Y.-L. Wu, B. A. Bernevig, and N. Regnault. Zoology of fractional Chern insulators. *Phys. Rev. B*, 85(7):075116, February 2012.

[136] Adolfo G. Grushin, Álvaro Gómez-León, and Titus Neupert. Floquet Fractional Chern Insulators. *Phys. Rev. Lett.*, 112:156801, Apr 2014.

[137] Andrew A. Houck, Hakan E. Türeci, and Jens Koch. On-chip quantum simulation with superconducting circuits. *Nature Physics*, 8:292299, 2012.

[138] A. Wallraff, D. I. Schuster, A. Blais, L. Frunzio, R.-S. Huang, J. Majer, S. Kumar, S. M. Girvin, and R. J. Schoelkopf. Strong coupling of a single photon to a superconducting qubit using circuit quantum electrodynamics. *Nature*, 431:162–167, September 2004.

[139] M. J. Hartmann, F. G. S. L. Brandao, and M. B. Plenio. Quantum Many-Body Phenomena in Coupled Cavity Arrays. *ArXiv e-prints*, August 2008.

[140] A. Tomadin and R. Fazio. Many-body phenomena in QED-cavity arrays. *Journal of the Optical Society of America B Optical Physics*, 27:130, April 2010.

[141] R. J. Schoelkopf and S. M. Girvin. Wiring up quantum systems. *Nature*, 451:664–669, Feb 2008.

[142] Jaynes, E.T. and Cummings, F.W. Comparison of quantum and semiclassical radiation theories with application to the beam maser. *Proceedings of the IEEE*, 51(1):89–109, Jan 1963.

[143] Jens Koch and Karyn Le Hur. Superfluid-Mott-insulator transition of light in the Jaynes-Cummings lattice. *Phys. Rev. A*, 80:023811, Aug 2009.

[144] A. D. Greentree, C. Tahan, J. H. Cole, and L. C. L. Hollenberg. Quantum phase transitions of light. *Nature Physics*, 2:856–861, December 2006.

[145] Dimitris G. Angelakis, Marcelo Franca Santos, and Sougato Bose. Photon-blockade-induced Mott transitions and XY spin models in coupled cavity arrays. *Phys. Rev. A*, 76:031805, Sep 2007.

[146] M. J. Hartmann, F. G. S. L. Brandão, and M. B. Plenio. Strongly interacting polaritons in coupled arrays of cavities. *Nature Physics*, 2:849–855, December 2006.

[147] Davide Rossini and Rosario Fazio. Mott-Insulating and Glassy Phases of Polaritons in 1D Arrays of Coupled Cavities. *Phys. Rev. Lett.*, 99:186401, Oct 2007.

[148] Markus Aichhorn, Martin Hohenadler, Charles Tahan, and Peter B. Littlewood. Quantum Fluctuations, Temperature, and Detuning Effects in Solid-Light Systems. *Phys. Rev. Lett.*, 100:216401, May 2008.

[149] Neil Na, Shoko Utsunomiya, Lin Tian, and Yoshihisa Yamamoto. Strongly correlated polaritons in a two-dimensional array of photonic crystal microcavities. *Phys. Rev. A*, 77:031803, Mar 2008.

[150] S. Schmidt and G. Blatter. Strong Coupling Theory for the Jaynes-Cummings-Hubbard Model. *Phys. Rev. Lett.*, 103:086403, Aug 2009.

[151] M. Schiró, M. Bordyuh, B. Öztop, and H. E. Türeci. Phase Transition of Light in Cavity QED Lattices. *Physical Review Letters*, 109(5):053601, August 2012.

[152] M. Leib and M. J. Hartmann. Bose-Hubbard dynamics of polaritons in a chain of circuit quantum electrodynamics cavities. *New Journal of Physics*, 12(9):093031, September 2010.

[153] S. L. Sondhi, S. M. Girvin, J. P. Carini, and D. Shahar. Continuous quantum phase transitions. *Rev. Mod. Phys.*, 69:315–333, Jan 1997.

[154] Subir Sachdev. *Quantum Phase Transitions*. Cambridge University Press, 2001.

[155] Popov, Viktor Nicolayevich. *Functional integrals in quantum field theory and statistical physics*. D. Reidel Publishing Company, 1983.

[156] Sebastian D. Huber and Ehud Altman. Bose condensation in flat bands. *Phys. Rev. B*, 82:184502, Nov 2010.

[157] F. Baboux, L. Ge, T. Jacqmin, M. Biondi, A. Lemaître, L. Le Gratiet, I. Sagnes, S. Schmidt, H. E. Türeci, A. Amo, and J. Bloch. Bosonic condensation in a flat energy band. *ArXiv e-prints*, May 2015.

[158] Jaeyoon Cho, Dimitris G. Angelakis, and Sougato Bose. Fractional Quantum Hall State in Coupled Cavities. *Phys. Rev. Lett.*, 101:246809, Dec 2008.

[159] Andrew L. C. Hayward, Andrew M. Martin, and Andrew D. Greentree. Fractional Quantum Hall Physics in Jaynes-Cummings-Hubbard Lattices. *Phys. Rev. Lett.*, 108:223602, Jun 2012.

[160] R. O. Umucalilar and I. Carusotto. Fractional Quantum Hall States of Photons in an Array of Dissipative Coupled Cavities. *Phys. Rev. Lett.*, 108:206809, May 2012.

[161] A. A. Clerk, M. H. Devoret, S. M. Girvin, Florian Marquardt, and R. J. Schoelkopf. Introduction to quantum noise, measurement, and amplification. *Rev. Mod. Phys.*, 82:1155–1208, Apr 2010.

[162] Doron L. Bergman, Congjun Wu, and Leon Balents. Band touching from real-space topology in frustrated hopping models. *Phys. Rev. B*, 78:125104, Sep 2008.

[163] H. Katsura, I. Maruyama, A. Tanaka, and H. Tasaki. Ferromagnetism in the Hubbard model with topological/non-topological flat bands. *EPL (Europhysics Letters)*, 91:57007, September 2010.

[164] X. G. Wen. *Quantum Field Theory of Many-Body Systems*. Oxford University Press, 2010.

[165] F. D. M. Haldane. Berry Curvature on the Fermi Surface: Anomalous Hall Effect as a Topological Fermi-Liquid Property. *Phys. Rev. Lett.*, 93:206602, Nov 2004.

[166] I. S. Gradshteyn and I. M. Ryzhik. *Table of Integrals, Series, and Products. Seventh Edition*. Elsevier. Academic Press, 2007.

[167] Naoto Nagaosa, Jairo Sinova, Shigeki Onoda, A. H. MacDonald, and N. P. Ong. Anomalous Hall effect. *Rev. Mod. Phys.*, 82:1539–1592, May 2010.

[168] T. Jungwirth, Qian Niu, and A. H. MacDonald. Anomalous Hall Effect in Ferromagnetic Semiconductors. *Phys. Rev. Lett.*, 88:207208, May 2002.

[169] J. Bellissard, A. van Elst, and H. Schulz-Baldes. The Non Commutative Geometry of the Quantum Hall Effect . *J. Math. Phys.*, 35:5373–5471, 1994.

[170] Emil Prodan, Taylor L. Hughes, and B. Andrei Bernevig. Entanglement Spectrum of a Disordered Topological Chern Insulator. *Phys. Rev. Lett.*, 105:115501, Sep 2010.

[171] E. Prodan. Disordered topological insulators: a non-commutative geometry perspective. *Journal of Physics A Mathematical General*, 44(11):113001, March 2011.

[172] H. M. Price and N. R. Cooper. Mapping the Berry curvature from semiclassical dynamics in optical lattices. *Phys. Rev. A*, 85(3):033620, March 2012.

[173] Ming-Che Chang and Qian Niu. Berry Phase, Hyperorbits, and the Hofstadter Spectrum. *Phys. Rev. Lett.*, 75:1348–1351, Aug 1995.

[174] Ming-Che Chang and Qian Niu. Berry phase, hyperorbits, and the Hofstadter spectrum: Semiclassical dynamics in magnetic Bloch bands. *Phys. Rev. B*, 53:7010–7023, Mar 1996.

[175] Di Xiao, Ming-Che Chang, and Qian Niu. Berry phase effects on electronic properties. *Rev. Mod. Phys.*, 82:1959–2007, Jul 2010.

[176] A. Polkovnikov. Phase space representation of quantum dynamics. *Annals of Physics*, 325:1790–1852, August 2010.

[177] Robert Karplus and J. M. Luttinger. Hall Effect in Ferromagnetics. *Phys. Rev.*, 95:1154–1160, Sep 1954.

[178] L.D. Landau and E.M. Lifshitz. *Course of theoretical physics Vol. 1. Mechanics*. Pergamon, 3ed. edition, 1976.

[179] M. Ya. Azbel. Energy spectrum of a conduction electron in a magnetic field. *Sov. Phys. JETP*, 19, 1964.

[180] L. D. Landau. *Phys. Z. Sowjetunion*, 2:46, 1932.

[181] C. Zener. Non-adiabatic crossing of energy levels. *Proc. R. Soc.*, 137:696, 1932.

[182] D. Pesin and L. Balents. Mott physics and band topology in materials with strong spinorbit interaction. *Nat. Phys.*, 6:376 – 381, 2010.

[183] S. Rachel and K. Le Hur. Topological insulators and Mott physics from the Hubbard interaction. *Phys. Rev. B*, 82(7):075106, August 2010.

[184] S. Raghu, X.-L. Qi, C. Honerkamp, and S.-C. Zhang. Topological Mott Insulators. *Physical Review Letters*, 100(15):156401, April 2008.

[185] C. H. Wong and R. A. Duine. Topological transport in spin-orbit coupled bosonic mott insulators. *Phys. Rev. Lett.*, 110:115301, Mar 2013.

[186] Clement H. Wong and R. A. Duine. Quasiparticle Berry curvature and Chern numbers in spin-orbit-coupled bosonic Mott insulators. *Phys. Rev. A*, 88:053631, Nov 2013.

[187] C.-E. Bardyn, T. Karzig, G. Refael, and T. C. H. Liew. Chiral Bogoliubons in Nonlinear Bosonic Systems. *ArXiv e-prints*, March 2015.

[188] G. Engelhardt and T. Brandes. Topological Bogoliubov excitations in inversion-symmetric systems of interacting bosons. *Phys. Rev. A*, 91:053621, May 2015.

[189] Ryuichi Shindou, Jun-ichiro Ohe, Ryo Matsumoto, Shuichi Murakami, and Eiji Saitoh. Chiral spin-wave edge modes in dipolar magnetic thin films. *Phys. Rev. B*, 87:174402, May 2013.

[190] Ryuichi Shindou, Ryo Matsumoto, Shuichi Murakami, and Jun-ichiro Ohe. Topological chiral magnonic edge mode in a magnonic crystal. *Phys. Rev. B*, 87:174427, May 2013.

[191] S. Schmidt and G. Blatter. Excitations of Strongly Correlated Lattice Polaritons. *Phys. Rev. Lett.*, 104:216402, May 2010.

[192] L. D. Landau, E. M. Lifshitz, and L. P. Pitaevskii. *Statistical Physics Part 2*. Pergamom Press, Oxford, 1980.

[193] Arya Dhar, Maheswar Maji, Tapan Mishra, R. V. Pai, Subroto Mukerjee, and Arun Paramekanti. Bose-Hubbard model in a strong effective magnetic field: Emergence of a chiral Mott insulator ground state. *Phys. Rev. A*, 85:041602, Apr 2012.

[194] Arya Dhar, Tapan Mishra, Maheswar Maji, R. V. Pai, Subroto Mukerjee, and Arun Paramekanti. Chiral Mott insulator with staggered loop currents in the fully frustrated Bose-Hubbard model. *Phys. Rev. B*, 87:174501, May 2013.

[195] Michael P. Zaletel, S. A. Parameswaran, Andreas Rüegg, and Ehud Altman. Chiral bosonic Mott insulator on the frustrated triangular lattice. *Phys. Rev. B*, 89:155142, Apr 2014.

[196] Akiyuki Tokuno and Antoine Georges. Ground states of a bosehubbard ladder in an artificial magnetic field: field-theoretical approach. *New Journal of Physics*, 16:073005, 2014.

[197] Vivek Aji and C. M. Varma. Spin order accompanying loop-current order in cuprate superconductors. *Phys. Rev. B*, 75:224511, Jun 2007.

[198] Sudip Chakravarty, Hae-Young Kee, and Chetan Nayak. Orbital Magnetism in the Cuprates. *International Journal of Modern Physics B*, 16(20n22):3140–3146, 2002.

[199] Victor Chua, Hong Yao, and Gregory A. Fiete. Exact chiral spin liquid with stable spin Fermi surface on the kagome lattice. *Phys. Rev. B*, 83:180412, May 2011.

[200] Laura Messio, Bernard Bernu, and Claire Lhuillier. Kagome Antiferromagnet: A Chiral Topological Spin Liquid? *Phys. Rev. Lett.*, 108:207204, May 2012.

[201] Simeng Yan, David A. Huse, and Steven R. White. Spin-Liquid Ground State of the S = 1/2 Kagome Heisenberg Antiferromagnet. *Science*, 332(6034):1173–1176, 2011.

[202] D. Huerga, J. Dukelsky, N. Laflorencie, and G. Ortiz. Chiral phases of two-dimensional hard-core bosons with frustrated ring exchange. *Phys. Rev. B*, 89(9):094401, March 2014.

[203] Lindsay J. LeBlanc, Karina Jimnez-Garca, Ross A. Williams, Matthew C. Beeler, Abigail R. Perry, William D. Phillips, and Ian B. Spielman. Observation of a superfluid Hall effect. *Proc. Natl. Acad. Sci. U. S. A.*, 109(27):10811–10814, 2012.

[204] Stephen Powell, Ryan Barnett, Rajdeep Sensarma, and Sankar Das Sarma. Interacting Hofstadter Spectrum of Atoms in an Artificial Gauge Field. *Phys. Rev. Lett.*, 104:255303, Jun 2010.

[205] Stephen Powell, Ryan Barnett, Rajdeep Sensarma, and Sankar Das Sarma. Bogoliubov theory of interacting bosons on a lattice in a synthetic magnetic field. *Phys. Rev. A*, 83:013612, Jan 2011.

[206] Hannah M. Price and Nigel R. Cooper. Effects of Berry Curvature on the Collective Modes of Ultracold Gases. *Phys. Rev. Lett.*, 111:220407, Nov 2013.

[207] Krzysztof Byczuk and Dieter Vollhardt. Correlated bosons on a lattice: Dynamical mean-field theory for Bose-Einstein condensed and normal phases. *Phys. Rev. B*, 77:235106, Jun 2008.

[208] Wen-Jun Hu and Ning-Hua Tong. Dynamical mean-field theory for the Bose-Hubbard model. *Phys. Rev. B*, 80:245110, Dec 2009.

[209] A. Hubener, M. Snoek, and W. Hofstetter. Magnetic phases of two-component ultracold bosons in an optical lattice. *Phys. Rev. B*, 80:245109, Dec 2009.

[210] Peter Anders, Emanuel Gull, Lode Pollet, Matthias Troyer, and Philipp Werner. Dynamical Mean Field Solution of the Bose-Hubbard Model. *Phys. Rev. Lett.*, 105:096402, Aug 2010.

[211] M. Snoek and W. Hofstetter. Bosonic Dynamical Mean-Field Theory. In N. Proukakis and et al., editors, *Quantum Gases: Finite Temperature and Non-Equilibrium Dynamics.*, pages 355–365. World Scientific Publishing Co. Pte. Ltd., 2013., February 2013.

[212] L. Pitaevskii and S. Stringari. *Bose-Einstein Condensation.* Clarendon Press, Oxford, 2003.

[213] A. J. Leggett. Bose-Einstein condensation in the alkali gases: Some fundamental concepts. *Rev. Mod. Phys.*, 73:307–356, April 2001.

[214] Xiaopeng Li, Stefan S. Natu, Arun Paramekanti, and S. Das Sarma. Chiral spin superfluidity and spontaneous spin Hall effect of interacting bosons. *Nat. Commun.* , 5:5174, May 2014.

[215] G. Möller and N. R. Cooper. Condensed ground states of frustrated Bose-Hubbard models. *Phys. Rev. A*, 82:063625, Dec 2010.

[216] D. van Oosten, P. van der Straten, and H. T. C. Stoof. Quantum phases in an optical lattice. *Phys. Rev. A*, 63:053601, Apr 2001.

[217] K. Sengupta and N. Dupuis. Mott-insulator-to-superfluid transition in the Bose-Hubbard model: A strong-coupling approach. *Phys. Rev. A*, 71:033629, Mar 2005.

[218] J. K. Freericks, H. R. Krishnamurthy, Yasuyuki Kato, Naoki Kawashima, and Nandini Trivedi. Strong-coupling expansion for the momentum distribution of the Bose-Hubbard model with benchmarking against exact numerical results. *Phys. Rev. A*, 79:053631, May 2009.

[219] J. K. Freericks, H. R. Krishnamurthy, Yasuyuki Kato, Naoki Kawashima, and Nandini Trivedi. Erratum: Strong-coupling expansion for the momentum distribution of the Bose-Hubbard model with benchmarking against exact numerical results [Phys. Rev. A **79**, 053631 (2009)]. *Phys. Rev. A*, 85:019913(E), Jan 2012.

[220] Konstantin V. Krutitsky and Patrick Navez. Excitation dynamics in a lattice Bose gas within the time-dependent Gutzwiller mean-field approach. *Phys. Rev. A*, 84:033602, Sep 2011.

[221] B Bauer, L D Carr, H G Evertz, A Feiguin, J Freire, S Fuchs, L Gamper, J Gukelberger, E Gull, S Guertler, A Hehn, R Igarashi, S V Isakov, D Koop, P N Ma, P Mates, H Matsuo, O Parcollet, G Pawlowski, J D Picon, L Pollet, E Santos, V W Scarola, U Schollwöck, C Silva, B Surer, S Todo, S Trebst, M Troyer, M L Wall, P Werner, and S Wessel. The ALPS project release 2.0: open source software for strongly correlated systems. *J. Stat. Mech. Theor. Exp.*, 2011(05):P05001, 2011.

[222] Jane Cullum and Ralph A. Willoughby. *Lanczos Algorithms for Large Symmetric Eigenvalue Computations: Vol. 1: Theory*. SIAM, 1985.

[223] S. Pairault, D. Sénéchal, and A.-M. S. Tremblay. Strong-coupling perturbation theory of the Hubbard model. *Eur. Phys. J. B*, 16:85–105, October 2000.

[224] D. Sénéchal, D. Perez, and M. Pioro-Ladrière. Spectral Weight of the Hubbard Model through Cluster Perturbation Theory. *Phys. Rev. Lett.*, 84:522–525, Jan 2000.

[225] David Sénéchal, Danny Perez, and Dany Plouffe. Cluster perturbation theory for Hubbard models. *Phys. Rev. B*, 66:075129, Aug 2002.

[226] Ryuichi Shindou and Leon Balents. Artificial Electric Field in Fermi Liquids. *Phys. Rev. Lett.*, 97:216601, Nov 2006.

[227] Ulf Bissbort, Sören Götze, Yongqiang Li, Jannes Heinze, Jasper S. Krauser, Malte Weinberg, Christoph Becker, Klaus Sengstock, and Walter Hofstetter. Detecting the Amplitude Mode of Strongly Interacting Lattice Bosons by Bragg Scattering. *Phys. Rev. Lett.*, 106:205303, May 2011.

[228] Nathan Goldman, Jérôme Beugnon, and Fabrice Gerbier. Detecting Chiral Edge States in the Hofstadter Optical Lattice. *Phys. Rev. Lett.*, 108:255303, Jun 2012.

[229] J. T. Stewart, J. P. Gaebler, and D. S. Jin. Using photoemission spectroscopy to probe a strongly interacting Fermi gas. *Nature*, 454:744–747, August 2008.

[230] A. J. Hoffman, S. J. Srinivasan, S. Schmidt, L. Spietz, J. Aumentado, H. E. Türeci, and A. A. Houck. Dispersive Photon Blockade in a Superconducting Circuit. *Phys. Rev. Lett.*, 107:053602, Jul 2011.

[231] Karyn Le Hur and T. Maurice Rice. Superconductivity close to the mott

state: From condensed-matter systems to superfluidity in optical lattices. *Annals of Physics*, 324(7):1452 – 1515, 2009.

[232] Wei Wu, Michael M. Scherer, Carsten Honerkamp, and Karyn Le Hur. Correlated Dirac particles and superconductivity on the honeycomb lattice. *Phys. Rev. B*, 87:094521, Mar 2013.

[233] Rahul Nandkishore, L. S. Levitov, and A. V. Chubukov. Chiral superconductivity from repulsive interactions in doped graphene. *Nat. Phys.*, 8:158–163, 2012.

[234] A. M. Black-Schaffer and C. Honerkamp. Chiral d-wave superconductivity in doped graphene. *J. Phys.: Condens. Matter*, 26:3201P, October 2014.

[235] Annica M. Black-Schaffer, Wei Wu, and Karyn Le Hur. Chiral d-wave superconductivity on the honeycomb lattice close to the Mott state. *Phys. Rev. B*, 90:054521, Aug 2014.

[236] G. Pagano, M. Mancini, G. Cappellini, P. Lombardi, F. Schäfer, H. Hu, X.-J. Liu, J. Catani, C. Sias, M. Inguscio, and L. Fallani. A one-dimensional liquid of fermions with tunable spin. *Nature Physics*, 10:198–201, March 2014.

[237] Markus Greiner, Olaf Mandel, Tilman Esslinger, Theodor W. Hänsch, and Immanuel Bloch. Quantum phase transition from a superfluid to a Mott insulator in a gas of ultracold atoms. *Nature*, 415:39–44, 2001.

[238] Xu, C. and Senthil, T. Wave functions of bosonic symmetry protected topological phases. *Phys. Rev. B*, 87(17):174412, May 2013.

[239] Zheng-Xin Liu, Zheng-Cheng Gu, and Xiao-Gang Wen. Microscopic realization of two-dimensional bosonic topological insulators. *Phys. Rev. Lett.*, 113:267206, Dec 2014.

[240] F. D. M. Haldane. Nonlinear Field Theory of Large-Spin Heisenberg Antiferromagnets: Semiclassically Quantized Solitons of the One-Dimensional Easy-Axis Néel State. *Phys. Rev. Lett.*, 50:1153–1156, Apr 1983.

[241] Ian Affleck, Tom Kennedy, Elliott H. Lieb, and Hal Tasaki. Rigorous results on valence-bond ground states in antiferromagnets. *Phys. Rev. Lett.*, 59:799–802, Aug 1987.

[242] Yuan-Ming Lu and Ashvin Vishwanath. Theory and classification of interacting integer topological phases in two dimensions: A Chern-Simons approach. *Phys. Rev. B*, 86:125119, Sep 2012.

[243] O. M. Sule, X. Chen, and S. Ryu. Symmetry-protected topological phases and orbifolds: Generalized Laughlin's argument. *Phys. Rev. B*, 88(7):075125, August 2013.

[244] X. Chen, Z.-C. Gu, Z.-X. Liu, and X.-G. Wen. Symmetry protected topological orders and the group cohomology of their symmetry group. *Phys. Rev. B*, 87(15):155114, April 2013.

[245] N. Regnault and T. Senthil. Microscopic model for the boson integer quantum Hall effect. *Phys. Rev. B*, 88:161106, Oct 2013.

[246] William S. Cole, Shizhong Zhang, Arun Paramekanti, and Nandini Trivedi. Bose-Hubbard Models with Synthetic Spin-Orbit Coupling: Mott Insulators, Spin Textures, and Superfluidity. *Phys. Rev. Lett.*, 109:085302, Aug 2012.

[247] J. Radić, A. Di Ciolo, K. Sun, and V. Galitski. Exotic Quantum Spin Models in Spin-Orbit-Coupled Mott Insulators. *Phys. Rev. Lett.*, 109:085303, Aug 2012.

[248] Saptarshi Mandal, Kush Saha, and K. Sengupta. Superfluid-insulator transition of two-species bosons with spin-orbit coupling. *Phys. Rev. B*, 86:155101, Oct 2012.

[249] Zi Cai, Xiangfa Zhou, and Congjun Wu. Magnetic phases of bosons with synthetic spin-orbit coupling in optical lattices. *Phys. Rev. A*, 85:061605, Jun 2012.

[250] Daniel Cocks, Peter P. Orth, Stephan Rachel, Michael Buchhold, Karyn Le Hur, and Walter Hofstetter. Time-Reversal-Invariant Hofstadter-Hubbard Model with Ultracold Fermions. *Phys. Rev. Lett.*, 109:205303, Nov 2012.

[251] P. P. Orth, D. Cocks, S. Rachel, M. Buchhold, K. Le Hur, and W. Hofstetter. Correlated topological phases and exotic magnetism with ultracold fermions. *Journal of Physics B Atomic Molecular Physics*, 46(13):134004, July 2013.

[252] E. Orignac and T. Giamarchi. Meissner effect in a bosonic ladder. *Phys. Rev. B*, 64:144515, Sep 2001.

[253] M. Kardar. Josephson-junction ladders and quantum fluctuations. *Phys. Rev. B*, 33:31253128, 1986.

[254] Marie Piraud, Zi Cai, Ian P. McCulloch, and Ulrich Schollwöck. Quantum magnetism of bosons with synthetic gauge fields in one-dimensional optical lattices: A density-matrix renormalization-group study. *Phys. Rev. A*, 89:063618, Jun 2014.

[255] M. Piraud, F. Heidrich-Meisner, I. P. McCulloch, S. Greschner, T. Vekua, and U. Schollwöck. Vortex and Meissner phases of strongly interacting bosons on a two-leg ladder. *Phys. Rev. B*, 91:140406, Apr 2015.

[256] C. L. Kane, Ranjan Mukhopadhyay, and T. C. Lubensky. Fractional Quantum Hall Effect in an Array of Quantum Wires. *Phys. Rev. Lett.*, 88:036401, Jan 2002.

[257] W. Meissner and R. Ochsenfeld. Ein neuer Effekt bei Eintritt der Supraleitfähigkeit. *Naturwissenschaften*, 21:787, 1933.

[258] P. W. Anderson. Coherent Excited States in the Theory of Superconductivity: Gauge Invariance and the Meissner Effect. *Phys. Rev.*, 110:827–835, May 1958.

[259] P. G. de Gennes. *Superconductivity of Metals and Alloys*. Addison-Wesley, 1989.

[260] Rosario Fazio and Herre van der Zant. Quantum phase transitions and vortex dynamics in superconducting networks. *Physics Reports*, 355:235 – 334, 2001.

[261] Michel H. Devoret. Course 10. Quantum fluctuations in electrical circuits. In S. Reynaud, E. Giacobino, and J. Zinn-Justin, editors, *Les Houches, Session LXIII, 1995. Fluctuations quantiques*. Elsevier, New York, 1997.

[262] Devoret, Michel H. and Martinis, John M. Implementing Qubits with Superconducting Integrated Circuits. *Quantum Information Processing*, 3:163, 2004.

[263] P. Donohue and T. Giamarchi. Mott-superfluid transition in bosonic ladders. *Phys. Rev. B*, 63:180508, Apr 2001.

[264] Lih-King Lim, C. Morais Smith, and Andreas Hemmerich. Staggered-Vortex Superfluid of Ultracold Bosons in an Optical Lattice. *Phys. Rev. Lett.*, 100:130402, Apr 2008.

[265] Lih-King Lim, Andreas Hemmerich, and C. Morais Smith. Artificial staggered magnetic field for ultracold atoms in optical lattices. *Phys. Rev. A*, 81:023404, Feb 2010.

[266] Francois Crépin, Nicolas Laflorencie, Guillaume Roux, and Pascal Simon. Phase diagram of hard-core bosons on clean and disordered two-leg ladders: Mott insulator–Luttinger liquid–Bose glass. *Phys. Rev. B*, 84:054517, Aug 2011.

[267] V. Kalmeyer and R. B. Laughlin. Equivalence of the resonating-valence-bond and fractional quantum Hall states. *Phys. Rev. Lett.*, 59:2095–2098, Nov 1987.

[268] Vadim Kalmeyer and R. B. Laughlin. Theory of the spin liquid state of the Heisenberg antiferromagnet. *Phys. Rev. B*, 39:11879–11899, Jun 1989.

[269] R.B Laughlin. Spin hamiltonian for which quantum hall wavefunction is exact. *Annals of Physics*, 191(1):163 – 202, 1989.

[270] Darrell F. Schroeter, Eliot Kapit, Ronny Thomale, and Martin Greiter. Spin Hamiltonian for which the Chiral Spin Liquid is the Exact Ground State. *Phys. Rev. Lett.*, 99:097202, Aug 2007.

[271] Jeffrey C. Y. Teo and C. L. Kane. From Luttinger liquid to non-Abelian quantum Hall states. *Phys. Rev. B*, 89:085101, Feb 2014.

[272] F D M Haldane. 'Luttinger liquid theory' of one-dimensional quantum fluids. I. Properties of the Luttinger model and their extension to the general 1D interacting spinless Fermi gas. *Journal of Physics C: Solid State Physics*, 14(19):2585, 1981.

[273] Alexander O. Gogolin, Alexander A. Nersesyan, and Alexei M. Tsvelik. *Bosonization and Strongly Correlated Systems*. Cambridge University Press, Cambridge, United Kingdom, 2003.

[274] P. W. Anderson. Plasmons, Gauge Invariance, and Mass. *Phys. Rev.*, 130:439–442, Apr 1963.

[275] Jasper van Wezel and Jeroen van den Brink. Spontaneous symmetry breaking and decoherence in superconductors. *Phys. Rev. B*, 77:064523, Feb 2008.

[276] P. Lebwohl and M. J. Stephen. Properties of Vortex Lines in Superconducting Barriers. *Phys. Rev.*, 163:376–379, Nov 1967.

[277] Alexander L. Fetter and Michael J. Stephen. Fluctuations in a Josephson Junction. *Phys. Rev.*, 168:475–480, Apr 1968.

[278] Belén Paredes, Artur Widera, Valentin Murg, Olaf Mandel, Simon Fölling, Ignacio Cirac, Gora V. Shlyapnikov, Theodor W. Hänsch, and Immanuel Bloch. TonksGirardeau gas of ultracold atoms in an optical lattice. *Nature*, 429:277–281, 2004.

[279] Toshiya Kinoshita, Trevor Wenger, and David S. Weiss. Observation of a One-Dimensional Tonks-Girardeau Gas. *Science*, 305:1125–1128, 2004.

[280] V. L. Pokrovsky and A. L. Talapov. The theory of two-dimensional incommensurate crystals. *Sov. Phys. JETP*, 51:134, 1980.

[281] H. J. Schulz. Critical behavior of commensurate-incommensurate phase transitions in two dimensions. *Phys. Rev. B*, 22:5274, 1980.

[282] T. Giamarchi and H. J. Schulz. Theory of spin-anisotropic electron-electron interactions in quasi-one- dimensional metals. *J. Phys. France*, 49:819–835, 1988.

[283] M. Klanjšek, H. Mayaffre, C. Berthier, M. Horvatić, B. Chiari, O. Piovesana, P. Bouillot, C. Kollath, E. Orignac, R. Citro, and T. Giamarchi. Controlling Luttinger Liquid Physics in Spin Ladders under a Magnetic Field. *Physical Review Letters*, 101(13):137207, September 2008.

[284] B. Thielemann, C. Rüegg, K. Kiefer, H. M. Rønnow, B. Normand, P. Bouillot, C. Kollath, E. Orignac, R. Citro, T. Giamarchi, A. M. Läuchli, D. Biner, K. W. Krämer, F. Wolff-Fabris, V. S. Zapf, M. Jaime, J. Stahn, N. B. Christensen, B. Grenier, D. F. McMorrow, and J. Mesot. Field-controlled magnetic order in the quantum spin-ladder system $(\mathrm{Hpip})_2\mathrm{CuBr}_4$. *Phys. Rev. B*, 79(2):020408, January 2009.

[285] D. J. Thouless. Quantization of particle transport. *Phys. Rev. B*, 27:6083–6087, May 1983.

[286] Xiao-Gang Wen and A. Zee. Classification of abelian quantum hall states and matrix formulation of topological fluids. *Phys. Rev. B*, 46:2290–2301, Jul 1992.

[287] I Safi and H.J. Schulz. Transport in an inhomogeneous interacting one-dimensional system. *Phys. Rev. B*, 52(24):17040 (R), 1995.

[288] K.-V. Pham, M. Gabay, and P. Lederer. Fractional excitations in the Luttinger liquid. *Phys. Rev. B*, 61:16397–16422, Jun 2000.

[289] Karyn Le Hur, Bertrand I. Halperin, and Amir Yacoby. Charge Fractionalization in nonchiral Luttinger systems. *Ann. Phys.*, 323:3037–3058, 2008.

[290] H. Steinberg, G. Barak, A. Yacoby, L. N. Pfeiffer, K. W. West, B. I. Halperin, and K. Le Hur. Charge fractionalization in quantum wires. *Nature Physics*, 4:116–119, February 2008.

[291] E. Berg, Y. Oreg, E.-A. Kim, and F. von Oppen. Fractional Charges on an Integer Quantum Hall Edge. *Phys. Rev. Lett.*, 102:236402, Jun 2009.

[292] C. L. Kane and Matthew P. A. Fisher. Nonequilibrium noise and fractional charge in the quantum Hall effect. *Phys. Rev. Lett.*, 72:724–727, Jan 1994.

[293] R de Picciotto, M. Reznikov, M. Heiblum, V. Umansky, G. Bunin, and D. Mahalu. Direct observation of a fractional charge. *Nature*, 389:162, 1997.

[294] Iuliana P. Radu, J. B. Miller, C. M. Marcus, M. A. Kastner, L. N. Pfeiffer, and K. W. West. Quasi-Particle Properties from Tunneling in the $\nu = 5/2$ Fractional Quantum Hall State. *Science*, 320:899, 2008.

[295] Jean-Philippe Brantut, Jakob Meineke, David Stadler, Sebastian Krinner, and Tilman Esslinger. Conduction of Ultracold Fermions Through a Mesoscopic Channel. *Science*, 337(6098):1069–1071, 2012.

[296] J.-P. Brantut, C. Grenier, J. Meineke, D. Stadler, S. Krinner, C. Kollath, T. Esslinger, and A. Georges. A Thermoelectric Heat Engine with Ultracold Atoms. *Science*, 342:713–715, November 2013.

[297] S. Krinner, D. Stadler, D. Husmann, J.-P. Brantut, and T. Esslinger. Observation of quantized conductance in neutral matter. *Nature*, 517:64–67, January 2015.

[298] Xiao-Gang Wen. Theory of the edge states in fractional quantum Hall effects. *Int. J. Mod. Phys. B*, 6:1711–1762, 1992.

[299] A. H. MacDonald, S. M. Girvin, and D. Yoshioka. $\frac{t}{U}$ expansion for the Hubbard model. *Phys. Rev. B*, 37:9753–9756, Jun 1988.

[300] A. H. MacDonald, S. M. Girvin, and D. Yoshioka. Reply to "Comment on ' t/U expansion for the Hubbard model"'. *Phys. Rev. B*, 41:2565–2568, Feb 1990.

[301] L.-M. Duan, E. Demler, and M. D. Lukin. Controlling Spin Exchange Interactions of Ultracold Atoms in Optical Lattices. *Phys. Rev. Lett.*, 91:090402, Aug 2003.

[302] Ehud Altman and Walter Hofstetter and Eugene Demler and Mikhail D Lukin. Phase diagram of two-component bosons on an optical lattice. *New Journal of Physics*, 5(1):113, 2003.

[303] A. B. Kuklov and B. V. Svistunov. Counterflow Superfluidity of Two-Species Ultracold Atoms in a Commensurate Optical Lattice. *Phys. Rev. Lett.*, 90:100401, Mar 2003.

[304] A. Isacsson, Min-Chul Cha, K. Sengupta, and S. M. Girvin. Superfluid-insulator transitions of two-species bosons in an optical lattice. *Phys. Rev. B*, 72:184507, Nov 2005.

[305] Karyn Le Hur. Andreev scattering in the asymmetric ladder with preformed bosonic pairs. *Phys. Rev. B*, 64:060502, Jul 2001.

[306] T. M. Rice, K.-Y. Yang, and F. C. Zhang. A phenomenological theory of the anomalous pseudogap phase in underdoped cuprates. *Reports on Progress in Physics*, 75(1):016502, January 2012.

[307] H. J. Schulz. Superconductivity and Antiferromagnetism in the Two-Dimensional Hubbard Model: Scaling Theory. *EPL (Europhysics Letters)*, 4(5):609, 1987.

[308] D. Zanchi and H. J. Schulz. Weakly correlated electrons on a square lattice: A renormalization group theory. *EPL (Europhysics Letters)*, 44(2):235, 1998.

[309] Christoph J. Halboth and Walter Metzner. Renormalization-group analysis of the two-dimensional Hubbard model. *Phys. Rev. B*, 61:7364–7377, Mar 2000.

[310] C. Honerkamp, M. Salmhofer, N. Furukawa, and T. M. Rice. Breakdown of the Landau-Fermi liquid in two dimensions due to umklapp scattering. *Phys. Rev. B*, 63:035109, Jan 2001.

[311] Leon Balents, Matthew P. A. Fisher, and Chetan Nayak. Nodal liquid theory of the pseudo-gap phase of high-T_c superconductors. *International Journal of Modern Physics B*, 12:1033–1068, 1998.

[312] V. B. Geshkenbein, L. B. Ioffe, and A. I. Larkin. Superconductivity in a system with preformed pairs. *Phys. Rev. B*, 55:3173–3180, Feb 1997.

[313] L. B. Ioffe and A. J. Millis. Zone-diagonal-dominated transport in high-T_c cuprates. *Phys. Rev. B*, 58:11631–11637, Nov 1998.

[314] V. B. Geshkenbein, L. B. Ioffe, and A. J. Millis. Theory of the Resistive Transition in Overdoped $Tl_2Ba_2CuO_{6+\delta}$: Implications for the Vortex Vis-

cosity and the Quasiparticle Scattering Rate in High- T_c Superconductors. *Phys. Rev. Lett.*, 80:5778–5781, Jun 1998.

[315] M. Franz, D. E. Sheehy, and Z. Tešanović. Magnetic Field Induced Charge and Spin Instabilities in Cuprate Superconductors. *Physical Review Letters*, 88(25):257005, June 2002.

[316] K. Fujita, M. H. Hamidian, S. D. Edkins, C. K. Kim, Y. Kohsaka, M. Azuma, M. Takano, H. Takagi, H. Eisaki, S.-i. Uchida, A. Allais, M. J. Lawler, E.-A. Kim, S. Sachdev, and J. C. S. Davis. Direct phase-sensitive identification of a d-form factor density wave in underdoped cuprates. *Proceedings of the National Academy of Science*, 111:3026–E3032, July 2014.

[317] Debanjan Chowdhury and Subir Sachdev. Feedback of superconducting fluctuations on charge order in the underdoped cuprates. *Phys. Rev. B*, 90:134516, Oct 2014.

[318] C. Pépin, V. S. de Carvalho, T. Kloss, and X. Montiel. Pseudogap, charge order, and pairing density wave at the hot spots in cuprate superconductors. *Phys. Rev. B*, 90:195207, Nov 2014.

[319] A. M. Tsvelik and A. V. Chubukov. Composite charge order in the pseudogap region of the cuprates. *Phys. Rev. B*, 89:184515, May 2014.

[320] G. Grissonnanche, O. Cyr-Choinière, F. Laliberté, S. René de Cotret, A. Juneau-Fecteau, S. Dufour-Beauséjour, M.-È. Delage, D. Leboeuf, J. Chang, B. J. Ramshaw, D. A. Bonn, W. N. Hardy, R. Liang, S. Adachi, N. E. Hussey, B. Vignolle, C. Proust, M. Sutherland, S. Krämer, J.-H. Park, D. Graf, N. Doiron-Leyraud, and L. Taillefer. Direct measurement of the upper critical field in cuprate superconductors. *Nature Communications*, 5, February 2014.

[321] N. Doiron-Leyraud, C. Proust, D. Leboeuf, J. Levallois, J.-B. Bonnemaison, R. Liang, D. A. Bonn, W. N. Hardy, and L. Taillefer. Quantum oscillations

and the Fermi surface in an underdoped high-T_c superconductor. *Nature*, 447:565–568, May 2007.

[322] D. Leboeuf, N. Doiron-Leyraud, J. Levallois, R. Daou, J.-B. Bonnemaison, N. E. Hussey, L. Balicas, B. J. Ramshaw, R. Liang, D. A. Bonn, W. N. Hardy, S. Adachi, C. Proust, and L. Taillefer. Electron pockets in the Fermi surface of hole-doped high-T_c superconductors. *Nature*, 450:533–536, November 2007.

[323] S. T. Carr, B. N. Narozhny, and A. A. Nersesyan. Spinless fermionic ladders in a magnetic field: Phase diagram. *Phys. Rev. B*, 73(19):195114, May 2006.

[324] G. Kotliar. Resonating valence bonds and d-wave superconductivity. *Phys. Rev. B*, 37:3664–3666, Mar 1988.

[325] Ian Affleck and J. Brad Marston. Large-n limit of the Heisenberg-Hubbard model: Implications for high-T_c superconductors. *Phys. Rev. B*, 37:3774–3777, Mar 1988.

[326] J. Brad Marston and Ian Affleck. Large-n limit of the Hubbard-Heisenberg model. *Phys. Rev. B*, 39:11538–11558, Jun 1989.

[327] B. N. Narozhny, S. T. Carr, and A. A. Nersesyan. Fractional charge excitations in fermionic ladders. *Phys. Rev. B*, 71(16):161101, April 2005.

[328] U. Schollwöck, Sudip Chakravarty, J. O. Fjærestad, J. B. Marston, and M. Troyer. Broken Time-Reversal Symmetry in Strongly Correlated Ladder Structures. *Phys. Rev. Lett.*, 90:186401, May 2003.

[329] S. T. Carr and A. M. Tsvelik. Superconductivity and charge-density waves in a quasi-one-dimensional spin-gap system. *Phys. Rev. B*, 65(19):195121, May 2002.

[330] G. Roux, E. Orignac, S. R. White, and D. Poilblanc. Diamagnetism of doped

two-leg ladders and probing the nature of their commensurate phases. *Phys. Rev. B*, 76(19):195105, November 2007.

[331] Hong-Chen Jiang, Matthew S. Block, Ryan V. Mishmash, James R. Garrison, D. N. Sheng, Olexei I. Motrunich, and Matthew P. A. Fisher. Non-Fermi-liquid d-wave metal phase of strongly interacting electrons. *Nature*, 493:39–44, 2013.

[332] A. Luther and V. J. Emery. Backward Scattering in the One-Dimensional Electron Gas. *Phys. Rev. Lett.*, 33:589–592, Sep 1974.

[333] K. W. Madison, F. Chevy, V. Bretin, and J. Dalibard. Stationary States of a Rotating Bose-Einstein Condensate: Routes to Vortex Nucleation. *Physical Review Letters*, 86:4443, May 2001.

[334] J. R. Abo-Shaeer, C. Raman, J. M. Vogels, and W. Ketterle. Observation of Vortex Lattices in Bose-Einstein Condensates. 292, 2001.

[335] Y. Shin, G.-B. Jo, M. Saba, T. A. Pasquini, W. Ketterle, and D. E. Pritchard. Optical Weak Link between Two Spatially Separated Bose-Einstein Condensates. *Phys. Rev. Lett.*, 95:170402, Oct 2005.

[336] L. J. Leblanc, A. B. Bardon, J. McKeever, M. H. T. Extavour, D. Jervis, J. H. Thywissen, F. Piazza, and A. Smerzi. Dynamics of a Tunable Superfluid Junction. *Physical Review Letters*, 106(2):025302, January 2011.

[337] A. R. Kolovsky. Creating artificial magnetic fields for cold atoms by photon-assisted tunneling. *EPL (Europhysics Letters)*, 93:20003, January 2011.

[338] Olaf Mandel, Markus Greiner, Artur Widera, Tim Rom, Theodor W. Hänsch, and Immanuel Bloch. Coherent Transport of Neutral Atoms in Spin-Dependent Optical Lattice Potentials. *Phys. Rev. Lett.*, 91:010407, Jul 2003.

[339] Waseem S. Bakr, Jonathon I. Gillen, Amy Peng, Simon Fölling, and Markus Greiner. A quantum gas microscope for detecting single atoms in a Hubbard-regime optical lattice. *Nature*, 462:74–77, 2009.

[340] J. F. Sherson, C. Weitenberg, M. Endres, M. Cheneau, I. Bloch, and S. Kuhr. Single-atom-resolved fluorescence imaging of an atomic Mott insulator. *Nature*, 467:68–72, September 2010.

[341] Dan M. Stamper-Kurn and Masahito Ueda. Spinor Bose gases: Symmetries, magnetism, and quantum dynamics. *Rev. Mod. Phys.*, 85:1191–1244, Jul 2013.

[342] Cheng Chin, Rudolf Grimm, Paul Julienne, and Eite Tiesinga. Feshbach resonances in ultracold gases. *Rev. Mod. Phys.*, 82:1225–1286, Apr 2010.

[343] M. Saffman, T. G. Walker, and K. Mølmer. Quantum information with Rydberg atoms. *Rev. Mod. Phys.*, 82:2313–2363, Aug 2010.

[344] L. Béguin, A. Vernier, R. Chicireanu, T. Lahaye, and A. Browaeys. Direct Measurement of the van der Waals Interaction between Two Rydberg Atoms. *Phys. Rev. Lett.*, 110:263201, Jun 2013.

[345] P. Schauß, J. Zeiher, T. Fukuhara, S. Hild, M. Cheneau, T. Macrì, T. Pohl, I. Bloch, and C. Gross. Crystallization in Ising quantum magnets. *Science*, 347(6229):1455–1458, 2015.

[346] T Lahaye, C Menotti, L Santos, M Lewenstein, and T Pfau. The physics of dipolar bosonic quantum gases. *Reports on Progress in Physics*, 72(12):126401, 2009.

[347] C. Trefzger, C. Menotti, B. Capogrosso-Sansone, and M. Lewenstein. Ultracold dipolar gases in optical lattices. *Journal of Physics B Atomic Molecular Physics*, 44(19):193001, October 2011.

[348] Enzo Granato. Phase transitions in Josephson-junction ladders in a magnetic field. *Phys. Rev. B*, 42:4797–4799, Sep 1990.

[349] Colin Denniston and Chao Tang. Phases of Josephson Junction Ladders. *Phys. Rev. Lett.*, 75:3930–3933, Nov 1995.

[350] C. D. Chen, P. Delsing, D. B. Haviland, Y. Harada, and T. Claeson. Scaling behavior of the magnetic-field-tuned superconductor-insulator transition in two-dimensional Josephson-junction arrays. *Phys. Rev. B*, 51:15645–15648, Jun 1995.

[351] H. S. J. van der Zant, W. J. Elion, L. J. Geerligs, and J. E. Mooij. Quantum phase transitions in two dimensions: Experiments in Josephson-junction arrays. *Phys. Rev. B*, 54:10081–10093, Oct 1996.

[352] Matthew P. A. Fisher. Quantum phase transitions in disordered two-dimensional superconductors. *Phys. Rev. Lett.*, 65:923–926, Aug 1990.

[353] M. Y. Choi. Quantum Hall effect in ideal superconducting arrays at zero temperature. *Phys. Rev. B*, 50:10088–10091, Oct 1994.

[354] Ady Stern. Quantum Hall fluid of vortices in a two-dimensional array of Josephson junctions. *Phys. Rev. B*, 50:10092–10106, Oct 1994.

[355] A.A. Odintsov and Yu.V. Nazarov. Quantum hall states of cooper pairs and vortices in josephson arrays. *Physica B: Condensed Matter*, 203:513 – 519, 1994.

[356] Nicholas Adam Masluk. *Reducing the losses of the fluxonium artificial atom.* Yale University Doctoral Dissertation, 2012.

[357] E. Bibow, P. Lafarge, and L. P. Lévy. Resonant Cooper Pair Tunneling through a Double-Island Qubit. *Phys. Rev. Lett.*, 88:017003, Dec 2001.

[358] Jens Koch and Karyn Le Hur. Discontinuous Current-Phase Relations in Small One-Dimensional Josephson Junction Arrays. *Phys. Rev. Lett.*, 101:097007, Aug 2008.

[359] Hsiu-Hau Lin, Leon Balents, and Matthew P. A. Fisher. N-chain Hubbard model in weak coupling. *Phys. Rev. B*, 56:6569–6593, Sep 1997.

[360] Urs Ledermann, Karyn Le Hur, and T. M. Rice. Successive opening of the Fermi surface in doped N-leg Hubbard ladders. *Phys. Rev. B*, 62:16383–16391, Dec 2000.

[361] Karyn Le Hur and T. Maurice Rice. Superconductivity close to the Mott state: From condensed-matter systems to superfluidity in optical lattices. *Ann. Phys.*, 324:1452, 2009.

[362] Rochus Klesse and Ady Stern. Coulomb drag between quantum wires. *Phys. Rev. B*, 62:16912–16925, Dec 2000.

[363] Gregory A. Fiete, Karyn Le Hur, and Leon Balents. Coulomb drag between two spin-incoherent Luttinger liquids. *Phys. Rev. B*, 73:165104, Apr 2006.

[364] Karsten Flensberg. Coulomb Drag of Luttinger Liquids and Quantum Hall Edges. *Phys. Rev. Lett.*, 81:184–187, Jul 1998.

[365] M. Pustilnik, E. G. Mishchenko, L. I. Glazman, and A. V. Andreev. Coulomb Drag by Small Momentum Transfer between Quantum Wires. *Phys. Rev. Lett.*, 91:126805, Sep 2003.

[366] D. Laroche, G. Gervais, M. P. Lilly, and J. L. Reno. 1D-1D Coulomb Drag Signature of a Luttinger Liquid. *Science*, 343:631, 2014.

[367] C. Repellin, B. Andrei Bernevig, and N. Regnault. $\mathbb{Z}_2$ fractional topological insulators in two dimensions. *Phys. Rev. B*, 90:245401, Dec 2014.

[368] Gunnar Möller, Layla Hormozi, Joost Slingerland, and Steven H. Simon. Josephson-coupled Moore-Read states. *Phys. Rev. B*, 90:235101, Dec 2014.

[369] T. Giamarchi and H. J. Schulz. Anderson localization and interactions in one-dimensional metals. *Phys. Rev. B*, 37:325–340, Jan 1988.

[370] Thierry Giamarchi and Pierre Le Doussal. Elastic theory of pinned flux lattices. *Phys. Rev. Lett.*, 72:1530–1533, Mar 1994.

[371] Zoran Ristivojevic, Aleksandra Petković, Pierre Le Doussal, and Thierry Giamarchi. Phase Transition of Interacting Disordered Bosons in One Dimension. *Phys. Rev. Lett.*, 109:026402, Jul 2012.

[372] Ehud Altman, Yariv Kafri, Anatoli Polkovnikov, and Gil Refael. Superfluid-insulator transition of disordered bosons in one dimension. *Phys. Rev. B*, 81:174528, May 2010.

[373] Fabian Grusdt and Michael Höning. Realization of fractional Chern insulators in the thin-torus limit with ultracold bosons. *Phys. Rev. A*, 90:053623, Nov 2014.

[374] W. Wu, M. M. Scherer, C. Honerkamp, and K. Le Hur. Correlated Dirac particles and superconductivity on the honeycomb lattice. *Phys. Rev. B*, 87(9):094521, March 2013.

[375] A. Celi, P. Massignan, J. Ruseckas, N. Goldman, I. B. Spielman, G. Juzeliūnas, and M. Lewenstein. Synthetic Gauge Fields in Synthetic Dimensions. *Phys. Rev. Lett.*, 112:043001, Jan 2014.

[376] N. R. Cooper and A. M. Rey. Adiabatic Control of Atomic Dressed States for Transport and Sensing. *ArXiv e-prints*, March 2015.

[377] M. Mancini, G. Pagano, G. Cappellini, L. Livi, M. Rider, J. Catani, C. Sias, P. Zoller, M. Inguscio, M. Dalmonte, and L. Fallani. Observation of chiral edge states with neutral fermions in synthetic Hall ribbons. *ArXiv e-prints*, February 2015.

[378] Chong Wang and T. Senthil. Boson topological insulators: A window into highly entangled quantum phases. *Phys. Rev. B*, 87:235122, Jun 2013.

[379] S. A. Parameswaran, R. Roy, and S. L. Sondhi. Fractional quantum Hall physics in topological flat bands. *Comptes Rendus Physique*, 14:816–839, November 2013.

[380] Itamar Kimchi, S. A. Parameswaran, Ari M. Turner, Fa Wang, and Ashvin Vishwanath. Featureless and nonfractionalized mott insulators on the honeycomb lattice at 1/2 site filling. *Proceedings of the National Academy of Sciences*, 110(41):16378–16383, 2013.

[381] Lukasz Fidkowski and Alexei Kitaev. Topological phases of fermions in one dimension. *Phys. Rev. B*, 83:075103, Feb 2011.

[382] Ari M. Turner, Frank Pollmann, and Erez Berg. Topological phases of one-dimensional fermions: An entanglement point of view. *Phys. Rev. B*, 83:075102, Feb 2011.

[383] W. P. Su, J. R. Schrieffer, and A. J. Heeger. Solitons in Polyacetylene. *Phys. Rev. Lett.*, 42:1698–1701, Jun 1979.

[384] E. H. Rezayi and F. D. M. Haldane. Laughlin state on stretched and squeezed cylinders and edge excitations in the quantum Hall effect. *Phys. Rev. B*, 50:17199–17207, Dec 1994.

[385] Alexander Seidel, Henry Fu, Dung-Hai Lee, Jon Magne Leinaas, and Joel Moore. Incompressible Quantum Liquids and New Conservation Laws. *Phys. Rev. Lett.*, 95:266405, Dec 2005.

[386] Frank Pollmann and Ari M. Turner. Detection of symmetry-protected topological phases in one dimension. *Phys. Rev. B*, 86:125441, Sep 2012.

[387] E. Cornfeld and E. Sela. Chiral currents in one-dimensional fractional quantum Hall states. *ArXiv e-prints*, June 2015.

[388] J. R. Johansson, G. Johansson, C. M. Wilson, and Franco Nori. Dynamical Casimir Effect in a Superconducting Coplanar Waveguide. *Phys. Rev. Lett.*, 103:147003, Sep 2009.

[389] M. Sandberg, F. Persson, I. C. Hoi, C. M. Wilson, and P. Delsing. Exploring circuit quantum electrodynamics using a widely tunable superconducting resonator. *Physica Scripta*, 2009(T137):014018, 2009.

[390] C. M. Wilson, T. Duty, M. Sandberg, F. Persson, V. Shumeiko, and P. Delsing. Photon Generation in an Electromagnetic Cavity with a Time-Dependent Boundary. *Phys. Rev. Lett.*, 105:233907, Dec 2010.

[391] J. H. P. Colpa. Diagonalization of the quadratic boson Hamiltonian. *Physica*, 93A:327–353, 1978.

[392] Till D. Kühner, Steven R. White, and H. Monien. One-dimensional Bose-Hubbard model with nearest-neighbor interaction. *Phys. Rev. B*, 61:12474–12489, May 2000.